March 2015

Transport Limitations in Zeolites and Biomass Pyrolysis

Andrew Robert Teixeira
UMass Amherst

TRANSPORT LIMITATIONS IN ZEOLITES AND BIOMASS PYROLYSIS

A Dissertation Presented

by

ANDREW ROBERT TEIXEIRA

Submitted to the Graduate School of the Department of Chemical Engineering
University of Massachusetts Amherst in partial fulfillment
of the requirements for the degree of

DOCTOR OF PHILOSOPHY

February 2015

Department of Chemical Engineering

TRANSPORT LIMITATIONS IN ZEOLITES AND BIOMASS PYROLYSIS

A Dissertation Presented

by

ANDREW ROBERT TEIXEIRA

Approved as to style and content by:

_____
Paul J. Dauenhauer, Chair

_____
Wei Fan, Member

_____
David Ford, Member

_____
Scott Auerbach, Member

_____
Triantafillos J. Mountziaris, Department Head
Department of Chemical Engineering

DEDICATION

I would like to dedicate this thesis to those without whom I would not have been able to achieve any of this: my family and Dani

ACKNOWLEDGMENTS

First, I would like to express my sincere thanks to Professor Paul Dauenhauer for his mentorship over the past five years. Paul has continuously allowed and encouraged me to pursue my diverse research interests. He treated me as a colleague and provided invaluable insight and debates about teaching, research and management. Additionally, thanks for the midnight pancakes celebrating fresh-off-the-GC, "slam dunk, awesome data."

I would like to acknowledge the support of my colleagues in the Dauenhauer Research Group, many of whom I have been fortunate to collaborate with on several papers. Particularly, I would like to thank Luke Williams, Christoph Krumm and Alex Paulsen for being springboards for me to bounce some outlandish ideas off of, and who have supported several of such ideas with their time and research.

The work on understanding the dynamics and pathways during the high temperature pyrolysis of cellulose was a collaborative effort. From the experimental standpoint, I appreciate the work of Alex Paulsen, Christoph Krumm, Luke Williams, Cheng Zhu and Saurabh Maduskar. Additionally, many undergraduates have invested significant time on the various projects presented. I would also like to extend my appreciation to Professor Jonathan Rothstein whose insight into the Leidenfrost phenomena was invaluable. Computational support for elucidating the aerosol ejection mechanism was provided by Kyle Mooney and Professor David Schmidt.

The diffusion work focused on identifying surface barriers was also a very collaborative effort. Firstly, I would like to acknowledge and thank Chun-Chih Chang for synthesizing and characterizing all silicalite-1 particles used in the experimental studies and delving into this research project with me. I would also like to thank Xiaoduo Qi for the partnership we put together to re-establish and model the frequency response system. Several faculty members have greatly assisted by providing fundamental and specific insight along the way. First, I thank Professor Wei Fan who has greatly helped me to understand the intricacies involved in zeolite structures, their synthesis and perhaps most importantly pushing me to ask the correct questions

about the structural dependence of diffusion in zeolites. I would also like to thank Professor Scott Auerbach whose insight into the fundementals of diffusion in zeolites provided a strong base for my further research. Lastly, I would like to thank Professor David Ford who challenged me to further explore the observed diffusion limitations computationally. He invigorated my interest in understanding the mechanism dominating surface barriers, and greatly supported my Monte Carlo simulation work. To all three of these faculty, thank you for your time, insight, advise and for serving on my thesis committee.

It is not possible to list all the graduate students who have assisted me along my way assisting with everything from running my samples on your equipment to debugging code with me. Many thanks to you all. I would like to thank my entering class without whom I would not have completed my first year of studies. From a personal stance, I need to thank my various housemates (Tim Hanley, Whitney Stoppel, Sarah Wilson, Erika Saffer, Alex Paulsen, Christoph Krumm, Ray Gasper) --- you have all kept me sane and made Amherst feel like home. To the greater group of graduate students, ChEGS, you have helped make the past five years an unforgettable experience that I will certainly cherish.

From a personal standpoint, I want to thank my family and Dani. To my father, thank you for always being on top of me to do my best, and giving me the opportunities to pursue my passions. Your organization, checklists and encouragements and utter pride in what I do really helped me get to push myself to achieve what I have. To my mother, thank you for encouraging my curiosity even when it proved daunting. You've helped me to balance my scientific curousity, life and ambitions and always supported my decisions, even when it meant staying in school for life. To my older sisters, Andrea and Leanne, and their beautiful families, thank you for always keeping me as a part of the family even when my work life got crazy—it really helped me keep my sanity. Cristina, little sister, we went through a lot of this together. Whether it was your phone calls, visits to Boston, or back home, you have always been a huge part of my life and I'm really thankful that you've always been there. Lastly, to Danielle Volpe—Dani. You have been a

constant source of love and support through everything. You have motivated me beyond my own ambitions, and lifted me up when work seems impossible.

ABSTRACT

TRANSPORT LIMITATIONS IN ZEOLITES AND BIOMASS PYROLYSIS

February, 2015

ANDREW ROBERT TEIXEIRA, B.S., WORCESTER POLYTECHNIC INSTITUTE

Ph.D., UNIVERSITY OF MASSACHUSETTS AMHERST

Directed by: Professor Paul J. Dauenhauer

Biomass pyrolysis has been widely explored for its potential to generate a sustainable chemical source capable of producing synthetic fuels and chemicals. Lignocellulosic biomass is the carbon rich, inedible fraction of wood that is comprised of long oxygenated biopolymers, primarily cellulose, hemicellulose and the highly aromatic lignin. High temperature thermal conversion of biomass to bio-oil (pyrolysis oil) occurs on the order of milliseconds and converts long chain biopolymers to a carbon-rich liquid crude. The chemistry of biomass pyrolysis is greatly complicated by significant heat and mass transport challenges. The complex fluid dynamics of the reactive liquid intermediate are examined in situ with high temperature spatiotemporally resolved techniques (T = 450 – 1000 °C, 1 μm, 1 ms), chemical analyses and computational fluid dynamics. Discoveries include the mechanism for aerosol generation during pyrolysis, existence and control of the Leidenfrost effect, and understanding bio-oil microexplosions.

Zeolites are widely utilized to catalytically upgrade fuels by cracking, hydrogenation and hydrodeoxegenation as well as having applications in separations, sorption, ion-exchange. While new hierarchical materials are synthesized with transport lengthscales that are increasingly smaller, substantial diffusional transport limitations persist in small particles, often dominating the observed rates. The presence of these transport limitations remains a significant technical

challenge. In this work, a mechanistic understanding is developed to describe such limitations. The potential for surface barriers to diffusion are experimentally assessed by Zero Length Chromatography and frequency response methods, and further confirmed by dynamic Monte Carlo simulations.

TABLE OF CONTENTS

Page

LIST OF TABLES

Table Page

LIST OF FIGURES

Figure Page

SECTION I

DYNAMICS AND TRANSPORT OF CELLULOSE FAST PYROLYSIS

Section I—Introduction

Lignocellulosic biomass, including fast-growing trees and grasses, has been identified as major source of sustainable carbon capable of generating renewable fuels and chemicals.[1, 2] With over one billion dry tons of lignocellulosic biomass available in the United States,[3, 4] the U.S. Department of Energy has made it a goal to replace 30% of all transportation fuels with biofuels.[1] Thermochemical technologies for biomass conversion such as 'fast pyrolysis' to produce bio-oil and biomass gasification to produce syngas exhibit high throughput, the capability to produce existing commodity scale products (e.g. plastics or chemicals), and the potential to generate liquid transportation fuels.[5-7] Pyrolysis processes operate at high temperatures (400 – 800 °C) to break down biopolymers (20,000 to 400,000 a.m.u.) into smaller molecules (less than 200 a.m.u.) that are condensed at room temperature to form a liquid referred to as 'bio-oil.'[8-11] Currently, bio-oil is a viable replacement for heavy heating oils,[12] and it has the potential to replace traditional fossil fuel sources of gasoline and diesel via downstream catalytic upgrading.[13-17] However, widespread commercialization of fast pyrolysis technologies will first require a fundamental understanding of the processes involved during biomass fast pyrolysis including the heat, mass and kinetic dominated pathways.

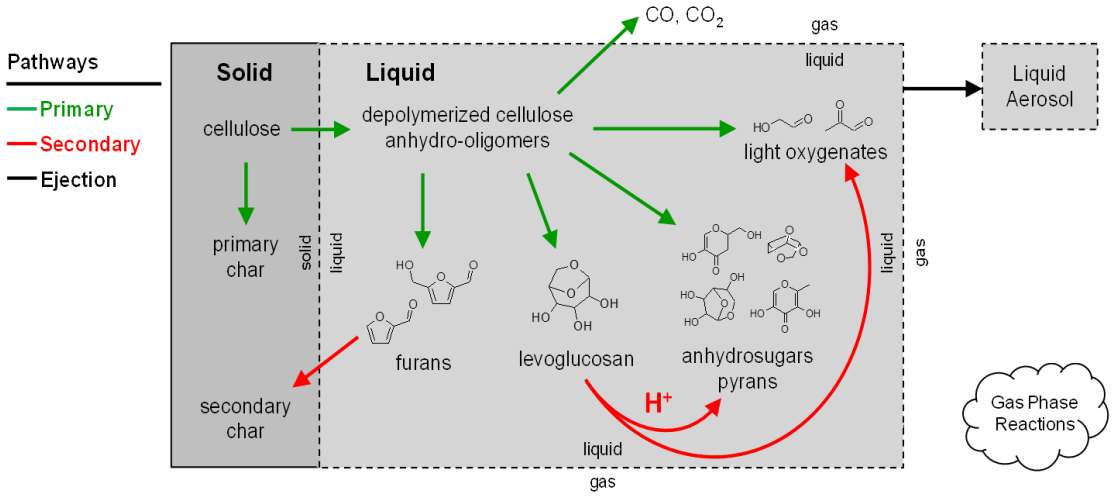

Figure 1-1: Primary and secondary pathways dominating biomass pyrolysis.

Significant progress has been made by the Dauenhauer group in understanding the liquid melt, including the existence of primary and secondary reaction pathways, as well as momentum transport mechanisms for non-volatile compounds (Figure 1). However, the system is greatly complicated by multiphase, multiscale nature of the complex system.

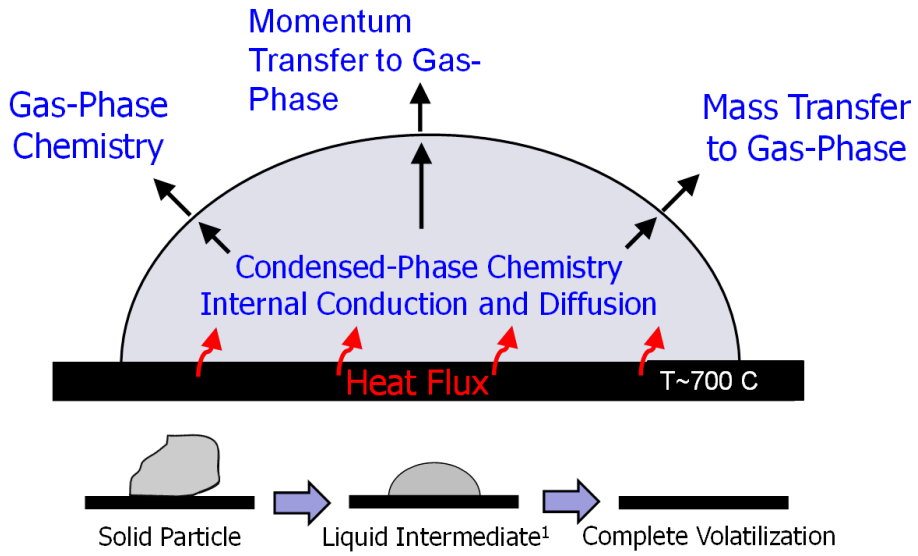

Figure 1-2: Overview of complexity of heat, mass and kinetic phenomena during biomass fast pyrolysis with a reactive liquid intermediate.

Progress toward mechanistic understanding of fast pyrolysis is limited by the complexity of the reaction environment.[18] As described in Figure 2, biomass pyrolysis reactions occur in three distinct phases: solid virgin biopolymers,[19, 20] gas-phase pyrolysis vapors, and a short-lived (<100 ms) liquid intermediate.[21, 22] At the industrial scale, these phases exist within a multi-scale system consisting of atomic-scale biopolymer/melt chemistry (10^{-10} to 10^{-9} m), particle/cellular heating and reaction (10^{-6} to 10^{-3} m), and reactor conversion (10^{-1} to 10^{1} m).[18] A complete kinetic description of pyrolysis systems will utilize a bottom-up approach (Figure 3), whereby biopolymer chemistry is integrated within reaction/transport particle models, which are ultimately included in complex fluid bed reactor models.

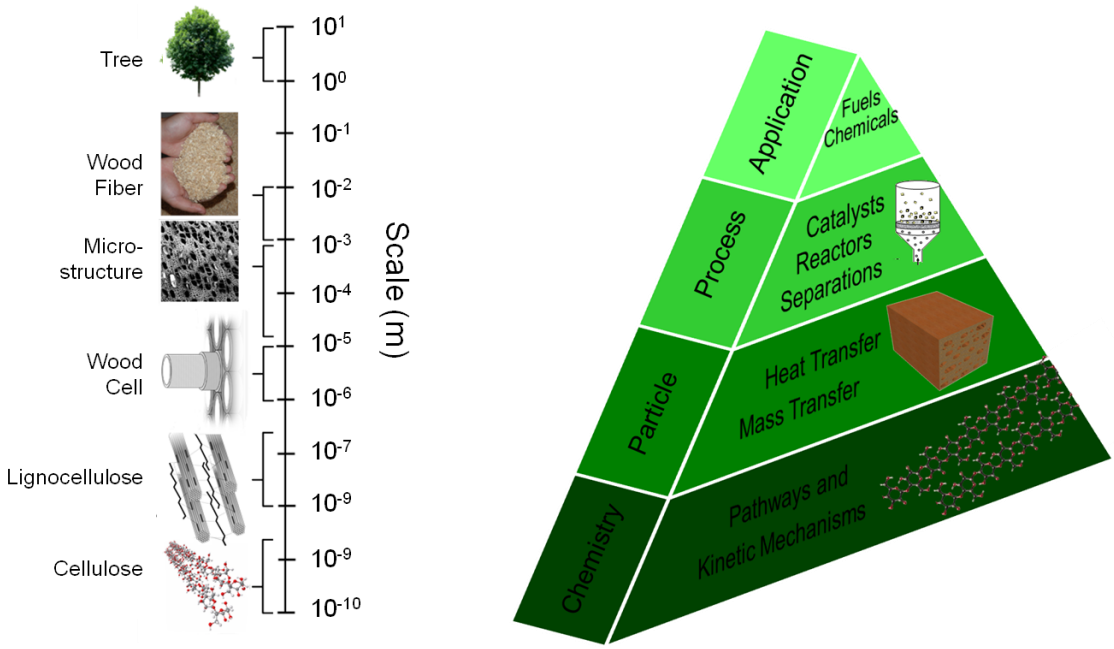

Figure 1-3: Bottom-up approach for understanding biomass pyrolysis.

The following sections will describe advances in understanding of the transport dominated liquid cellulose melt, including the discovery and mechanistic description of the aerosol pathway and the Leidenfrost effect. Additionally, new techniques including Quantitative Carbon Detection (QCD) and Diffuse Reflectance *in situ* Spectoscopy of Particles (DRiSP) were developed to approach the complex multi-scale systems.

References

1. A. J. Ragauskas, C. K. Williams, B. H. Davison, G. Britovsek, J. Cairney, C. A. Eckert, W. J. Frederick, J. P. Hallett, D. J. Leak, C. L. Liotta, J. R. Mielenz, R. Murphy, R. Templer, T. Tschaplinski, The path forward for biofuels and biomaterials. *Science* **311**, 484-489 (2006)10.1126/science.1114736).
2. K. Sanderson, A field in ferment. *Nature* **444**, 673-676 (2006)10.1038/444673a).
3. R. D. Perlack, L. L. Wright, A. F. Turhollow, R. L. Graham, B. J. Stokes, D. C. Erbach, "Biomass as a Feedstock for a Bioenergy and Bioproducts Industry: The Technical Feasibility of a Billion-Ton Annual Supply," (Oak Ridge National Laboratory, Oak Ridge, TN, 2005).
4. R. D. Perlack, B. J. Stokes, "U.S. Billion-Ton Update: Biomass Supply for a Bioenergy and Bioproducts Industry," (Oak Ridge National Laboratory, Oak Ridge, TN, 2011).
5. R. P. Anex, A. Aden, F. K. Kazi, J. Fortman, R. M. Swanson, M. M. Wright, J. A. Satrio, R. C. Brown, D. E. Daugaard, A. Platon, G. Kothandaraman, D. D. Hsu, A. Dutta, Techno-economic comparison of biomass-to-transportation fuels via pyrolysis, gasification, and biochemical pathways. *Fuel* **89**, S29-S35 (2010); published online EpubNov 1 (10.1016/j.fuel.2010.07.015).
6. P. J. Dauenhauer, B. J. Dreyer, N. J. Degenstein, L. D. Schmidt, Millisecond reforming of solid biomass for sustainable fuels. *Angewandte Chemie-International Edition* **46**, 5864-5867 (2007); published online Epub2007 (10.1002/anie.200701238).
7. D. Sutton, B. Kelleher, J. R. H. Ross, Review of literature on catalysts for biomass gasification. *Fuel Processing Technology* **73**, 155-173 (2001); published online EpubNov 13 (10.1016/s0378-3820(01)00208-9).
8. A. V. Bridgwater, D. Meier, D. Radlein, An overview of fast pyrolysis of biomass. *Organic Geochemistry* **30**, 1479-1493 (1999); published online Epub1999 (10.1016/s0146-6380(99)00120-5).
9. S. Czernik, A. V. Bridgwater, Overview of Applications of Biomass Fast Pyrolysis Oil. *Energy & Fuels* **18**, 590-598 (2004)10.1021/ef034067u).
10. T. P. Vispute, H. Zhang, A. Sanna, R. Xiao, G. W. Huber, Renewable Chemical Commodity Feedstocks from Integrated Catalytic Processing of Pyrolysis Oils. *Science* **330**, 1222-1227 (2010); published online EpubNov 26 (10.1126/science.1194218).
11. A. V. Bridgwater, Review of fast pyrolysis of biomass and product upgrading. *Biomass & Bioenergy* **38**, 68-94 (2012); published online EpubMar (10.1016/j.biombioe.2011.01.048).
12. J. G. Brammer, M. Lauer, A. V. Bridgwater, Opportunities for biomass-derived "bio-oil" in European heat and power markets. *Energy Policy* **34**, (2006); published online EpubNov (10.1016/j.enpol.2005.05.005).
13. G. W. Huber, S. Iborra, A. Corma, Synthesis of transportation fuels from biomass: Chemistry, catalysts, and engineering. *Chemical Reviews* **106**, 4044-4098 (2006); published online EpubSep 13 (10.1021/cr068360d).
14. T. R. Carlson, T. R. Vispute, G. W. Huber, Green gasoline by catalytic fast pyrolysis of solid biomass derived compounds. *Chemsuschem* **1**, 397-400 (2008); published online Epub2008 (10.1002/cssc.200800018).
15. T. R. Carlson, G. A. Tompsett, W. C. Conner, G. W. Huber, Aromatic Production from Catalytic Fast Pyrolysis of Biomass-Derived Feedstocks. *Topics in Catalysis* **52**, 241-252 (2009); published online EpubApr (10.1007/s11244-008-9160-6).
16. J. D. Adjaye, N. N. Bakhshi, PRODUCTION OF HYDROCARBONS BY CATALYTIC UPGRADING OF A FAST PYROLYSIS BIO-OIL .1. CONVERSION OVER VARIOUS CATALYSTS. *Fuel Processing Technology* **45**, 161-183 (1995); published online EpubDec (10.1016/0378-3820(95)00034-5).

17. S. P. Zhang, Y. J. Yan, T. C. Li, Z. W. Ren, Upgrading of liquid fuel from the pyrolysis of biomass. *Bioresource Technology* **96**, 545-550 (2005); published online EpubMar (10.1016/j.biortech.2004.06.015).
18. M. S. Mettler, D. G. Vlachos, P. J. Dauenhauer, Top ten fundamental challenges of biomass pyrolysis for biofuels. *Energy & Environmental Science* **5**, 7797-7809 (2012); published online EpubJul (10.1039/c2ee21679e).
19. V. Agarwal, P. J. Dauenhauer, G. W. Huber, S. M. Auerbach, Ab initio dynamics of cellulose pyrolysis: nascent decomposition pathways at 327 and 600 °c. *Journal of the American Chemical Society* **134**, (2012); published online Epub2012-Sep-12 (
20. J. Cho, S. Chu, P. J. Dauenhauer, G. W. Huber, Kinetics and reaction chemistry for slow pyrolysis of enzymatic hydrolysis lignin and organosolv extracted lignin derived from maplewood. *Green Chemistry* **14**, 428-439 (2012); published online Epub2012 (10.1039/c1gc16222e).
21. P. J. Dauenhauer, J. L. Colby, C. M. Balonek, W. J. Suszynski, L. D. Schmidt, Reactive boiling of cellulose for integrated catalysis through an intermediate liquid. *Green Chemistry* **11**, 1555-1561 (2009)10.1039/b915068b).
22. A. R. Teixeira, K. G. Mooney, J. S. Kruger, C. L. Williams, W. J. Suszynski, L. D. Schmidt, D. P. Schmidt, P. J. Dauenhauer, Aerosol generation by reactive boiling ejection of molten cellulose. *Energy & Environmental Science* **4**, 4306-4321 (2011).

CHAPTER 1

AEROSOL GENERATION BY REACTIVE BOILING EJECTION OF MOLTEN CELLULOSE

1.1 Introduction

The thermal degradation of lignocellulosic biomass and cellulose-based materials is the enabling chemical process occurring during forest fires, the smoking of cigarettes, and the combustion, fast pyrolysis, and gasification of biomass for conversion to power and biofuels.[1-3] The fuel value and environmental and health impacts of thermally degrading biomass and bio-derived cellulose-based materials depend upon the types of vapor products produced as well as the quantity, composition, and size distribution of aerosols and particulate emitted. As much as 30% of degrading biomass can be converted to aerosols and particulate.[4, 5] Additionally, as much as 60% of the inorganic content in the condensable products of biomass pyrolysis results from the generation of aerosols.[6] Significant technical effort has focused on understanding the degradation process to characterize and predict the distribution of pyrolysis products.[7]. However, the mechanism of aerosol generation directly from cellulose and lignocellulosic materials remains unknown.[6]

1.1.1 Origin of Nonvolatile Pyrolysis Species

The dominant experimental approach to understanding lignocellulose and cellulose decomposition has focused on identifying and quantifying the product gases and hundreds of condensable vapor species[8]. Exhaustive characterization of condensed vapors from lignocellulose pyrolysis reveals numerous key degradation pathways to volatile components including levoglucosan, hydroxymethyl furfural, and monolignols such as 2-ethylphenol and vanillin.[8, 9] However, the analytical identification of pyrolysis products from biomass has also observed a

significant fraction of heavy, nonvolatile products including carbohydrate[4, 10] and lignin oligomers,[11, 12] as well as nonvolatile inorganic compounds including SiO2, CaO, and MgO.[2]

The origin of higher molecular weight and nonvolatile species from the thermal degradation of lignocellulose and cellulose is currently unknown. One proposed explanation suggests that volatile organics produced by degradation re-condense to secondary aerosols and react to form higher molecular weight species[13, 14]. As depicted in Figure 1, thermal degradation of lignocellulosic biomass increases volatility of organic material until it evaporates producing organic vapors. Organic vapors can thermally decompose and/or oxidize to produce permanent gases (e.g. CO or CO2). Organic vapors can also react to form aromatics which polymerize to poly-aromatic hydrocarbons (PAHs) and form soot. Alternatively, organic vapors can condense to bio-oils or nucleate and grow secondary organic aerosols wherein re-combination reactions can occur to higher molecular weight species.

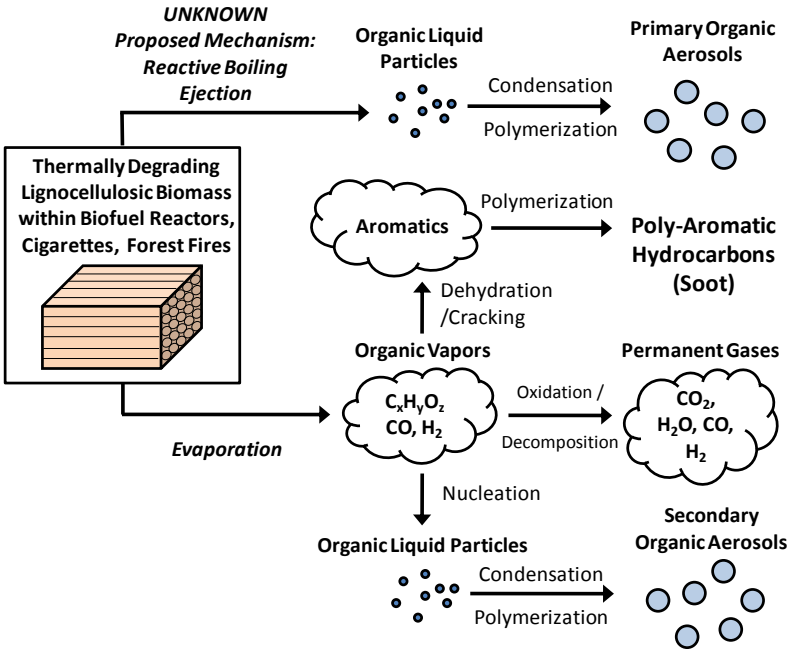

Figure 1-1: Organic Aerosol Generation and Formation Pathways. Aerosol formation occurs through the evaporation of organic vapors. Subsequent cracking and dehydration produces aromatics that can polymerize to poly-aromatic hydrocarbons. Vapors can also thermally decompose to permanent gases. Additionally, organic vapors can nucleate small liquid particles which condense and grow to larger secondary organic aerosols. Alternatively, we propose a new mechanism whereby organic liquid particles are generated directly from solid biomass by reactive boiling ejection to primary organic aerosols.

The evaporation mechanisms account for some nonvolatile pyrolysis products, but this argument does not explain the existence of intact biomass-derived oligomers, some of which are tetramers of lignin or carbohydrate polymers up to nine monomers long[4, 11, 15, 16]. This mystery has led to the postulation of a 'thermo-mechanical ejection' mechanism whereby biomass fragment particles are entrained in the product gases and carried away as aerosols[4, 17]. This mechanism hypothesizes that the rapid increase in volume resulting from the degradation of biopolymers to gases results in 'explosive destruction' of the cellulose or lignocellulosic structures, thereby entraining particle fragments within the gaseous products.[4, 18]

1.1.2 Reactive Boiling Ejection of Cellulose

We propose a new, alternative biomass-ejection mechanism referred to here as 'reactive boiling ejection' whereby primary aerosols are spontaneously generated directly from cellulose during pyrolysis. Thermal decomposition of solid, crystalline cellulose produces a short-lived (<100 ms) intermediate liquid state which exhibits violent boiling as it further degrades to vapors and gases.[19] By experimentally characterizing the ejection phenomenon using high speed photography, the formation and collapse of vapour bubbles within reacting molten cellulose is identified as the driving force for ejection. The bursting of bubbles generates a liquid cavity which collapses and forms a liquid jet. Subsequent jet fragmentation produces high-velocity liquid aerosols which are entrained in the gas phase. The sequence of reaction and fluid events leading to aerosol ejection are confirmed here by high speed photography, sampling of the produced aerosols, and computational fluid dynamics (CFD) simulation of the ejection phenomenon.

The approach of combined experimental characterization and fluid modelling of reactive boiling ejection is complicated by the difficulty in describing the composition and physical properties of the intermediate cellulose liquid. While the existence of an intermediate liquid state has been proposed for over two decades,[20, 21] its existence was only recently confirmed.[19]

Consequently, reaction and transport characteristics of the intermediate liquid have not been previously measured. The intermediate cellulose liquid is a highly non-equilibrium, high-temperature condensed fluid that exists for only a fraction of a second. Therefore, it exhibits extreme physical properties such as low surface tension consistent with high temperature fluids near their critical point.[22] These characteristics prevent utilization of conventional techniques for measurement of physical properties of stable fluids. For these reasons, we provide an estimate of the surface tension based on the ejection speeds of generated aerosols that is supported by CFD simulation. The combination of estimation of fluid properties with visual observation, chemical characterization, and simulation strongly supports the reactive boiling ejection mechanism.

1.2 Methods

Evidence for the reactive boiling ejection mechanism was obtained with several experimental and simulation methods. Observation of aerosol ejection and measurement of ejection characteristics occurred with high speed photography of molten cellulose. Aerosols ejected from molten cellulose were collected and analyzed, and their composition was compared with independent high-temperature carbohydrate experiments. The ejection events observed experimentally were compared with CFD simulations. The simulations support the estimated physical properties of intermediate liquid cellulose and provide insight into the precise details of the mechanism of the ejection phenomenon.

1.2.1 Materials

Microcrystalline cellulose samples (Lattice NT-200) were obtained from FMC Biopolymer and sieved to particles greater than 250 μm. Samples of cellulose exposed to the air naturally absorbed ~5 wt% moisture. Moisture content was determined gravimetrically by drying in a vacuum oven. Levoglucosan was purchased from Sigma-Aldrich (99%, #316555). Sucrose

was purchased from Fischer Scientific (Crystalline, S5-500). γ-Al_2O_3 was purchased from Sigma-Adrich (97%, #13-2525). Trimethylsilylimidazole was purchased from Sigma-Aldrich (#92751). All chemicals were used as received.

1.2.2 High Speed Photography

The experimental apparatus consisted of a heated surface of either α-Al_2O_3 or Fecralloy (Fe-Cr-Al-alloy). A solid α-Al_2O_3 disk (2 mm thick by 22 mm diameter) was held inside a stainless steel block for thermal and structural stability. The α-Al_2O_3 disk was prepared by pressing γ-Al_2O_3 particles to 5000 psi in a hydraulic press and sintering at 1150°C for 12 hours. The disk was seated on a stainless steel cylinder, and it was thermally insulated and shielded from hot combustion gases. Nitrogen gas was supplied with a metering valve through a quartz tube positioned 2 cm above the disk surface to maintain an oxygen-free environment. Heat was applied directly to the stainless steel block with a MAPP torch, and the temperature of the disk was measured by direct contact with a Type K thermocouple on the reactive surface. Particles were delivered to the disk by a controlled gravity fed addition system that entrained the particles in the nitrogen gas prior to reaction.

A similar setup was used for heating particles on the Fecralloy surface, except that a Fecralloy disk was suspended over a Bunsen burner**.** The Fecralloy surface was calcined beforehand at 1150 °C for 12 hours prior to use in the experiment.

Image sequences were recorded at 1000 frames per second with a Photron Fastcam Ultima APX Imager by Photron USA, Inc. Three magnifying components were employed in series with the Infinity Long Distance Microscope by Infinity Photo-Optical Company: a TR 2x tube, a Model K2 lens, and a CF-3 Objective. Auxiliary lighting was required for use at high speeds and was provided by a Solarc LB50 lamp by Welch Allyn, Inc.. The image size was

calibrated by direct photographs of objects with known dimensions with identical camera configuration and focal length.

Original photographs were captured at 1024x1112 pixels and were cropped as needed. Electronic image adjustments were uniformly applied to entire images and image sequences. The NIH's ImageJ 1.43u[23] and GIMP 2.6.10[24] were used to perform uniform adjustments of contrast and brightness to grayscale images. No selective enhancements were made. Figures. 3, 5 & 6 were cropped and contrast/brightness adjusted. The image sequences can be observed in full video form in Videos S1, S2, and S3[†], respectively. Additionally, original frames corresponding with Figure 3 can be observed in Figure 1-16.

ImageJ was also used to process frame differenced image sequences (Figure 3). The original image sequence was contrast and brightness adjusted using ImageJ, followed by application of a mathematical differencing technique by which two consecutive frames were subtracted. The images were subtracted on a pixel level, such that the resulting value of each pixel represented the change in grayscale over 1 ms. Negligible change between frames results in a dark/black pixel, whereas significant change between frames results in a grey/white pixel. This operation was performed across the entire sequence, and both original and differenced sequences can be seen in Video S2[†].

1.2.3 Levoglucosan Polymerization

For a controlled comparison, levoglucosan reaction chemistry was examined using a custom built polymerization apparatus constructed from a glass Pasteur pipette. After purging nitrogen through the glass pasteur pipette to remove atmospheric oxygen, the narrow end was sealed with a torch**.** The sample of levoglucosan was then added to the open end of the pipette and tapped down to the sealed end**.** More nitrogen was flushed through the headspace before the open end was sealed about 5 cm from the sample. This reaction tube was then placed in a furnace at specified temperatures and time durations.

A second polymerization experiment was performed using an amber 2 mL vial that was left open to the atmosphere with the levoglucosan dispersed in the bottom of the vial based on the procedure of Radlein et al..[4] This vial was kept at 240°C for 20 minutes.

1.2.4 Aerosol Characterization

An apparatus, depicted in Figure 1-12, similar to that used in the high speed photography was adapted to collect and rapidly quench aerosol products. A stainless steel heating block and α-alumina disk were used in conjunction with a MAPP torch to provide heat for the pyrolysis surface. Additionally, a stainless steel gas addition halo was used to deliver nitrogen to the surface and ensure a non-oxidative environment.

Aerosols were collected using a glass slide held at a 45 degree angle about one centimeter above the reactive surface. Glass slide temperatures did not exceed 200 °C, ensuring minimal secondary reactions. Cellulose particles about 300 μm in size were slowly added to the surface in a continuous manner.

Direct measurement of the size distribution of sampled aerosols was obtained by use of visual microscopy and image processing tools. A 10x optical microscope equipped with a visual light source was used to obtain images covering an area of about 0.57 cm^2 each. This design allowed for quantitative measurement and qualitative visualization of aerosol particles in the range of 0.9 to 10 micron. The NIH program ImageJ was used to systematically count all particles with a sphericity index of 0.8-1, and the results are shown in histogram form in Figure 5A of the manuscript.

For the purpose of identification, aerosols were extracted from the slides by ultrasonication in deionized water for five minutes. This procedure involved breaking the slide into small fragments and submerging the pieces in 5 mL of deionized water inside a 20 mL vial, then placing the vial into the ultrasonicator bath. This solution was then pipetted into a 3 mL syringe and filtered through a 0.2 micron PTFE filter into a 2 ml amber vial where it was left to

evaporate overnight under vacuum at 70 °C. The dried aerosols were then derivatized using a 1:1 mixture of pyridine and trimethylsilylimidazole (TMSI) to a total volume of 1.5 mL. This mixture of methylating agent and sample was placed in a water bath at 60 °C for 30 minutes and immediately analyzed on an Agilent 7890 gas chromatograph with a 5975C mass spectrophotometer. The method used a G4513A auto injector and had a split/splitless injection port temperature of 280 °C and an injection volume of 1-2 μL. The column used was a 30 m DB-5 with a 320 μm diameter and a 1.5 μm film. Separation was obtained with the use of a temperature programmed ramp that started at 65 °C, held for 2 minutes, ramped to 300 °C at 6 °C per minute, and held for 30 minutes as suggested by Medeiros et al..[25]

1.2.5 CFD Modeling

The hypothesized ejection mechanism was examined by comparing the measured ejection velocities (Figure 5A) to a transient axisymmetric CFD simulation (Figure 7). Based on first principles, specifically the conservation of mass and momentum, the incompressible Navier-Stokes equations are solved using the finite volume numerical method. This approach to cavity collapse simulation, similar to the process by Duchemin, et al.,[26] models interface transport and capillary effects with the Eulerian volume of fluids (VOF) method. However, the current approach is capable of handling topological changes in the interface, such as the formation of droplets and bubbles. Unlike previous work, the current simulation specifically considers ejection from the curved interface of a droplet, rather than an infinite pool with a flat surface.[26]

Flow simulations were performed within the OpenFOAM CFD framework described by Weller.[27] The code solves the discretized unsteady Navier-Stokes equation with nominally second-order accurate spatial discretization**.** An incompressible, laminar flow is assumed**.** Pressure-velocity field coupling is accomplished with the pressure-implicit split-operator (PISO) method.[28] The VOF method identifies fluid phases with a dimensionless scalar color function α

which is advected conservatively with the flow**.** The piecewise expression for α from Rusche[29] is defined in eqn. 1.

$$f(x) = \begin{cases} 1 & \text{for a point inside fluid a} \\ 0 < \alpha < 1 & \text{for a point in the transitional region} \\ 0 & \text{for a point inside fluid b} \end{cases} \qquad 1\text{-}1$$

The unsteady evolution of the α field follows the transport equation shown in eqn. 2 with **u** being the underlying velocity field. Due to smearing of the interface, density and viscosity values in mixed cells are weighted by α using a harmonic mean weighting scheme[30, 31] as shown in (eqn. 3).

$$\frac{\partial \alpha}{\partial t} + \mathbf{u} \cdot \nabla \alpha = 0 \qquad 1\text{-}2$$

$$\mu_{HM} = \frac{\mu_1 \mu_2}{\alpha \mu_2 + (1-\alpha)\mu_1} \qquad 1\text{-}3$$

Interface sharpness is maintained with the counter-gradient compression method described in Berberović et al.[32] Capillary forces are incorporated into the cell-centered pressure field by means of the continuum surface force (CSF) model by Brackbill.[33]

The computational domain is comprised of an axisymmetric, uniform, structured mesh of one million 2D cells with a bubble resolution of 100 cells across the radius R_{bubble} as shown in Figure 2. The ratio of the bubble radius to droplet radius R_{bubble} /$R_{droplet}$ is approximately equal to 0.13.

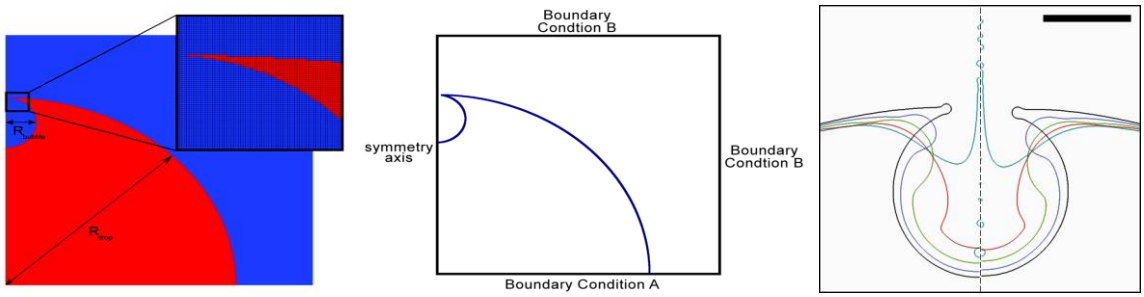

Figure 1-2: Bubble Collapse Simulation Design. A.) Initial Conditions. Computational domain and α field initial conditions (red: α = 1, blue: α = 0). For all simulations Rbubble = 15 µm and Rdroplet = 113 microns with the bubble cavity initially resolved with 100 grid cells. B.) Boundary Conditions. Illustration of domain boundary conditions for all ejection computations. C.) Mesh Resolution Test. Simulated cavity collapse sequences using identical material properties with two different mesh resolutions. All but the smallest scale phenomena are fully resolved and mesh independent. RB=15 µm, Rdroplet=113 µm, γ=5e-6 N/m, µ= 1e-5 kg/m·s. Left Panel: 1 million cells. Right Panel: 1.25 million cells. The time duration between interface profiles is 750 µs. Scale bar = 15 µm.

Boundary conditions for the pressure (p) and velocity (**u**) fields are described in Table 1 and applied in the manner shown in Figure 2. Boundary condition "A" represents a no-penetration, no-slip wall with the liquid-solid interface contact angle pinned at 90°. Boundary condition "B" represents approximate far-field ambient conditions (i.e. a constant pressure and a uniform flow field). The variable ***n*** represents the outward pointing unit vector orthogonal to the boundary face. The absolute value of p_0 is inconsequential as the incompressible Navier-Stokes equation uses only the gradient of the pressure.

Table 1-1: Simulation Boundary Conditions

Field	Condition A	Condition B
P	$\frac{\partial p}{\partial \boldsymbol{n}} = 0$	$\mathbf{p = p_0}$
U	**u = (0 0 0)**	$\frac{\partial \boldsymbol{u}}{\partial \boldsymbol{n}} = 0$

1.3 Results

The presented experiments include the observation of the ejection phenomenon from cellulose, the characterization of ejected aerosol particles, the observation of the mechanism within a carbohydrate surrogate, and the simulation of the proposed mechanism by computational fluid dynamics.

1.3.1 Cellulose Aerosol Ejection

We show, using high speed photography, that primary aerosols are produced from molten cellulose by the collapse of bubbles which subsequently form a liquid jet. As depicted in Figure 3A and observed in Video S1[†], solid particles of microcrystalline cellulose initially (0 ms) impact a 700 °C alumina surface before coming to rest. After one-tenth of a second, the particle is fully molten as previously reported by the investigators and appears to 'wet' the surface forming a hemispherical droplet.[19]

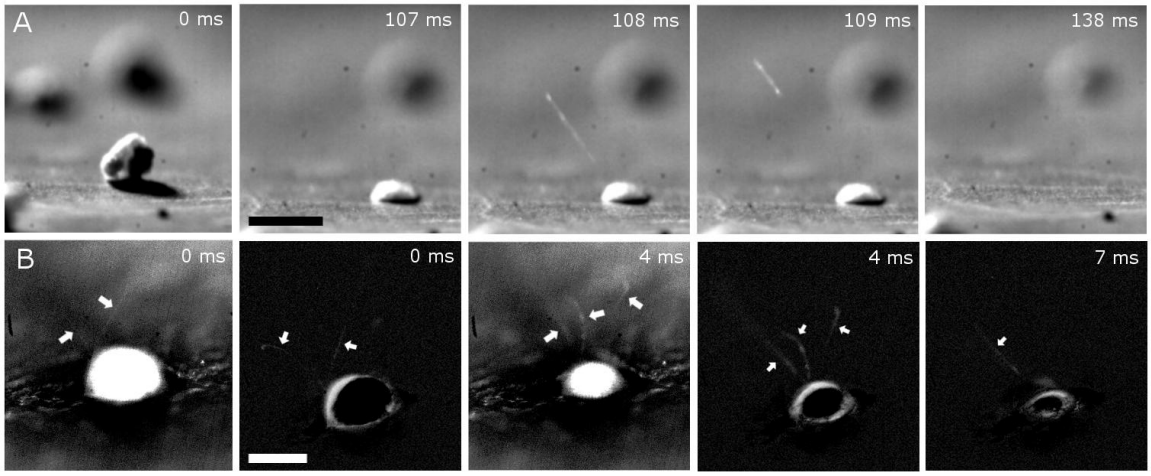

Figure 1-3: Organic Aerosol Generation and Formation Pathways. Aerosol formation occurs through the evaporation of organic vapors. Subsequent cracking and dehydration produces aromatics that can polymerize to poly-aromatic hydrocarbons. Vapors can also thermally decompose to permanent gases. Additionally, organic vapors can nucleate small liquid particles which condense and grow to larger secondary organic aerosols. Alternatively, we propose a new mechanism whereby organic liquid particles are generated directly from solid biomass by reactive boiling ejection to primary organic aerosols.

Spontaneous ejection of an aerosol particle occurs at 107 ms and is visible as the trace of an ejected particle (108 ms) moving in a one millisecond increment of time. One millisecond later

(109 ms), the ejected particle appears to slow considerably as determined by the length of the particle trace. While the sizes of particles cannot be precisely determined directly from photography, the range of observed particle diameters must be greater than 0.3 microns, as limited by conventional light microscopy.[34] Also, the observed particles must be less than the width of particle streaks in the photographs (<10 μm). Finally, the molten droplet fully converts to gases, vapors, and aerosols leaving a clean surface (138 ms).

Molten cellulose continuously ejects aerosols. As depicted in Figure 3B and Video S2[†], a single droplet of cellulose degrading on a 700 °C α-alumina surface ejects six independent particles, highlighted by arrows, over a period of seven milliseconds. Frames collected at 0 ms and 4 ms are presented in two formats to highlight the shape of the molten droplet and the path of the ejected particles. The first and third panels are presented in greyscale, high-contrast format which reveals the highly reflective, white cellulose droplet. From these images, the lens depth of field is visible as the region 'in focus' extending from the back to the front of the particle. Particles are only visible with the photographic system and lighting scheme if their path traverses through the lens depth of field. Particles ejected towards and away from the camera are not detected.

The remaining three panels (0, 4, and 7 ms) of Figure 3B are presented by differentiating between frames in series. By this technique, differences between sequential frames resulting from motion are indicated as white, while motionless objects which appear in repeated frames appear as black. Within these frames, multiple ejected aerosols are visible as white streaks. Additionally, the movement of the molten droplet resulting from aerosol ejection and evaporation of volatile organics is visible as a white line encircling the entire droplet. From this analysis, all of the ejected aerosols appear to exhibit initial velocities within the same order of magnitude. Also, many of the particles appear to exhibit curved trajectories.

1.3.2 Aerosol Ejection Velocity

Due to the extremely short time scale, small droplet size, and the opaque nature of cellulose, the mechanism resulting in the ejection of intermediate cellulose cannot be directly observed from droplets (Figure 3). However, by measuring the distance traversed of a single ejected particle across a single frame, it is possible to determine the velocity of the ejected particle. Measurement of numerous ejection events from cellulose on high temperature surfaces leads to the distribution of velocities of observable ejected particles as shown in Figure 4A. By this method, particles ejected from cellulose exhibit ejection velocities of 0.05-0.50 m/s.

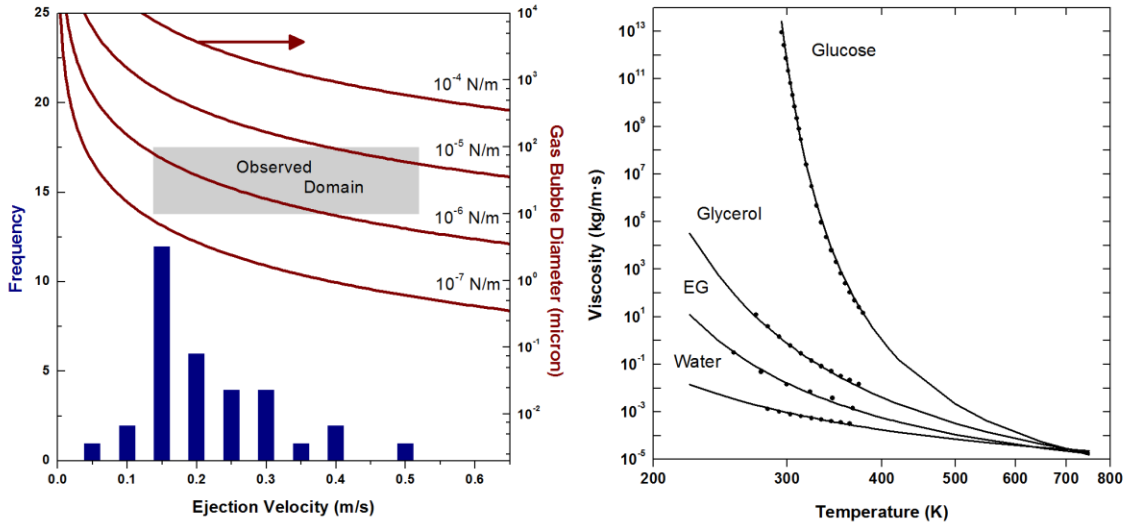

Figure 1-4: Physical Properties of Molten Cellulose. A.) Droplets of molten intermediate cellulose exhibit ejection of aerosol particles in the range of 0.05-0.50 m/s. The relationship between ejection velocity and vapor bubble size (equation 1) varies with surface tension (solid lines). Comparison of observed ejection velocities with observed bubble sizes (grey box) indicates a molten cellulose surface tension of 10-6 to 10-5 N/m. B.) The viscosity of various oxygenated liquids including glucose, glycerol, ethylene glycol, and water exhibits strong temperature dependence. Extrapolation to 750 °C using the Vogel-Fulcher-Tammann relation indicates that viscosity of oxygenated fluids approach 10-5 kg/m*sec.

Additionally, high speed photography of cellulose particles on high temperature (700 °C) α-alumina reveals the formation of gas bubbles within the intermediate liquid cellulose in the size range of 10-100 microns as observed in previous high speed videos.[19]

1.3.3 Ejected Aerosol Size Distribution and Composition

Aerosol particles generated directly from molten cellulose on a 700 °C alumina surface surrounded by inert nitrogen were quenched and collected on a glass slide shown in Figure 5. The collected particle dimensions were observed by light microscopy, and the size distribution indicates that the particle size range with the maximum number of particles is less than one micron which is consistent with existing literature.[2-4]

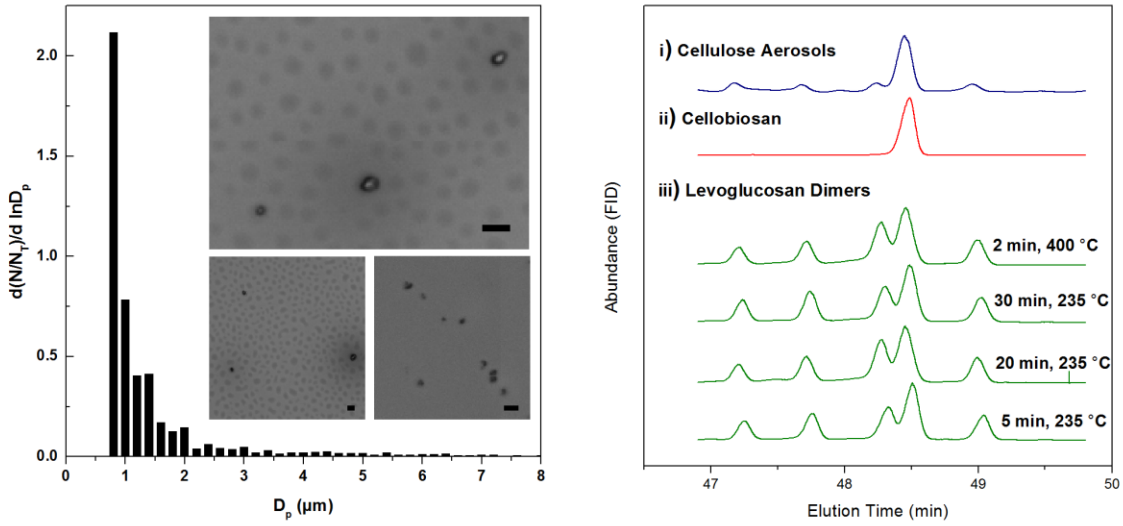

Figure 1-5: Ejected Particle Characterization. A.) Ejected aerosols (inset photographs) exhibit a particle diameter (DP) distribution with a maximum less than one micron. B.) Chemical analysis of the collected aerosols (i) by silyl-methylation and gas-chromatography/mass-spectrometry indicates that aerosols contain only one dominant carbohydrate dimer, cellobiosan, as shown in (ii). However, re-polymerization of levoglucosan (iii) is shown to produce nearly equal amounts of multiple different carbohydrate dimers. All chromatograms are scaled vertically for equal cellobiosan peak area between trials for comparison of relative dimer quantities. Scale bars = 10 μm.

The ejected aerosol particles transport nonvolatile chemical species from the pyrolyzing biopolymer. Collected, methylated aerosol particles (Figure 5B, chromatograph iii) contained levoglucosan as well as a single dominant carbohydrate dimer, cellobiosan (1,6-Anhydro-β-D-cellobiose), and almost negligible quantities of other carbohydrate dimer stereoisomers. The identity of cellobiosan within the aerosol sample was confirmed by comparison of retention times and mass spectrometry patterns with a pure cellobiosan sample that had undergone the same methylation procedure (chromatograph ii). The potential for the production of cellobiosan by

dimerization of levoglucosan was examined experimentally by controlled pyrolysis of levoglucosan within an inert reaction chamber. Methylation and characterization of the levoglucosan reaction products over a temperature range of 100-500 °C indicates that levoglucosan polymerization produces carbohydrate dimers with nearly equal quantities of cellobiosan and maltosan (1:0.9). The observation of a single, dominant dimer exhibiting the β-glycosidic linkage existing in cellulose confirms that the observed cellobiosan resulted predominately from the decomposition of cellulose and was ejected as an aerosol particle. Therefore, nonvolatile cellobiosan was transported within the ejected particle and not created via condensation and reaction of evaporated species.

1.3.4 Mechanism Observation

While bubble collapse and jet ejection cannot be directly observed within cellulose, a molten carbohydrate surrogate (β-D-Fructofuranosyl-α-D-glucopyranoside) was selected that exhibits a transparent molten state and produces pyrolysis products similar to cellulose (e.g. levoglucosan, furans, glycoaldehyde). As depicted in Figure 6 and Video S3[†], the carbohydrate surrogate melts to form a 500-800 μm diameter liquid droplet on 650 °C Fecralloy before decomposing to gases/vapors. Fecralloy was selected as the heating material for this specific experiment, because molten carbohydrates visibly de-wet thereby eliminating the role of the surface from the ejection mechanism.

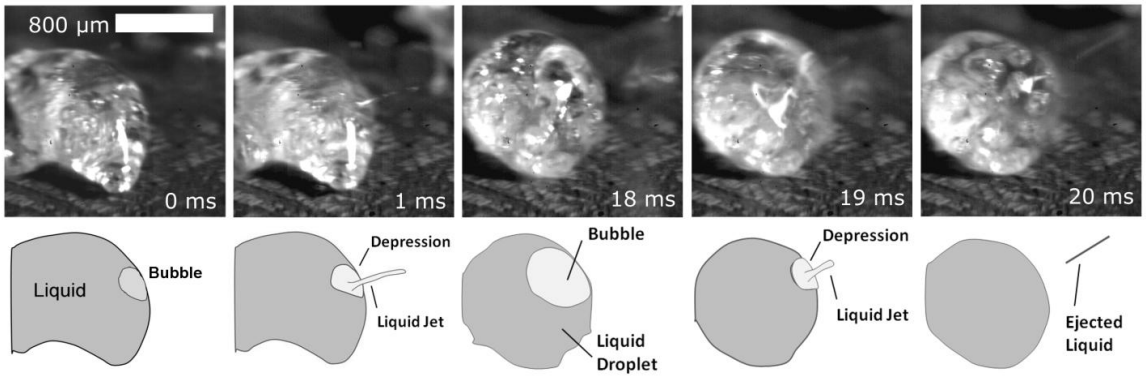

Figure 1-6: Molten Carbohydrate Ejection Mechanism. A non-wetting droplet of molten carbohydrate (β-D-fructofuranosyl-α-D-glucopyranoside) thermally decomposes on a 650 °C Fecralloy (Fe-Cr-Al-alloy) surface. Thermal decomposition nucleates a bubble of vapor products (0 ms) which subsequently collapses forming a liquid jet extending from the liquid droplet (1 ms). Scale bar = 500 µm

Two independent ejection events are visible within 20 milliseconds which support the bubble collapse ejection mechanism. Diagrams are provided for each photographic frame highlighting the key ejection phenomena. Within the molten liquid droplet (0 ms), thermal degradation produces volatile organics and gases producing a gas bubble. One millisecond later (1 ms), the bubble bursts producing a depression on the surface of the liquid droplet and a liquid jet extending 500 µm from the liquid droplet.

A second event occurs later (16 ms, not shown) which forms a second vapor/gas bubble which grows to a diameter of 400 µm in diameter. The bubble rises and eventually rests (18 ms) beneath a thin layer of intermediate liquid near the upper right side of the droplet. Within one millisecond (19 ms), the surface tension maintaining the intermediate liquid is overcome by the vapor pressure within the bubble. The thin layer of liquid ruptures and the gas bubble collapses forming a depression and liquid jet extending out of the molten liquid droplet. The subsequent frame (20 ms) visibly depicts the liquid droplet returned to the spherical conformation and the ejected aerosol particle moving with high velocity (0.35 m/s) as a streak through the frame.

1.3.5 Surface Tension and Viscosity Estimation

The general mechanism of bubble disintegration, jet formation, and subsequent fragmentation leading to ejection permits estimation of the surface tension of molten cellulose by comparison of experimental ejection velocities with an energy balance. The initial state of a submerged bubble exhibits initial potential energy in the form of surface tension as, $E_i=\gamma A_B$, where γ is the surface tension and A_B is the surface area of the liquid/vapor-bubble interface. The final state of an ejected particle of mass, m, velocity, v, and surface area, A_{AP}, has a final energy, $E_f=\gamma A_{AP} + 0.5mv^2$. By assuming inviscid flow, these two energy states can be equated, providing an order of magnitude estimate of the surface tension, γ, as a function of the ejection velocity, the liquid density, ρ, the gas bubble size, R_B, and the size ratio, φ, as related by the Weber number in eqn. 4,

$$We = \frac{\rho v^2 R_B}{\gamma} = \frac{3(1-\varphi^2)}{\varphi^3} \qquad 1\text{-}4$$

By using a particle-to-bubble ratio of $R_{AP}/R_B = \varphi=0.20$ and a liquid density of $\rho=1000$ kg/m^3 (Appendix A) [35] (estimated by extrapolating to the predicted reaction temperature of 693-753 K),[36, 37] it is possible to relate bubble size to ejection velocity as a function of surface tension as depicted in Figure 4. Based on the observation that internal gas bubbles are 10-100 μm in size, and bounded by the observed domain of ejection velocities (grey box), it is possible to estimate the surface tension of the liquid-cellulose/vapor interface as 10^{-6} to 10^{-5} N/m. This low range of surface tension is consistent with high temperature, boiling liquids near the critical point.[22]

Viscosity of the high temperature, highly non-equilibrium intermediate cellulose liquid is unknown. To proceed, we estimated the liquid viscosity by extrapolation of known oxygenates and supported the resulting viscosity estimate with subsequent fluid simulations. As depicted in Figure 4B, the viscosity of water, ethylene glycol (EG), glycerol, and sub-cooled glucose have been measured as a function of temperature.[38, 39] These molecules contain multiple hydroxyl

groups consistent with anhydrosugars and anhydro-oligomers thought to comprise the intermediate cellulose liquid. Extrapolation of the measured viscosities to the considered reaction temperature of 750 °C indicates a dynamic viscosity of 10^{-5} kg/m•sec. Extrapolation was conducted using the Vogel-Fulcher-Tammann equation relating viscosity to temperature.[40, 41]

1.3.6 Ejection Simulation

In this work, CFD simulations are used to corroborate the estimated surface tension, as well as the hypothesized droplet ejection mechanism. Simulation results, depicted in Figure 7, support the proposed molten cellulose ejection mechanism and predicted fluid properties. A 3D revolved surface showing particle ejection ($\gamma=5\bullet10^{-6}$ N/m) in Figure 7A-B indicates that the bubble cavity collapses forming a liquid jet which is observed to fragment to liquid aerosol particles. Additionally, the jet is observed to extend from a liquid depression consistent with observations in Figure 6 with the surrogate carbohydrate.

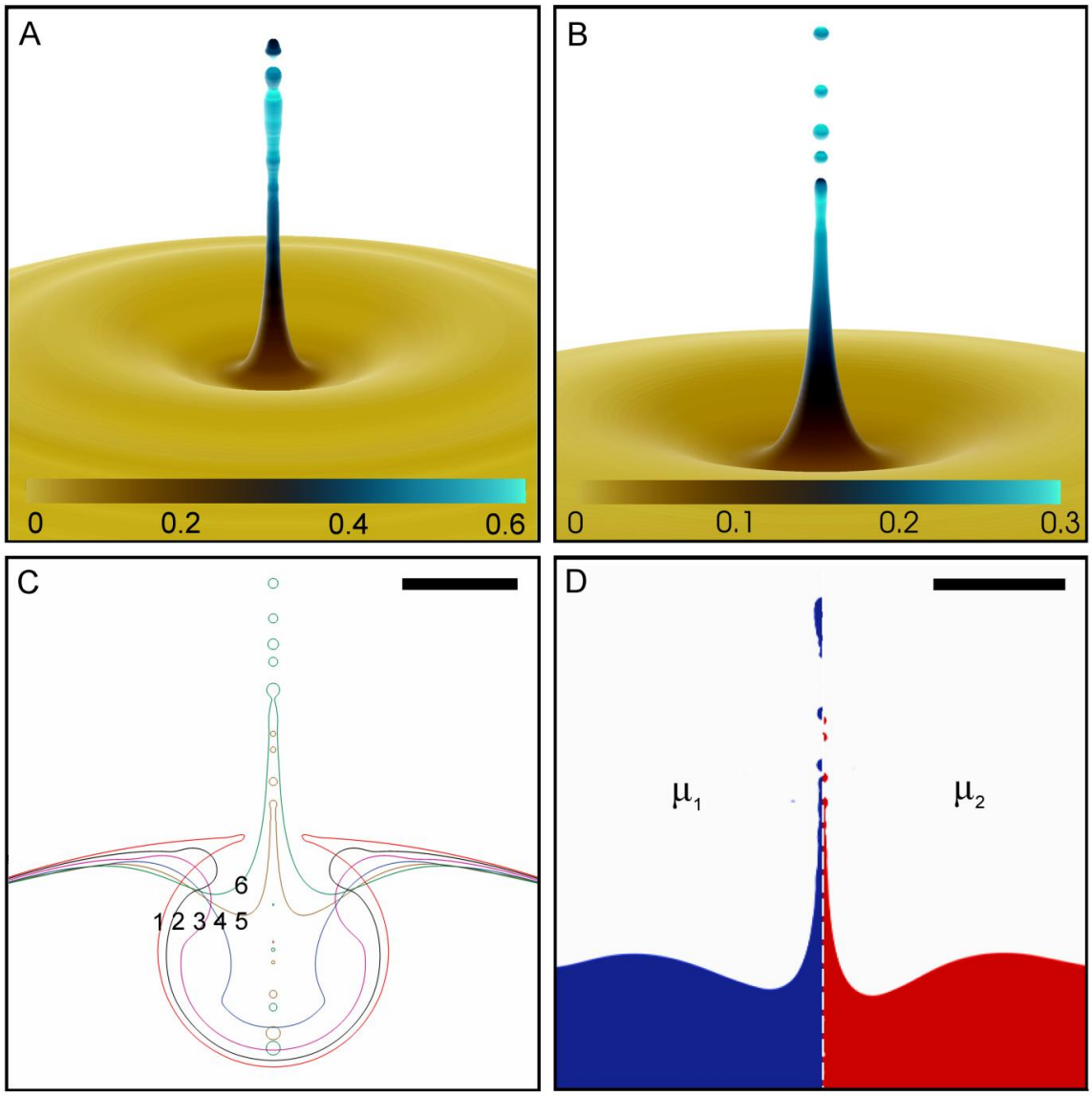

Figure 1-7: Molten Carbohydrate Ejection Mechanism. (A) Case 3: Simulated bubble collapse and liquid jet formation depicting a resolved α=0.5 iso-surface at t=0.38 ms colored by velocity magnitude (RB=15 µm, Rdroplet=113 µm, γ=5•10-6 N/m, µ=10-5 kg/m•s). (B) Case 2: Simulated bubble collapse and liquid jet formation depicting a resolved α=0.5 iso-surface at t=0.38 ms colored by velocity magnitude (RB=15 µm, Rdroplet=113 µm, γ=5•10-6 N/m, µ=10-6 kg/m•s). (C) Simulated bubble collapse sequence. Liquid ejection occurs through the disintegration and collapse of a gas bubble and subsequent formation of a liquid jet protruding from a molten liquid depression. The duration between images is 75 µs. Scale bar = 15 µm. (D) Variation of viscosity by an order of magnitude (µ1=10-6 kg/m•s and µ2=10-5 kg/m•s) with identical initial geometry and γ=5•10-6 N/m produces only modest changes in ejection morphology and ejecta velocity. Time=375 µs. Scale bar = 15 µm.

Simulated jet and particle velocities are in the range of 0.1-0.5 m/s in agreement with the experimentally observed ejection speeds (Figure 4). Surface tension values used in simulations ($5 \bullet 10^{-6} < \gamma < 1 \bullet 10^{-5}$ N/m) are within the range bound by the experimental observations and analytical deduction. The variation of material property values between simulations is outlined in Table 2. Without *a priori* adjustments, the simulation accurately matched observed ejection velocities, giving strong support to the surface tension approximation.

Table 1-2: Table 2. Physical Properties of Simulation Runs.

Case	μ (kg•m^{-1}•s^{-1})	γ (N•m^{-1})	Figure	Video
1	$1 \bullet 10^{-5}$	$1 \bullet 10^{-5}$	Figure S13	S4
2	$1 \bullet 10^{-6}$	$5 \bullet 10^{-6}$	Figure 8	S5
3	$1 \bullet 10^{-5}$	$5 \bullet 10^{-6}$	Figure S12	S6

The minor importance of viscosity is verified through the comparison of the results of simulation runs "2" and "3" as depicted in Figure 7D. Here, an order of magnitude change in viscosity within the predicted viscosity range yields only a modest change in jet morphology and ejected droplet velocities after 375 μs. Negligible loss of kinetic energy to viscous dissipation during bubble collapse and ejection affirms the secondary role of viscous forces.

To ensure adequate mesh resolution, an identical case is run on the standard grid (one million cells) and a second more resolved grid (1.25 million cells). As illustrated in Figure 2, the one million cell mesh satisfactorily produces grid-independent results for all the large-scale features.

1.3.7 Simulation Mechanism

The simulated fluid collapse sequence illustrated in Figure 7C depicts liquid film retraction and bubble collapse occurring within 375 μs, leading to the formation of a fragmenting jet. The initial state, depicted earlier in Figure 2, initializes the process just after the liquid film between the gas bubble and the external gas phase has ruptured. In the 75 μs following perforation of the film (interface 1), the liquid begins to retract but retains very sharp features

with extremely high curvature. Subsequent outlines depicting interface 2 (150 μs) and interface 3 (225 μs) indicate that the liquid rapidly retracts under the influence of surface tension.

After 300 μs (interface 4) the bubble cavity begins to significantly collapse as fluid halfway between the top and bottom of the bubble gains radial momentum. Within the next 75 μs, the bubble completely collapses focusing liquid momentum to a smaller quantity of fluid. During this span of 75 μs, liquid coalescence occurs at a position above the bottom of the vapor cavity, thereby trapping small vapor bubbles within the liquid. Subsequent momentum focusing results in the formation of a liquid jet (interface 5, 375 μs) which extends from the liquid depression and has fragmented to three liquid particles. Continued extension of the liquid jet (interface 6, 450 μs) slightly reduces the depth of the liquid depression. Additionally, the liquid jet has fragmented into a fourth liquid particle.

The effects of bubble-collapse on the entire liquid droplet are visible in Figure 8, a simulation output depicting jet formation within a 270° revolved iso-surface colored by velocity magnitude. After 75 μs, the potential energy within the highly curved liquid interface has translated to an increase in surface velocity primarily at the top of the liquid droplet. As time progresses the velocity of the liquid/gas interface increases at deeper positions within the bubble cavity. After 264 μs, the cavity coalesces and the interfacial velocity achieves almost 0.5 m/s depicted as an aqua-blue surface. At this time, the liquid jet forms and a new gas bubble is entrained within the large liquid droplet. After coalescence, the liquid jet continues to increase in length and fragment to produce aerosol particles (279 μs). Subsequent jet growth includes the fragmentation of several new aerosol particles. However, aerosol particles observed from initial fragmentation of the jet are observed to slow and recombine to form larger aerosol particles (35 μs).

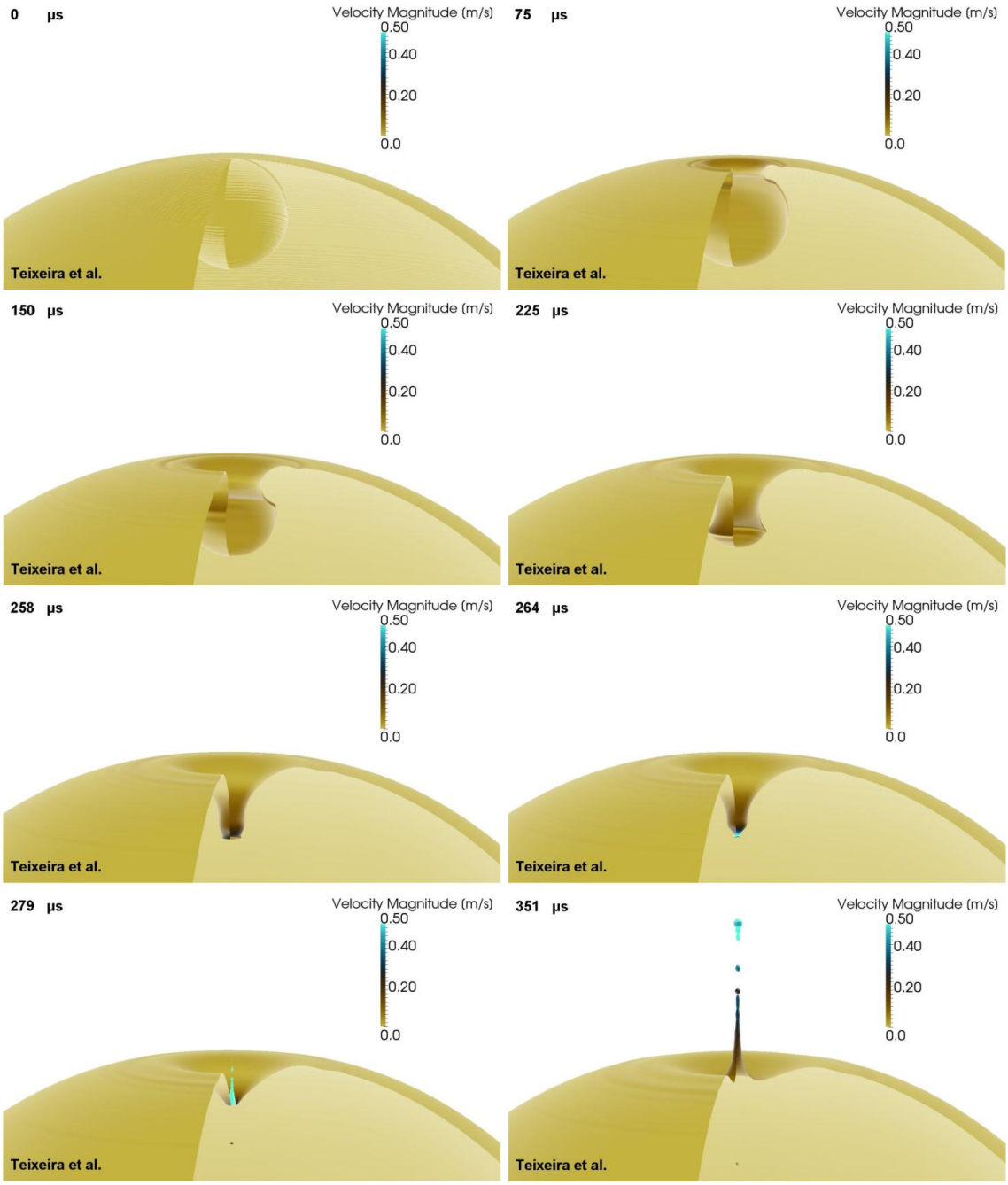

Figure 1-8: Ejection CFD Simulation. Simulated bubble collapse and liquid jet formation depicting a 270° revolved α=0.5 iso-surface colored by velocity magnitude (RB=15 µm, Rdroplet=113 µm, γ=5*10-6 N/m, µ=10-6 kg/m*s).

Bubble collapse and jet fragmentation are observed to generate a second liquid jet extending downward into the liquid droplet. As depicted in Figure 9, vorticity iso-lines indicate significant fluid circulation directly below the vapor cavity during (0.220 ms, frame A) and after (0.250 ms, frame B) collapse. After cavity collapse (Figure 9B), the liquid jet extends from the surface and gas bubbles are entrained within the liquid. Relative to the size of the drop, this circulation zone is mainly localized around the cavity site. In general, even though vorticity is localized, pressure effects could potentially extend further from the jet. However, in this case, the presence of the gas-liquid interface constrains pressure. Away from the jet the surface curvature of the droplet is nearly uniform, indicating a nearly uniform pressure on the liquid side of the interface, as required by the balance of normal forces. Hence, neither vorticity nor pressure effects due to the jetting extend very far. This observation suggests that multiple jets emanating from a single droplet would not interfere with each other unless they were located close together.

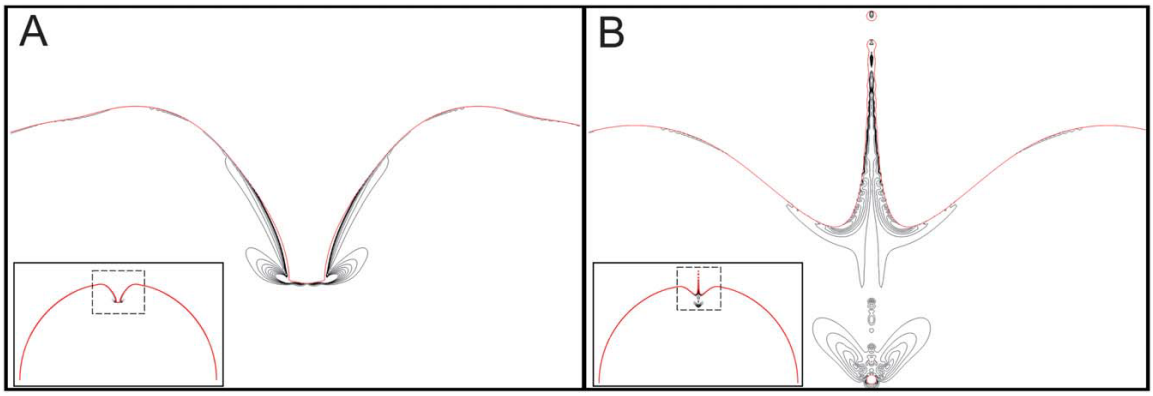

Figure 1-9: Molten Cellulose Ejection – Simulation Vorticity. Vorticity magnitude iso-lines (colored black) of simulation case #1 before (panel A: t=0.220 ms) and during (panel B: t=0.250 ms) ejection. Each figure shows ten iso-lines uniformly spanning 0 – 10,000 s-1. The inset figures show the scope of magnification with the gas/liquid interface colored red

The kinetic energy of the downward jet is comparable to the kinetic energy of the ejected aerosol. Integration of the kinetic energy throughout the entire liquid droplet relative to the kinetic energy of the ejected aerosols post-ejection indicates that both kinetic energies are about the same. Fluid motion throughout the droplet is distributed around the region of cavity collapse, but the liquid motion is considerably slower than the aerosol ejection velocity. This conclusion

supports the adequacy of eqn. 4, which relies on the measurement of aerosol kinetic energy, to estimate the surface tension of the intermediate liquid cellulose within an order of magnitude.

1.4 Discussion

The entire process of generating an aerosol particle from solid cellulosic biomass by reactive boiling ejection requires thermal decomposition to a liquid intermediate, nucleation and growth of vapor bubbles, and eventual bubble rupture and collapse followed by jet formation and fragmentation to aerosols. This entire sequence of events occurs extremely quickly (<400 μs), within a very high temperature system (>400 °C), and at very small length scales (10^0-10^1 μm).

1.4.1 Stage I. Intermediate Cellulose Liquid Formation.

The ejection process is enabled by the formation of an intermediate liquid from cellulose. Conclusive evidence for the existence of this intermediate liquid state has previously been identified as the key problem for understanding and predicting the thermochemical conversion of cellulose.[42] An intermediate liquid was hypothesized to exist when pyrolyzing biomass was observed to behave like meltable solids on high temperature, moving surfaces[20]. Subsequent experiments reported that rapid heating and cooling produced solid cellulose products with smooth surfaces indicative of a liquid intermediate.[21] Recently, the liquid intermediate was confirmed to exist by high speed photography[19] as a short-lived intermediate that exhibits violent boiling and evaporation. This evidence is consistent with several cellulose decomposition chemical kinetic mechanisms which include an 'active cellulose' intermediate to describe pyrolysis product formation. [43-46]

The composition of the intermediate liquid phase is unknown. A common hypothesis states that cellulose with initial chain lengths exceeding 1000 glucan monomers initially undergoes glycosidic cleavage and depolymerisation to shorter chain polymers capable of melting to a liquid.[13] This was supported by experiments that characterized the solid residue remaining

from very short residence time flash pyrolysis of pure cellulose and observed a series of anhydro-oligomers that were two-to-seven units long.[47] These results were supported by independent experiments which exposed cellulose to brief flashes of radiant heat. After characterization of the products, the authors concluded that the intermediate liquid is comprised of anhydro-oligomers,[4] as illustrated by the first three anhydro-oligomers in Figure 10.

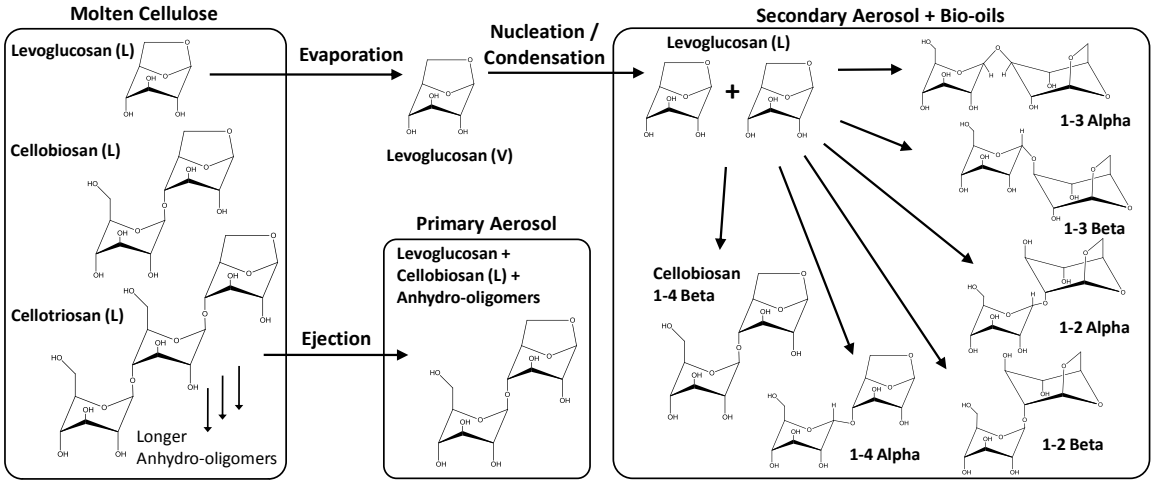

Figure 1-10: Pathways Determining the Composition of Primary and Secondary Aerosols. The intermediate chemical species within liquid (L) molten cellulose are transported to the gas phase (V) through evaporation and aerosol ejection. Primary liquid aerosols are produced by the ejection of aerosols directly from molten cellulose, and they are comprised of the reaction products of cellulose including cellobiosan (1,4-beta linkage). Secondary liquid aerosols form from the evaporation of levoglucosan and volatile organics. Subsequent nucleation generates a secondary liquid aerosol wherein levoglucosan can dimerize to form both alpha and beta glucosidic linkages between the C1,C2, C3, and C4 carbons.

1.4.2 Stage II. Vapor Bubble Nucleation and Growth

The process of bubble nucleation and growth initiates a stage of potential energy generation proportional to the surface area of the vapor bubble. While the origin of vapor bubbles cannot be identified from the present experiments, at least three potential nucleation options exist: (i) homogeneous nucleation, (ii) heterogeneous nucleation, and (iii) vapor bubble entrainment.

The thermodynamic driving force for nucleation is the increased vapor pressure of evolving pyrolysis products. As pyrolysis of the nonvolatile original cellulose polymer proceeds, smaller chemical compounds are produced by reaction within the intermediate liquid which exhibit increasing volatility. The identified products of pyrolysis are primarily volatile and

include a range of molecular sizes from C_1 (e.g. CO, CO_2), C_2 (e.g. glycoaldehyde), C_3 (e.g. acetone), to C_6 (levoglucosan).[8] Anhydrosugars have been shown to exhibit vapor pressures several orders of magnitude greater than sugars, and are likely evaporated as pyrolysis products directly from the intermediate liquid.[48]

Homogeneous nucleation can occur throughout the intermediate liquid.[49, 50] Alternatively, cellulose particle pyrolysis on high temperature surfaces and within fluidized reactors occurs within a thermally thick particle.[51] Therefore, conversion of solid cellulose to the liquid intermediate occurs as a reacting wave through the particle.[52, 53] The presence of a solid/liquid interface introduces the potential for continuous heterogeneous nucleation of vapor bubbles within pyrolyzing biomass particles.

An alternative bubble generation process occurs through vapor entrainment during bubble collapse. As depicted in Figure 8, the vapor cavity resulting from bursting bubbles collapses inward and can lead to several entrained gas bubbles. Coalescence near the bottom of the cavity entrains a pocket of vapor which remains within the fluid near the base of the jet. These results are consistent with the previous discovery of bubble entrainment within vapor cavities.[26] This observation indicates that a single ejection event can lead to the initiation of one or more subsequent ejection events, depending on the number of entrained vapor bubbles. This indicates that once the process of ejection is initiated, it can potentially continue independently of gas nucleation.

Once formed, gas bubbles grow and rise subject to buoyancy forces within the molten cellulose liquid until they reach the liquid droplet/gas interface. Bubble growth is observed within the carbohydrate surrogate (Figure 6 and Video S3[†]). Additionally, bubbles can coalesce with other bubbles or fragment to separate, smaller bubbles.

The size of the vapor bubble prior to rupturing is important, because it determines the quantity of interfacial surface area and potential energy of the system. Vapor bubble size is ultimately determined by the relationship between vapor generation (reaction) and the time

required for the bubble to approach the droplet interface. Bubbles approaching the free surface require the draining of the film and thinning of the liquid interface.[54] Experimental measurement of film thickness during thinning has indicated that the rate of thinning increases with decreasing film viscosity.[55] Fluid modelling of film drainage using the lubrication approximation also indicates increased thinning rate as the density difference between the liquid and vapor phases increases, as the interfacial surface tension decreases, and as the vapor bubble diameter decreases.[56, 57] Additionally, the velocity of the bubble approaching the free surface has been observed to alter the time required for film thinning.[58]

The resulting liquid film separating the bubble at the free surface from the external atmosphere can achieve very thin liquid film thicknesses. This thin liquid film is visible in the surrogate carbohydrate in Figure 6 (18 ms). A critical thickness of the liquid film identifies the unstable conditions whereby perturbations within the film result in a sufficiently large hole which subsequently expands due to surface tension and ruptures the film.[59] Instability is thought to occur when the film has achieved thicknesses less than 100 nm, at which point London-van der Waals forces acting over a very short range are able to pull the two sides of the film together and initiate film rupture.[26, 54, 56, 60]

1.4.3 Stage III. Bubble Rupture, Collapse and Jet Fragmentation

Rupture of the thin liquid film initiates the collapse mechanism converting the potential surface energy within the gas bubble to liquid momentum within aerosol particles. The specific mechanism for liquid jet and aerosol particle generation has been extensively studied for numerous applications.[61-63] After the liquid film is perforated, it has been shown to retract forming an expanding toroidal rim[63, 64] similar to that observed in Figure 8 (150 μs). As retraction occurs, gases flow out from within the vapor cavity resulting from the difference between the vapor pressure and the environmental gas pressure.

The retracting rim of the liquid film potentially breaks up into tiny droplets referred to as 'film droplets'.[65, 66] These small droplets are ejected in multiple directions resulting from the radial momentum of the film during retraction and the upward flow of gas escaping the vapor cavity. The mechanism of film droplet generation occurs through asynchronous breakup resulting from surface tension and film thickness variations in addition to turbulence from air escaping from the cavity.[63] Fragmentation is not thought to occur by capillary ripples, which propagate too slowly relative to the rate of film retraction.[54, 64]

Film droplets and their mechanism of production are not observed with the present high speed photography technique which would be incapable of observing these small particles at short timescales. Additionally, the contribution of film drops to the production of cellulose-based aerosols is unknown. However, it has been shown that the number of film drops produced increases linearly with surface area of the liquid film,[67, 68] thereby indicating that their relative importance decreases with decreasing vapor bubble size.

The cavity collapse predicted by our simulation for molten cellulose is consistent with existing literature describing collapse driven by the surface tension of the free interface. A time sequence diagram of a collapsing bubble at 6000 frames/second obtained from high speed photography of a bursting bubble reveals the transition from vapor cavity to depression and liquid jet.[69] The liquid protrusion at the top of the vapor cavity produced from the retracting film appears to grow in size and move downward into the cavity. Ahead of the protrusion, capillary waves are observed along the vapor cavity wall. [69, 70]

The resulting liquid jets observed in our work are consistent with known jet formation mechanisms. Cavity collapse has been shown repeatedly to form two liquid jets.[71-73] One liquid jet extends downward into the bulk liquid forming a vortex ring made visible within experiment using a liquid dye.[69] This is consistent with fluid simulations which predict regions of increased vorticity within the liquid directly below the collapsed vapor cavity.[26, 54, 74] For comparison, our

system (Figure 9) exhibits a similar downward flowing liquid jet observable as vorticity isolines surrounding entrained vapor bubbles.

The other more visible liquid jet extends upward from the liquid cavity and is surrounded by a distinctive vapor depression. This liquid jet is observed twice in our experiments from separate ejection events from the surrogate carbohydrate in Figure 6 (1 ms and 19 ms).

The upward flowing jet extends from the free surface and potentially fragments to produce aerosols travelling at high velocity relative to the surrounding fluids. Extension of the jet above the original liquid level results in one of two potential outcomes. For initial vapor bubbles above a critical size, the jet is produced and subsequently retracts without releasing a jet drop.[62] The critical bubble size for each liquid/vapor combination has been identified for numerous systems.[62, 75, 76] However, a systematic method for predicting the critical vapor bubble size remains to be developed. Alternatively, below the critical vapor bubble size, jets are observed to breakup due to surface tension producing one or more liquid aerosol particles.[62]

Jet fragmentation is known to produce one or more aerosol particles as demonstrated in the fluid simulation of Figure 8. Hydrodynamic instability of the liquid jet results from the reduction in surface area from the formation spherical droplets. Fragmentation is induced through the growth of sinusoidal perturbations in the jet radius which exhibit wavelengths in excess of the jet radius.[77] This is consistent with Figures. 7 and 8 and Videos S5-S7[†] which depict capillary waves and liquid jet fragmentation into several droplets.

The number and size of droplets produced from fragmenting jets resulting from bubble collapse is highly variable and dependent on the properties of the fluid. Numerous experimental sources report a size ratio, φ, of the aerosol particle radius, R_{AP}, to the bubble radius, R_B, as $0.1 < R_{AP}/R_B = \varphi < 0.3$.[62, 78, 79] This range of aerosol-particle-to-bubble ratios is consistent with our experimental measurements of aerosol particles in Figure 5 which exhibit particles smaller than 10 μm, while vapor bubbles are observed in size up to 100 μm. The size distribution of multiple aerosol particles from a single droplet has been shown to vary minimally from the first to last

ejection .[79] The range of size-ratios and variation in consecutive aerosol particle generation is consistent with the fluid simulations in Figure 7 and 8.

1.4.4 Physical Properties of Molten cellulose

The method of surface tension estimation (Figure 4A) based on an energy balance (eqn. 4) between stationary bubbles and high velocity aerosols has basis in previous bubble collapse ejection simulations which develop criteria for inviscid flow. Jet velocity (measured when the jet reaches the original liquid interface level) has been shown to be predictable for large dimensionless bubble radii defined as the $(R_B/R_V)=\gamma R_B\rho/\mu^2$, where R_B is the radius of the vapor bubble, R_V is the viscous capillary length, and μ and ρ are the viscosity and density of the liquid, respectively.[26] Above $(R_B/R_V=10^3)$, jet velocity is in agreement with the inviscid scaling relationship, and the dimensionless jet velocity $(V\mu/\rho)$ is predictable as: $(V\mu/\rho)=C*(R_B/R_V)^{-0.5}$, where C is a constant. For these conditions, the energy balance assumes that viscous dissipation is negligible, and all of the potential energy of the vapor bubble is converted to the surface energy of the aerosol and the kinetic energy of the ejected aerosol and droplet. While the kinetic energy within the droplet after bubble collapse cannot be measured by experiment, simulation of the ejection phenomenon estimates that the droplet kinetic energy is about the same as the ejected aerosol kinetic energy. Therefore, this method (eqn. 4) can sufficiently predict surface tension correctly within an order of magnitude as depicted in Figure 4.

Confirmation of the surface tension range of approximately 10^{-6}-10^{-5} N/m of intermediate liquid cellulose by simulation also affirms the secondary role of viscous forces by dimensional analysis. The low surface tension exhibits a viscous capillary length, defined as $R_v=\mu^2/\rho\gamma$, in the range of 10^{-2}-10^{-1} microns with the viscosity, $\mu=10^{-5}$ kg/m•s. Since the observed internal vapor bubbles (10^1-10^2 μm) are several orders of magnitude greater than the viscous capillary length ($R_B >> R_V$), viscous effects are expected to be of secondary importance. This also supports the assumption of negligible viscous dissipation in the derivation in eqn. 4, and permits simple

prediction based on surface tension of ejection velocities and particle quantities from natural materials. Additionally, calculation of the Ohnesorge number of the vapor bubble collapse mechanism indicates the minimal effect of viscous forces. Defined as $Oh=\mu/(\rho\gamma L)^{0.5}$, the Ohnesorge number for vapor bubbles of radius L=18 μm and liquid density ρ=1000 kg/m^3, exhibits a range of $2*10^{-3} < Oh < 8*10^{-2}$ for the surface tension range $10^{-6} < \gamma < 10^{-5}$ N/m and viscosity range $10^{-6} < \mu < 10^{-5}$ kg/m*s.

The estimated surface tension range of approximately 10^{-6}-10^{-5} N/m used in simulations of intermediate liquid cellulose is also consistent with existing theory and relationships between surface tension, gravitational forces and temperature. In this range, the capillary length can be calculated as $a=(\gamma/\rho g)^{1/2}$ which predicts $10 < a < 30$ μm. This is consistent with the liquid intermediate cellulose droplets depicted in Figure 3A-B which exhibit significant sagging due to gravity. The radius of curvature is significantly reduced at the edges of the liquid droplet in comparison to the top. Additionally, the low surface tension is consistent with existing theory that predicts significant reduction of surface tension as the temperature of the liquids approaches the critical point.[22]

1.4.5 Transport of Nonvolatile Material within Aerosols

A key result of the reactive boiling ejection mechanism is its ability to transport nonvolatile material from solid biomass such as cellulose to the gas phase. As depicted in Figure 5, aerosols ejected from the molten state contain only one dominant carbohydrate dimer (cellobiosan). As depicted in Figure 10, this supports the hypothesis that cellulose decomposes primarily through glycosidic cleavage to anhydro-oligomers.[47] Therefore, fluid ejected from the molten state should only contain a single linkage type (β-1-4) in the form of cellobiosan. This is in agreement with Radlein et al.[4] which demonstrated that anhydro-dissacharides within bio-oils must result from primary pyrolysis, but the mechanism of transport of cellobiosan to the vapor phase was unknown.

Alternatively, anhydro-disaccharides and larger anhydro-oligomers can form within liquid products through evaporation and secondary polymerization as depicted in Figure 10. Levoglucosan exhibits sufficiently high vapor pressure relative to glucose, carbohydrate dimers, and larger carbohydrate polymers that it significantly evaporates during pyrolysis.[48] Once evaporated, levoglucosan (and other vapors) can condense to a secondary liquid (bio-oils and secondary aerosols) wherein they can re-polymerize. Nucleophilic attack of one of three levoglucosan hydroxyl groups on C_1 of a second molecule of levoglucosan by two potential orientations produces at least six potential isomers of anhydro-dimers. Some of these dimers, including maltosan (α-1-4) and cellobiosan (β-1-4) were observed by polymerization of the pure levoglucosan sample (Figure 5B). For a wide range of temperatures (235-400 °C), nearly a one-to-one ratio (1:0.9) of cellobiosan-to-maltosan was observed indicating that these two stereoisomers are formed at about the same rate. This is inconsistent with the composition of measured aerosols, and the absence of a strong maltosan peak in the aerosol chromatogram supports the conclusion that nonvolatile cellobiosan originated from the molten liquid.

1.4.6 Implications and Future Directions

While cellulose and carbohydrates visibly exhibit particle ejections, there is interest in the ejection phenomenon in lignocellulosic materials such as trees and grasses which contain inorganic species and a significant amount of lignin. Lignocellulosic materials are predicted to exhibit an intermediate liquid phase.[20, 36] Additionally, high speed photography of hardwood lignin samples on 700 °C α-alumina (Figure 11 and Video S4[†]) clearly exhibits decomposition of lignin through an intermediate liquid with bursting bubbles. However, the intermediate lignin liquid and significant char product exhibit high light absorptivity, preventing the observation of ejected particles with the current high speed photography experimental setup.

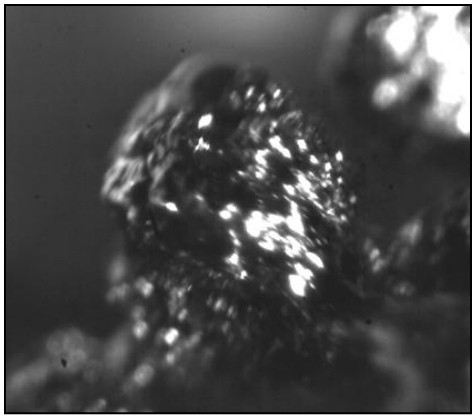

Figure 1-11: Molten Lignin Bubble Generation and Collapse. Molten lignin on 700 °C alumina decomposes through a bubbling intermediate liquid before reacting to form secondary solid char. Numerous white specular highlights indicate a smooth liquid surface surrounding each gas bubble, which are observed to burst in Supplementary Video 7 [33]33. Scale: Frame Width = 2.0 mm.

Reactive boiling ejection is a mechanism by which a distinct class of products, nonvolatile organic compounds (e.g. tars) or potentially entrained inorganic material (e.g. SiO_2), can be transported from solid biomass to the gas phase. This phenomenon explains at a more fundamental level the release of inorganic particulate into the atmosphere from forest fires, the emission of heavy tars from cigarette smoke, and the production of heavy sludge observed in bio-oils. Future experiments and fluid modeling will attempt to understand the effect of variable biomass intermediate liquid properties on the generation of film/jet particles and identify the critical bubble radius whereby particle ejection is suppressed.[62] This knowledge will address the relative importance of the reactive boiling ejection mechanism to known aerosol formation mechanisms including gas phase nucleation shown to produce secondary aerosol particles from biomass. A more complete understanding and predictive capability of these phenomena will potentially lead to reduced aerosol generation, decreased transport of nonvolatile material, and higher quality product streams from high temperature biomass reactions.

1.5 Conclusions

Cellulose spontaneously ejects primary liquid aerosol particles during thermal decomposition, as observed by high speed photography and confirmed by computational fluid

dynamics. A single molten cellulose droplet continuously ejects multiple aerosols indicating that the ejection event is not a unique, singular phenomenon during cellulose pyrolysis. Sampling and characterization of the ejected aerosols reveals a significant quantity of the nonvolatile anhydro-dimer, cellobiosan, indicating that primary, ejected aerosols are capable of transporting nonvolatile material from cellulose to the gas phase. Measurement of the aerosol ejection velocity distribution and comparison with a simple energy balance estimates the surface tension of the intermediate cellulose liquid in the range of $10^{-6} < \gamma < 10^{-5}$ N/m.

The mechanism of reactive boiling ejection was determined to occur through three stages. During the initial stage solid cellulose thermally degrades to a molten intermediate liquid. In the second stage, vapor bubbles nucleate within the molten liquid and rise to the liquid/gas interface. Finally, the liquid film separating vapor bubble and external gas atmosphere ruptures. Subsequent film retraction and vapor cavity collapse produces a liquid jet protruding from a vapor depression. The extending liquid jet fragments producing liquid aerosol particles moving with high velocity (0.1-0.5 m/s). The bubble collapse mechanism was supported by agreement of experimental observation of ejection velocity with fluid simulation utilizing the estimated cellulose liquid properties.

1.6 Appendix A:Supporting Information

1.6.1 Supplementary Videos

Supporting videos are available with the original published manuscript at:

http://dx.doi.org/10.1039/c1ee01876k

The following is a brief description of each Video file.

Video S1 – Cellulose Ejection

Video S1 depicts a droplet of intermediate cellulose liquid on a 700 °C surface ejecting a liquid droplet. The ejected droplet is visible in multiple frames as it slows down while passing through the surrounding nitrogen gas. Frames from this video were used to produce Figure 3A. A brightness and contrast adjustment has been applied to all of the frames of the video uniformly using video software Virtualdub 1.9.9.

Video S2 – Multiple Cellulose Ejections

Video S2 depicts a droplet of intermediate cellulose liquid on a 700 °C surface near the end of its lifetime. Multiple ejections are visible within the focused region between the front and back of the particle. Ejections are visible as white streaks for 1-3 frames. Frames from this Video were used to produce Figure 1B. A brightness and contrast adjustment has been applied to all of the frames of the video equally using software Virtualdub 1.9.9. Frames were then differenced using the image subtraction technique in ImageJ as described earlier. The two sequences are displayed side by side. The original video frames are visible in Figure 1-16.

Video S3 – Sucrose Ejection and Mechanism

Video S3 depicts a droplet of molten sucrose liquid on 650 °C Fecralloy after it has melted to a liquid. A vapor bubble grows in size and rises to the upper right of the liquid droplet. Subsequent rupture of the liquid layer between the vapor bubble and the external gas results in the formation of a jet followed by fragmentation to an ejected droplet. A brightness and contrast

adjustment has been applied to all of the frames of the video equally using software Virtualdub 1.9.9.

Video S4 – CFD Ejection Simulation Case 1

Animation of the simulation shown in Figure 1-24. (R_B=15 μm, R_{drop}=113 μm, $\gamma=10^{-5}$ N/m, $\mu=10^{-5}$ kg/m·s)

Video S5 – CFD Ejection Simulation Case 2

Animation of the simulation shown in Figure 8. (R_B=15 μm, R_{drop}=113 μm, $\gamma=5\cdot10^{-6}$ N/m, $\mu=10^{-6}$ kg/m·s)

Video S6 – CFD Ejection Simulation Case 3

Animation of the simulation shown in Figure 1-23. (R_B=15 μm, R_{drop}=113 μm, $\gamma=5\cdot10^{-6}$ N/m, $\mu=10^{-5}$ kg/m·s)

Video S7 – Molten, Bubbling Lignin

Particles of lignin were pressed and sieved to 300 μm in diameter then pyrolyzing on a 700°C flat α-alumina surface via a liquid intermediate. An evolving liquid is observed rising from the bottom of the particle to the top as time progresses.

1.6.2 Supplementary Figures

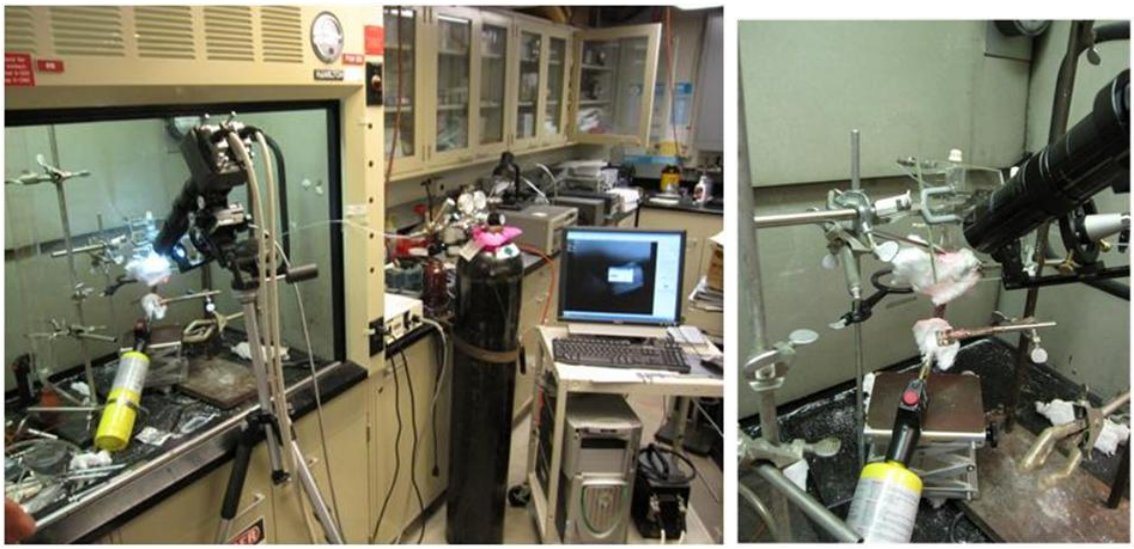

Figure 1-12: Experimental Setup for High Temperature Particle Visualization. Left. The high speed photography camera directly connects to a personal computer. Nitrogen gas is supplied to the pyrolysis experiment by a high pressure gas cylinder and controlled with a gas metering valve. Right: The high temperature surface is held in place by a metal cylinder supported with clamps and wrapped in white ceramic insulation. The assembly is heated from below by a MAPP torch capable of moving up and down to control the ceramic surface temperature. A quartz tube is held in place above the ceramic surface to provide nitrogen gas and particles to the surface in an inert environment. Lighting is provided from the right of the camera. A panel of glass is held in place between the camera lens and the surface.

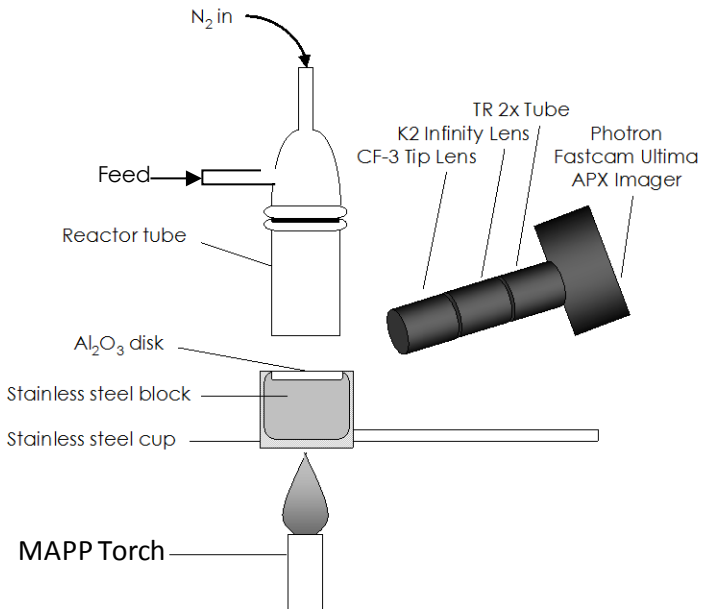

Figure 1-13: Schematic of the aerosol apparatus and system using an Al2O3 disk.

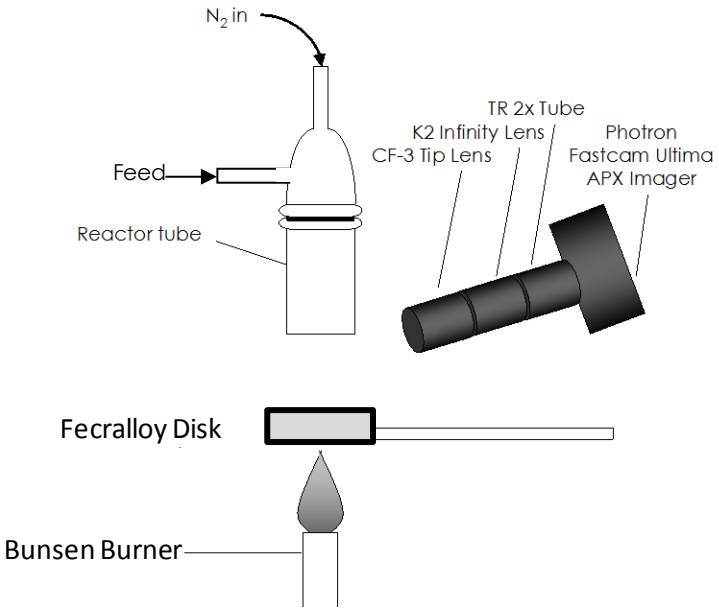

Figure 1-14: Schematic of the aerosol apparatus and system using a Fecralloy disk.

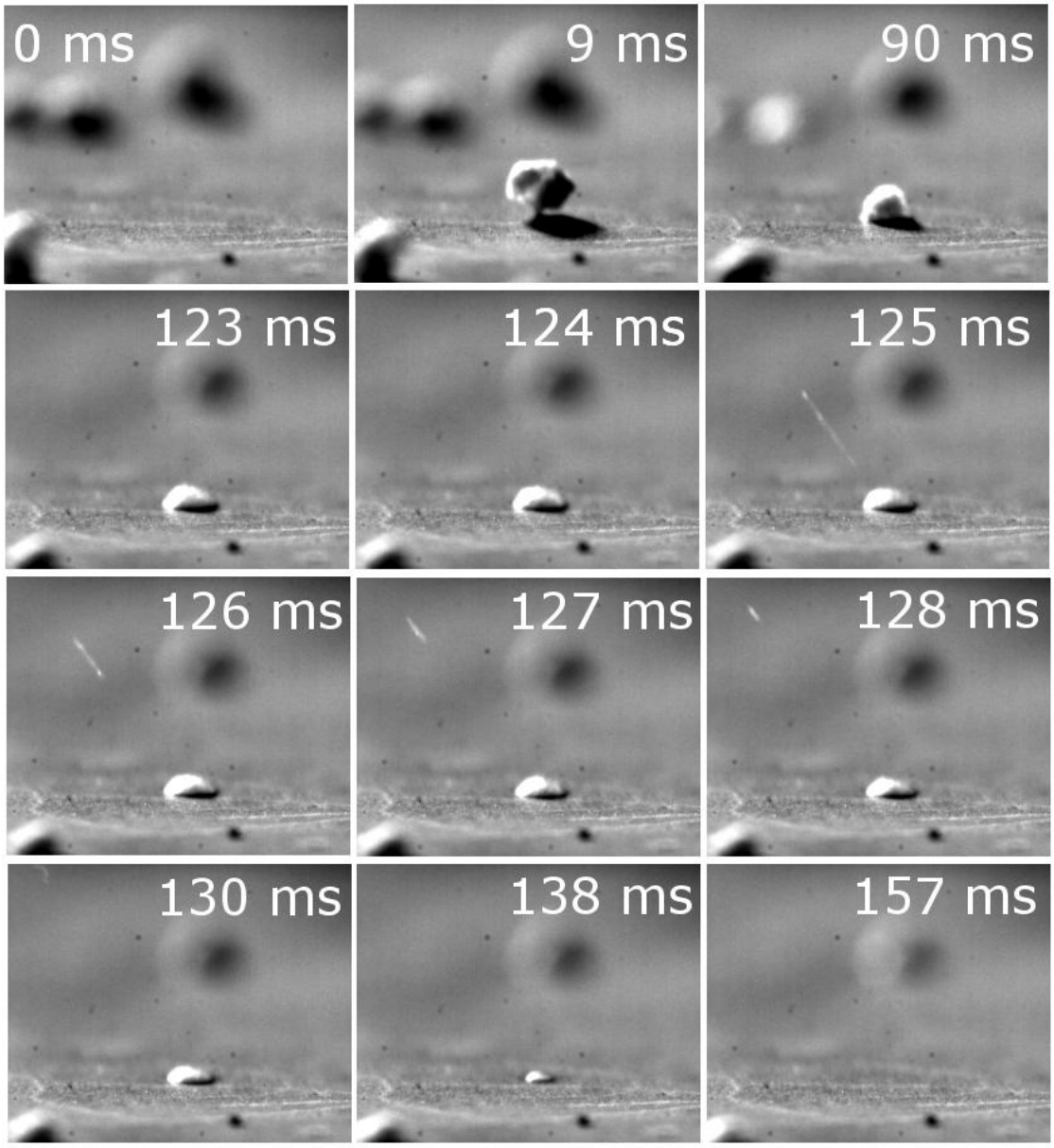

Figure 1-15: Droplet ejection from Intermediate Liquid Cellulose. A particle of cellulose (300 micron diameter) drops on a 700°C α-alumina surface (9 ms) and decomposes to a liquid intermediate. Droplet ejection is initiated (124 ms), and the ejected droplet is observed as a streak (125 ms). Frames 123-127 comprise Figure 3A of the manuscript.

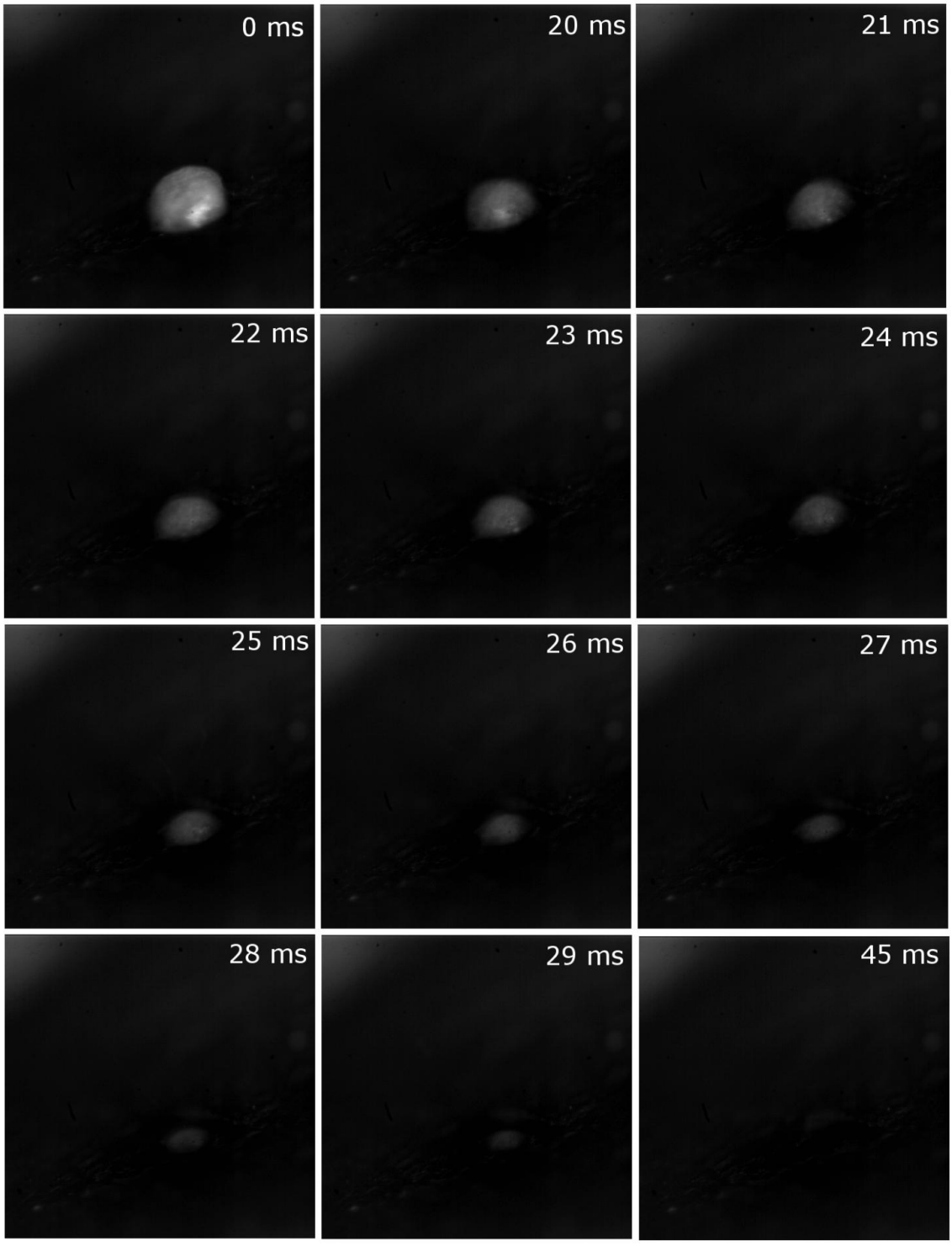

Figure 1-16: Multiple Drop Ejection from Liquid Intermediate Cellulose, Original Photography. A particle of liquid intermediate cellulose (250 micron diameter) on a 700°C α-alumina surface exhibits multiple ejections. All frames are derived from the original photography.

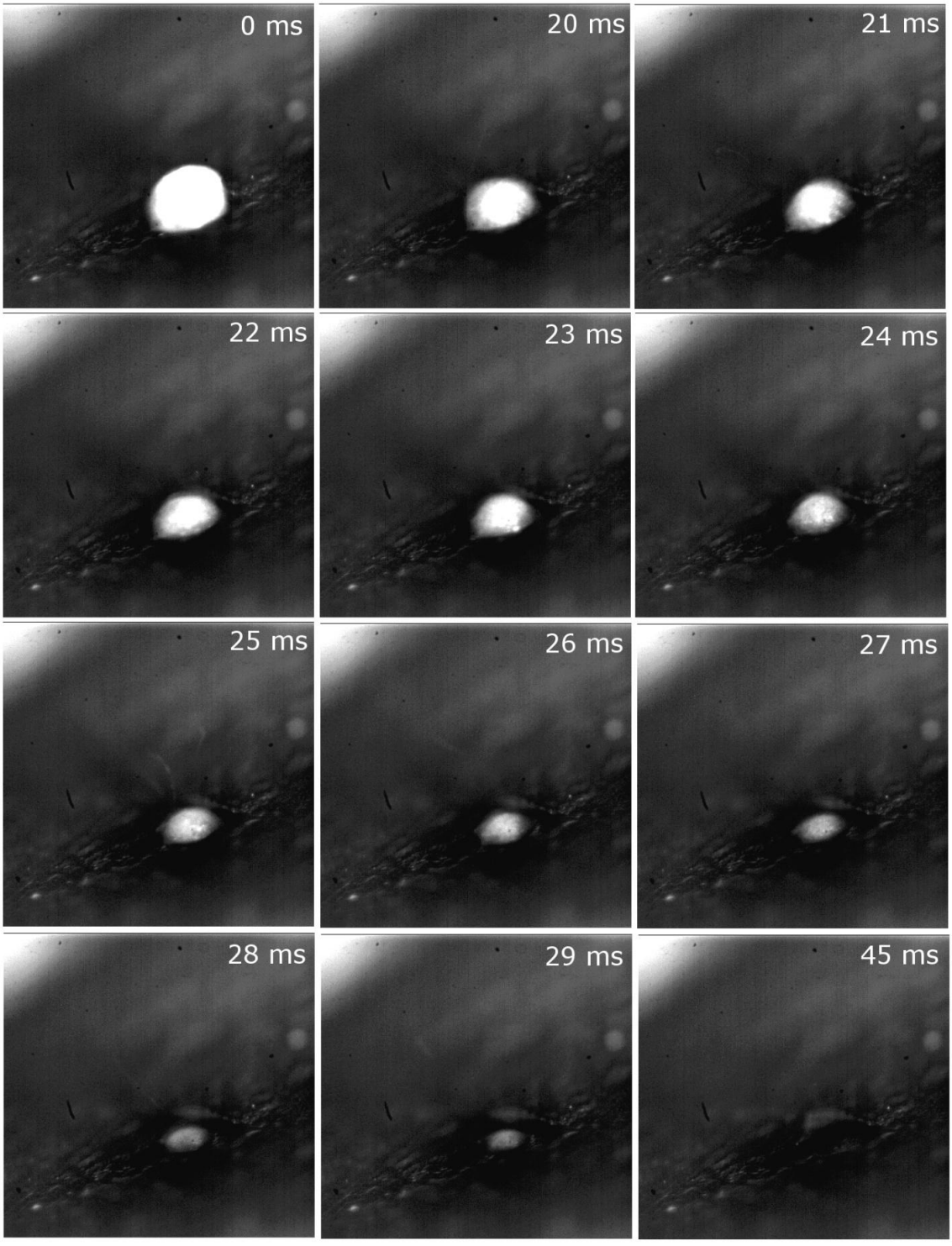

Figure 1-17: Multiple Drop Ejection from Liquid Intermediate Cellulose. A particle of liquid intermediate cellulose (250 micron diameter) on a 700°C α-alumina surface exhibits multiple ejections. The image has been contrast and brightness adjusted equally over the entire set; the original frames are visible in Figure 1-16.

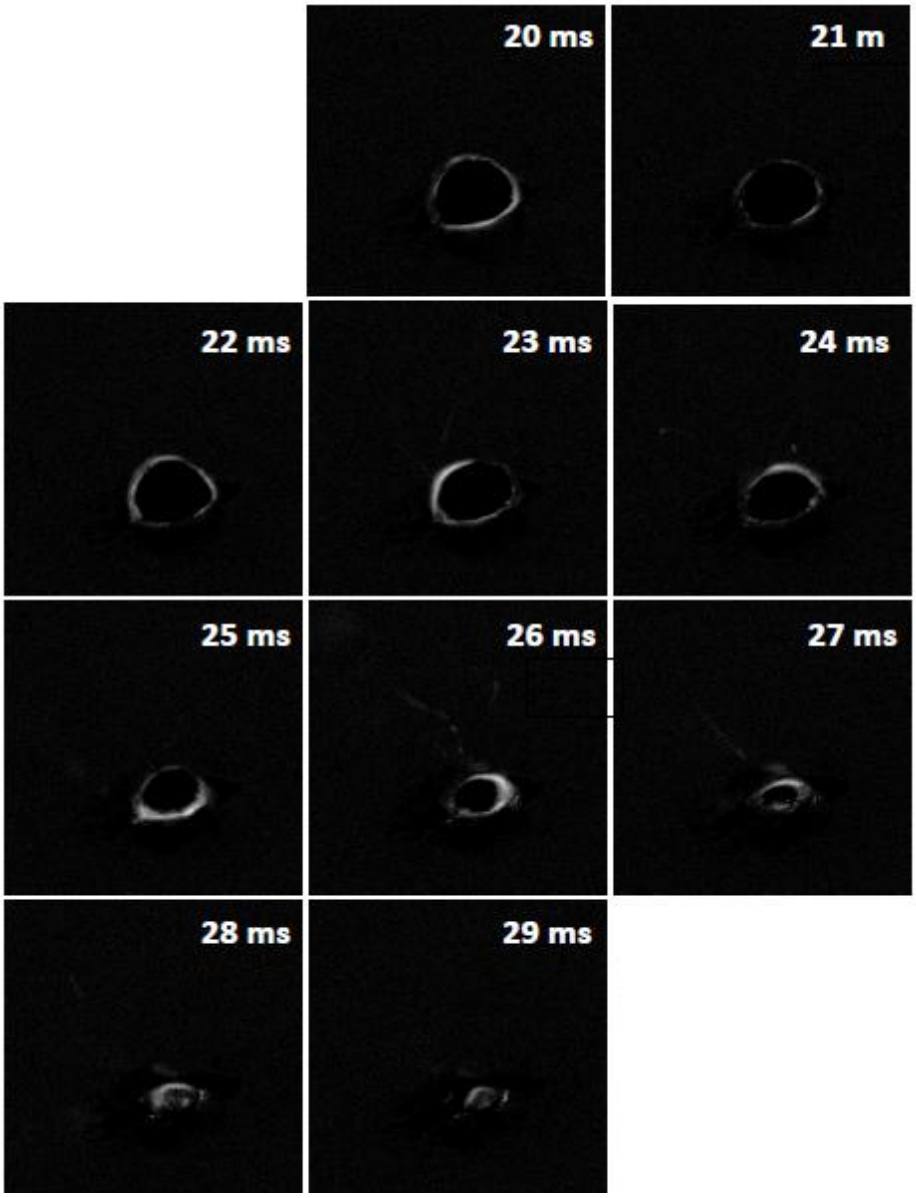

Figure 1-18: Multiple Drop Ejection from Liquid Intermediate Cellulose, Differenced. A particle of liquid intermediate cellulose (250 micron diameter) on a 700°C α-alumina surface exhibits multiple ejections. The image has been contrast and brightness adjusted equally over the entire set as observed in Figure 1-16.

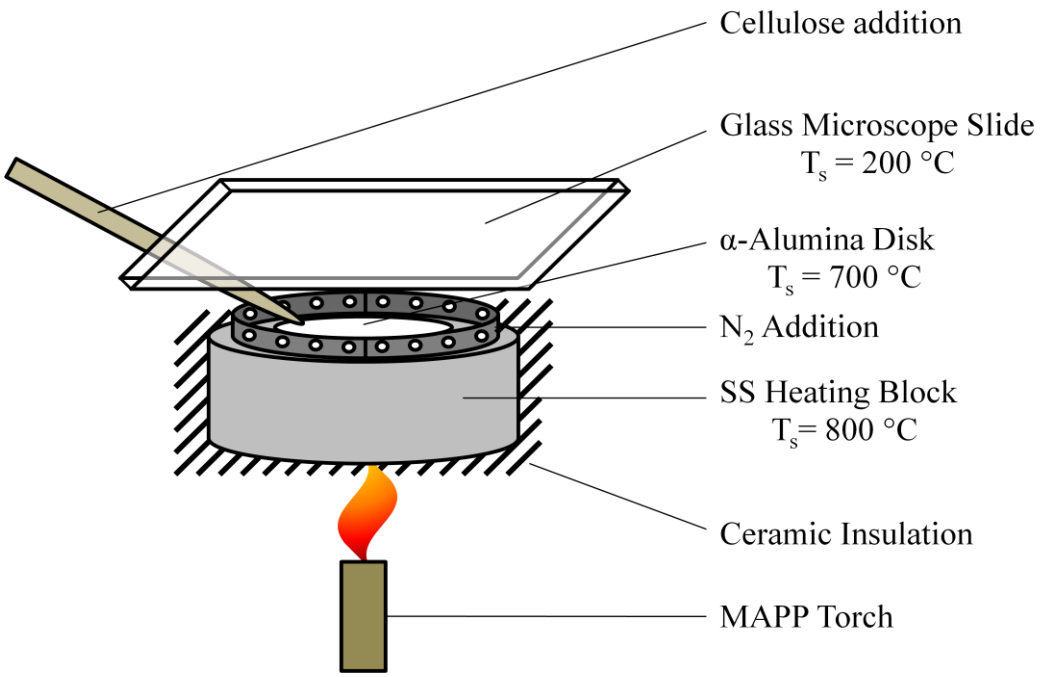

Figure 1-19: Aerosol Collection Apparatus. An α-alumina disk rests within a stainless steel cup encased in a ceramic insulation. Reaction surface temperatures are maintained at 700°C by use of a MAPP torch from below. As aerosols form, they adhere to the inclined glass slide.

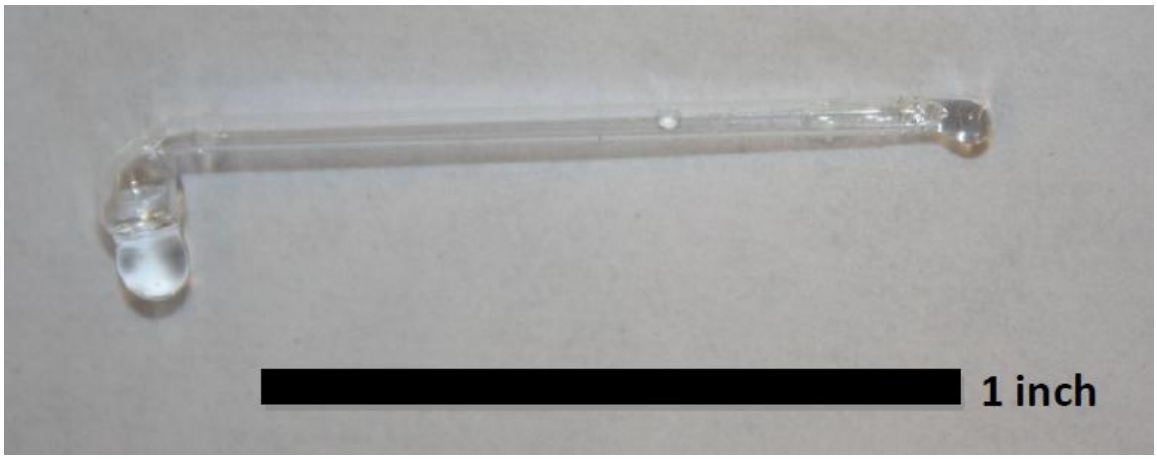

Figure 1-20: Custom-made Pyrolysis Tube. A custom-built pyrolysis tube used to generate the data in Figure 5B was made using a 9" Pasteur pipet, torch, and a tank of nitrogen. Particles of solid levoglucosan were placed within the pipet within an inert atmosphere, and the ends of the glass tube were sealed. The clear colorless liquid visible within the glass tube is pyrolyzed and reacted levoglucosan.

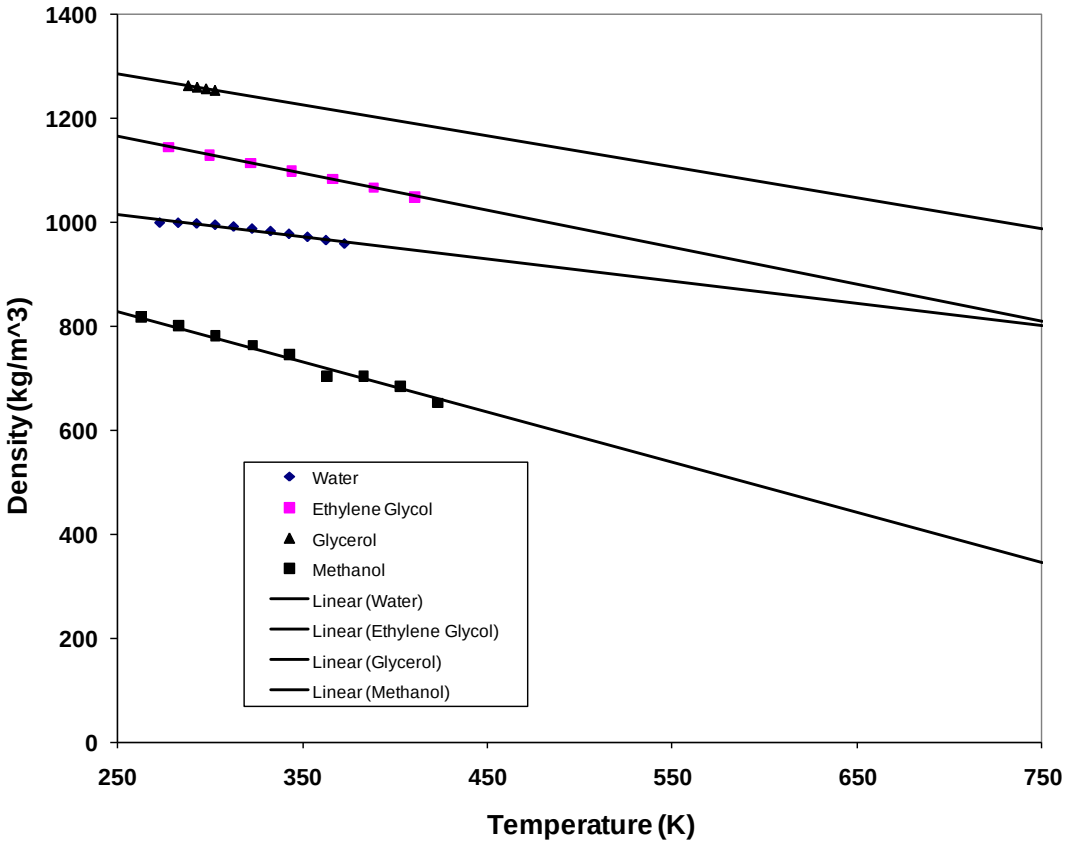

Figure 1-21: Prediction of Intermediate Liquid Cellulose Density. The density of the intermediate liquid cellulose has been predicted by extrapolation of oxygenated hydrocarbons and water below their boiling point to 750 K.

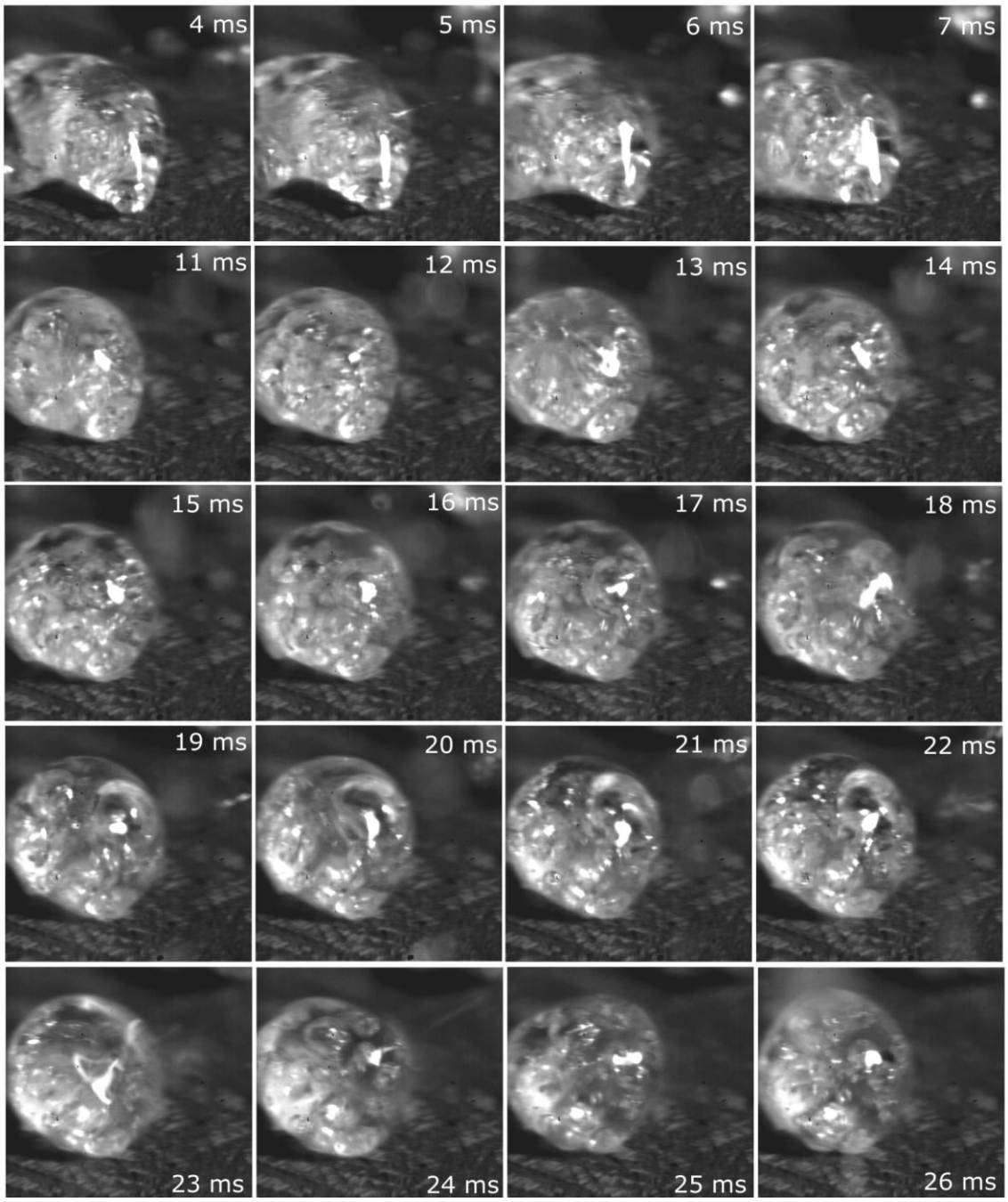

Figure 1-22: Sucrose Ejection on 650°C Fecralloy. Solid carbohydrate (β-D-fructofuranosyl-α-D-glucopyranoside) of 800 micron diameter on a 650°C Fecralloy surface (0 ms – not shown) melts and decomposes through a liquid intermediate. Bubble formation (19-22 ms) is followed by jet formation (23 ms) and subsequent particle ejection observed as a streak (24 ms). The jet observed at Frame 5 ms comprises Figure 6A. Frames are extracted from Supplementary Video S3.

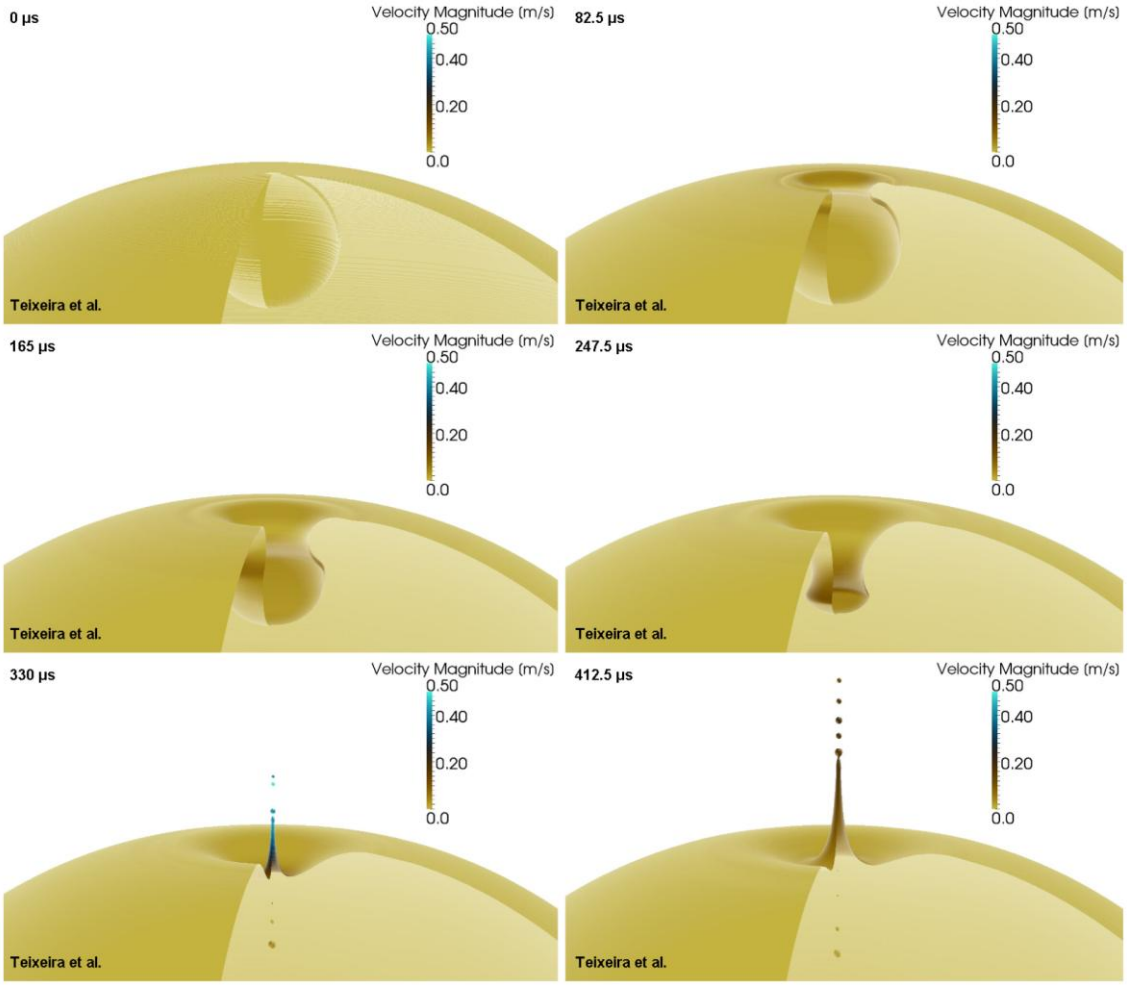

Figure 1-23: Supporting Simulation 3. Simulated bubble collapse and liquid jet formation depicting a 270° revolved α=0.5 iso-surface colored by velocity magnitude (RB=15 µm, Rdrop=113 µm, γ=5·10-6 N/m, μ=10-5 kg/m·s).

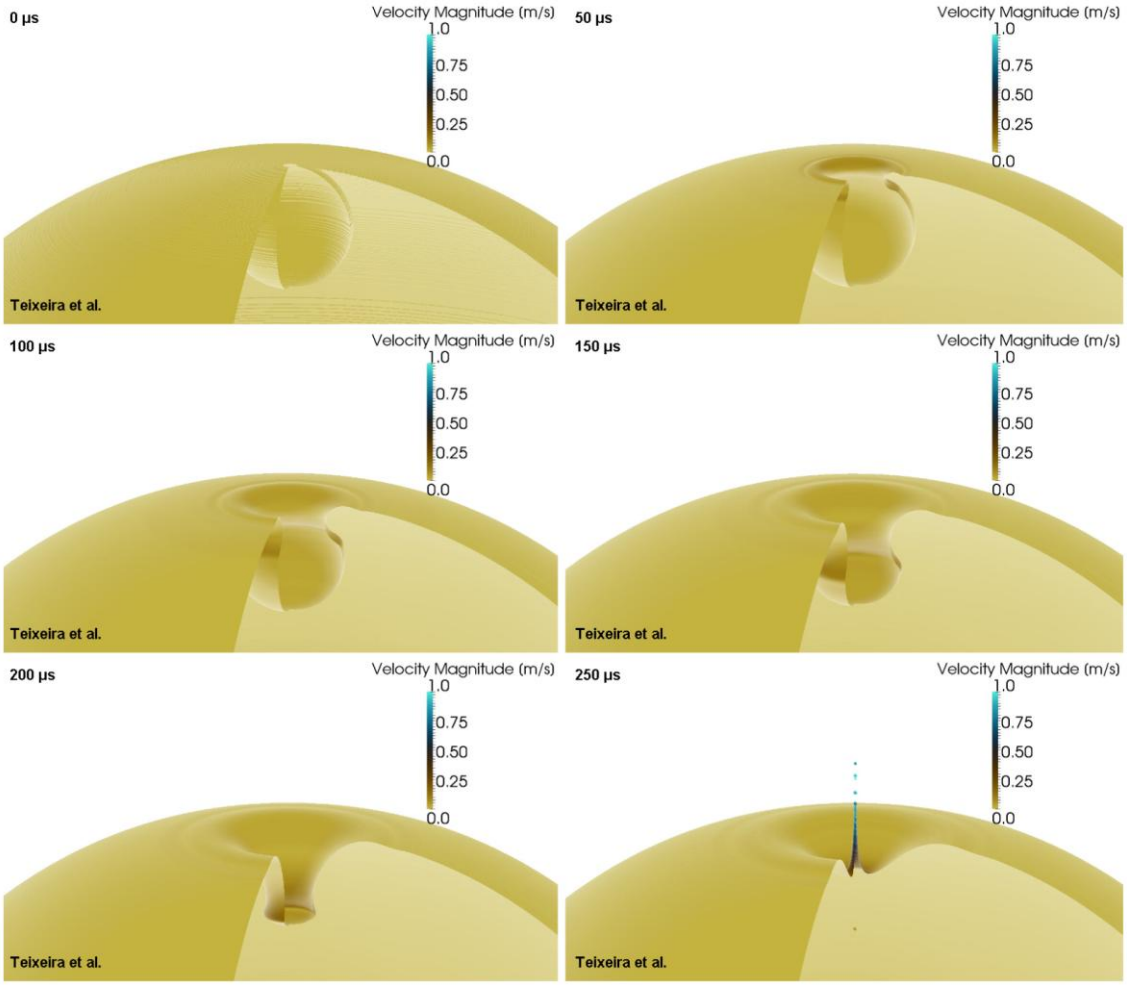

Figure 1-24: Supporting Simulation 1. Simulated bubble collapse and liquid jet formation depicting a 270° revolved α=0.5 iso-surface colored by velocity magnitude (RB=15 µm, Rdrop=113 µm, γ=10-5 N/m, µ=10-5 kg/m·s).

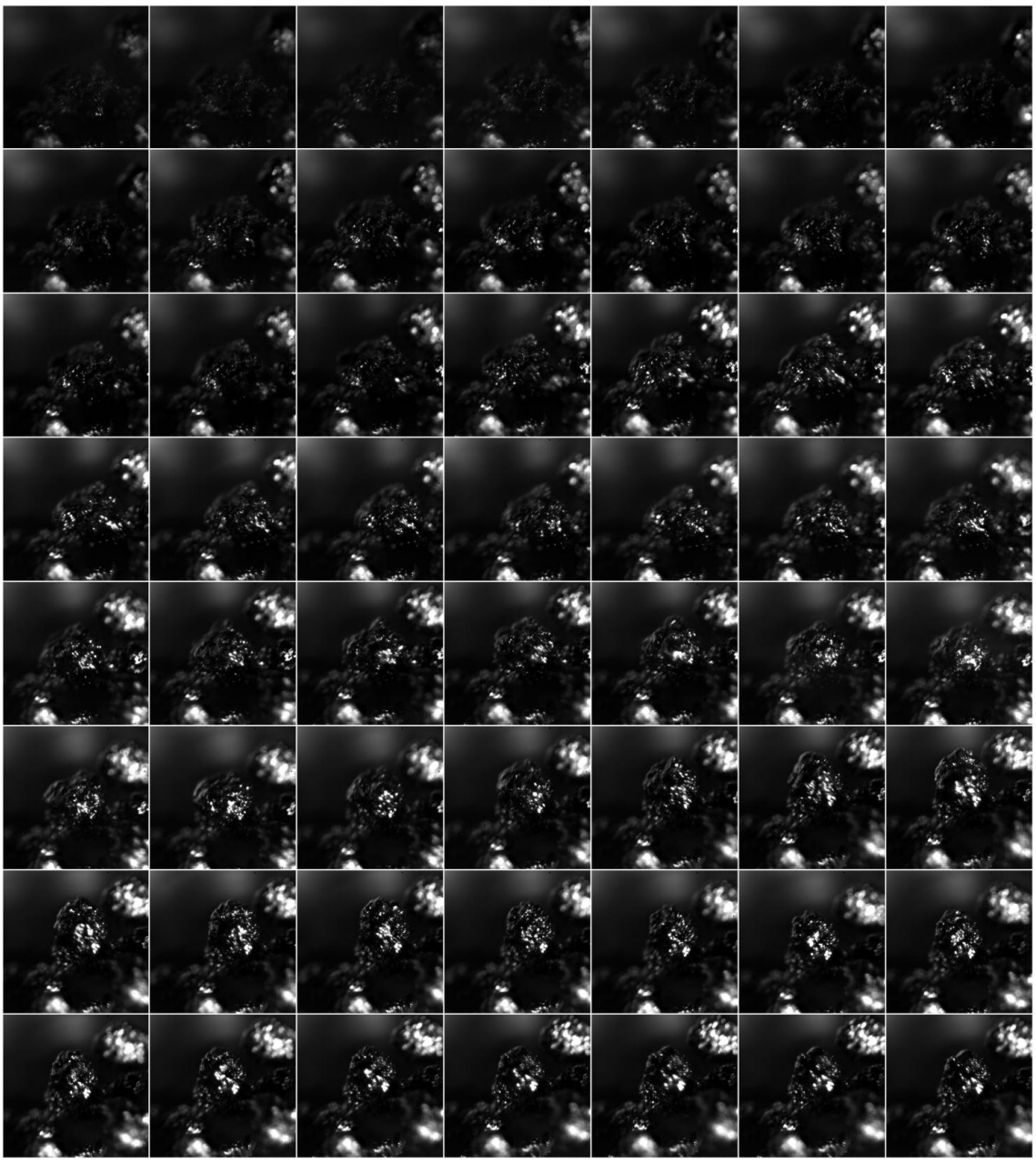

Figure 1-25: Molten Lignin Intermediate. Particles of lignin were pressed and sieved to 300 μm in diameter then pyrolyzed on a 700°C flat α-alumina surface via a liquid intermediate. The full video can be observed in Video S7†. An evolving liquid interface is observed rising from the bottom of the particle to the top as time progresses. Time between frames = 4 ms.

1.7 References

1. A. Ragauskas, C. Williams, B. Davison, G. Britovsek, J. Cairney, C. Eckert, W. Frederick Jr, J. Hallett, D. Leak, C. Liotta, The path forward for biofuels and biomaterials. *Science* **311**, 484-489 (2006).
2. J. Reid, R. Koppmann, T. Eck, D. Eleuterio, A review of biomass burning emissions part II: intensive physical properties of biomass burning particles. *Atmos. Chem. Phys* **5**, 799–825 (2005).
3. A. Thielen, H. Klus, L. Muller, Tobacco smoke: Unraveling a controversial subject. *Experimental and Toxicologic Pathology* **60**, 141-156 (2008)10.1016/j.etp.2008.01.014).
4. J. Piskorz, P. Maherski, D. Radlein, in *Biomass, A Growth Opportunity in Green Energy and Value-Added Products: proceedings of the 4th Biomass Conference of the Americas,* R. P. Overend, E. Chornet, Eds. (Elsevier Science, Amsterdam, 1999), vol. 2, pp. 1153-1159.
5. D. Radlein, A. Grinshpun, J. Piskorz, D. S. Scott, On the presence of anhydro-oligosaccharides in the sirups from the fast pyrolysis of cellulose. *Journal of analytical and applied pyrolysis* **12**, 39-49 (1987).
6. N. Jendoubi, F. Broust, J. M. Commandre, G. Mauviel, M. Sardin, J. Lede, Inorganics distribution in bio oils and char produced by biomass fast pyrolysis: The key role of aerosols. *Journal of Analytical and Applied Pyrolysis* **92**, 59-67 (2011); published online EpubSep (10.1016/j.jaap.2011.04.007).
7. C. Di Blasi, Modeling chemical and physical processes of wood and biomass pyrolysis. *Progress in Energy and Combustion Science* **34**, 47-90 (2008).
8. P. R. Patwardhan, J. A. Satrio, R. C. Brown, B. H. Shanks, Product distribution from fast pyrolysis of glucose-based carbohydrates. *Journal of analytical and applied pyrolysis* **86**, 323-330 (2009)10.1016/j.jaap.2009.08.007).
9. M. Garcia-Perez, A. Chaala, H. Pakdel, D. Kretschmer, C. Roy, Characterization of bio-oils in chemical families. *Biomass and Bioenergy* **31**, 222-242 (2007).
10. A. D. Pouwels, G. B. Eijkel, P. W. Arisz, J. J. Boon, Evidence for oligomers in pyrolysates of microcrystalline cellulose. *Journal of analytical and applied pyrolysis* **15**, 71-84 (1989)Doi: 10.1016/0165-2370(89)85023-5).
11. B. Scholze, C. Hanser, D. Meier, Characterization of the water-insoluble fraction from fast pyrolysis liquids (pyrolytic lignin): Part II. GPC, carbonyl goups, and 13C-NMR. *Journal of analytical and applied pyrolysis* **58-59**, 387-400 (2001)Doi: 10.1016/s0165-2370(00)00173-x).
12. R. Bayerbach, D. Meier, Characterization of the water-insoluble fraction from fast pyrolysis liquids (pyrolytic lignin). Part IV: Structure elucidation of oligomeric molecules. *Journal of analytical and applied pyrolysis* **85**, 98-107 (2009).
13. F. Shafizadeh, Y. L. Fu, Pyrolysis of cellulose. *Carbohydrate Research* **29**, 113-122 (1973)Doi: 10.1016/s0008-6215(00)82074-1).
14. P. R. Patwardhan, D. L. Dalluge, B. H. Shanks, R. C. Brown, Distinguishing primary and secondary reactions of cellulose pyrolysis. *Bioresource Technology* **102**, 5265-5269 (2011)10.1016/j.biortech.2011.02.018).
15. E. Fratini, M. Bonini, A. Oasmaa, Y. Solantausta, J. Teixeira, P. Baglioni, SANS Analysis of the Microstructural Evolution during the Aging of Pyrolysis Oils from Biomass. *Langmuir* **22**, 306-312 (2006)10.1021/la051990a).
16. J. A. Lomax, J. M. Commandeur, P. W. Arisz, J. J. Boon, Characterisation of oligomers and sugar ring-cleavage products in the pyrolysate of cellulose. *Journal of analytical and applied pyrolysis* **19**, 65-79 (1991)Doi: 10.1016/0165-2370(91)80035-7).

17. D. Radlein, in *Fast Pyrolysis of Biomass: A Handbook*, A. Bridgwater, S. Czernik, J. Diebold, Eds. (CPL Press, Newbury, 1999), pp. 164.
18. J. Lédé, F. Blanchard, O. Boutin, Radiant flash pyrolysis of cellulose pellets: products and mechanisms involved in transient and steady state conditions. *Fuel* **81**, 1269-1279 (2002)Doi: 10.1016/s0016-2361(02)00039-x).
19. P. Dauenhauer, J. Colby, C. Balonek, W. Suszynski, L. Schmidt, Reactive boiling of cellulose for integrated catalysis through an intermediate liquid. *Green Chemistry* **11**, 1555-1561 (2009).
20. J. Lédé, H. Z. Li, J. Villermaux, H. Martin, Fusion-like behaviour of wood pyrolysis. *Journal of analytical and applied pyrolysis* **10**, 291-308 (1987)Doi: 10.1016/0165-2370(87)80019-0).
21. O. Boutin, M. Ferrer, J. Lédé, Radiant flash pyrolysis of cellulose--Evidence for the formation of short life time intermediate liquid species. *Journal of analytical and applied pyrolysis* **47**, 13-31 (1998).
22. E. Fischbach, D. Sudarsky, A. Szafer, C. Talmadge, S. H. Aronson, Long-range forces and the Eötvös experiment. *Annals of Physics* **182**, 1-89 (1988)Doi: 10.1016/0003-4916(88)90294-1).
23. W. S. Rasband. (National Institutes of Health, Bethesda, Maryland, 1997-2011).
24. . (2001).
25. P. Medeiros, B. Simoneit, Analysis of sugars in environmental samples by gas chromatography–mass spectrometry. *Journal of Chromatography A* **1141**, 271-278 (2007)10.1016/j.chroma.2006.12.017).
26. L. Duchemin, S. Popinet, C. Josserand, S. Zaleski, Jet formation in bubbles bursting at a free surface. *Physics of Fluids* **14**, 3000-3008 (2002)10.1063/1.1494072).
27. H. Weller, G. Tabor, H. Jasak, C. Fureby, A tensorial approach to computational continuum mechanics using object-oriented techniques. *Computers in physics* **12**, 620 (1998).
28. J. H. Ferziger, M. Perić, *Computational methods for fluid dynamics*. (Springer, 1999).
29. H. Rusche, Imperial College of Science, Technology & Medicine, London (2002).
30. S. V. Patankar, *Numerical heat transfer and fluid flow*. (Taylor & Francis, 1980).
31. A. V. Coward, Y. Y. Renardy, M. Renardy, J. R. Richards, Temporal Evolution of Periodic Disturbances in Two-Layer Couette Flow. *Journal of Computational Physics* **132**, 346-361 (1997)DOI: 10.1006/jcph.1996.5640).
32. E. Berberović, N. P. van Hinsberg, S. Jakirlicacute, I. V. Roisman, C. Tropea, Drop impact onto a liquid layer of finite thickness: Dynamics of the cavity evolution. *Physical Review E* **79**, 036306 (2009).
33. J. U. Brackbill, D. B. Kothe, C. Zemach, A continuum method for modeling surface tension. *Journal of Computational Physics* **100**, 335-354 (1992)Doi: 10.1016/0021-9991(92)90240-y).
34. B. Huang, W. Wang, M. Bates, X. Zhuang, Three-Dimensional Super-Resolution Imaging by Stochastic Optical Reconstruction Microscopy. *Science* **319**, 810-813 (2008)10.1126/science.1153529).
35. O. Boutin, M. Ferrer, J. Lede, Radiant flash pyrolysis of cellulose - Evidence for the formation of short life time intermediate liquid species. *Journal of Analytical and Applied Pyrolysis* **47**, 13-31 (1998); published online EpubSep (
36. J. Lédé, J. P. Diebold, G. V. C. Peacocke, J. Piskork, in *Fast Pyrolysis of Biomass: A Handbook*, A. Bridgwater, S. Czernik, J. Diebold, Eds. (1999).
37. C. Di Blasi, Kinetic and Heat Transfer Control in the Slow and Flash Pyrolysis of Solids. *Industrial & Engineering Chemistry Research* **35**, 37-46 (1996)10.1021/ie950243d).
38. G. S. Parks, L. E. Barton, M. E. Spaght, J. W. Richardson, The Viscosity of Undercooled Liquid Glucose. *Physics* **5**, 193-199 (1934)10.1063/1.1745251).

39. DOW. (2010).
40. G. S. Fulcher, Analysis of recent measurements of the viscosity of glasses. *Journal of the American Ceramic Society* **8**, 339-355 (1925)10.1111/j.1151-2916.1925.tb16731.x).
41. L. S. Garcia-Colin, L. F. del Castillo, P. Goldstein, Theoretical basis for the Vogel-Fulcher-Tammann equation. *Physical Review B* **40**, 7040 (1989).
42. Z. Luo, S. Wang, Y. Liao, K. Cen, Mechanism Study of Cellulose Rapid Pyrolysis. *Industrial & Engineering Chemistry Research* **43**, 5605-5610 (2004)10.1021/ie030774z).
43. A. G. W. Bradbury, Y. Sakai, F. Shafizadeh, A kinetic model for pyrolysis of cellulose. *Journal of Applied Polymer Science* **23**, 3271-3280 (1979).
44. J. Diebold, A unified, global model for the pyrolysis of cellulose. *Biomass and Bioenergy* **7**, 75-85 (1994).
45. A. Liden, F. Berruti, D. Scott, A kinetic model for the production of liquids from the flash pyrolysis of biomass. *Chemical engineering communications* **65**, 207-221 (1988).
46. J. Piskorz, D. Radlein, D. S. Scott, On the mechanism of the rapid pyrolysis of cellulose. *Journal of analytical and applied pyrolysis* **9**, 121-137 (1986)Doi: 10.1016/0165-2370(86)85003-3).
47. J. Piskorz, P. Majerski, D. Radlein, A. Vladars-Usas, D. S. Scott, Flash pyrolysis of cellulose for production of anhydro-oligomers. *Journal of analytical and applied pyrolysis* **56**, 145-166 (2000)Doi: 10.1016/s0165-2370(00)00089-9).
48. V. Oja, E. M. Suuberg, Vapor Pressures and Enthalpies of Sublimation of d-Glucose, d-Xylose, Cellobiose, and Levoglucosan. *Journal of Chemical & Engineering Data* **44**, 26-29 (1998)10.1021/je980119b).
49. S. Punnathanam, D. S. Corti, Cavity formation in the superheated Lennard-Jones liquid and its connection to homogeneous bubble nucleation: A density-functional theory study. *The Journal of Chemical Physics* **119**, 10224-10236 (2003).
50. S. Punnathanam, D. S. Corti, Critical cavities and the kinetic spinodal for superheated liquids. *The Journal of Chemical Physics* **120**, 11658-11661 (2004).
51. D. L. Pyle, C. A. Zaror, Heat transfer and kinetics in the low temperature pyrolysis of solids. *Chemical Engineering Science* **39**, 147-158 (1984)Doi: 10.1016/0009-2509(84)80140-2).
52. C. Di Blasi, Numerical simulation of cellulose pyrolysis. *Biomass and Bioenergy* **7**, 87-98 (1994)Doi: 10.1016/0961-9534(94)00040-z).
53. O. Authier, M. Ferrer, A.-E. Khalfi, J. Lédé, Solid Pyrolysis Modelling by a Lagrangian and Dimensionless Approach--Application to Cellulose Fast Pyrolysis. *International Journal of Chemical Reactor Engineering* **8**, (2010).
54. J. Boulton-Stone, J. Blake, Gas bubbles bursting at a free surface. *Journal of Fluid Mechanics* **254**, 437-466 (1993).
55. R. S. Allan, G. E. Charles, S. G. Mason, The approach of gas bubbles to a gas/liquid interface. *Journal of Colloid Science* **16**, 150-165 (1961)Doi: 10.1016/0095-8522(61)90014-9).
56. P.-S. Hahn, J.-D. Chen, J. C. Slattery, Effects of London-van der Waals forces on the thinning and rupture of a dimpled liquid film as a small drop or bubble approaches a fluid-fluid interface. *AIChE Journal* **31**, 2026-2038 (1985)10.1002/aic.690311212).
57. J.-D. Chen, P. S. Hahn, J. C. Slattery, Coalescence time for a small drop or bubble at a fluid-fluid interface. *AIChE Journal* **30**, 622-630 (1984)10.1002/aic.690300413).
58. R. D. Kirkpatrick, M. J. Lockett, The influence of approach velocity on bubble coalescence. *Chemical Engineering Science* **29**, 2363-2373 (1974)Doi: 10.1016/0009-2509(74)80013-8).
59. G. Taylor, D. Michael, On making holes in a sheet of fluid. *Journal of Fluid Mechanics* **58**, 625-639 (1973).

60. J. Koplik, J. R. Banavar, Molecular dynamics of interface rupture. *Physics of Fluids A: Fluid Dynamics* **5**, 521-536 (1993).
61. G. Liger-Belair, G. Polidori, P. Jeandet, Recent advances in the science of champagne bubbles. *Chemical Society Reviews* **37**, 2490 (2008)10.1039/b717798b).
62. S.-C. Georgescu, J.-L. Achard, É. Canot, Jet drops ejection in bursting gas bubble processes. *European Journal of Mechanics - B/Fluids* **21**, 265-280 (2002)Doi: 10.1016/s0997-7546(01)01177-3).
63. D. E. Spiel, On the births of film drops from bubbles bursting on seawater surfaces. *J. Geophys. Res.* **103**, 24907-24918 (1998)10.1029/98jc02233).
64. F. MacIntyre, Flow patterns in breaking bubbles. *Journal of Geophysical Research* **77**, 5211-5228 (1972).
65. F. Resch, G. Afeti, FILM DROP DISTRIBUTIONS FROM BUBBLES BURSTING IN SEAWATER. *J. Geophys. Res.* **96**, 10681-10688 (1991)10.1029/91jc00433).
66. F. Resch, G. Afeti, SUBMICRON FILM DROP PRODUCTION BY BUBBLES IN SEAWATER. *J. Geophys. Res.* **97**, 3679-3683 (1992)10.1029/91jc02961).
67. J. Wu, Film drops produced by air bubbles bursting at the surface of seawater. *Journal of Geophysical Research* **99**, 16403-16416,16407 (1994).
68. D. C. Blanchard, L. D. Syzdek, Film drop production as a function of bubble size. *Journal of Geophysical Research* **93**, 3649-3654 (1988).
69. F. MacIntyre, Bubbles. Boundary-layer "microtome" for micronthick samples of a liquid surface. *The Journal of Physical Chemistry* **72**, 589-592 (1968)10.1021/j100848a034).
70. C. F. Kientzler, A. B. Arons, D. C. Blanchard, A. H. Woodcock, Photographic Investigation of the Projection of Droplets by Bubbles Bursting at a Water Surface1. *Tellus* **6**, 1-7 (1954)10.1111/j.2153-3490.1954.tb01085.x).
71. D. E. Spiel, On the births of jet drops from bubbles bursting on water surfaces. *J. Geophys. Res.* **100**, 4995-5006 (1995)10.1029/94jc03055).
72. D. E. Spiel, More on the births of jet drops from bubbles bursting on seawater surfaces. *J. Geophys. Res.* **102**, 5815-5821 (1997)10.1029/96jc03582).
73. J. R. Blake, D. C. Gibson, Growth and collapse of a vapour cavity near a free surface. *Journal of Fluid Mechanics* **111**, 123-140 (1981)doi:10.1017/S0022112081002322).
74. J. M. Boulton-Stone, The effect of surfactant on bursting gas bubbles. *Journal of Fluid Mechanics* **302**, 231-257 (1995)doi:10.1017/S0022112095004083).
75. F. Garner, S. Ellis, J. Lacey, The size distribution and entrainment of droplets. *Chemical Engineering Research and Design* **32**, 222-235 (1954).
76. F. J. Resch, G. M. Afeti, in *Experimental heat transfer, fluid mechanics, and thermodynamics*, J. F. Keffer, R. K. Shah, E. N. Ganić, Eds. (Elsevier, 1991), pp. 1066-1076.
77. L. Rayleigh, On the instability of a cylinder of viscous liquid under capillary force. *Phil. Mag* **34**, 145–154 (1892).
78. A. Günther, S. Walchli, P. Rudolf von Rohr, Droplet production from disintegrating bubbles at water surfaces. Single vs. multiple bubbles. *International Journal of Multiphase Flow* **29**, 795-811 (2003)10.1016/s0301-9322(03)00041-7).
79. D. E. Spiel, The number and size of jet drops produced by air bubbles bursting on a fresh water surface. *J. Geophys. Res.* **99**, 10289-10296 (1994)10.1029/94jc00382).

† Supplemental videos available at http://dx.doi.org/10.1039/c1ee01876k

CHAPTER 2

SOPONTANEOUS AEROSOL EJECTION:

ORIGIN OF INORGANIC PARTICLES IN BIOMASS PYROLYSIS

2.1 Introduction

Biomass pyrolysis is an emerging pathway for renewable generation of liquid fuels and chemicals,[1-3] by which non-edible fractions of woody biomass (lignocellulose) can be thermochemically converted to bio-renewable crude oil.[4, 5] Lignocellulosic biomass is also an abundant source of carbon, with as much as one billion dry tons available sustainably per year in the United States,[6, 7] which is the energy equivalent of 3.8×10^9 barrels of oil per year.[8] During biomass fast pyrolysis, dry biomass is exposed to high thermal fluxes at temperatures above 400 °C in the absence of oxygen, producing highly oxygenated bio-crude oil (bio-oil),[9] which can be used directly as a heavy heating oil[10] or catalytically upgraded to produce fuels and chemicals.[8, 11-13] Technologies required to generate and process this new crude source are rapidly advancing, with global commercial facilities already pursuing pyrolysis-based conversion economically at industrial scales.[12, 14] While rapid influx of research and technology in bio-oil upgrading shows promise, the fundamental transport phenomena and chemistry dominating biomass fast pyrolysis are only beginning to be revealed.[15]

Biomass consists of three biopolymers (cellulose, hemicellulose, and lignin) which decompose under high heating rates to form a liquid intermediate composed initially of oligomers of the native biopolymer, as described in Figure 1.[16, 17] The oligomers continue to react, forming primary and secondary pyrolysis products within the liquid melt. As volatile products are formed, they diffuse through the liquid intermediate to the liquid/gas interface and evaporate; this is accompanied by vigorous internal bubbling. Secondary products are the result of heat and mass transfer limitations within the melt, causing the continued reaction of volatile compounds prior to

evaporation.[18-20] Vapors produced from pyrolysis can then be condensed to produce unprocessed bio-oil. The process also produces permanent gases (CO and CO_2), char (solid carbon), and ash (solid inorganic, non-combustible species).

Bio-oil obtained from fast pyrolysis is comprised primarily of $C_2 - C_6$ oxygenates.[19] The liquid is generally characterized as highly oxygenated, viscous, and acidic crude which varies significantly with feedstock, particle size, heating conditions, and moisture content.[21, 22] Bio-oil also contains a non-negligible fraction of non-volatile organics including solid or dissolved oligomers,[23] as well as inorganic materials (e.g. CaO, MgO, K_2O)[24, 25] which comprise less than 1 wt% of the crude mixture. Despite low concentration, inorganic components can have a strong impact on the distribution of compounds within bio-oil and its associated physical properties. Depending on the material and reaction environment, they catalyze desired chemistry such as hydrolysis and deoxygenation,[9, 18] or undesired reactions including oxidation,[26] polymerization and charring,[27, 28] or C-C cracking.[29, 30] Entrainment of inorganic material by aerosol generation may also catalyze downstream polymerization and aging, resulting in lower quality bio-oil.[31] Additionally, aerosol entrainment of undesirable compounds has relevance in a wide range of fields, including aerosols from tobacco smoke[32] and forest fires[33] which present major health risks.

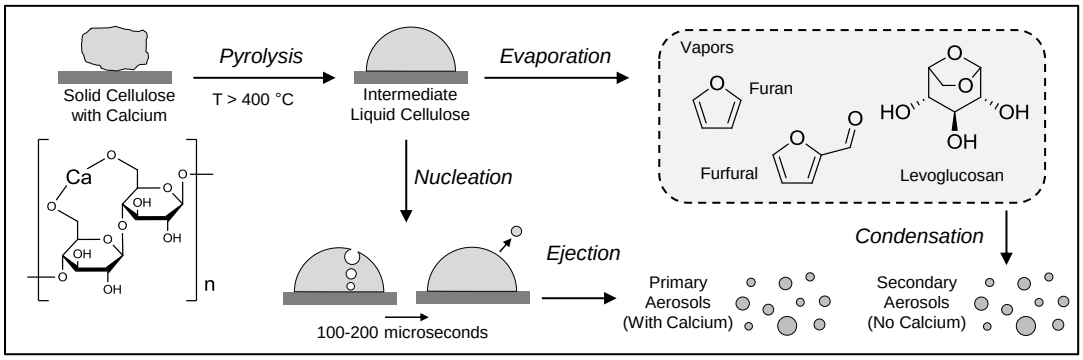

Figure 2-1: **Cellulose Pyrolysis - Pathways to Aerosols.** At high temperatures (>400 ºC) and under high heating flux, cellulose depolymerizes by glycosidic cleavage to form reactive liquid intermediate cellulose. Vigorous bubbling within the melt causes evaporation, permanent gases/char formation, and thermal ejection of primary liquid aerosols.

The presence of non-volatile compounds within bio-oil cannot be explained by evaporation and must result from a second, fundamentally different mechanism. In literature, two mechanisms have been proposed to explain the nonvolatile fraction of bio-oil. First, it has been proposed that volatile species are formed by oligomer degradation and evaporate to the gas phase; subsequent condensation produces a product liquid where repolymerization/reaction can occur to form non-volatile species. An example of this mechanism is polymerization of volatile anhydrosugars to form nonvolatile oligomers such as cellobiosan or maltosan. While these reactions have been shown to be important during the aging process of bio-oil,[31, 34] they do not explain nonvolatile products observed in the gas phase.[35] Additionally, this mechanism does not explain the gas-phase transfer of inorganic materials which have negligible vapor pressures yet are often observed in condensed pyrolysis products.[36, 37] It was recently shown that the biopolymer liquid intermediate vigorously produces bubbles during pyrolysis which burst to generate primary aerosols.[37] This 'reactive boiling ejection' mechanism has been identified as a pathway for producing entrained non-volatile organic compounds within primary aerosols during cellulose pyrolysis. While compelling evidence supporting this mechanism and its capability for transporting organic compounds has been shown, the potential transport of nonvolatile inorganic particles within primary aerosols remains to be shown.[38]

In this work, the first *direct* evidence of non-volatile inorganic particle transport is revealed to occur via *primary* aerosol ejection from molten biomass. The abundance of aerosol generation is quantified, and fractionation of the product distribution identifies the significance of the primary aerosol pathway for both transport of organic and inorganic species into vapor-phase products.

2.2 Experimental

Primary aerosol generation via reactive boiling ejection was characterized by high speed photography of reacting cellulose with and without impregnated calcium. Aerosols were collected

from a custom ablative fast pyrolysis reactor, and the composition of collected aerosols was evaluated via inductively-coupled plasma spectroscopy. Distributions of aerosol size were characterized by laser diffraction light scattering.

2.2.1 Materials

Microcrystalline cellulose (Lattice NT-200) was obtained from FMC Biopolymer and sieved to particles larger than 250 μm in diameter. ACS/USP grade ethanol (190 proof) used to quench pyrolysis vapor was purchased from Fisher Scientific. Grade 5.0 nitrogen (99.999 % purity) was purchased from Middlesex Gases & Technologies, Inc. ACS reagent grade nitric acid (> 99.9995% pure - metal basis; 69% pure by weight) purchased from Acros Organics was used to prepare samples for inductively coupled plasma optical emission spectrometry (ICP-OES, PerkinElmer Inc. Optima 4300 DV ICP-OES) analysis via acid digestion by standard methods (described below). Crystalline cellulose was impregnated with calcium by first dissolving the appropriate amount of $Ca(NO_3)_2 \cdot 4H_2O$ (purchased from Acros, ACS grade with >99% purity) in 20 ml deionized water. The solution was added to two grams of cellulose (Alfa Aesar P/N: A17730) and stirred at RT for two hours. The sample was then dried in an oven at 70 °C overnight to obtain Ca-impregnated cellulose. The final impregnated cellulose contained 5.13 mg Ca/g-cellulose compared to 0.062 mg Ca/g-cellulose in the pure sample, as measured by ICP-OES.

2.2.2 Ablative Fast Pyrolysis Reactor

Pure crystalline and calcium-impregnated cellulose were pyrolyzed in an ablative pyrolysis system with product fractionation capabilities shown in Figure 2. Cellulose was introduced into the top of a stainless steel reactor at a rate of 6 mg/min. Generated particles were entrained in a positive pressure nitrogen stream of 35 sccm before impinging on a half inch, porous, stainless steel frit (5 μm, Applied Porous Media 10192-050). The reactor temperature was

maintained at 500 °C in a narrowly heated region (4 cm) using a resistive band heater centered on the frit. Reactor temperature was maintained using a PID controller with temperature measurement at the frit surface using a type K thermocouple. Pyrolysis product gases entrained in the nitrogen stream were passed through an ethanol quench contained within a 5 cm segment of ¼" stainless steel tubing and maintained at 0 °C using an ice bath. Non-condensable products were captured in a gas collection bag located downstream from the quench. Immediately after reaction, quenched products were stored at 5 °C to prevent further reactions. Solid residual char and ash fractions were analyzed using ashing methods described below.

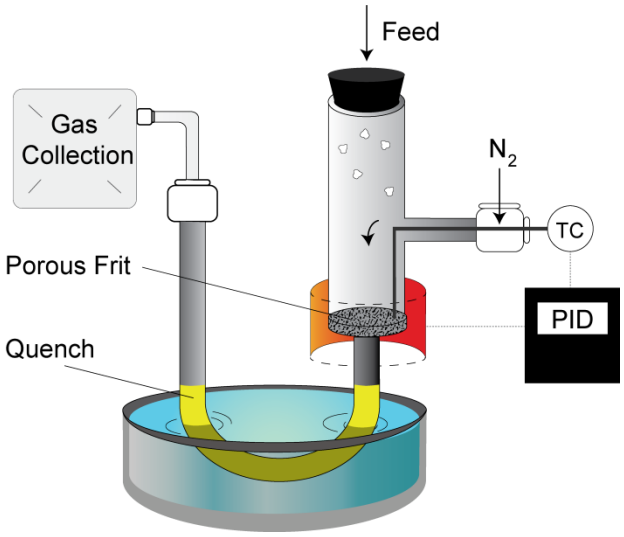

Figure 2-2: **Ablative Cellulose Pyrolysis Reactor.** Cellulose particles entrained in a nitrogen stream were pyrolyzed upon a 500 ºC porous frit. Vapors and entrained aerosols (< 200 nm) were quenched in a chilled trap, and permanent gases and high volatility vapors were collected in a gas sampling bag. Solid residual ash and char fractions were retained on the frit.

2.2.3 Imaging Techniques

High speed imaging experiments were performed using an Olympus BX51 microscope with long working distance lenses (Olympus LMPLFLN20x, LMPLFLN50x) and an aluminum coated optical grade mirror (Edmund Optics, 49-405) to obtain tangential images. A Phantom eX2 camera allowed for imaging at 1000 frames per second, with exposure times adjusted to observe aerosols (~10 µs), or liquid intermediate cellulose (~100 µs). Lighting was provided from behind the droplet using a high intensity mercury light source (Prior Lumen 200) focused on the

pyrolyzing particle. Image sequences were processed using the NIH program, ImageJ. Uniform contrast and brightness adjustment were applied equally to the entire image sequence to visualize the dynamics. Qualitative aerosol visualization was evaluated with the ImageJ particle counting feature (exclusion criteria: D_p <10 μm). Identified aerosols were then colored red (binary) and overlaid with the original contrast adjusted image (16 bit) to obtained the colored aerosol image (Figure 3b). For Transmission Electron Microscopy (TEM), samples were prepared by dispersing the aerosols in ethanol using a sonicator, after which the liquid samples were pipetted onto a TEM grid. The samples were dried overnight and TEM was performed using a JEOL JEM-2200FS.

2.2.4 Analytical Methods

Gaseous fractions collected in a gas-collection bag and vapor fractions obtained by ethanol quench were quantified via off-line gas chromatography using an Agilent 7890 GC-MS-TCD-FID and previously established methods.[9, 18, 39, 40]

Residual char and non-volatilized organic fractions were quantified using standard burn-off methods (ASTM E1755-01). Solid char was placed in a crucible and ashed at 595 °C in a VWR muffle furnace to determine the mass of char in the residual solid sample. The frit surface and surrounding reaction chamber were also ashed by recording the mass before and after heating with a butane torch in air until the frit glowed red-hot. The difference in mass before and after burn-off quantified char fractions.

Inorganic products in the char residual were quantified using the NREL ashing procedure.[41] Char/ash residuals were placed in a crucible and ashed for 24 hours at 595 °C in a VWR muffle furnace until only ash (CaO) remained. Inorganic products present in the ethanol quench were quantified using an acid digestion procedure (ASTM D5198–92)[42] followed by analysis using ICP-OES. The ethanol quench was digested using nitric acid by dissolving 1.0 ml of the quench with 10.0 ml of 34.5 wt% nitric acid. This solution was covered and heated at 95

°C for two hours with constant stirring. After acid digestion, the solution was diluted with DI water to 2 wt% nitric acid, and calcium was quantified via ICP-OES. Inorganic material remaining on the frit or in the crucible after carbon burn-off was also quantified by sonicating reactor components in dilute acid followed by ICP-OES analysis.

Aerosol particle size distributions were obtained using a Malvern Instruments Mastersizer 2000E. The instrument was calibrated using monodisperse (250 μm) microcrystalline cellulose. A range of cellulose concentrations was run on the particle sizer and a calibration curve was created by integrating the normalized response at each concentration. After calibration, the particle size distribution of aerosols produced was determined for the pure cellulose pyrolysis product samples.

Microscopy of quenched aerosols was performed with an Olympus BX51 optical microscope and objectives (Olympus LMPLFLN50x). A droplet of the ethanol quench was placed between a plastic cover slip and microscope slide and imaged to visualize aerosols entrained in the gas phase during pyrolysis.

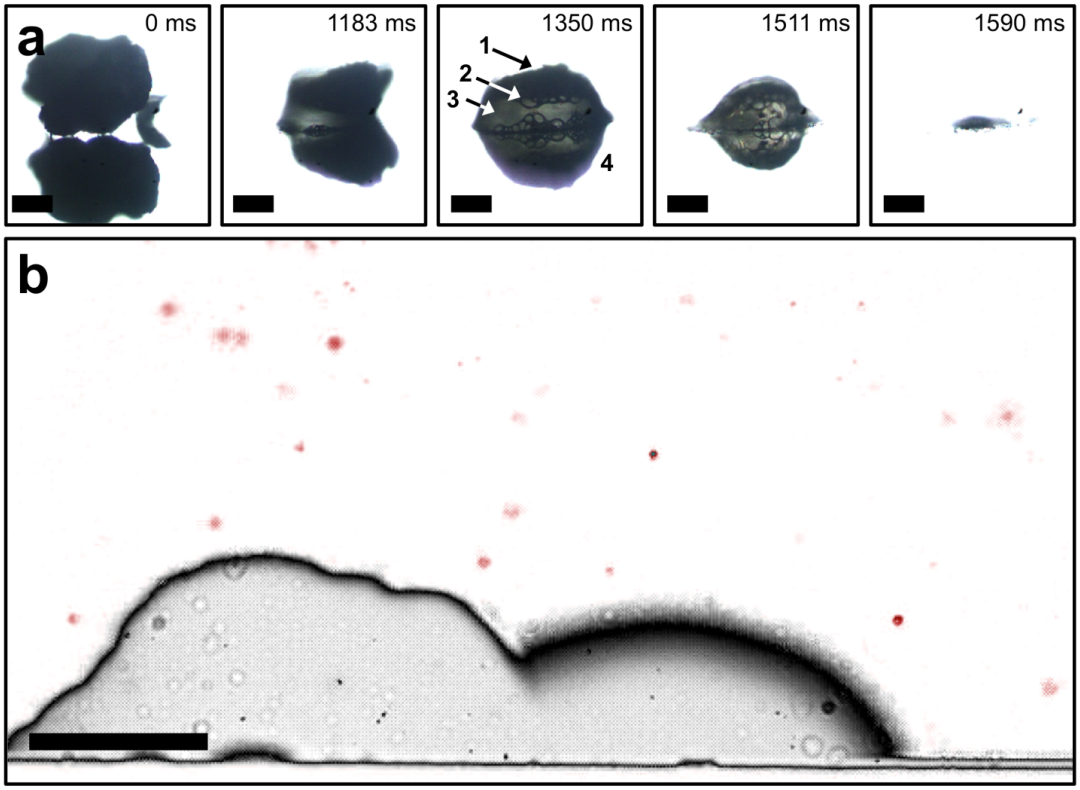

Figure 2-3: **Cellulose Pyrolysis – Aerosol Visualization.** High speed imaging of crystalline cellulose pyrolyzing on a 500 ºC aluminum nitride surface. a) Characteristic frames captured at five µs exposure (5e-6 sec) depict an impacting solid cellulose particle, transition to liquid, and finally bubbling and evaporation. At 1350 ms, labels indicate: (1) Solid cellulose, (2) vapor bubbles, (3) liquid intermediate, and (4) the polished, reflective surface. b) A background-corrected differencing technique identifies distinct entrained particles. Over forty aerosols (in red) were observed over the course of one millisecond within detection limits. Scale bars designate 100 µm.

2.3 Results

Primary aerosols were directly observed ejecting from vigorously bubbling liquid intermediate cellulose (Figure 3). Sequential frames in Figure 3a depict the solid particle (0 ms) contacting a 500 °C aluminum nitride surface, reacting to form a liquid at the particle/surface interface, and subsequently wetting the surface (1183 ms). Thermal gradients within the particle resulted in liquid intermediate at the bottom of the particle (1350 ms, #3), a solid cellulose 'cap' (1350 ms, #1), and a solid/liquid interface between the phases (1350 ms, #2). Bubbles within the liquid intermediate were observed to nucleate at the liquid/aluminum nitride surface and the cellulose solid/liquid interface. Vigorous bubbling in Figure 3b was imaged from the side and exhibited a large number of primary aerosols ejected from liquid intermediate cellulose; ejected particles are highlighted in red with varying degrees of clarity due to a narrow depth of field. More than forty large aerosol particles were observed by high speed imaging over a one millisecond time period.

Both pure cellulose and calcium-doped cellulose were pyrolyzed and fractionated; compositional results are summarized in Figure 4. In both cases aerosols were observed to be present in the liquid quench. Organic aerosols accounted for approximately 3% of the carbon yield in both the pure cellulose and Ca-doped cellulose pyrolysis cases. In addition to transporting organic molecules, aerosols also transported approximately 3% of initial calcium to the bio-oil fraction. Yields of permanent gases and total volatile organic compounds were determined in addition to the yield of char/ash. In the case of pure cellulose pyrolysis, approximately 52% of the carbon was recovered as volatile organics (bio-oil) while only 2% was recovered as char/ash. Ca-doped cellulose produced significantly more char at about 21% of the initial carbon, while the yield of volatile organics was reduced to 43%.

Aerosols collected in a liquid quench were characterized by laser diffraction light scattering as shown in Figure 5. The distribution of aerosols exhibited a maximum based on

aerosol mass at 70 nm, but particles were quantified as large as 200 nm. Quenched aerosols were also observed using visible light microscopy as shown in the inset images of Figure 5. By comparison with the measured aerosol size distribution (Figure 5, 10-100 nm), particles visualized by light microscopy were the largest detected aerosols and represent only a small fraction of generated aerosol products. Figure 6 shows aerosols via TEM imaging. Imaged aerosols were spherical with a diameter of approximately 100 nanometers.

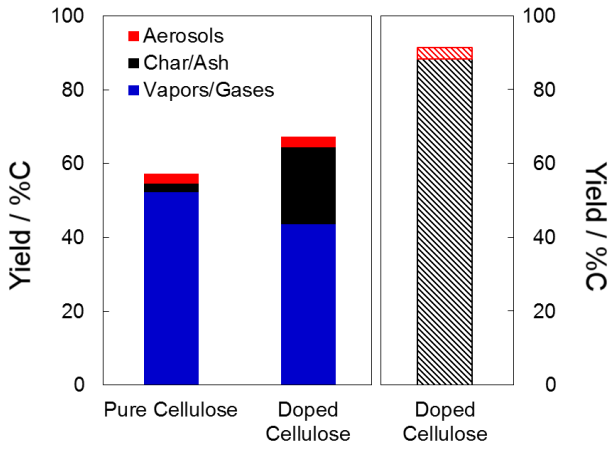

Figure 2-4: **Cellulose Pyrolysis – Product Yields.** The carbon yield of pure and Ca-doped cellulose were fractionated into the vapor, char, and aerosol fractions shown on the left axis. The yield of calcium was similarly fractionated as shown on the right for Ca-doped cellulose right axis.

2.4 Discussion

While secondary aerosols (formed by downstream condensation of pyrolysis vapors) have always been acknowledged, *primary* aerosols have only recently been discovered to exist during biomass fast pyrolysis.[37] The mechanism by which they are generated has been proposed, but little is known regarding their size distribution, composition, and capability for transporting additional materials existing within biomass (such as inorganic impurities).

2.4.1 Carbonaceous Aerosols.

Generation of a primary aerosols was recently shown to progress through a reactive liquid intermediate during pyrolysis of cellulose.[37] As cellulose undergoes transglycosylation at

350-500 °C to shorter anhydro-oligomer chains, it forms a liquid melt. Subsequent degradation produces volatile organic compounds and permanent gases, which form gas/vapor bubbles within the melt. Bubble growth over 5-10 milliseconds generates surface energy, which is rapidly converted upon bubble rupture to a liquid jet via surface tension driven cavity collapse. Subsequent jet fragmentation produces one or more aerosols ejected into the gas. Aerosols produced by this mechanism were directly observed in previous work ejecting from intermediate liquid cellulose and chemically identified to be present in the gas stream as nonvolatile oligomers characteristic of liquid intermediate cellulose.

Utilizing a magnified, high speed (Δt = 1 ms) imaging technique with a broad focal range, the prevalence of aerosols being ejected from the reactive liquid was demonstrated in this study. Figure 3b reveals the presence of more than 40 aerosols (> 200 nm, optical detection limit) being ejected over the period of a single millisecond at late droplet lifetime (1600 of 2140 ms). From the size distribution of quenched aerosols represented in Figure 5, we postulate that aerosols observed by high-speed imaging are rare events; a substantial fraction of submicron aerosols exist below the optical detection limits and thus cannot be directly visualized. Additionally, using optical microscopy, quenched primary aerosols were observed to exhibit high curvature with smoothed surfaces (Figure 5, inset micrographs and Figure 6), unlike the native fibrous and crystalline cellulose samples from which they were derived. This indicates aerosols undergo a liquid transition before freezing in their final state.

The prominence of carbonaceous aerosols was further confirmed by quantifying product fractions produced from ablative fast pyrolysis. Permanent gas and char fractions were close to the expected product distributions for pure cellulose pyrolysis (2–10 % and 10–20 %, respectively).[39, 43] Detection of the bio-oil products yielded a substantial fraction of quantifiable volatiles in the liquid quench (> 50% detectable). With improved sampling methodology, the total carbon yield would be expected to exceed 90%, as shown in previous work.[43] The remaining aerosol fraction, characterized by laser light diffraction, was the result of nonvolatile primary

products captured in the liquid quench. This fraction can be attributed to primary aerosols from cellulose pyrolysis, and was observed to consist of 2.8 % of the initial cellulose feed.

Bubbling within liquid intermediate cellulose was captured with high-speed photography by performing backlit experiments at high magnification. Under these conditions, heterogeneous nucleation was observed to contribute to bubble formation at the liquid intermediate cellulose interface with both the reactor surface and the remaining solid cellulose (Figure 3a). Near the end of the cellulose particle lifetime, bubbles comprised the bulk of the cellulose melt droplet. Bubble sizes were also clearly observed to exist in the range of 10^{-1}-10^{0} μm, confirming previous approximations.[37]

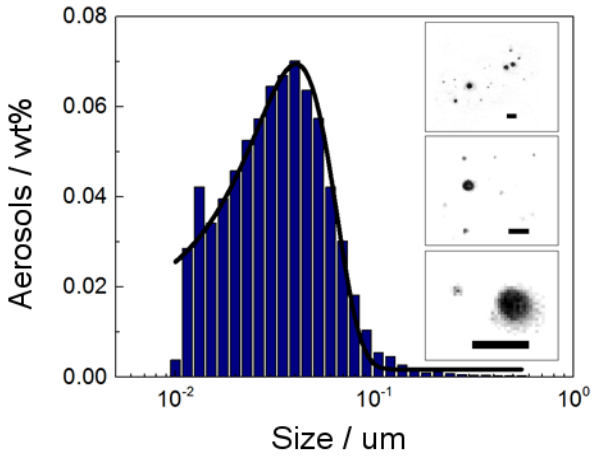

Figure 2-5: **Aerosol Particle Size Distribution.** Aerosols collected in the liquid quench are characterized using laser diffraction light scattering, demonstrating a submicron size distribution centered between 10-100 nm. Inset micrographs show the larger observable aerosols with characteristic smoothing of the surface. Scale bars = 10 μm.

While direct observation of bubble formation and visualization of large primary aerosol ejections (100 nm – 10 μm) in this work supports the bubble collapse/jet formation mechanism, the presence of submicron aerosols indicates the potential for film aerosol generation. Film aerosols arise from shear thinning of the liquid film between the vapor bubble and the surrounding gas phase until instabilities in the film result in rupture.[44] As the bubble film ruptures, liquid droplets are entrained in the vapors evacuating the bubble. The film aerosol

mechanism typically dominates aerosol generation when large bubbles (> 40 μm) are present, which is due to the inherent instabilities present in a large, shear-thinned film.[45] Conversely, the bubble collapse/jet formation mechanism typically dominates aerosol generation in small bubbles (< 40 μm). In this work, we observed small aerosols and large bubbles with a size ratio (ϕ = $\text{diameter}_{\text{aerosol}}/\text{diameter}_{\text{bubble}}$) of 10^{-2} – 10^{-1}, which suggests the presence of film droplets (small aerosols, large bubbles) in addition to the established jet droplets mechanism (large aerosols, small bubbles).

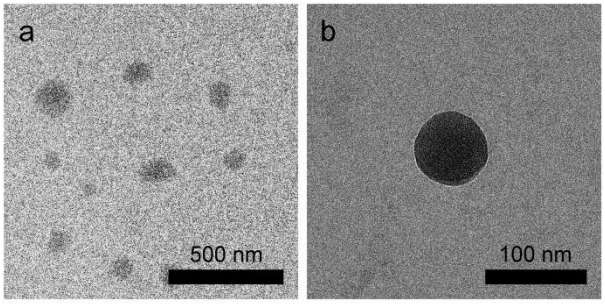

Figure 2-6: **TEM images of aerosols.** a) TEM image of aerosol particles on a silicon monoxide grid at 15,000X magnification. b) TEM image of a single aerosol particle on a carbon coated grid at 80,000X magnification.

2.4.2 Inorganic Aerosols.

After pyrolysis, the vast majority of inorganic materials present in native biomass remain as solid ash residue. In this work, the amount of inorganic material found in the ash after pyrolysis was greater than 88% of inorganic material in the feed, which is consistent with literature.[35] The presence of inorganic material within the cellulose feed increased the char yield from approximately 2% to 20% (Figure 4). Inorganic materials from biomass typically exhibit extremely low volatilities ($P^{sat}_{Calcium}(500\ °C) < 10^{-3}$ torr[46]), yet they are observed in quenched bio-oils.[25, 35] In other, non-reactive systems, such as the bubbling and churning of the ocean, aerosols have been shown to transport nonvolatile salts to the atmosphere by both jet and film aerosol mechanisms.[47] Similarly, we have shown here that reactive liquid intermediate cellulose continuously generates bubbles which burst to generate entrained aerosols (Figure 3). The

collected aerosols were qualitatively shown to transport nonvolatile inorganic material. Approximately 3% of impregnated calcium (Figure 4) was transported from the initial feed to the gas stream via aerosols. This result reveals the pathway by which similar fractions of nonvolatile inorganic materials (0.9 – 6.2%) are observed in bio-oil produced from bench-scale and industrial pyrolysis reactors.[35]

2.5 Conclusions

Transport of inorganic chemical species such as calcium oxide via generation of primary aerosols from liquid intermediate cellulose was revealed as the origin of inorganic products in bio-oil. Primary aerosol distributions were characterized via light microscopy and laser diffraction light scattering, with most particles existing in the range of 10-100 nm in diameter. Small aerosol-to-bubble size ratios provided the first evidence for both film and jet aerosol generation mechanisms. Direct evidence for calcium transport within primary aerosols was provided by inductively coupled plasma spectroscopy, which identified calcium within ejected aerosol particles. Contribution of primary aerosols to the product yield during biomass fast pyrolysis was substantial, with chemical compositions representative of the liquid melt being ejected in quantities equal to ~3% of the initial feed, consistent with industrial pyrolysis reactors.

2.6 References

1. A. Bridgwater, Principles and practice of biomass fast pyrolysis processes for liquids. *Journal of analytical and applied pyrolysis* **51**, 3-22 (1999).
2. G. Huber, Breaking the Chemical and Engineering Barriers to Lignocellulosic Biofuels: Next Generation Hydrocarbon Biorefineries. *Univ. of Massachusetts Amherst*, (2007).
3. P. Dauenhauer, Handbook of Plant-Based Biofuels. Edited by Ashok Pandey. *ChemSusChem* **3**, 386-387 (2010).
4. K. Sanderson, A field in ferment. *Nature* **444**, 673-676 (2006)10.1038/444673a).
5. S. Kersten, M. Garcia-Perez, Recent developments in fast pyrolysis of ligno-cellulosic materials. *Current Opinion in Biotechnology* **24**, 414-420 (2013); published online EpubJun (10.1016/j.copbio.2013.04.003).
6. R. D. Perlack, L. L. Wright, A. F. Turhollow, R. L. Graham, B. J. Stokes, D. C. Erbach, "Biomass as a Feedstock for a Bioenergy and Bioproducts Industry: The Technical Feasibility of a Billion-Ton Annual Supply," (Oak Ridge National Laboratory, Oak Ridge, TN, 2005).
7. R. D. Perlack, B. J. Stokes, "U.S. Billion-Ton Update: Biomass Supply for a Bioenergy and Bioproducts Industry," (Oak Ridge National Laboratory, Oak Ridge, TN, 2011).
8. G. W. Huber, S. Iborra, A. Corma, Synthesis of transportation fuels from biomass: Chemistry, catalysts, and engineering. *Chemical Reviews* **106**, 4044-4098 (2006); published online EpubSep 13 (10.1021/cr068360d).
9. M. S. Mettler, S. H. Mushrif, A. D. Paulsen, A. D. Javadekar, D. G. Vlachos, P. J. Dauenhauer, Revealing pyrolysis chemistry for biofuels production: Conversion of cellulose to furans and small oxygenates. *Energy Environ. Sci.* **5**, 5414-5424 (2011).
10. J. G. Brammer, M. Lauer, A. V. Bridgwater, Opportunities for biomass-derived "bio-oil" in European heat and power markets. *Energy Policy* **34**, (2006); published online EpubNov (10.1016/j.enpol.2005.05.005).
11. T. P. Vispute, H. Zhang, A. Sanna, R. Xiao, G. W. Huber, Renewable Chemical Commodity Feedstocks from Integrated Catalytic Processing of Pyrolysis Oils. *Science* **330**, 1222-1227 (2010); published online EpubNov 26 (10.1126/science.1194218).
12. S. Czernik, A. V. Bridgwater, Overview of Applications of Biomass Fast Pyrolysis Oil. *Energy & Fuels* **18**, 590-598 (2004)10.1021/ef034067u).
13. V. K. Venkatakrishnan, J. C. Degenstein, A. D. Smeltz, W. N. Delgass, R. Agrawal, F. H. Ribeiro, High-pressure fast-pyrolysis, fast-hydropyrolysis and catalytic hydrodeoxygenation of cellulose: production of liquid fuel from biomass. *Green Chemistry* **16**, 792-802 (2014); published online EpubFeb (10.1039/c3gc41558a).
14. A. V. Bridgwater, Review of fast pyrolysis of biomass and product upgrading. *Biomass & Bioenergy* **38**, 68-94 (2012); published online EpubMar (10.1016/j.biombioe.2011.01.048).
15. X. Zhou, M. W. Nolte, B. H. Shanks, L. J. Broadbelt, Experimental and Mechanistic Modeling of Fast Pyrolysis of Neat Glucose-Based Carbohydrates. 2. Validation and Evaluation of the Mechanistic Model. *Industrial & Engineering Chemistry Research* **53**, 13290-13301 (2014); published online EpubAug 27 (10.1021/ie502260q).
16. P. J. Dauenhauer, J. L. Colby, C. M. Balonek, W. J. Suszynski, L. D. Schmidt, Reactive boiling of cellulose for integrated catalysis through an intermediate liquid. *Green Chemistry* **11**, 1555-1561 (2009)10.1039/b915068b).
17. O. Boutin, M. Ferrer, J. Lede, Radiant flash pyrolysis of cellulose - Evidence for the formation of short life time intermediate liquid species. *Journal of Analytical and Applied Pyrolysis* **47**, 13-31 (1998); published online EpubSep (

18. M. S. Mettler, A. D. Paulsen, D. G. Vlachos, P. J. Dauenhauer, Pyrolytic conversion of cellulose to fuels: levoglucosan deoxygenation via elimination and cyclization within molten biomass. *Energy & Environmental Science* **5**, 7864-7868 (2012).
19. M. S. Mettler, A. D. Paulsen, D. Vlachos, P. J. Dauenhauer, Tuning Cellulose Pyrolysis Chemistry: Selective Decarbonylation via Catalyst-Impregnated Pyrolysis. *Catalysis Science & Technology*, (2014).
20. A. D. Paulsen, Hough, B. R., Williams, C. L., Teixeira, A. R., Schwartz, D. T., Pfaendtner, J., & Dauenhauer, P. J., Fast Pyrolysis of Wood for Biofuels: Spatiotemporally Resolved Diffuse Reflectance In situ Spectroscopy of Particles. *ChemSusChem* **7**, 765-776 (2014).
21. C. R. Shaddix, D. R. Hardesty, "Combustion Properties of Biomass Flash Pyrolysis Oils: Final Project Report," (Sandia National Laboratories, 1999).
22. A. V. Bridgwater, S. Czernik, J. Piskorz, in *Progress in Thermochemical Biomass Conversion*. (Blackwell Science Ltd, 2008), pp. 977-997.
23. E. Fratini, M. Bonini, A. Oasmaa, Y. Solantausta, J. Teixeira, P. Baglioni, SANS analysis of the microstructural evolution during the aging of pyrolysis oils from biomass. *Langmuir* **22**, 306-312 (2006); published online EpubJan 3 (10.1021/la051990a).
24. H. B. Goyal, D. Seal, R. C. Saxena, Bio-fuels from thermochemical conversion of renewable resources: A review. *Renewable & Sustainable Energy Reviews* **12**, 504-517 (2008); published online EpubFeb (10.1016/j.rser.2006.07.014).
25. D. Mohan, C. U. Pittman, Jr., P. H. Steele, Pyrolysis of wood/biomass for bio-oil: A critical review. *Energy & Fuels* **20**, 848-889 (2006); published online EpubMay (10.1021/ef0502397).
26. C. W. Klampfl, G. Breuer, C. Schwarzinger, B. Koll, Investigations on the effect of metal ions on the products obtained from the pyrolysis of cellulose. *Acta chimica slovenica* **53**, 437 (2006).
27. K. Raveendran, A. Ganesh, K. C. Khilar, Influence of mineral matter on biomass pyrolysis characteristics. *Fuel* **74**, 1812-1822 (1995)Doi: 10.1016/0016-2361(95)80013-8).
28. J. G. Lee, E.-J. Shin, R. A. Pavelka, M. S. Kirchner, D. Dounas-Frazer, B. D. McCloskey, D. E. Petrick, J. T. McKinnon, A. M. Herring, Effect of Metal Doping on the Initial Pyrolysis Chemistry of Cellulose Chars. *Energy & Fuels* **22**, 2816-2825 (2008); published online Epub2008/07/01 (10.1021/ef700637s).
29. M. S. Mettler, A. D. Paulsen, D. G. Vlachos, P. J. Dauenhauer, Tuning cellulose pyrolysis chemistry: selective decarbonylation via catalyst-impregnated pyrolysis. *Catalysis Science & Technology*, (2014)10.1039/C4CY00676C).
30. P. R. Patwardhan, J. A. Satrio, R. C. Brown, B. H. Shanks, Influence of inorganic salts on the primary pyrolysis products of cellulose. *Bioresource Technology* **101**, 4646-4655 (2010)10.1016/j.biortech.2010.01.112).
31. J. P. Diebold, *A review of the chemical and physical mechanisms of the storage stability of fast pyrolysis bio-oils*. (2000).
32. R. R. Baker, Smoke generation inside a burning cigarette: Modifying combustion to develop cigarettes that may be less hazardous to health. *Progress in Energy and Combustion Science* **32**, 373-385 (2006); published online Epub// (http://dx.doi.org/10.1016/j.pecs.2006.01.001).
33. J. S. Reid, R. Koppmann, T. F. Eck, D. P. Eleuterio, A review of biomass burning emissions part II: intensive physical properties of biomass burning particles. *Atmos. Chem. Phys.* **5**, 799-825 (2005)10.5194/acp-5-799-2005).
34. D. C. Elliott, A. Oasmaa, F. Preto, D. Meier, A. V. Bridgwater, Results of the IEA Round Robin on Viscosity and Stability of Fast Pyrolysis Bio-oils. *Energy & Fuels* **26**, (2012); published online EpubJun (10.1021/ef300384t).

35. N. Jendoubi, F. Broust, J. M. Commandre, G. Mauviel, M. Sardin, J. Lede, Inorganics distribution in bio oils and char produced by biomass fast pyrolysis: The key role of aerosols. *Journal of Analytical and Applied Pyrolysis* **92**, 59-67 (2011); published online EpubSep (10.1016/j.jaap.2011.04.007).
36. B. Scholze, C. Hanser, D. Meier, Characterization of the water-insoluble fraction from fast pyrolysis liquids (pyrolytic lignin) Part II. GPC, carbonyl goups, and C-13-NMR. *Journal of Analytical and Applied Pyrolysis* **58**, 387-400 (2001); published online EpubApr (10.1016/s0165-2370(00)00173-x).
37. A. R. Teixeira, K. G. Mooney, J. S. Kruger, C. L. Williams, W. J. Suszynski, L. D. Schmidt, D. P. Schmidt, P. J. Dauenhauer, Aerosol generation by reactive boiling ejection of molten cellulose. *Energy & Environmental Science* **4**, 4306-4321 (2011).
38. M. S. Mettler, D. G. Vlachos, P. J. Dauenhauer, Top ten fundamental challenges of biomass pyrolysis for biofuels. *Energy & Environmental Science* **5**, 7797-7809 (2012); published online EpubJul (10.1039/c2ee21679e).
39. A. D. Paulsen, M. S. Mettler, P. J. Dauenhauer, The Role of Sample Dimension and Temperature in Cellulose Pyrolysis. *Energy & Fuels* **27**, 2126-2134 (2013); published online Epub2013/04/18 (10.1021/ef302117j).
40. M. S. Mettler, A. D. Paulsen, D. G. Vlachos, P. J. Dauenhauer, The chain length effect in pyrolysis: bridging the gap between glucose and cellulose. *Green Chemistry* **14**, 1284-1288 (2012).
41. A. Sluiter, B. Hames, R. Ruiz, C. Scarlata, J. Sluiter, D. Templeton. (*National Renewable Energy Laboratory*, 2008), pp. 1-5.
42. . (ASTM International, West Conshohocken, PA, 1992 (2003)).
43. M. S. Mettler, S. H. Mushrif, A. D. Paulsen, A. D. Javadekar, D. G. Vlachos, P. J. Dauenhauer, Revealing pyrolysis chemistry for biofuels production: Conversion of cellulose to furans and small oxygenates. *Energy & Environmental Science* **5**, 5414-5424 (2012); published online EpubJan (10.1039/c1ee02743c).
44. D. E. Spiel, On the births of film drops from bubbles bursting on seawater surfaces. *J. Geophys. Res.* **103**, 24907-24918 (1998)10.1029/98jc02233).
45. F. Resch, G. Afeti, FILM DROP DISTRIBUTIONS FROM BUBBLES BURSTING IN SEAWATER. *J. Geophys. Res.* **96**, 10681-10688 (1991)10.1029/91jc00433).
46. N. B. Pilling, Vapor Pressure of Metallic Calcium. *Physical Review* **18**, 362-368 (1921); published online Epub11/01/ (
47. D. C. Blanchard, in *Progress in oceanography*, M. Sears, Ed. (Pergamon Press, 1963), pp. 71.

CHAPTER 3

REACTIVE LIFTOFF OF CRYSTALLINE CELLULOSE PARTICLES

3.1 Introduction

A pyrolyzing microcrystalline cellulose particle can be analogous to a boiling water droplet on a heated surface. When subjected to high temperatures (>400 °C), long chain biopolymers such as cellulose decompose into smaller, more valuable products used for renewable fuels and chemicals. The chemistry of cellulose decomposition is the subject of ongoing investigation;[1,2] promotion of the desirable reaction pathways and/or variation of the heating rate can strongly alter product distribution consisting of hundreds of chemicals.[3,4] Recent work has shown that long chain, crystalline cellulose reacts to a short-lived liquid intermediate with millisecond lifetime comprised of molten oligomers before decomposing to vapors.[5] Despite strong dependence on heat transfer, there is limited understanding of the multi-phase behavior of non-volatile molten cellulose on high temperature surfaces.[5] Here, we show that surface structure and temperature strongly alter pyrolyzing cellulose as the microcrystalline particle evolves into a liquid intermediate droplet and transitions through heat transfer regimes, including the film-boiling Leidenfrost effect, where complete particle liftoff is observed. The resulting heat transfer rates vary by nearly an order of magnitude across a temperature range commonly used for pyrolysis. Surface macropores, such as those found on catalysts, suppress cellulose droplet liftoff and enhance heat transfer to the intermediate liquid. Discovery of the cellulose Leidenfrost effect as a result of reactive vapor production from an initially crystalline solid provides the first detailed understanding of biopolymer/surface interactions which help contextualize the importance of heat transfer in pyrolysis.

Design of inorganic surfaces for enhanced heat transfer aims to control the interface with droplets, with increased wetting and surface area providing greater contact and transfer of thermal energy. However, at higher surface temperatures, liquids such as water undergo a transition to

Leidenfrost film boiling, where vapor production reaches a critical rate such that a vapor/gas layer forms between the heated surface and the liquid.[6] The transition to a completely de-wetted state is accompanied by a dramatic reduction in heat transfer into the liquid, greatly increasing the lifetime of the droplet.[7]

In contrast, macromolecules such as cellulose are not known to lift off of high temperature surfaces. Comprised of long chains of six-carbon sugars (10^2-10^3 units long), cellulose forms microcrystalline domains in solid particles with sharp edges and macropores. It has previously been shown that chain size reduction via intra-chain (glycosidic) cleavage forms short-chain oligomers, which melt and form liquid droplets for 100-200 ms before further reacting to volatile species (less than six carbons in size) and evaporating. However, intermediate liquid cellulose has previously been shown to wet surfaces such as alumina at temperatures as high as 700 °C.

In this work, it is shown through high-speed visualization that crystalline cellulose exhibits the Leidenfrost film boiling effect as a result of reactive gas and vapor production during the millisecond-scale liquid intermediate lifetime. Molten cellulose droplets are observed lift off of high temperature surfaces move erratically driven by off gas flow. With the introduction of macroporous heated substrates, complete suppression of the Leidenfrost effect is observed, with vapor flowing through surface. Vapor layer inhibition further suppresses droplet motion with improved heat transfer due to improved droplet/surface contacting.

3.2 Methods

Imaging of reacting particles was performed using combined in situ high-speed photography and microscopy with a temperature controlled reaction stage. A 90-degree

mirror was used for profile visualization, allowing for determination of wetting behavior and contact angles of droplets. Microcrystalline cellulose with a 220 μm average particle diameter was impinged upon the hot stage, and the resulting liquid intermediate evaporation rate was measured for temperatures between 500 °C and 775 °C. Experiments were performed on a silicon substrate polished to 5 μm surface roughness as well as silica and alumina particles that were pressed to 15 kpsi and calcined, creating a macroporous surface.

3.3 Results and Discussion

For cellulose impinging on a polished silicon surface, the solid particle transitions to a liquid droplet, after which the liquid droplet reacts to primarily form gases and vapors. The reactive evaporation rate, which is directly proportional to the rate of heat transfer into the particle,[7] is defined as the change in the apparent area of the particle from the time it was completely liquid until it fully reacts divided by that time interval. For low temperatures (500-650 °C), intermediate liquid evaporation rate increases nearly linearly with temperature (Figure 1a). In this regime, liquid intermediate cellulose wets the surface, providing rapid solid-liquid heat transfer (Figure 1b). Receding contact angles for wetting intermediate liquid cellulose were measured[†]. However, between 675 °C and 750 °C, the evaporation rate decreases with increasing temperature. At these temperatures, the rate of vapor and gas production is sufficient such that film boiling was observed, with a gas layer greatly reducing heat transfer between the surface and the particle. Above 750 °C, the intermediate liquid fully de-wets the surface and evaporation rate increases with further increases in temperature. For these conditions, intermediate cellulose liquid moved erratically on polished silica surfaces driven by off gas flow.

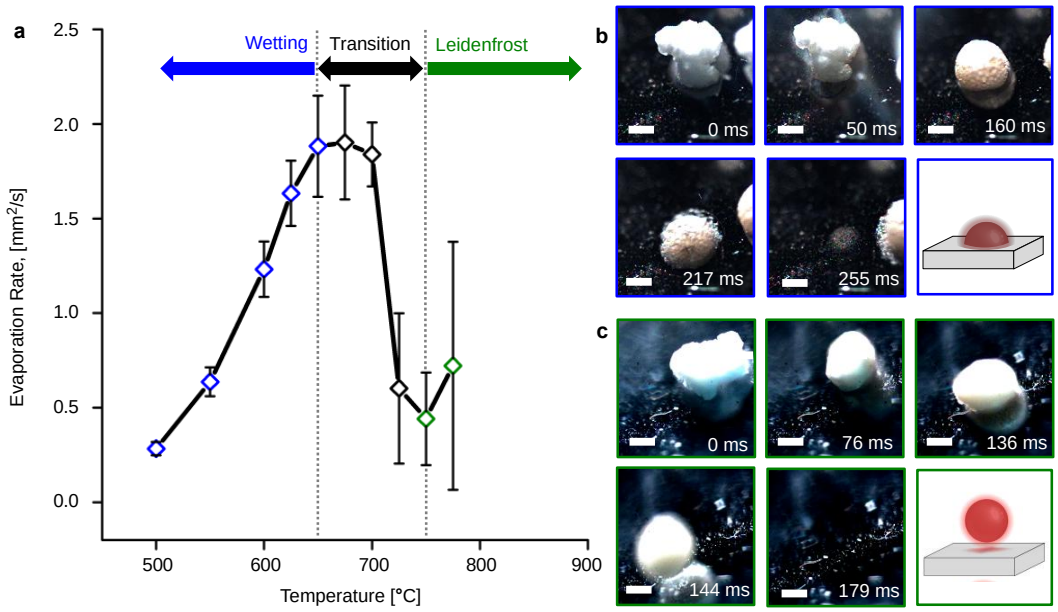

Figure 3-1: Reactive Liftoff of Crystalline Cellulose Particles on Polished Silicon. A. The rate of evaporation of initially crystalline cellulose particles (average 220 µm) varies by an order of magnitude as the intermediate droplet transitions from low temperature wetting (blue) to film boiling (black) and into the Leidenfrost regime (green). B. Initially microcrystalline cellulose forms a melt (160 ms), wets polished silicon, and completely evaporates by 250 ms. C. Microcrystalline cellulose particles form a melt on polished silicon which lifts off the surface and moves out of frame (179 ms).

The heat transfer curve measured in Figure 1a closely resembles those measured in conventional liquid evaporation Leidenfrost curves. Observed heat transfer rates vary by nearly an order of magnitude as the particle is subject to transitioning modes of heat transfer. At low temperatures, solid-liquid conduction via wetting provides rapid thermal flux into the particle. With the onset of film boiling, convection through the gas layer becomes the dominant mode of heat transfer. This result indicates that the lifetime of a reacting cellulose particle is determined by the rate of heat transfer into the particle above 650 °C. However, reacting cellulose intermediate liquid differs from conventional Leidenfrost droplets volatile liquids in that the heat flux supplied to the droplet is balanced by both heat of vaporization as well as heat of reaction for cellulose. Comparison of these two thermodynamic quantities, as presented in the supplementary information, shows that the majority of heat supplied at the interface is consumed for

cellulose reaction to volatile products. Moreover, comparison of the timescale for reaction based on cellulose pyrolysis kinetics and experimentally measured particle lifetimes indicates that kinetics of vapor and gas production are not rate limiting.[8]

The apparent cross-sectional particle area as viewed from above was traced with time between 500 °C and 800 °C and plotted in figure 2a normalized to the original particle area. At 500 °C and 600 °C, the particle area first increases, as the intermediate liquid cellulose spreads to wet the surface. This is followed by rapid decrease in area as the intermediate liquid reacts, evaporates and shrinks. At 800 °C – in the Leidenfrost regime – the particle does not spread to wet the surface and shows significantly reduced heat transfer as the particle slowly reacts. Even at 800 °C, the particle exhibits an overall lifetime similar to that observed below 600 °C. Figures 2b and 2c depict cellulose on a polished surface at 625 °C and 750 °C respectively, showing the qualitative differences between droplet spreading and wetting at lower temperatures and de-wetting in the Leidenfrost regime above 750 °C. Previous studies have shown that the vapor layer underneath a Leidenfrost droplet is very thin (particle radius >> vapor film height) for the majority of the droplet lifetime.[9] As observed in figure 2c, the particle height is on the same order of magnitude as droplet radius, indicating a substantial rate of gas and vapor production.

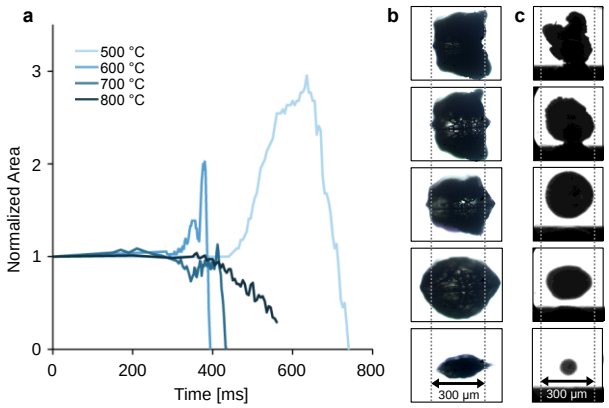

Figure 3-2: Individual Cellulose Particles on Polished Silica. A. Cross sectional area of cellulose particles (initially ~300 µm) normalized to initial values with reaction time (0-800 ms) for 500-800 °C on polished silica. B. Profile images of droplets at lower temperature, which liquefy and wet with increased contact area before rapidly evaporating. C. Side images of droplets at higher temperatures, where crystalline cellulose liquefies and off gases at sufficient rate to lift molten cellulose droplets above the surface.

Deviation from the Leidenfrost curve in Figure 1a was observed when cellulose was pyrolyzed on porous pressed silica and alumina surfaces. Under these conditions, there was no observable transition to Leidenfrost behavior with increased temperature. As a result, the heat transfer rate shown in figure 3a is nearly linear with temperature across the measured range (500-750 °C). Additionally, at temperatures below 675 °C, the observed heat transfer rates are lower compared with those from the polished silicon surface, indicating a lower solid-liquid heat transfer coefficient. However, at 775 °C the heat transfer rate for the porous surfaces is higher that that observed for the polished surface. This results indicates that particle liftoff from vapor generation is completely inhibited across this temperature range, which agrees with previous work that suggests that vapors and gases from an evaporating liquid droplet penetrate into surface features, such as channels and macropores, thereby suppressing the Leidenfrost effect.[10-13] In figure 3b, a snapshot of a pyrolyzing cellulose particle on porous alumina at 750 °C, an expected Leidenfrost regime, shows no particle liftoff.

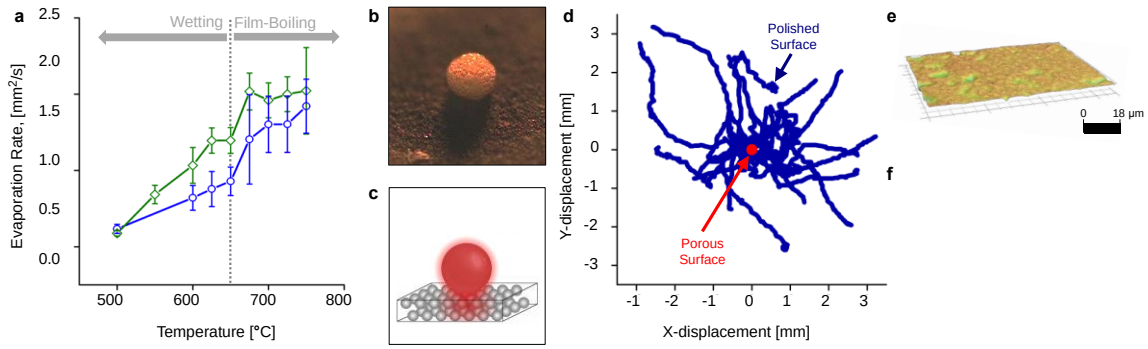

Figure 3-3: Structured Surfaces for Suppression of Cellulose Particle Liftoff. A. Cellulose particles (~300 µm) liquefy and evaporate at increasing rate as temperature increases on porous silica (color) and alumina (color), with no measurable transition to film boiling. B-C. Droplet of molten cellulose on porous silica. D. Position of cellulose particles on polished alumina (blue) and porous alumina (red) indicate suppressed liftoff and motion (skittering) on porous materials. E. 3D profilometry of porous alumina indicates minimal surface roughness.

A common characteristic of droplets exhibiting the Leidenfrost effect is the 'skittering' or dancing motion across the surface, as is commonly observed with a superheated water droplet on metal surfaces. Traces of individual particle motion from high speed imaging for cellulose and polished and porous alumina surfaces are shown in figure 3c, with each trace starting at the plot origin. Significant particle motion was observed for the polished surface, with droplets moving in a generally consistent direction once initiated. However, in the case of the porous surfaces, almost no particle motion was observed (see supplementary video†). Optical surface profilometry in Figure 3d depicts flat surface topography, with peak to valley height of only 10-20 µm, indicating that the surface of porous alumina was relatively flat compared to the lengthscale of cellulose particles. SEM micrographs in figure 3e indicate visible macropores between alumina particles, supporting the mechanism of gas flow through surface pores suppression of Leidenfrost behavior.

Dramatic difference in biopolymer behavior on heated, structured surfaces is integral to reactor design for utilization of natural resources such as biomass. Industrial scale pyrolysis reactions are commonly carried out in the presence of pressed silica and

alumina based catalysts with macropores, while the majority of fundamental pyrolysis studies are carried out on smooth stainless steel surfaces. The impact of porous structures and dramatic role of temperature on the de-wetting liftoff behavior of cellulose at high temperature allows for tuning to increase heat transfer and dramatically alter the throughput of biomass reactors, which are overall heat transfer limited systems. Alternatively, surface design to enhance cellulose particle liftoff has potential for separating biomass from product vapors, which could be used to separate inorganic material (ash such as SiO_2) within biomass during reaction. Additionally, enhancement of biomass particle liftoff could reduce contact with solid surfaces, which serve as heterogeneous nucleation sites and lead to enhanced formation of molten cellulose aerosols. Further research into cellulose liftoff on structured surfaces will allow for precise design of structured surfaces for new biomass reactors.

3.4 References

1 Mettler, M. S., Paulsen, A. D., Vlachos, D. G. & Dauenhauer, P. J. Pyrolytic conversion of cellulose to fuels: levoglucosan deoxygenation via elimination and cyclization within molten biomass. *Energy & Environmental Science* **5**, 7864-7868, doi:10.1039/C2EE21305B (2012).

2 Bridgwater, A. V., Meier, D. & Radlein, D. An overview of fast pyrolysis of biomass. *Organic Geochemistry* **30**, 1479-1493, doi:http://dx.doi.org/10.1016/S0146-6380(99)00120-5 (1999).

3 Paulsen, A. D., Mettler, M. S. & Dauenhauer, P. J. The Role of Sample Dimension and Temperature in Cellulose Pyrolysis. *Energy & Fuels* **27**, 2126-2134, doi:10.1021/ef302117j (2013).

4 Mettler, M. S. *et al.* Revealing pyrolysis chemistry for biofuels production: Conversion of cellulose to furans and small oxygenates. *Energy & Environmental Science* **5**, 5414-5424, doi:10.1039/C1EE02743C (2012).

5 Dauenhauer, P. J., Colby, J. L., Balonek, C. M., Suszynski, W. J. & Schmidt, L. D. Reactive boiling of cellulose for integrated catalysis through an intermediate liquid. *Green Chemistry* **11**, 1555-1561, doi:10.1039/B915068B (2009).

6 Biance, A.-L., Clanet, C. & Quéré, D. Leidenfrost drops. *Physics of Fluids (1994-present)* **15**, 1632-1637, doi:doi:http://dx.doi.org/10.1063/1.1572161 (2003).

7 Gottfried, B. S., Lee, C. J. & Bell, K. J. The leidenfrost phenomenon: film boiling of liquid droplets on a flat plate. *International Journal of Heat and Mass Transfer* **9**, 1167-1188, doi:http://dx.doi.org/10.1016/0017-9310(66)90112-8 (1966).

8 Bradbury, A. G. W., Sakai, Y. & Shafizadeh, F. A kinetic model for pyrolysis of cellulose. *Journal of Applied Polymer Science* **23**, 3271-3280, doi:10.1002/app.1979.070231112 (1979).

9 Celestini, F., Frisch, T. & Pomeau, Y. Take Off of Small Leidenfrost Droplets. *Physical Review Letters* **109**, 034501 (2012).

10 Avedisian, C. T. & Koplik, J. Leidenfrost boiling of methanol droplets on hot porous/ceramic surfaces. *International Journal of Heat and Mass Transfer* **30**, 379-393, doi:http://dx.doi.org/10.1016/0017-9310(87)90126-8 (1987).

11 Chandra, S. & Avedisian, C. T. Observations of droplet impingement on a ceramic porous surface. *International Journal of Heat and Mass Transfer* **35**, 2377-2388, doi:http://dx.doi.org/10.1016/0017-9310(92)90080-C (1992).

12 Arnaldo del Cerro, D. *et al.* Leidenfrost Point Reduction on Micropatterned Metallic Surfaces. *Langmuir* **28**, 15106-15110, doi:10.1021/la302181f (2012).

13 Kwon, H.-m., Bird, J. C. & Varanasi, K. K. Increasing Leidenfrost point using micro-nano hierarchical surface structures. *Applied Physics Letters* **103**, -, doi:doi:http://dx.doi.org/10.1063/1.4828673 (2013).

CHAPTER 4

ANALYTICAL TECHNIQUES FOR CELLULOSE PYROLYSIS: SPATIOTEMPORALLY RESOLVED DIFFUSE REFLECTANCE IN SITU SPECTROSCOPY OF PARTICLES (STR-DRISP) AND QUANTITATIVE CARBON DETECTOR FOR GAS CHROMATOGRAPHY (GC-QCD)

4.1 Introduction

Understanding of molecular-scale chemistry of pyrolysis has rapidly progressed from lumped-kinetic models of the past few decades. While initial lumped chemistries predicted the rate of generation of gases, vapors and char,[1, 2] new experimental and computational techniques are revealing the pathways, mechanisms and kinetics of cellulose and lignocellulose pyrolysis. For example, development of the technique, 'thin-film pyrolysis' (TFP), has characterized the first set of pyrolysis products produced by primary condensed-phase reactions absent heat and mass transport limitations.[3] TFP has also led to the discovery of a chain-length effect in cellulose pyrolysis[4] and the stability of the five-membered furan ring within the liquid intermediate.[5] Additionally, secondary condensed-phase reactions of cellulose have been examined by another experimental technique called, 'co-pyrolysis,' which has revealed the condensed-phase reactions of levoglucosan to produce pyrans, anhydrosugars, and light oxygenates.[6] In parallel, the use of *ab initio* molecular dynamics and DFT has described the high temperature behavior of cellulose,[7, 8] the mechanisms associated with glycosidic cleavage,[3, 9] and the formation of pyrolysis products including furans[3, 10, 11] and light oxygenates.[3, 11] These discoveries are rapidly leading to the development of molecular-level kinetic models of cellulose[12] and eventually lignocellulose pyrolysis.

While significant progress has been made in establishing pathways dominating model compound and cellulose pyrolysis, substantial limitations exist moving forward to more complex

systems. From an experimental standpoint, thousands of compounds are observed during biomass pyrolysis, many of which cannot be isolated and calibrated for. Instead, assumptions are often made as for class based detector response approximations. In this work, two new detection techniques are presented. First, a molecular level technique allows for absolute quantification of all carbon-containing volatile species. The Quantitative Carbon Detector (QCD), was developed and optimized for cellulose pyrolysis product detection.

For the more complex system with coupled heat, mass and kinetic control, a second technique is developed. Difuse Reflectance in situ spectroscopy of particles (DRiSP) is used to quantify the conversion of wood particles during ablative pyrolysis with spatial resolution on the order of microns and temporal resolution as low as 1 ms.

4.2 Spatiotemporally-Resolved Diffuse Reflectance in situ Spectroscopy of Particles (STR-DRiSP)

Despite significant improvement in understanding molecular-level cellulose pyrolysis chemistry, progress towards the modeling of lignocellulose pyrolysis chemistry and transport phenomena within wood fibers during pyrolysis remains a challenge. Over the past few decades, it has been conclusively shown that heating rates of lignocellulosic particles/fibers in the range of 0.1-1.0 MW m^{-2} produces higher yields of bio-oil.[1, 2, 13-15] At these conditions, initial heating of a particle conducts thermal energy through the cellular structure of lignocellulosic biomass. In turn, the particles exhibit a propagating thermal front, consistent with high Biot numbers (Bi >>1) which drives pyrolysis chemistry in multiple zones[16] as depicted by the cutaway in Figure 1a. Leading this front is a drying zone, wherein moisture evaporates.[17] This is followed by the pyrolysis zone wherein the lignocellulosic biopolymers are depolymerized to form intermediate liquids, driving microstructural collapse (shrinkage) of biomass[18, 19] and producing vapors and aerosols.[20] As pyrolysis goes to completion, the resulting porous char zone (which will comprise

the entire wood particle upon 100% conversion) conducts heat, transports volatiles, and traps aerosols produced earlier in pyrolysis.

The experimental challenge of acquiring a detailed description of particle pyrolysis arises from the small size of wood fibers (1-2 mm), the fast time-scales of the reaction (1-5 seconds), and the compositional complexity of lignocellulose which is difficult to characterize. Existing experimental data sets of wood particle pyrolysis focus primarily on conversion time, reactant weight loss, and lumped-product yields,[21] which do not provide the spatiotemporally-resolved compositional data needed for validation of complex multi-scale models. Additionally, many experimental data sets of pyrolyzing particles, such as thermogravimetric analysis (TGA), utilize low heating rates with only moderate rates of temperature change (1 – 150 °C min^{-1}) not reflective of fast pyrolysis conditions (>10^3 °C min^{-1}). In contrast, spatially-resolved temperature profiles of wood particles have been collected (requiring particles as large as two-to-five centimeters), but they are unable to achieve sub-millimeter spatial resolutions necessary for tracking pyrolysis reaction zones.[22] A recent review of pyrolysis modeling by Di Blasi states that "significant effort, in both theoretical and experimental research activities, is still required to formulate and validate truly comprehensive models."[21] For this reason, overcoming the experimental challenges required to generate a data set of composition within reacting particles has recently been identified by us as one of the major fundamental challenges of biomass pyrolysis.[18]

Direct observation of the pyrolysis reaction front on the external particle surface allows for compositional characterization by diffuse reflectance. Diffuse reflectance of visible and near infrared light (400 nm – 2500 nm) on particle surfaces has been used for characterization of woody biomass samples.[23-25] The characterization of wood chip composition, including initial lignin content and breakdown of sugars, has been demonstrated using only the 800-1100 nm spectrum.[26] Similarly, more general characterization of composition is available within the visible spectrum region, where lignin (highly absorptive) and carbohydrates (highly reflective) are easily

distinguished.[27, 28] The distinct absorptive differences between lignin, carbohydrates (five- and six-carbon sugar-based biopolymers), and char over a broad range in the visible spectrum allows for characterization of moving or reacting wood fibers with limited spectral filtering.[24]

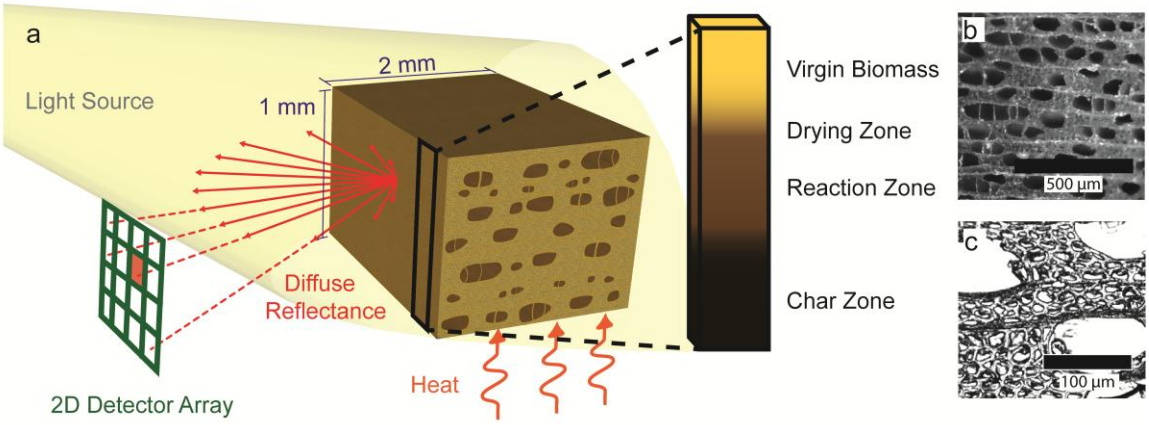

Figure 4-1: Diffuse Reflectance in situ Spectroscopy of Particles. (a) Fast pyrolysis experimental setup with a cutaway demonstrating the zones that exist during biomass pyrolysis at one moment in time, and bright field micrographs of yellow poplar structure (b) at 5x and (c) 50x magnification

In the technique introduced here (Figure 1), Spatiotemporally-Resolved Diffuse Reflectance in situ Spectroscopy of Particles (STR-DRiSP), visible light (maximum intensity at 900 nm) is applied to the external side surface of a yellow poplar wood particle (1.0 mm by 2.0 mm by 4.0 mm), and diffusely reflected light is captured using a high-speed, monochrome camera. The overlap of detector absorption range and incident light allows for spectroscopic characterization in the range of 400 – 1100 nm, where significant differences in absorption between lignin/char and carbohydrates are maximized. Rapid response time of the camera (1000 Hz) combined with the capability for focusing on a two-dimensional surface (in focus on the particle surface) allows for the compositional characterization of carbohydrates within reacting particles in both position (ten micron resolution) and time (one millisecond temporal resolution).

The spatio-temporally resolved compositional data set is compared with a robust model for wood fiber pyrolysis at industrial conditions. Carbohydrate compositions within yellow poplar are measured for both position and time over a range of ablative surface temperatures (500 – 700

°C). A reaction-transport model is developed by modifying the kinetic reaction model of Miller & Bellan[29] and combining it with a transport model developed for experiments described here.

4.2.1 Experimental Diffuse Reflectance Approach

Experimental conditions were designed to capture the compositional transition from carbohydrate-rich biomass feedstock (cellulose and hemicellulose) to carbon rich char. The technique employed here utilizes diffuse reflectance due to its relative ease in distinguishing between the key components in the visible and near infrared regions. Due to the Lambertian nature of wood fibers (surface roughness on the order of the wavelengths of light) it is appropriate to neglect the presence of specular reflectance and assume that all observed light is from diffuse reflectance.[30]

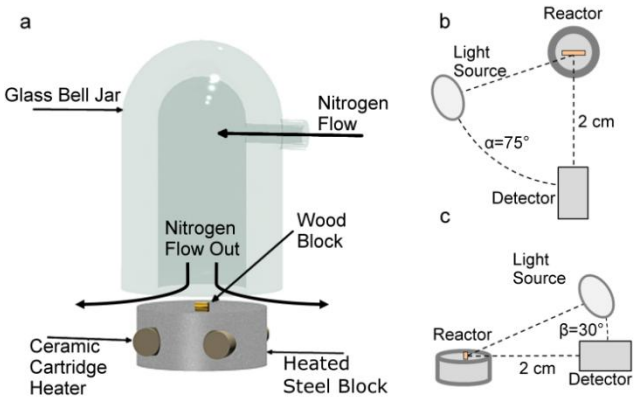

Figure 4-2: Fast pyrolysis experimental reactor design. (a) Front face view of the reactor setup. A steel block was heated using ceramic cartridge heaters, while nitrogen passed over the steel block inside a glass bell jar. Wood particles were placed on the heated steel surface at the start of the experiment, and the subsequent pyrolysis behavior was captured with spectroscopy. (b) Overhead view of the source/sample/detector arrangement. (c) Side view of the source/sample/detector arrangement.

Figure 3a shows the percent of incident light that is reflected by the three dominant constituents of biomass (cellulose, hemicellulose, and lignin) and the primary solid pyrolysis product (char). Cellulose was purchased from Alfa Aesar (Part Number: A17730), xylose was purchased from Sigma Aldrich (Part Number: X1500), lignin was obtained from the Kraft process, and char was produced by pyrolyzing yellow poplar at 500 °C as described previously.

All diffuse reflectance measurements were conducted using a Shimadzu UV-3600 (UV-Vis-NIR spectrometer) with a Harrick Scientific Praying Mantis assembly for capturing diffusely reflected light. The baseline (100% reflectance) was measured using a spectrolon disk and the reflectance spectrum for each sample was obtained by lightly covering the spectrolon disk with the desired powder sample. All diffuse reflectance measurements were collected over the spectral range of 350 nm to 3200 nm and were conducted at room temperature in air.

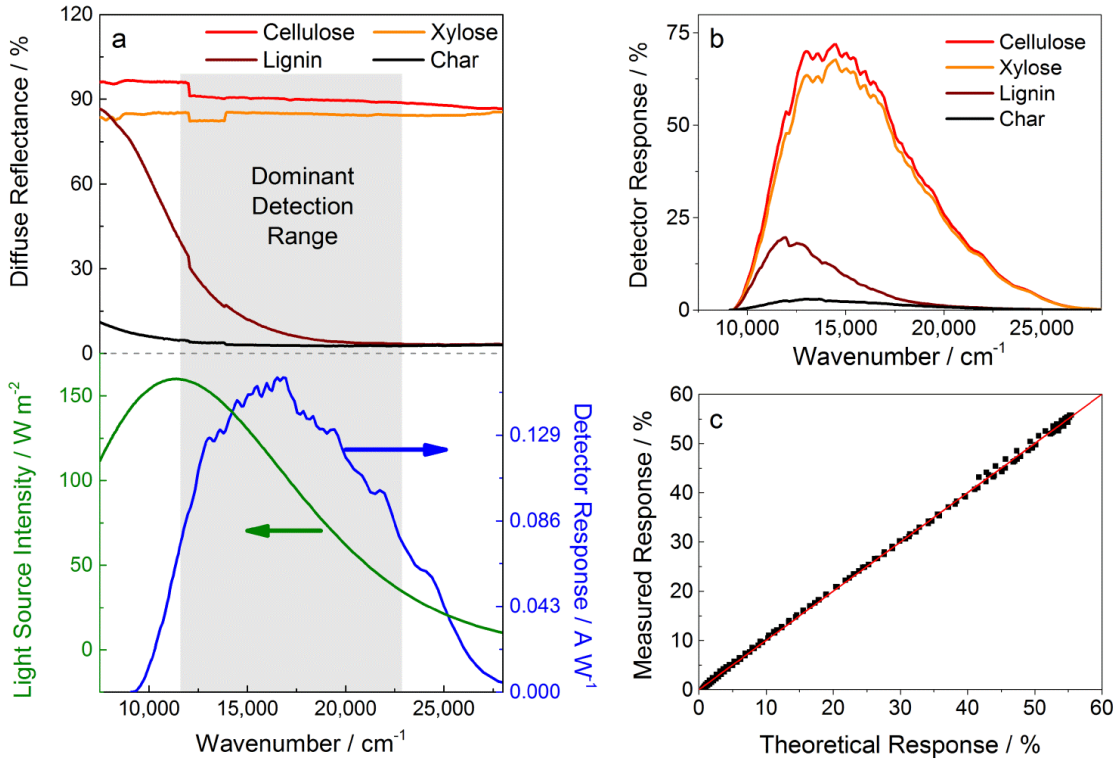

Figure 4-3: . Diffuse reflectance spectroscopy. (a). Diffuse reflectivity of the components of wood shows a distinct difference in reflectivity within the range of the light source intensity, and the detector response. (b) Electrical response of the camera detector to different wood components and pyrolysis products shows a strong response to cellulose and xylose. (c) Parity plot demonstrating the effectiveness of modeling the reflectance of wood using a simple linear combination model of the components of wood.

Figure 3a presents the spectral range of the high-speed camera detector (detector specific data provided by Vison Research, an AMETEK company), demonstrating the selective detector response to excitement from incident light in the range of 9,000 - 25,000 cm^{-1} (400 – 1100 nm). The intensity of the 3300 K tungsten light source (a black body radiator) was calculated using

Planck's Law and is represented in Figure 3a. From the overlap of these two curves, it is clear that the dominant detection region is between 9,000 - 25,000 cm^{-1} where the light source emits and the detector is sensitive to light. Figure a shows cellulose and xylose (an approximation of hemicellulose) as highly reflective within this dominant detection range, while lignin and char are highly absorptive, indicating the ability to use diffuse reflectance to differentiate the two classes of compounds.

This contrast between the carbohydrates and the char/lignin species is made even starker when examining the predicted spectral response of the camera to the different species. When light reflected from the wood particle reaches the detector, an electrical response is triggered and the relative response is sensitive to the wavelength of light, which is demonstrated by the spectral response curve (Figure 3a). The predicted detector response, R^{λ}, is the product of the spectral response of the detector, $R^{\lambda}_{spectral}$, (Figure 3b) and the incident power observed by the detector at a particular wavelength, P^{λ}_{in}, to give, $R^{\lambda} = R^{\lambda}_{spectral} * P^{\lambda}_{in}$. If it is assumed that the incoming power is proportional to the total incident light and the diffuse reflectance of a particular sample, r^{λ}, then the electrical response of the detector can be described by Equation 1 where λ is the wavelength of light, h is Planck's constant, c is the speed of light, and k_B is Boltzmann's constant,

$$R^{\lambda} \propto \frac{R^{\lambda}_{spectral} r^{\lambda}}{\lambda^5 \exp\left(\frac{hc}{\lambda k_B T_{3300}}\right) - 1} \qquad 4\text{-}1$$

The detector response to cellulose, xylose, lignin and char are predicted using Equation 1 and shown graphically in Figure 3b. This data again shows that the predicted detector response by the STR-DRiSP technique due to carbohydrates is overwhelmingly dominant relative to the response of the highly absorptive lignin and char in the visible and near-IR regions.

The diffusely reflected light from STR-DRiSP can be directly converted into a carbohydrate composition by assuming that the observed reflected light is a linear combination of

the individual components where r_i^{λ} is the diffuse reflectance and X_i is the mass fraction of species i respectively,

$$r^{\lambda} = r_{cell}^{\lambda}X_{cell} + r_{hemi}^{\lambda}X_{hemi} + r_{lignin}^{\lambda}X_{lignin} + r_{char}^{\lambda}X_{char} \qquad 4\text{-}2 \qquad ($$

This assumption is verified by calculating the predicted detector response of yellow poplar (Equation 1) from diffuse reflectance spectroscopic data obtained for ball milled yellow poplar ($r^{\lambda} = r_{wood}^{\lambda}$). This is directly compared against the linear approximation for the experimental system here by substituting Equation 2 into the detector response relationship (Equation 1), to obtain the theoretical predicted detector response for the sum of the components. Using the measured diffuse reflectance of cellulose, xylose, and lignin (Figure 3a) with the known mass fractions of each of the three components in the yellow poplar sample (Table 1), the actual and theoretical detector response for yellow poplar is shown in Figure 3c as a parity plot; this comparison demonstrates good agreement by accurately predicting the reflectance of a virgin wood sample. The linear combination of the component reflections are shown to approximate the predicted detector response for the yellow poplar, validating the ability of the linear combination model to accurately describe the experimental system.

Substituting Equation 2 into Equation 1 and integrating over all wavelengths for each pure component species data set ($X_{j=i} = 1, X_{j\neq i} = 0$) allows for the determination of a response factor (α_i) for each individual component *i* (i.e. cellulose, xylose, lignin, and char) to be calculated for the STR-DRiSP system,

$$\alpha_i = \int_0^{\infty} R^{\lambda}\, d\lambda \qquad 4\text{-}3$$

Equation 3 can then be reduced to the total observed response at each pixel, R_t, (corresponding to the grayscale experimental pyrolysis data) by,

$$R_t = \alpha_{cell}X_{cell} + \alpha_{hemi}X_{hemi} + \alpha_{lignin}X_{lignin} + \alpha_{char}X_{char} \qquad 4\text{-}4$$

Utilizing this analysis, we are able to convert one-dimensional spatially resolved experimental data to carbohydrate mass fraction by using the following equation where I_{carb} is the

Intensity measured at a specific position and time and I_{max} and I_{min} are the maximum and minimum observed intensities.

$$X_{carb} = \frac{I_{carb} - I_{min}}{I_{max} - I_{min}} \quad 4\text{-}5$$

4.3 Quantitative Carbon Detector

Quantification of unresolved complex mixtures (UCMs) is a major analysis obstacle in a number of emerging chemical and energy applications. For example, development of renewable, biomass-derived fuels has led to increasing complexity of liquid mixtures (10^2-10^3 compounds) as refinery feed stocks.[31, 32] In the case of fast pyrolysis of biomass, lignocellulosic biomass is thermochemically converted to produce a liquid intermediate called 'bio-oil' which can be integrated within the existing fuel infrastructure[33,34] Rapid thermal breakdown of lignocellulose occurs through high temperature heating, resulting in biopolymer degradation to a liquid mixture consisting of hundreds of oxygenated compounds with wide-ranging properties.[1,35] Subsequent hydroprocessing produces reduced hydrocarbons which can be economically converted to liquid fuels including gasoline, diesel or jet fuel.[36,37] Analytical quantification and identification of UCMs, such as those produced from pyrolysis and subsequent upgrading, remains a limiting research capability. Using the standard methods of gas chromatography/EI-CI mass spectrometry, characterizing this mixture requires identification and quantification of sufficient number of chemical species to close the carbon balance to >90 C%.[38,39] This analytical approach relies on the ability to identify chemical species, which must then be purchased and injected for calibration of each individual chemical.[40,41] When mixtures contain several hundred species, this methodology breaks down due to: (i) the inability to effectively identify every species, (ii) limited potential for purchasing standards, and (iii) excessive time and resources needed for routinely calibrating hundreds of chemical vapors. For these reasons, quantification of bio-oil vapors for molecular-level study remains a significant challenge.

Previous chemical studies have demonstrated the potential of combined oxidation and methanation as a method for calibration-free carbon quantification of alkanes.[42] Further development extended this method for oxygenates and phthalates.[43, 44] In this work, we develop a new design using tandem catalytic oxidation/methanation to provide calibration-free carbon quantification as a drop-in, fully-integrated microreactor. Thermodynamic calculations confirm operability at a wide range of conditions, identify fundamental detection limits, and extend the technology to a variety of analytes. Additionally, characterization of the device residence time distribution allows for optimal peak resolution for analysis of UCMs.

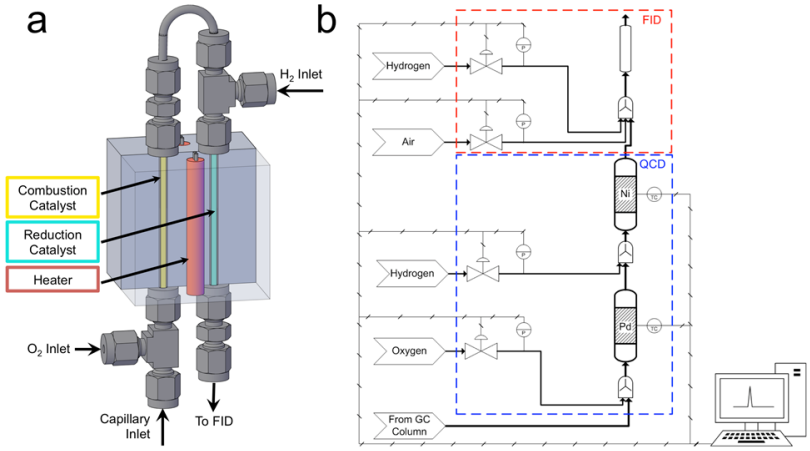

Figure 4-4: **Design and Integration of the Quantitative Carbon Detector (QCD).** a) The QCD utilizes two integrated microreactors in series for combustion and methanation to convert 99.9% of hydrocarbons to methane. b) Miniaturization of the QCD allows for drop-in integration with existing analytical tools including gas chromatography.

Utilization of an integrated microreactor (Figure 4) with additional gas flows controlled with an electronic pressure controller in a gas chromatograph allows for individual species to be converted as they exit a separating GC column by the following reactions: (a) complete oxidation (X_C>99.9%) converts organic carbon within vapors to CO_2 (Rxn. 1), and (b) the second microreactor converts all CO_2 (X_{CO2}>99.9%) to methane (Rxn. 2).

$$C_xH_yO_z + nO_2 \xrightarrow{\text{Pt on Silica/Al}_2O_3} xCO_2 + \frac{1}{2}xO_2 \qquad \text{Rxn. 1}$$

$$xCO_2 + 4xH_2 \xrightarrow{\text{Ni on Al}_2O_3} xCH_4 + 2xH_2O \qquad \text{Rxn. 2}$$

By this method, all organic vapors exiting a packed/capillary column are converted to methane before entering the GC Flame Ionization Detector (FID); FID response per mole of carbon then remains constant for all organic species. Sufficiently robust system design ensures that all possible carbonaceous species are converted to CO_2, while the integrated reactor minimizes mixing and maintains resolution necessary for analytical separation. Here, we provide experimental evidence that the QCD technique provides broad capability for carbon quantification for a wide range of species found in liquid/vapor mixtures such as bio-oil.

4.3.1 Experimental Methods.

The QCD was designed for integration within existing gas chromatographs equipped with a capillary column and flame ionization detector. Feasibility of the QCD system to fully oxidize and methanate analytes (>99.9%) was shown via thermodynamic calculations. Residence time distribution experiments were conducted to demonstrate that the QCD technology does not interfere with chromatographic separation. Experiments demonstrated that the QCD output has identical carbon quantification capabilities to conventional FID-calibration methods. Finally, the QCD methodology was utilized in the pyrolysis of cellulose to demonstrate its capability for quantifying complex mixtures with high resolution.

4.3.2 Design and Implementation of QCD.

The QCD consisted of an insulated, aluminum block (2 in. by 2 in. by 2 in.) with four cylindrical holes machined lengthwise (Figure 4). Two holes each contained a cylindrical, electrically-resistive heater (Omega Engineering PN CIR 3021, 100W), which heated the entire assembly to 500 °C. The two remaining holes housed catalytic reactor chambers comprised of 1/8” stainless steel tubing with 1/16" zero dead volume reducing union (Vici Valco PN ZRUF211) on either end. A fifth cylindrical hole was drilled to a depth of 1.0 inch at the center of the block for a thermocouple (Omega Engineering PN TC-GG-K-20-36). Temperature was

controlled with an Omega CN7823 PID controller performing a feedback loop measuring the temperature within the heating block and triggering AC pulses (120 V) through a solid state relay. The first catalytic reactor chamber was utilized for catalytic oxidation. 115 milligrams of 10% Pd/Alumina (Sigma-Aldrich #440086) was packed within the first catalytic reactor chamber. Prior to entering the reactor chamber, a 1/16" zero dead volume reducing tee (Vici Valco P/N# TCEF211) combined the capillary GC column effluent with flowing oxygen (to ensure complete oxidation). Effluent from the catalytic oxidation reactor chamber was transferred to the second catalytic reactor chamber for methanation via a 1/16" stainless steel capillary transfer line. The transfer line connected to a reducing tee, which combined the effluent of the first catalytic reactor chamber with flowing hydrogen gas (to ensure complete methanation). The second catalytic reactor chamber was packed with 124 milligrams of Nickel catalyst (Agilent Technologies, P/N 5080-8761). Gases exited the second catalytic reaction chamber through a reducing union (VICI Valco PN ZRUF211) into a deactivated capillary column (8 inches long), which directed flow to the existing flame ionization detector (FID). Figure 4b includes a detailed schematic of the QCD system.

Implementation of the QCD within a gas chromatograph with an existing flame ionization detector (FID) required two supplementary gas flow lines (oxygen and hydrogen), as shown in Figure 4b. Oxygen flow was supplied to the QCD by an electronic pressure controller (EPC, Agilent PN 7890A). Excess oxygen served to ensure complete combustion of GC analytes. Total required oxygen gas flow to guarantee high yield of CO_2 (>99.9%) in the first catalytic reactor chamber of the QCD was determined by the thermodynamic calculations described in section 2.2. Implementation of oxygen flow was achieved in the experimental system by varying the oxygen set pressure and measuring the resulting oxygen flow with a bubble column. Oxygen pressure was set in all experiments to maintain oxygen flow at 1.0 sccm.

Hydrogen gas flow was controlled by the existing EPC (Agilent PN 7890A), which adjusts the hydrogen gas pressure at the inlet to the QCD. Hydrogen gas serves two purposes: (i)

promotes methanation of CO_2 to CH_4, and (ii) converts excess O_2 from the combustion reactor to water. Total required hydrogen gas flow to guarantee high yield of methane (>99.9%) was determined by the thermodynamic calculations of section 2.2. Implementation of this flow was achieved in the experimental system by varying the hydrogen set pressure and measuring the resulting hydrogen flow with a bubble column. Hydrogen pressure was set in all experiments to maintain hydrogen flow at 10.0 sccm.

4.3.3 Calculation of Thermodynamic Microreactor Output.

Thermodynamic ternary maps shown in Figure 5 were generated using a Gibbs free energy minimization method within Aspen Plus 7.3. Calculations were performed to determine the amount of supplementary hydrogen flow needed to fully methanate the carbon from the injected sample. The stoichiometry from reactions 1 and 2 was defined as a constraint on the calculations, where the injected carbon was allowed to react with supplementary oxygen and hydrogen to form CO, CO_2, CH_4, H_2O, H_2, or O_2.

$$x\mathrm{C} + y\mathrm{O_2} + z\mathrm{H_2} \rightarrow \mathrm{CO} + \mathrm{CO_2} + \mathrm{CH_4} + \mathrm{H_2O} + \mathrm{H_2} + \mathrm{O_2} \qquad \text{Rxn. 3}$$

Calculations were performed at varying temperature for a fixed pressure of one atmosphere with the constraint of 99.9% conversion of carbon to methane. Property estimations were derived from the Peng-Robinson property method in ASPEN PLUS software, and all calculations were performed using the ‘design specifications’ function. The overall C:H:O ratios so obtained were plotted on ternary maps (Figure 5a).

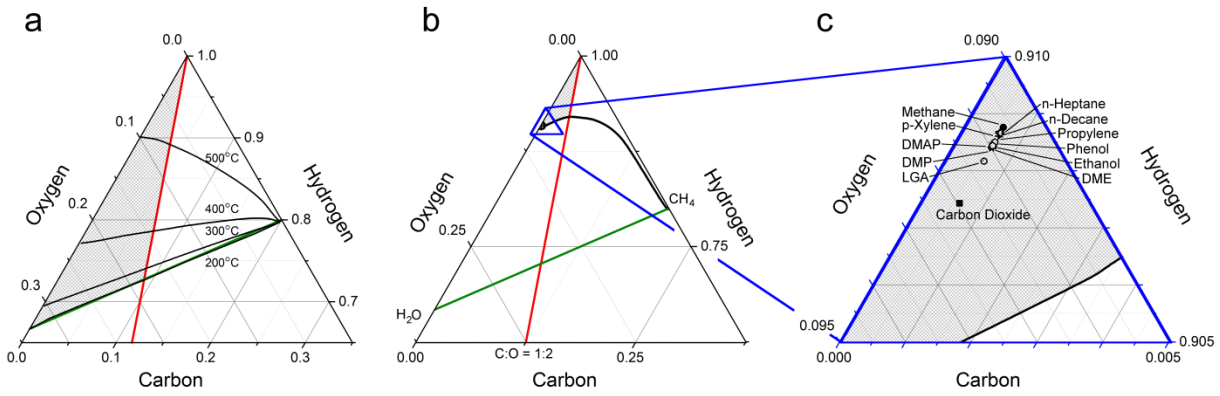

Figure 4-5: **Thermodynamic Regimes of Operable QCD Parameters.** a) Temperature dependence of thermodynamic feasibility for C:H:O ratios to achieve 99.9% conversion to methane. The shaded region envelops stoichiometric and thermodynamic bounds defining a region of QCD operability. b) At 500 °C, various compounds are plotted under dilute (He:C = 10) conditions. c) All compounds are within the operable region and are converted to methane under reaction conditions (inset).

Figures 5b and 5c depict the thermodynamics of Rxn. 1, 2 and 3 in the presence of helium carrier gas. ASPEN PLUS calculations were repeated to simulate a helium-to-carbon molar ratio of 10:1 at 500 °C. The helium-to-carbon ratio was chosen to replicate a common injection volume (one microliter) such that the injected moles of carbon divided by the peak width yields a 1:10 ratio with the carrier gas molar flowrate. The same calculations were performed using the same helium-to-carbon ratio for 12 different compounds which are plotted in Figure 5b and 5c.

4.3.4 Evaluation of QCD Residence Time Distribution.

Residence time distribution (RTD) analysis was carried out to verify that the QCD does not significantly reduce chromatographic peak resolution. A tracer of methane gas was injected as a pulse and the resulting detector response was measured with an FID. Equal amount of methane gas (0.5 ml) was injected into the system for four different configurations: (i) a base case with conventional FID only, (ii) QCD reactor with no catalyst packing and no supplementary oxygen or hydrogen, (iii) QCD reactor with catalyst packing and no supplementary oxygen or hydrogen, and (iv) QCD reactor with catalyst packing and oxygen and hydrogen flows. The variance of each

RTD curve was calculated and used to characterize the effect of packing and supplementary flows on GC peak resolution. Variance was calculated by first determining the exit age distribution as a function of time (Equation 1).

$$E(t) = \frac{C(t)}{\int_0^\infty C(t)dt} \quad (1)$$

The age distribution was then used to calculate the average residence time for each system configuration (Equation 2).

$$\bar{t} = \int_0^\infty tE(t)dt \quad (2)$$

Equation 1 and 2 were then used to calculate the variance of each RTD curve (Equation 3).

$$\sigma^2 = \int_0^\infty (t - \bar{t})^2 E(t)dt \quad (3)$$

4.3.5 Calibration and Quantification of Individual Species.

Fifteen chemicals were independently injected into the gas chromatograph splitless inlet at varying concentration (2.0 to 3.0 carbon-millimole per mL solution). Both the QCD and standard Agilent FID were used in separate trials to quantify injected compounds. Fifteen compounds were selected to represent a range of sizes, chemical compositions, and functionalities including: (i) methyl furan, furfural, and levoglucosan, which are representative of compounds derived from cellulose pyrolysis, (ii) carbon dioxide and acetol, which are representative of compounds derived from hemicellulose pyrolysis, (iii) phenol, 2,6-dimethoxyphenol (DMP), and 3,4-dimethoxyacetophenone (DMAP), which are representative of compounds derived from lignin pyrolysis, and (iv) methane, ethanol, dimethyl ether (DME), propylene, p-xylene, n-heptane, and n-decane, which are representative of compounds derived from petroleum processing.

The GC inlet was maintained at 250 °C (320 °C for levoglucosan injections) and 25 psi under splitless inlet conditions. The pressure was selected to achieve a column flow of

approximately 1.0 mL/min. The inlet was connected to an HP-5 column (Agilent PN 19091J-102), which connected directly to the QCD. The oven temperature was increased from 70 °C to 250 °C at a rate of 20 °C/min. Liquid samples were prepared in methanol or water to 5 wt% of the analyte with five injections ranging from 0.2-1.0 μl with an autosampler (Agilent PN 7693, Syringe PN G4513-8021). Gas samples were injected using two mass flow controllers (Brooks, PN 5850E) and a power supply with control module (Brooks, PN 0254). The concentration of analyte gas was controlled by varying the ratio of helium and analyte flow from the two controllers. The combined output from both mass flow controllers was injected into the GC inlet through a six-port switching valve (Vici Valco PN A26WT). Moles of injected compounds quantified by GC-QCD were compared with moles of injected compounds quantified by conventional GC-FID by generating calibration curves for each compound (Supplementary Section).

4.3.6 Application of QCD for Cellulose Pyrolysis.

To demonstrate the capability of the QCD to analyze complex mixtures, a bio-oil sample from cellulose fast pyrolysis was injected into the GC-QCD system. Bio-oil samples were collected using an ablative fast pyrolysis reactor, where product vapors were collected in a water quench, as previously described.[45] Microcrystalline cellulose (FMC Biopolymer PN Lattice NT-200) was pyrolyzed under nitrogen flow at 500 ºC. The quench was transferred to a 2 mL vial, and 1.0 μl was injected directly into the GC inlet.

4.4 Results and Discussion.

The Quantitative Carbon Detector (QCD) is a modular carbon detection microreactor for direct integration with existing GC-FID systems, with a compact design that allows for installation within a GC oven. Modular design makes the catalytic reactor chambers interchangeable, allowing for additional applications such as oxygenate flame ionization

detection (O-FID) to detect the moles of oxygen in a sample.[46] Characterization of the residence time distribution combined with thermodynamic calculation of regions of operability confirms the viability of the design. Response factors of conventional GC-FID and GC-QCD were compared to validate the ability of the QCD to reproduce FID results without prior calibration. Finally, a sample of bio-oil from cellulose pyrolysis was analyzed via GC-QCD to demonstrate negligible loss in chromatographic resolution of the QCD reactor with a complex mixture.

4.4.1 Evaluation of QCD thermodynamics.

Figure 5a depicts a C-H-O ternary plot, which describes the calculated conditions under which the QCD reactions are thermodynamically favorable; for complete detection and quantification, each analyte must achieve full conversion to methane (>99.9%) within the QCD. Four black lines, each representing a different reaction temperature, envelop the region in which full conversion to methane is achieved for any given combination of molecules at given C-H-O ratios. C-H-O ratios that fall above a line are thermodynamically predicted to achieve >99.9% conversion to methane at the corresponding temperature. In addition, colored lines are drawn to indicate the stoichiometric constraints of the combustion and methanation reactions. The red 'combustion line' indicates a carbon-to-oxygen ratio of one-to-two, which is a requirement for complete combustion. The green 'combustion/methanation line' is drawn between points representing methane and water, indicating the overall stoichiometric requirement of the two combined reactions. The shaded region of Figure 5a represents the C-H-O ratios which satisfy both thermodynamic requirements for methane conversion and stoichiometric constraints for the QCD reactions (combustion and methanation), thereby defining a region of operability (shaded, grey).

In Figure 5b, the 500 °C boundary from Figure 5a is modified to include helium carrier gas flow with a helium-to-carbon molar ratio of 10:1, representative of common operating conditions. The addition of inert carrier gas raises the curve and reduces the region of

thermodynamic operability with respect to Figure 5a. Finally, the C-H-O ratios of 12 compounds injected into the GC-QCD are plotted in Figure 5c. All 12 compounds exist within the thermodynamically possible regime under considered experimental conditions, indicating that all compounds should achieve high conversion to methane if the combined reactions of catalytic combustion and methane proceed to approach equilibrium.

Thermodynamic calculations predict that there exists a broad region of operability for the QCD across which analytes are completely converted to methane (>99.9). The results of these calculations were validated by the tests conducted to ensure complete conversion in the reactors (Supplementary Section). Additionally, the absence of catalyst deactivation within the QCD was confirmed by monitoring reactor conversion after 200 sample injections.

4.4.2 Effect of QCD on Peak Resolution.

Design of the QCD results in negligible mixing or loss in peak resolution in comparison to a chromatogram obtained by conventional GC-FID. Figure 6 depicts the detected residence time distribution (RTD) from an injected pulse of methane for GC-FID and three different GC-QCD configurations. The conventional GC-FID system resulted in a sharp, narrow peak (black line) with variance of 18.2 x 10^4 s^2. The RTD obtained from the GC-QCD system with no catalyst (red line) resulted in a shallow, broad peak with an increased variance of 41.2 x 10^4 s^2. Introduction of catalyst into the QCD reactor (blue line) decreased the variance (27.3 x10^4 s^2), while supplementary oxygen and hydrogen flows (green line) further reduced the variance in RTD (24.3 x10^4 s^2).

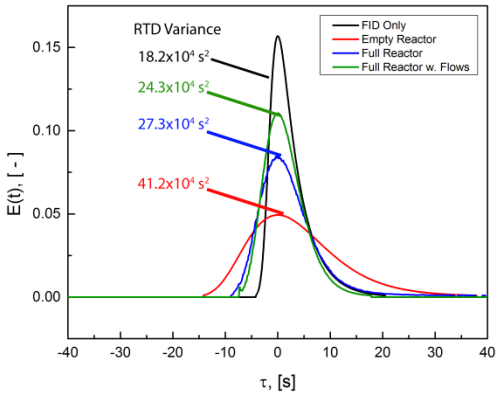

Figure 4-6: **Residence Time Distributions in FID and QCD Detectors.** RTD analysis shows minimal loss in peak resolution between GC-FID and GC-QCD. Peak resolution of the QCD is enhanced by the addition of catalyst (red versus blue) and the addition of oxygen and hydrogen flows (blue versus green).

RTD studies shown in Figure 6 verify that GC-QCD retains peak resolution comparable to GC-FID. Variance calculated from the GC-QCD peak is only slightly higher than that of the GC-FID system, indicating minimal loss in chromatographic separation. Small values in variance indicate a sharp, narrow peak, which makes separation of complex mixtures less time consuming. In the case of the GC-QCD reactor absent catalyst packing, the variance was more than double the variance with conventional GC-FID, likely due to increased residence time and increased axial mixing within the catalyst reactor chambers. The addition of catalyst and supplementary flows reduces gas residence time and mitigates the effects of the QCD reactor on peak resolution.

4.4.3 Comparison of GC-QCD and GC-FID.

Figure 7 depicts parity plots comparing GC-QCD response to GC-FID response for all 15 selected compounds. Micromoles of carbon detected for both the GC-QCD and GC-FID are shown to be nearly identical for the each of the identified compounds with the exception of carbon dioxide. While carbon dioxide was not detectable with GC-FID (and normally requires a second detector such as a thermal conductivity detector, TCD), detection within the GC-QCD occurs via conversion to methane. Additionally, carbon monoxide was also quantifiable using the

GC-QCD, because it was converted to carbon dioxide within the first catalytic reactor chamber and subsequently converted to methane downstream.

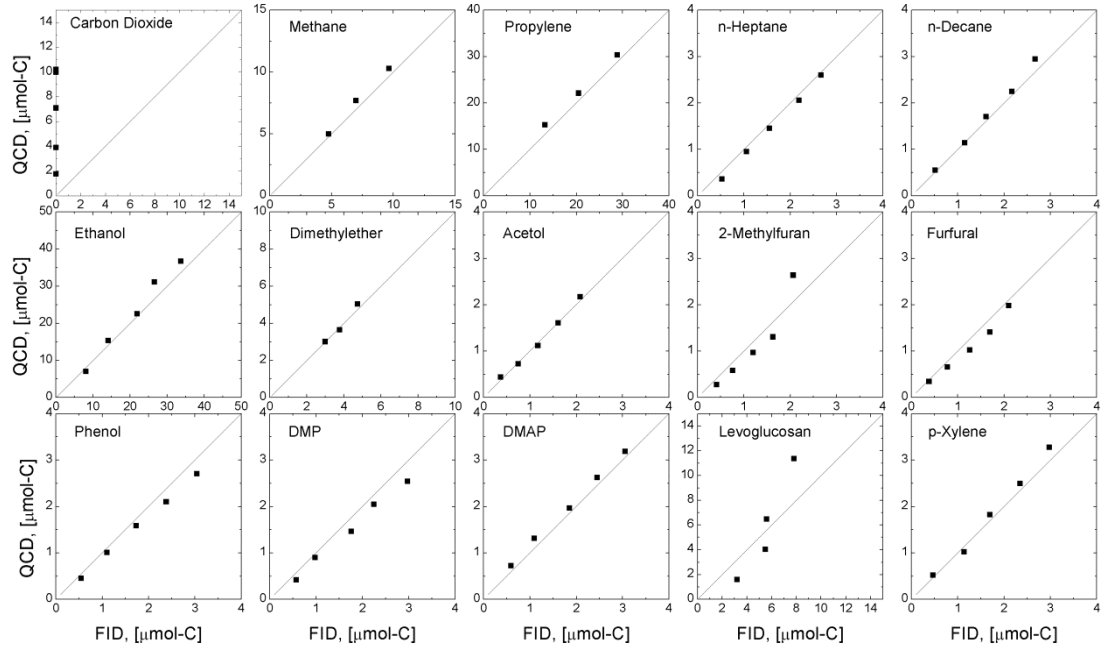

Figure 4-7: **Individual Compound Parity of QCD and Conventional FID Quantification.** Comparison of molar quantification of identical samples by both QCD and conventional, calibrated FID yield equivalent responses for a range of cellulose-, hemicellulose-, and lignin-derived pyrolysis compounds. Carbon dioxide (first panel) can only be detected by QCD (not FID).

Figure 8 condenses the data from Figure 7 into a single log-scale parity plot for comparison between chemical species. All of the data points in Figure 8 collapse to a single line, further confirming that GC-QCD is capable of duplicating the results of GC-FID without the need for individual calibration.

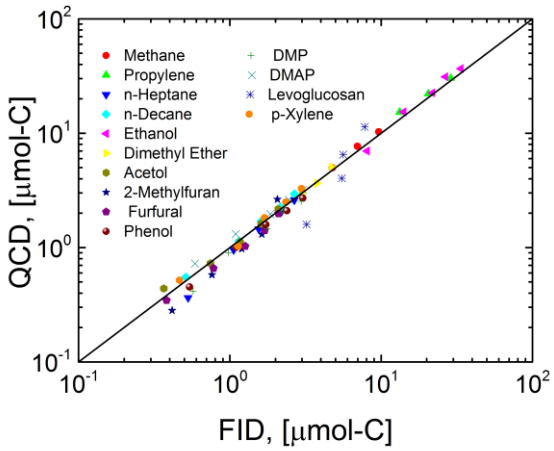

Figure 4-8: **Collective Parity of QCD and Conventional FID Quantification.** Comparison of molar quantification of identical samples by both QCD and conventional, calibrated FID yield equivalent responses for a wide range of cellulose-, hemicellulose-, and lignin-derived pyrolysis compounds.

Response factors were determined for each chemical species for the GC-FID and GC-QCD techniques as depicted in Figure 9. Response factors were scaled using a methane internal standard to account for day-to-day variability in the FID (see Supplementary Section). GC-FID response factors for all 15 compounds are shown in Figure 9 as red bars and vary over an order of magnitude between compounds. In comparison, response factors calculated using GC-QCD are nearly constant across all 15 compounds within experimental error. As demonstrated, an identical GC-QCD response factor across a range of gases and condensable liquids indicates that quantification of a broad range of chemical mixtures can be achieved.

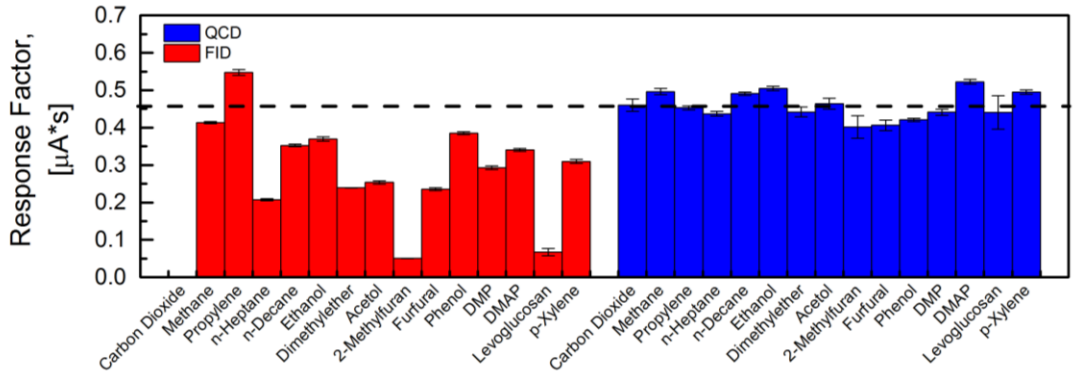

Figure 4-9: Response Factors of Conventional FID (Red) and QCD (Blue). Compound response factors (scaled using an internal standard of methane) analyzed using GC-FID vary over an order of magnitude, while response factors for compounds using GC-QCD are nearly constant within experimental error.

4.4.4 Application of QCD for Complex Mixtures.

Figure 10 depicts a GC-QCD chromatogram of a sample of cellulose fast pyrolysis bio-oil to demonstrate separation of a complex mixture. Separation with sufficient chromatographic resolution to resolve independent peaks was obtained within a 15 minute run. While the compounds in Figure 10 are unknown, the total amount of carbon can be rapidly quantified by integrating all peaks individually (multiple integrations) or simultaneously (a single integration), because the response factor for all compounds was the same. Similarly, the total amount of carbon in two overlapping peaks can be determined without complete separation or knowledge of peak identities. Rapid quantification of complex mixtures is also relevant in applications such as two-dimensional gas chromatography (GCxGC), where hundreds of compounds are separated, which makes the QCD an optimal detector for such applications.

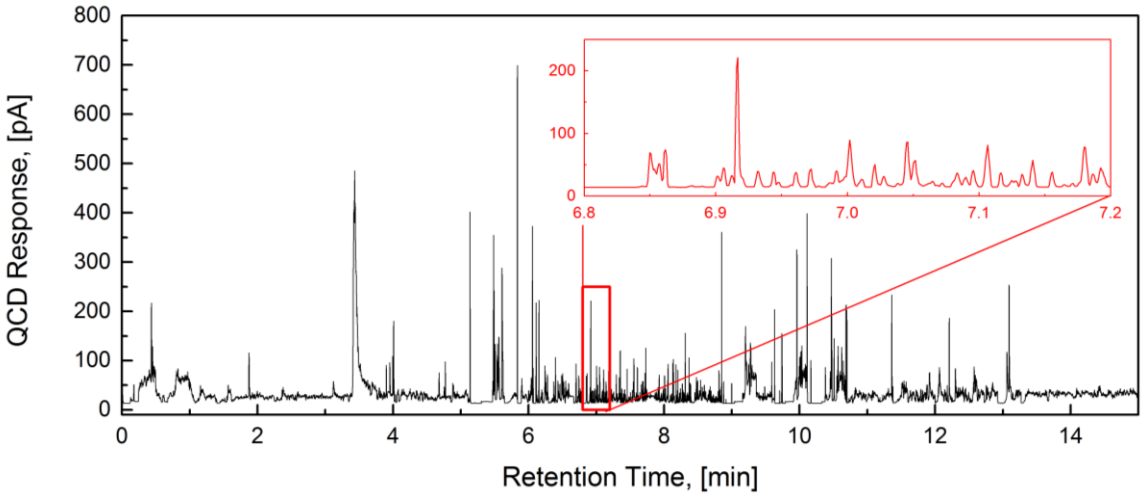

Figure 4-10: **GC-QCD of Complex Mixtures Derived from Cellulose Pyrolysis.** Chromatographic separation of products from ablative fast pyrolysis of microcrystalline cellulose at 500 ℃ was achieved for the complex mixture while maintaining peak resolution.

4.5 Conclusions.

The Quantitative Carbon Detector (QCD) is a fully-integrated, drop-in microreactor for calibration-free carbon quantification in gas chromatography. Combination of tandem catalytic oxidation and methanation converts all analyte carbon to >99.9% methane, leading to identical

response factors for all separated species. Quantification of carbon eliminates the need to identify and calibrate individual compounds and provides the capability to detect and quantify both carbon monoxide and carbon dioxide. Integrated microreactor design utilized thermodynamic calculations to identify regions of operability that ensured complete conversion of all possible carbonaceous analytes to methane. Microreactor design including flows, catalyst chambers and fittings was characterized via residence time distribution to ensure minimal loss of resolution in analyte separation.

4.6 References

1. A. Broido, M. A. Nelson, Char Yield on Pyrolysis of Cellulose. *Combustion and Flame* **24**, 263-268 (1975).
2. A. G. W. Bradbury, Y. Sakai, F. Shafizadeh, Kinetic-Model for Pyrolysis of Cellulose. *Journal of Applied Polymer Science* **23**, 3271-3280 (1979).
3. M. S. Mettler, S. H. Mushrif, A. D. Paulsen, A. D. Javadekar, D. G. Vlachos, P. J. Dauenhauer, Revealing pyrolysis chemistry for biofuels production: Conversion of cellulose to furans and small oxygenates. *Energy & Environmental Science* **5**, 5414-5424 (2012); published online EpubJan (10.1039/c1ee02743c).
4. M. S. Mettler, A. D. Paulsen, D. G. Vlachos, P. J. Dauenhauer, The chain length effect in pyrolysis: bridging the gap between glucose and cellulose. *Green Chemistry* **14**, 1284-1288 (2012).
5. A. D. Paulsen, Mettler, M. S., Vlachos, D. G., & Dauenhauer, P. J., The Role of Sample Dimension and Temperature in Cellulose Pyrolysis. *Energy & Fuels*, (2013).
6. M. S. Mettler, A. D. Paulsen, D. G. Vlachos, P. J. Dauenhauer, Pyrolytic conversion of cellulose to fuels: levoglucosan deoxygenation via elimination and cyclization within molten biomass. *Energy & Environmental Science*, (2012).
7. J. F. Matthews, M. Bergenstrahle, G. T. Beckham, M. E. Himmel, M. R. Nimlos, J. W. Brady, M. F. Crowley, High-Temperature Behavior of Cellulose I. *Journal of Physical Chemistry B* **115**, 2155-2166 (2011); published online EpubMar 17 (10.1021/jp1106839).
8. V. Agarwal, G. W. Huber, W. C. Conner, Jr., S. M. Auerbach, Simulating infrared spectra and hydrogen bonding in cellulose I beta at elevated temperatures. *Journal of Chemical Physics* **135**, (2011); published online EpubOct 7 (10.1063/1.3646306).
9. H. B. Mayes, L. J. Broadbelt, Unraveling the Reactions that Unravel Cellulose. *Journal of Physical Chemistry A* **116**, 7098-7106 (2012); published online EpubJul 5 (10.1021/jp300405x).
10. V. Agarwal, P. J. Dauenhauer, G. W. Huber, S. M. Auerbach, Ab initio dynamics of cellulose pyrolysis: nascent decomposition pathways at 327 and 600 °c. *Journal of the American Chemical Society* **134**, (2012); published online Epub2012-Sep-12 (
11. V. Seshadri, P. R. Westmoreland, Concerted Reactions and Mechanism of Glucose Pyrolysis and Implications for Cellulose Kinetics. *Journal of Physical Chemistry A* **116**, 11997-12013 (2012); published online EpubDec 13 (10.1021/jp3085099).
12. R. Vinu, L. J. Broadbelt, A Mechanistic Model of Fast Pyrolysis of Glucose-Based Carbohydrates to Predict Bio-oil Composition. *Energy & Environmental Science*, (2012).
13. P. J. Dauenhauer, B. J. Dreyer, N. J. Degenstein, L. D. Schmidt, Millisecond reforming of solid biomass for sustainable fuels. *Angewandte Chemie-International Edition* **46**, 5864-5867 (2007); published online Epub2007 (10.1002/anie.200701238).
14. J. L. Colby, P. J. Dauenhauer, B. C. Michael, A. Bhan, L. D. Schmidt, Improved utilization of biomass-derived carbon by co-processing with hydrogen-rich feedstocks in millisecond reactors. *Green Chemistry* **12**, 378-380 (2010).
15. G. Varhegyi, E. Jakab, M. J. Antal, Is the Broido-Shafizadeh Model for Cellulose Pyrolysis True. *Energy & Fuels* **8**, 1345-1352 (1994); published online EpubNov-Dec (
16. D. L. Pyle, C. A. Zaror, HEAT-TRANSFER AND KINETICS IN THE LOW-TEMPERATURE PYROLYSIS OF SOLIDS. *Chemical Engineering Science* **39**, 147-158 (1984); published online Epub1984 (10.1016/0009-2509(84)80140-2).
17. K. M. Bryden, M. J. Hagge, Modeling the combined impact of moisture and char shrinkage on the pyrolysis of a biomass particle. *Fuel* **82**, 1633-1644 (2003); published online EpubSep (10.1016/s0016-2361(03)00108-x).

18. M. S. Mettler, D. G. Vlachos, P. J. Dauenhauer, Top ten fundamental challenges of biomass pyrolysis for biofuels. *Energy & Environmental Science* **5**, 7797-7809 (2012); published online EpubJul (10.1039/c2ee21679e).
19. V. Mamleev, S. Bourbigot, M. Le Bras, J. Yvon, The facts and hypotheses relating to the phenomenological model of cellulose pyrolysis Interdependence of the steps. *Journal of Analytical and Applied Pyrolysis* **84**, 1-17 (2009); published online EpubJan (10.1016/j.jaap.2008.10.014).
20. A. R. Teixeira, K. G. Mooney, J. S. Kruger, C. L. Williams, W. J. Suszynski, L. D. Schmidt, D. P. Schmidt, P. J. Dauenhauer, Aerosol generation by reactive boiling ejection of molten cellulose. *Energy & Environmental Science* **4**, 4306-4321 (2011).
21. C. Di Blasi, Modeling chemical and physical processes of wood and biomass pyrolysis. *Progress in Energy and Combustion Science* **34**, 47-90 (2008)10.1016/j.pecs.2006.12.001).
22. J. Cho, J. M. Davis, G. W. Huber, The Intrinsic Kinetics and Heats of Reactions for Cellulose Pyrolysis and Char Formation. *Chemsuschem* **3**, 1162-1165 (2010); published online Epub2010 (10.1002/cssc.201000119).
23. J. Soukupova, B. N. Rock, J. Albrechtova, Spectral characteristics of lignin and soluble phenolics in the near infrared - a comparative study. *International Journal of Remote Sensing* **23**, 3039-3055 (2002)10.1080/01431160110104683).
24. M. A. Sanderson, F. Agblevor, M. Collins, D. K. Johnson, Compositional analysis of biomass feedstocks by near infrared reflectance spectroscopy. *Biomass & Bioenergy* **11**, 365-370 (1996).
25. S. S. Kelley, T. G. Rials, R. Snell, L. H. Groom, A. Sluiter, Use of near infrared spectroscopy to measure the chemical and mechanical properties of solid wood. *Wood Science and Technology* **38**, 257-276 (2004)10.1007/s00226-003-0213-5).
26. L. Axrup, K. Markides, T. Nilsson, Using miniature diode array NIR spectrometers for analyzing wood chips and bark samples in motion. *Journal of Chemometrics* **14**, 561-572 (2000).
27. R. Bilbao, A. Millera, M. B. Murillo, TEMPERATURE PROFILES AND WEIGHT-LOSS IN THE THERMAL-DECOMPOSITION OF LARGE SPHERICAL WOOD PARTICLES. *Industrial & Engineering Chemistry Research* **32**, 1811-1817 (1993).
28. P. Malkavaara, R. Alen, A spectroscopic method for determining lignin content of softwood and hardwood kraft pulps. *Chemometrics and Intelligent Laboratory Systems* **44**, 287-292 (1998).
29. R. Miller, J. Bellan, A generalized biomass pyrolysis model based on superimposed cellulose, hemicellulose and lignin kinetics. *Combustion Science and Technology* **126**, 97-137 (1997)10.1080/00102209708935670).
30. M. Jackson, D. Yang, R. Parkin, Analysis of wood surface waviness with a two-image photometric stereo method. *Proceedings of the Institution of Mechanical Engineers Part I-Journal of Systems and Control Engineering* **221**, 1091-1099 (2007); published online EpubDec (10.1243/09596518jsce405).
31. A.V. Bridgwater, *J. Anal. Appl. Pyrolysis*, 1999, 51(1-2), 3-22.
32. Oasmaa and D. Meier, *J. Anal. Appl. Pyrolysis*, 2005, 73(2), 323.
33. A.V. Bridgwater, D. Meier, and D. Radlein, *Org. Geochem.*, 1999, 30, 1479-1493.
34. S. Kersten and M. Garcia-Perez, *Curr. Opin. Biotechnol.*, 2013, 24, 414.
35. A. Oasmaa and D. Meier, *J. Anal. Appl. Pyrolysis*, 2005, 73(2), 323.
36. A. Oasmaa and S. Czernik, *Energy Fuels*, 1999, 13, 914-921.
37. P.M. Mortensen, J.D. Grunwaldt, P.A. Jensen, K.G. Knudsen, and A.D. Jensen, *Appl. Catal., A*, 2011, 407, 1-19.
38. Paulsen, Alex D., Matthew S. Mettler, and Paul J. Dauenhauer. *Energy & Fuels* 27.4 (2013): 2126-2134.

39. Mettler, M. S., Paulsen, A. D., Vlachos, D., & Dauenhauer, P. J., Catalysis Science & Technology, 2014, 10.1039/C4CY00676C
40. Mettler, M. S., Paulsen, A. D., Vlachos, D. G., & Dauenhauer, P. J. *Energy & Environmental Science*, 2012, *5*(7), 7864-7868
41. Mettler, M. S., Mushrif, S. H., Paulsen, A. D., Javadekar, A. D., Vlachos, D. G., & Dauenhauer, P. J., *Energy & Environmental Science*, 2012, *5*(1), 5414-5424.
42. T. Watanabe, K. Kato, N. Matsumoto, and T. Maeda, *Chromatography*, 2006, 27(2), 49-55
43. T. Watanabe, K. Kato, N. Matsumoto, and T. Maeda, *Talanta* 2007, 72, 1655-1658
44. T. Watanabe, K. Kato, K. Tsunoda, and T. Maeda, *Anal. Chim. Acta*, 2008, 619, 26-29
45. A.R. Teixeira, K.G. Mooney, J.S. Kruger, C.L. Williams, W.J. Suszynski, L.D. Schmidt, D.P. Schmidt, and P.J. Dauenhauer, *Energy Environ. Sci.*, 2011, 4, 4306.
46. A. Sironi and G. Verga. U.S. Patent No. 5,373,725. 20 Dec. 1994.

CHAPTER 5

MICROEXPLOSIONS IN THE UPGRADING OF BIOMASS-DERIVED PYROLYSIS OILS AND THE EFFECTS OF SIMPLE FUEL PROCESSING

5.1 Introduction

Biomass is widely considered to be the only renewable source for the sustainable generation of liquid fuels.[1-4] Processes such as pyrolysis, liquefaction, and subsequent upgrading have led to a new class of biomass-based liquid fuels called bio-oils (pyrolysis oils).[2, 5, 6] Bio-oils are composed of hundreds of chemical species containing numerous functional groups including aromatics, carboxylic acids, phenols, furfurals, anhydrosugars and alcohols.[7-9] Researchers are currently examining upgrading technologies such as hydrodeoxygenation,[10] catalytic reforming[11, 12] and cracking [1, 13-15] of these highly oxidized fuels with the goal of making bio-oil a viable source for traditional fuel applications, including internal combustion, diesel and jet engines.

Bio-oils generally perform poorly when utilized for combustion. Sandia National Laboratories performed a bio-oil study to determine the potential for using lignocellulosic derived bio-oils as combustion fuels.[16] In pilot diesel engines, bio-oils demonstrated poor combustion characteristics including high CO and particulate emissions as well as poor ignition properties. These problems were attributed to the late-time gas-phase secondary pyrolysis of heavy vapors which leads to incomplete fuel combustion.[17]

An important, but not yet fully understood, phenomenon observed in numerous bio-oil combustion experiments was microexplosions, whereby droplets of bio-oil slowly combust before undergoing a violent and destructive explosion. Microexplosions are beneficial to fuel combustion, because they act as a means of secondary droplet atomization, thereby increasing fuel droplet surface area and promoting evaporation. Many studies have attempted to induce microexplosions in conventional fuels by the addition of water or methanol for this purpose.[18-21]

In instances where microexplosions occur, char formation significantly hinders the benefits from secondary atomization and fuel utilization.[19]

Though the mechanics of microexplosions are understood for relatively simple, nonreactive, binary mixtures of varying volatility, the phenomenon is greatly complicated in bio-oil by the diverse and highly reactive chemical composition. Mixtures and emulsions of binary and multicomponent fuels have demonstrated microexplosions occurring with components that include alkanes, alcohols, ethers, water, heavy fuels, and pyrolysis oils.[17, 18, 22] In these simple fuel mixtures, high heating rates and poor mass transfer leads to the formation of a volatile core and a low volatility shell with limited mass transfer capability. The outer shell is thought to lead to superheating of the core which results in subsequent flashing to a vapor, observed as a microexplosion.[23] The bio-oil case is complicated by the presence of reacting chemical species and wide range of species volatility. At room temperature, vapor pressures of bio-oil components are known to vary over 10 orders of magnitude.[24] Additives to pyrolysis oils have been considered to stabilize the fuel for storage and decrease the viscosity for optimal combustion properties. Light alcohols and ketones are specifically identified as cost-effective additives to bio-oils.[14, 25] Methanol was identified as an ideal additive, because it halves the viscosity and drastically reduces storage-related aging.[14, 25, 26] Little is known, however, about how methanol affects bio-oil combustion, particularly with respect to the explosion behavior.

Due to the complex chemical composition and functionality of bio-oil, droplets of traditional petroleum fuels and bio-oil evaporate differently. A conventional fuel droplet such as the diesel fraction, No. 2 fuel, evaporating in a motionless atmosphere evaporates at a rate proportional to the square of the diameter. This relationship is commonly referred to as the d^2-law,[16] which utilizes the evaporation proportionality rate constant, K_v.

$$d^2 = d_0^2 + K_v t \qquad \text{(Equation 1)}$$

Several sources have claimed based on experiments and computational modelling that bio-oils obey the d^2-law.[17, 27, 28] However, others claim that a combination of the gradient in

composition volatility and the complex and dynamic reactivity of bio-oil will make its evaporation behavior diverge from the d^2-law.[29-31] In general, bio-oil has been calculated to evaporate at rates substantially lower than traditional fuels ($K_{v,bio\text{-}oil}$ = 0.19-0.25 mm^2/s, and $K_{v,No.2}$ = 0.56, [16]), due to the high water content of bio-oil (up to 50%[8]).

Unlike traditional fuels, pyrolysis oils are highly reactive and have the ability to undergo one of three processes upon heating: (1) evaporation of light components, (2) pyrolysis to volatile species, and (3) polymerization to heavier compounds. Experimentally, exhaust streams have been characterized as having soot, large glassy solid residuals and hollow cenospheres. Cenospheres are hollow, glassy spheres that are often found in solid combustion residue, resulting from the incomplete combustion of fuel droplet.[32] The soot derives from secondary pyrolysis of gas phase species and visibly forms at late droplet residence times when the heavy volatile fraction evaporates.[17] When mass transfer limitations exist within the droplet, liquid phase pyrolysis dominates and cenospheres are formed.[17, 33] The remaining solid residuals, however, contain dense glassy solids that are still highly oxygenated and readily dissolve in methanol, indicating that they are likely the result of uncombusted fuel that has polymerized.

Bio-oils are also known to contain suspended solid char particles as well as dissolved and undissolved polymers. Natural bio-polymers can exist in the oil from aerosols generated during fast pyrolysis,[34] or they can form from secondary polymerization of the condensed oil due to aging.[26] These char particles and inorganic solids can remain in the bio-oil during utilization and are thought to affect the chemistry by providing nucleation sites which assist in evaporation or further polymerization.[30]

In this work, we directly observe the presence of microexplosions in biomass derived pyrolysis oils using high-speed photography and describe the sequence of events leading up to the explosion. We also examine the effects of methanol addition on the frequency and timing of microexplosions. The role of separable polymers on the microexplosion mechanism was elucidated by removal of dissolvable solids. We show that simple fuel processing can

dramatically tune the evaporation properties to promote or nearly eliminate microexplosions upon heating bio-oil.

5.2 Materials and Methods

Bio-oil was obtained from the U.S. National Renewable Energy Laboratory (NREL) and was produced from the fast pyrolysis of pine in a bubbling fluidized bed reactor at 500 °C.[35] The oil was characterized before use, and its properties are summarized in Table 1.

Table 5-1: Characterization and properties of pine-derived bio-oil

Elemental[a], (dry), wt.%	
- C	37.2
- H	8.0
- O	52.6
- N	<0.5%
Water, wt.% [b]	38.6
Ash, wt.%	0.32
Filterable Polymers[c], wt.%	1.6
Insoluble Solids[c], wt.%	0.6
pH	2.6

[a] Analysis performed by Galbraith Laboratories
[b] Karl Fischer water analysis, Galbraith Laboratories
[c] Solid analysis was done by 0.45 µm filtration followed by fractionation with THF.

Filtered samples were passed through a 0.45 µm syringe filter, removing a fraction of solids (2.2 wt.%). The solid fraction was then fractionated into polymer (dissolves in THF,[36] 1.6 wt.%) and insoluble solids (does not dissolve in THF, 0.6 wt.%) fractions. Gel permeation chromatography (GPC) suggests that the soluble solids fraction has an average molecular weight of 1000 Da, nearly an order of magnitude larger than observed in the filtered bio-oil (Appendix A, Figure 5-5[37]). Dilutions were made on a mass basis in twenty-five percent increments ranging from pure bio-oil (0%) to filtered bio-oil (100%) by micro-pipetting exact volumes of the two constituents and vigorously shaking.

Charcoal addition samples were prepared by blending activated charcoal into bio-oil in known mass fractions. The activated charcoal (Sigma Aldrich #05120 Fluka), has a known

particle size distribution with 75% of the particles less than 40 μm in diameter. Samples were blended in concentrations of 0.5, 1, 2, and 4 weight percent charcoal.

Methanol/bio-oil dilutions were also prepared on a mass basis. Methanol and bio-oil were pipetted and mixed in ratios ranging from pure bio-oil (0%) to pure methanol (100%) in increments of twenty-five weight percent.

Experimental methods were developed to assess the explosion frequency, droplet lifetime, and evaporation rate. The sequence of droplet evaporation events was qualitatively assessed directly from photographs. All methods examined the evaporation of a bio-oil droplet on a two centimeter pressed γ-alumina disc, calcined at 1100 °C. The experimental system consisted of a pressed disk seated on a copper surface and heated by three cartridge heaters vertically mounted in a copper heating block of 2.4 cm diameter.[37] Temperature was monitored with a thermocouple resting directly on the alumina surface prior to use and controlled by a variable voltage power supply to maintain constant temperature. Nitrogen was continuously purging parallel to the surface to maintain an oxygen-free environment. Experimental flow rates were maintained between 0.3-0.5 SLPM, which typically convectively cooled the surface by approximately 30 °C. Further information and an experimental schematic are available in Appendix A.

Bio-oil droplets were formed by dispensing 5 μL from a 50 μL Acura 825 micropipette approximately one centimeter above the surface. Stopwatch trials measured either the time required for the droplet to completely evaporate or the time until a microexplosion event occurred. Additionally, explosion frequency was assessed by comparing the ratio of exploding droplets to those that evaporate without exploding. In timed and frequency trials, all data sets were collected with at least 50 runs to ensure statistical relevance, and 95% confidence intervals are reported. Statistical data are represented in Appendix A.

High speed photography was used to assess evaporation rates and qualitatively describe the microexplosion phenomenon. Images were captured using a Photron Fastcam Ultima APX

Imager. Auxiliary lighting was supplied by a Solarc LB150 lamp. Images were recorded at 1000 fps, and image brightness and contrast adjustments were applied uniformly across all frames using the NIH program, ImageJ.[38] For the d^2-law analysis, droplet size was assessed in consecutive frames (15 fps), by manually fitting ellipses to the droplet periphery using ImageJ.

5.3 Results

Droplets of pure bio-oil were directly observed by high speed photography as they pyrolyzed and vaporized on a heated alumina surface (Fig. 1A, Supplementary Videos 1, 3 & 4). After an initial heating stage, the droplets underwent a motionless evaporation phase where the square of the diameter decreased linearly in accordance with the d^2-law, followed by a brief period of vibration directly preceding an explosion event. Fig. 1A shows the final frames of a microexplosion where the droplet had no visible expansion and spontaneously ruptured, creating an explosion lasting about 10 ms.

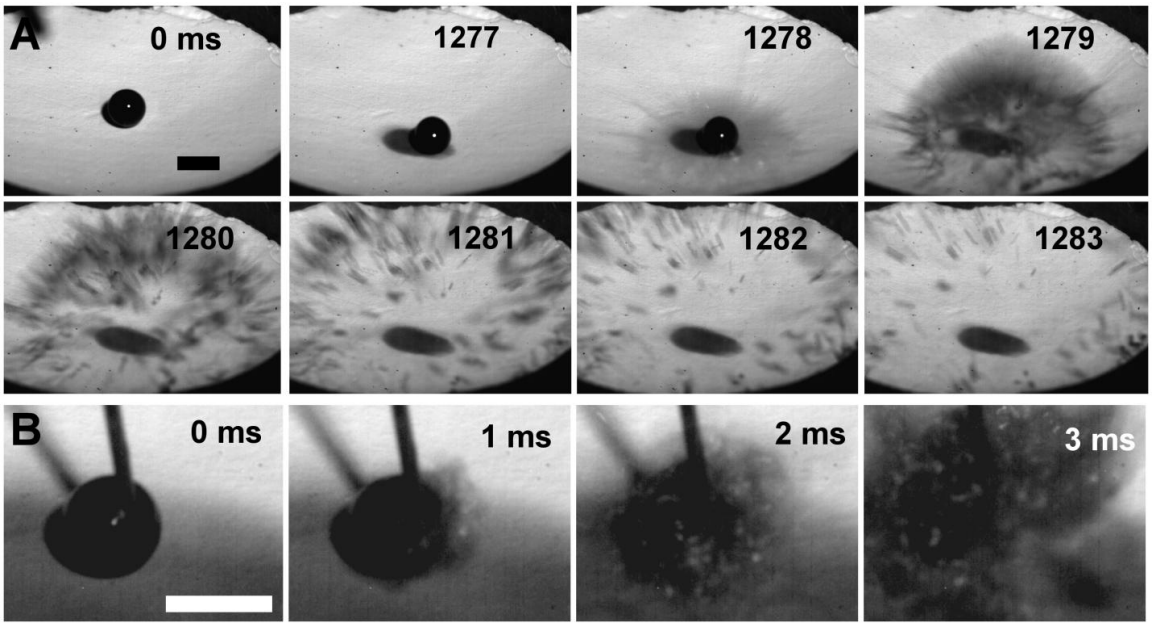

Figure 5-1: High Speed Photography of Bio-oil Microexplosions A.) A droplet of bio-oil evaporates on a 500 °C alumina surface. A microexplosion (1278-1279 ms) violently disperses the bio-oil over several milliseconds. B.) Late time (1273 ms) of a droplet is probed with a rod resulting in an instantaneous microexplosion. Scale bars = 1000 μm.

The explosion phenomenon was examined further in Fig. 1B where the late stages of the droplet lifetime (t~3000 ms) were probed with a 30 mm rod. The probe punctured the outer shell of the droplet, resulting in a violent explosion. When probed at earlier times (t~500 ms), the droplet behaved as a viscous oil and did not explode. The shell of the droplet had viscoelastic properties in both the probed and unprobed experiments, with less jetting and deformation in times leading up to the final microexplosion (Figure 5-10).

The evaporation rate was examined by performing a d^2-law analysis. For homogeneous fuels with a uniform or narrow range of chemical species volatilities, droplet evaporation in a stagnant atmosphere is known to evaporate at a rate proportional to the square of the diameter.[16] Fig. 2 shows the d^2-law relationship of bio-oil as it evaporates on an alumina surface. Due to early ($(d/d_0)^2 > 0.5$) microexplosions, d^2 data could only be obtained for approximately half of the droplet lifetime. However, after an initial heat-up period (~1 s), droplet vaporization conformed to the d^2-law relationship.

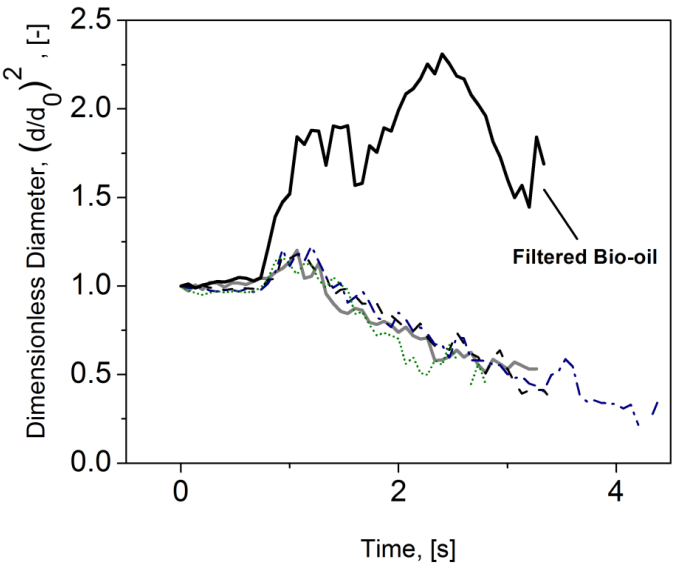

Figure 5-2: Evaporation of Filtered Bio-oils. After an initially flat heat-up period, pure bio-oil (——) evaporating on a 500 °C alumina surface is observed decreasing linearly in accordance with the d2-law. Filtered dilutions of 25% (- - -), 50% (-·-·-), and 75% (·····) demonstrate nearly identical evaporation profiles and rates. In the case of the 100% filtered bio-oil (——), significant char formation occurs and evaporation does not conform to the d2-law relationship.

Filtered samples exhibited a reduction in the frequency of microexplosions. Filtration of bio-oils through a 0.45 µm filter decreased the explosion frequency from above 50% to below 5% (Fig. 3A). Interestingly, the respective average lifetimes of droplets in both explosion and explosion-free cases remained unaffected within error by the extent of filtration.

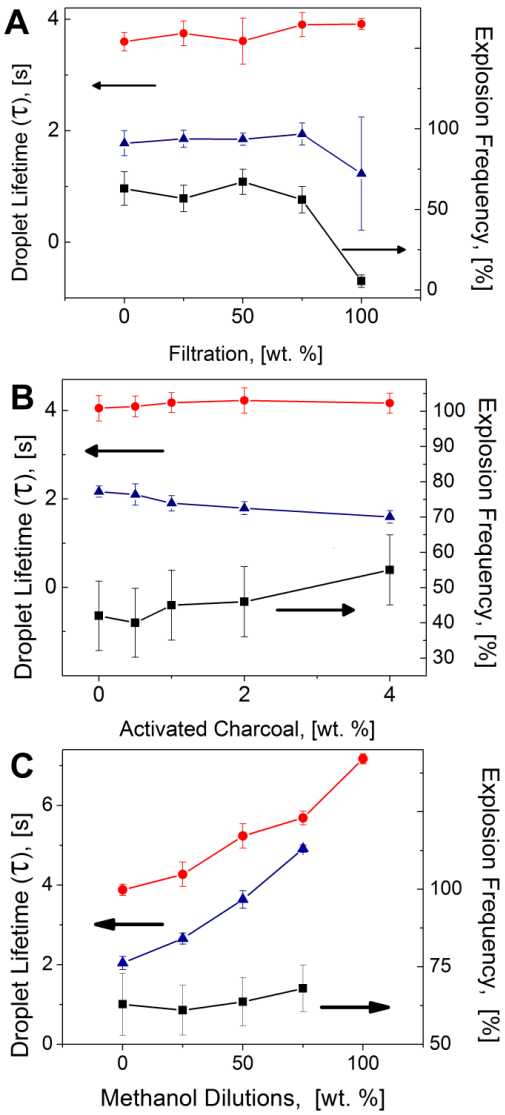

Figure 5-3: Lifetime analysis of bio-oil evaporation for the explosion-free case (●), explosion case (▲), and microexplosion frequency (■). A.) Filtration of bio-oil strongly reduces explosion frequency, however it does not change droplet lifetimes. B.) Increasing amounts of suspended activated charcoal decreases the pre-explosion time, and appears to increase explosion frequency. C.) Addition of methanol does not affect the explosion frequency; however, it strongly increases the droplet lifetimes in both the explosion and explosion-free cases.

The evaporation rates of 50 samples for each of five filtration dilutions were measured by performing a d^2-law analysis. After an initial heating period, a nearly identical vaporization period was observed for filtered samples 0-75%, and the explosion frequency and droplet lifetimes remain nearly constant. In the 100% filtered case, however, drastic differences were observed in the droplet evaporation. Significant bubbling occurred, resulting in pulsing and droplet expansion of over 200% at early times (< 2.5 s), followed by slow evaporation and steady char formation (Fig. 4B-C, Supplemental Video 2). Additionally, the explosion frequency was diminished to nearly zero, resulting in the weighted average droplet lifetime of the combined explosion and explosion-free cases to be extended.

The role of suspended solids was also explored, and the lifetimes and explosion frequencies are described in Fig. 3B, with additional statistical representation available in Appendix A.[37] As activated charcoal is added, a slight increase in explosion frequency was observed, increasing the average frequency by 15% at 4 wt.% charcoal. Similar to the filtered case, no significant decrease in the lifetime of the explosion-free case was observed. However, the addition of activated charcoal did cause the droplet explosion to occur slightly earlier. In a similar experiment, activated charcoal was added to filtered bio-oil and resulted in no statistical difference in microexplosion frequency from the base, filtered case.

Lifetime analysis and droplet frequency for bio-oil samples diluted with methanol have been studied. As shown in Fig. 3C, methanol addition appears to have no effect on the frequency of microexplosions, however it does appear to delay the onset of a microexplosion. Additionally, m lifetime of both the explosion and explosion-free cases appear to be approximately a linear combination of the pure bio-oil and methanol lifetimes.

5.4 Discussion

Microexplosions are known to exist in rapidly heated mixtures with chemical species of varying volatility.[39] Large droplets of bio-oil (d > 300 μm), have been qualitatively examined and characterized experimentally as undergoing several predictable events prior to microexplosion. In a combustive environment, droplets have previously been observed to undergo an initial evaporation stage, where the light compounds evaporate ($T_{droplet} \leq 100$ °C), followed by a vaporization phase in which the droplet is heated and the volatile components diffuse to and evaporate from the surface (100-500 °C). The temperature profile then stabilizes (~600°C), at which point the sequence culminates in rapid vibrations and ultimately a microexplosion.[16, 32, 33]

In our high speed photography experiments, a similar sequence of events is observed. The droplet moves freely on the surface without demonstrating any degree of wetting. After the initial heat-up period, the droplets evaporated in approximate agreement with the d^2-law relationship until undergoing an explosion. In the cases where nucleation occurred early (t < 300 ms, Fig 4A, Supplemental Video 1), the droplet underwent high frequency vibrations (> 30 hz), eventually leading to large bubbles, droplet deformation, and jetting (1000 ms). Jetting occurred as internal vapor bubbles burst, leading to the formation of a liquid jet extending from the liquid droplet that can be seen extensively in Supplementary Video 1 (1.2 < t < 2 s). Similarly, in the filtered case (Fig. 4B, Supplemental Video 2), bio-oil droplets were observed to bubble internally at early times. Unlike the pure case, however, the majority of the droplet lifetime (t > 300 ms) was dominated by a slow, even bubbling of hundreds of small bubbles until it formed a dark spherical droplet that slowly shrinks and collapses into a porous char particle. The droplet keeps its roughly spherical shape throughout its lifetime.

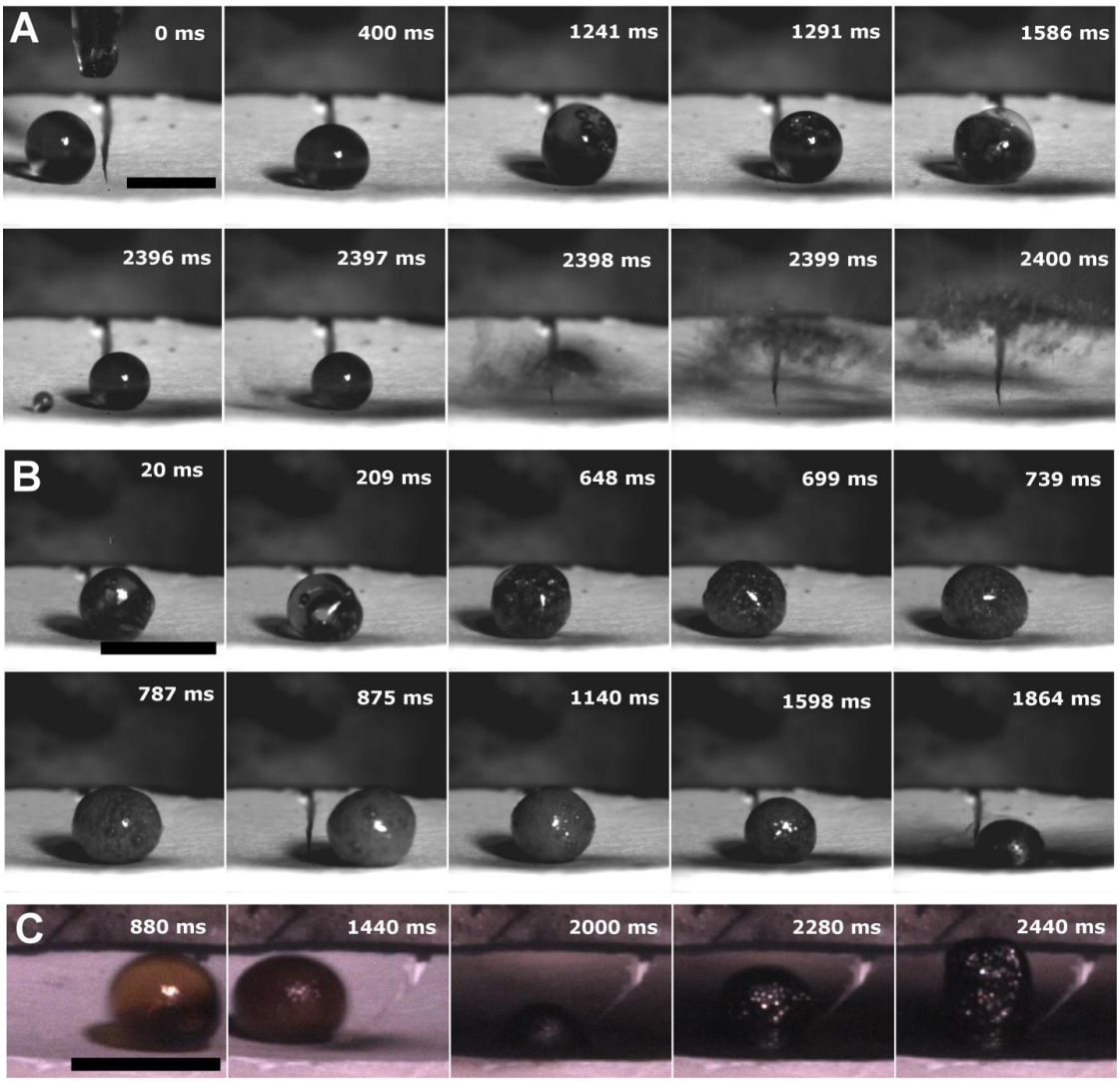

Figure 5-4: High Speed Photography of Evaporating Bio-oils A.) Bio-oil is heated on a 500 °C alumina surface for about one second. Large bubbles are observed throughout the droplet before bubbling ceases (~2 s) and ends in a microexplosion (2398 ms). Frames from Supplemental Video 1. Scale bar = 1 mm. B.) 100% Filtered bio-oil evaporates on a 500 °C alumina surface. Large bubbles are observed during early times. The droplet then lightens with many small droplets before retracting into a solid char particle. Frames from Supplementary Video 2. Scale bar = 1 mm. C.) Same conditions as B, however a slower frame rate allows for the observation of late time char formation. Evaporating filtered bio-oil does not explode, but rather reacts and expands at late times to produce a porous char scaffold.

The microexplosion phenomenon is thought to occur by one of two mechanisms which trap volatile components within the droplet. The first mechanism considers the formation of a viscous shell/volatile core model. The second mechanism proposes that the reactivity of the bio-oil forms a polymer shell around the volatile core.

The ‘viscous shell microexplosion mechanism’ has been examined using nonreactive multicomponent systems both experimentally and with liquid-phase diffusion-controlled transport modelli ng. Several groups have studied the microexplosion phenomenon during the vaporization of nonreactive binary and multicomponent mixtures, and they have outlined the key steps that the mixture undergoes leading up to the explosion event.[21, 23, 30, 39, 40] The initial phase is a quiescent, transient regime where the light volatiles diffuse to the surface and evaporate. The droplet then undergoes a strongly diffusion-limited phase where slow liquid-liquid diffusion dominates, leading to the formation of a viscous outer liquid layer (shell) around the lighter, volatile components remaining in the core. This shell acts as a barrier to the transfer of lighter components, which allows the droplet temperature to increase beyond the vaporization temperatures of the volatile core. The core is then superheated and rapidly flashes, causing a nearly instantaneous expansion and subsequent microexplosion. In this mechanism, the char particles are believed to act as vapor nucleation sites, thus lowering the transition temperature and allowing the core to more readily flash to vapor.[30]

In the alternative ‘polymer shell mechanism,’ it has been postulated that during the rapid liquid heating period, polymerization of the bio-oil occurs, leading to heavy components that form a solid shell.[32] In this scenario, pressure increases in the volatile core until the polymer shell ruptures, resulting in a rapid expansion over a short period of time, causing the observed microexplosion.

In the high speed photography sequences, drastic deformation, expansion and collapse of the bio-oil droplet without rupturing seems to indicate strong viscoelastic surface forces, but not formation of a solid shell at early times. This is further confirmed by probing the droplet at early times (t = 500 ms) with a rod before the core superheats. At these early times a viscous liquid is observed, and no microexplosions occur.

At late lifetimes ($(d/d_o)^2 < 0.7$, t > 1800 ms), however, a more viscous shell formed that did not deform or rupture easily. Droplet collisions observed in videos did not result in droplet

coalescence, suggesting the formation of a polymer shell, not simply the nonvolatile liquid fraction of the bio-oil. This shell potentially formed from the polymerization of the residual non-volatile fraction of bio-oil. As shown in Fig. 1B, when a bio-oil droplet was probed at late times (t = 1300 ms), a violent microexplosion occurred immediately upon puncturing the outer shell of the droplet. These qualitative findings support the conclusion that a polymer shell forms during the late droplet lifetimes resulting in microexplosions in pyrolysis oils.

The role of a heavy polymer fraction in bio-oil was further explored by examining the effect of filtration on microexplosions. Filtration through a 0.45 μm syringe filter removed 1.6 wt.% polymeric solids, resulting in substantial differences in the evaporation sequences of the filtered and unfiltered bio-oils. In the case of filtered bio-oil, gradual char formation was observed, and the microexplosion frequency was reduced from 60% to 5%. This indicates that the removed solids played a key role in formation of the viscous liquid or polymer shell and the microexplosion phenomenon within bio-oil.

It has been suggested that heterogeneous nucleation sites in bio-oil lower the transition temperature limit for flashing the volatile core, leading to microexplosions.[30, 41] However, the addition of 2 wt.% activated charcoal to the filtered bio-oil had no impact on the frequency of microexplosions, suggesting that the removed solids do not simply act as nucleation sites. This is consistent with experiments that have shown the presence of a suspension wire does not induce microexplosions[41] and other research that concludes that particle nucleation only plays a marginal role in the microexplosion phenomenon.[21] These results support the importance of the heavy fraction of bio-oil in the mechanism of microexplosions, which is needed in the formation of a polymer shell that entraps the volatile core.

Qualitative analysis of the evaporation phenomenon in both the filtered and unfiltered experiments also provides insight into the mechanism for microexplosions in bio-oil. In the pure bio-oil case, a cloudy quivering droplet was observed with several medium-sized (10-50 μm) vapor bubbles for the first 1000 ms (Fig 4A, Supplementary Video 1). More frequent vapor

bubble formation, growth, and jetting were observed in the next 1000 ms. The last 500 ms of the droplet lifetime was characterized by a period of no observed bubbling or jetting, and culminates in a microexplosion.

Filtered bio-oil did not undergo microexplosions. Instead, bubbling was observed early (200 ms) and continued with increasing intensity for the next 500 ms. Unlike the pure bio-oil, no jetting or physical distortions were observed. The droplet remained approximately spherical during its entire lifetime. However, at later times the entire droplet became more rigid as it solidified without the formation of a well defined liquid surface. Hundreds of small bubbles accumulated within the bio-oil droplet and resulted in slow char formation for the next 1000 ms (Fig. 4B-C).

This significant difference in the two evaporation phenomena (filtered versus unfiltered bio-oil) is consistent with the observed reduction of microexplosion frequency when samples are filtered. Additionally, it supports the conclusion that the heavy polymer fraction of bio-oil is needed for microexplosions to occur. Furthermore, internal droplet concentration gradients in the filtered bio-oil alone are not sufficient to form the shell/core system that results in a microexplosion, as supported by the lack of observed explosions (<3%, Fig. 3A) in the filtered bio-oil experiments.

In cases where microexplosions did not occur, the remaining viscous liquid solidified into a char which can be burned to CO and CO_2. Fig 4C shows the late time ($t > 3$ s) of an unfiltered bio-oil droplet that did not explode charring on the 500 °C surface. The droplet was initially observed to shrink as the volatile components evaporated. As the droplet solidified from the bottom upwards, it slowly bubbled and grew vertically, creating a porous char scaffold. At late times ($t > 2$ s), the only fraction remaining in the bio-oil was the heavy, non-volatile fraction that remained after pyrolysis. A significant amount of surface blackening was also observed from the secondary pyrolysis of the vapors at late times. These charring effects are not preferred due to

their slow combustion rates,[27] and inducing microexplosions would be preferable for use in the traditional combustion and refining processes.

Methanol is considered as an additive to bio-oil for its ability to prevent aging in which the oil viscosity increases with time.[25] In our experiments, methanol dilutions delay the time for microexplosions to occur in the fuel-methanol mixture. Additionally, it increases the mixture volatility, resulting in more rapid vaporization rates (Appendix A, Figure 5-11). The rate curve is linear, suggesting that the rate was a weighted average of the individual components (bio-oil/methanol). These rates were determined only for explosion-free case, and they did not account for the beneficial effects of secondary atomization due to the presence of microexplosions.

Based on the measured vaporization characteristics of both pure and methanol-diluted bio-oil, it was determined that pure bio-oil (1) vaporizes at the slowest rate, (2) exhibits microexplosions earlier. The addition of methanol to the fuel contributed significantly to the rate of change of the droplet size and resulted in a more uniform evaporation sequence. Additionally, delay observed in the onset of the microexplosion was consistent with other fuel additives described in the literature, where high moisture content was shown to delay explosion times in bio-oils.[30] While methanol did not promote earlier microexplosions in bio-oil, it did increase the evaporation rate and frequency of explosions, which reveals new ways for the fuel additive to improve the end-use of bio-oils.

5.5 Conclusions

Bio-oils derived from pyrolysis of biomass exhibited violent microexplosions when rapidly heated for the purpose of vaporization or combustion. Rapid droplet heating and reaction led to internal bubbling and ultimately a violent microexplosion. The addition of methanol did not increase microexplosion frequency and evaporation rates, while partial filtration of bio-oil increased the frequency of microexplosions. Filterable polymers present in the bio-oil were shown to be necessary for microexplosions to occur, while the presence of additional nucleation sites on solid particles within bio-oil seemed to have a minimal impact on microexplosion frequency or timing. Qualitatively, experimental results suggest the formation of a polymer shell upon heating of bio-oil droplets, leading to pressurization of the droplet core, thus resulting in a microexplosion from sudden expansion.

5.6 Appendix A: Supplemental Materials and Methods

5.6.1 Gel Permeation Chromatography (GPC)

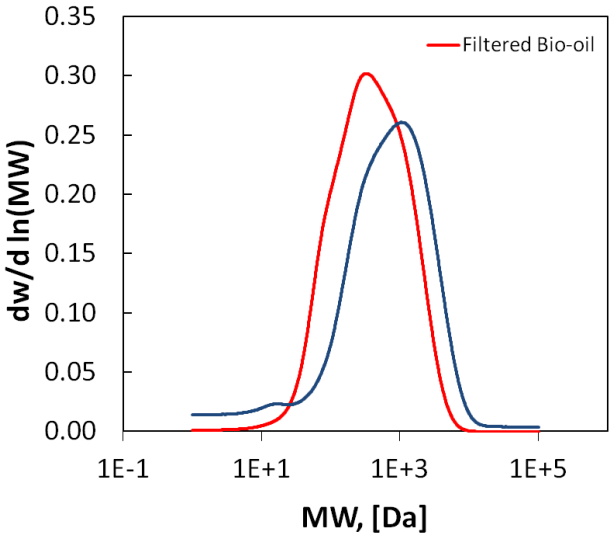

Figure 5-5: Gel permeation chromatography was performed by dissolving 0.01 mL filtered bio-oil into 1.0 mL tetrahydrofuran (THF). Polystyrene standards (Varian EasiVial PL2010-0402) were used to calibrate the size distribution. Results indicate a shift toward higher molecular weights in the solid sample.

5.6.2 Experimental Pyrolysis Setup

- Timed Trials

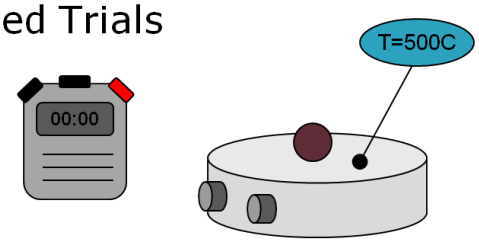

No. of Runs: 20-100

Data Recorded:
1. Time
2. Probability

T=500 °C, Flowing N_2

- High speed photography

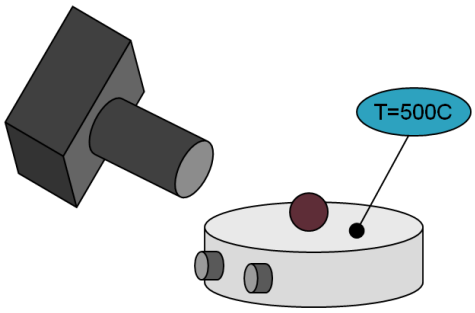

No. of Runs: 25-50

Data Recorded:
1. Qualitative observations, (1000fps)
2. d(t), (25 fps)

T=500 °C, Flowing N_2

Figure 5-6: Experimental bio-oil evaporation set-up.

5.6.3 Statistical Analysis of Timed Trials

5.6.3.1 Filtered Case

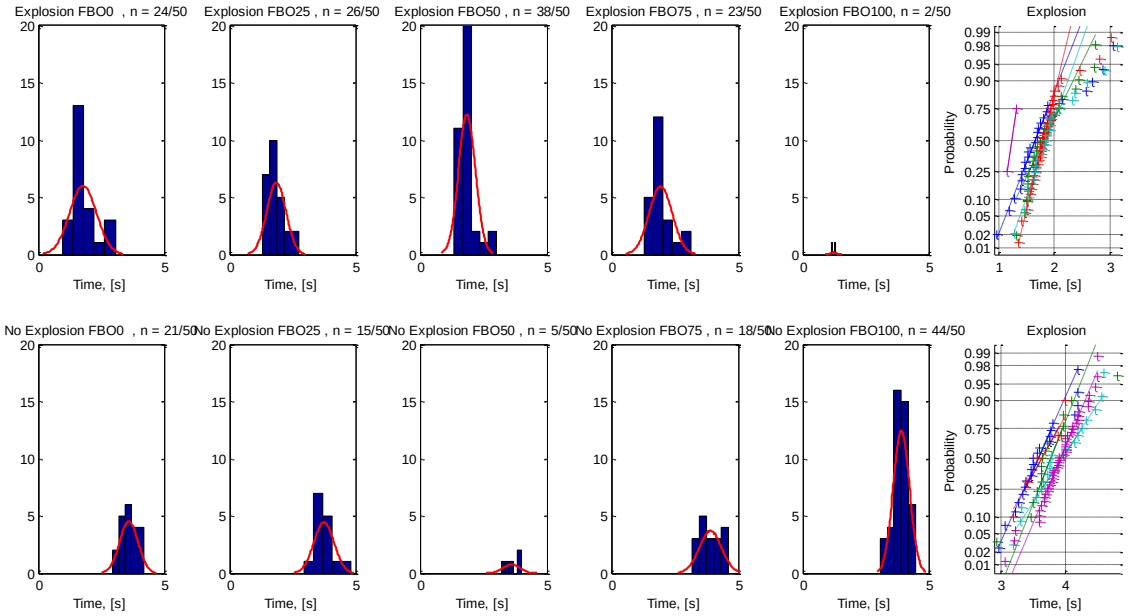

Figure 5-7: Statistical timed trials data for filtered bio-oil.

5.6.3.2 Activated Charcoal Case

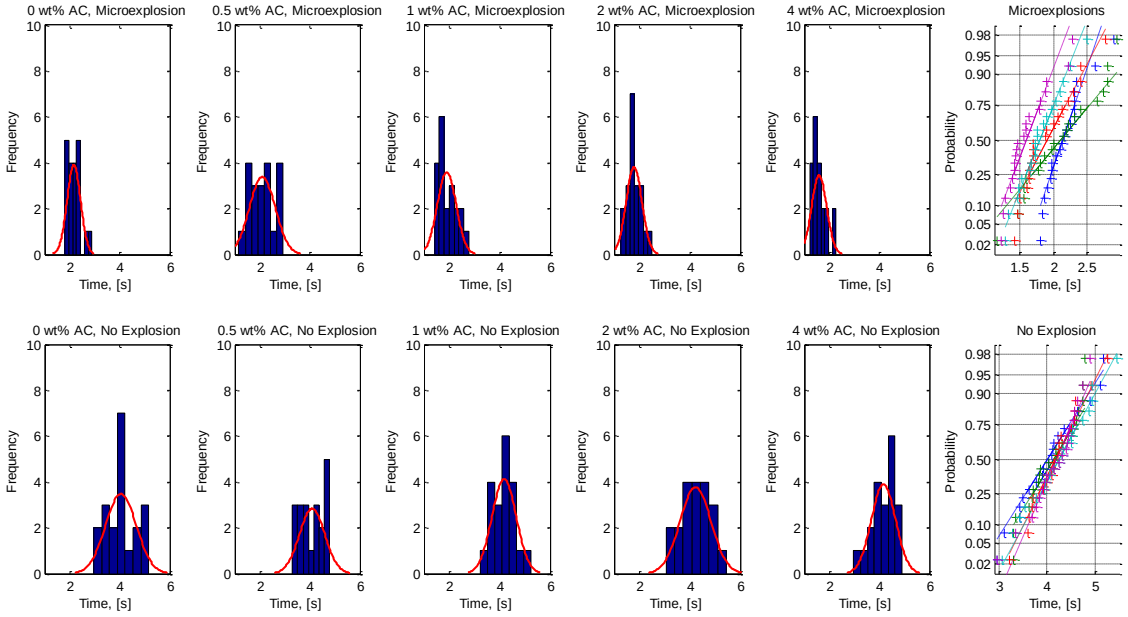

Figure 5-8: Statistical timed trials data for activated charcoal plus bio-oil.

5.6.3.3 Methanol Case

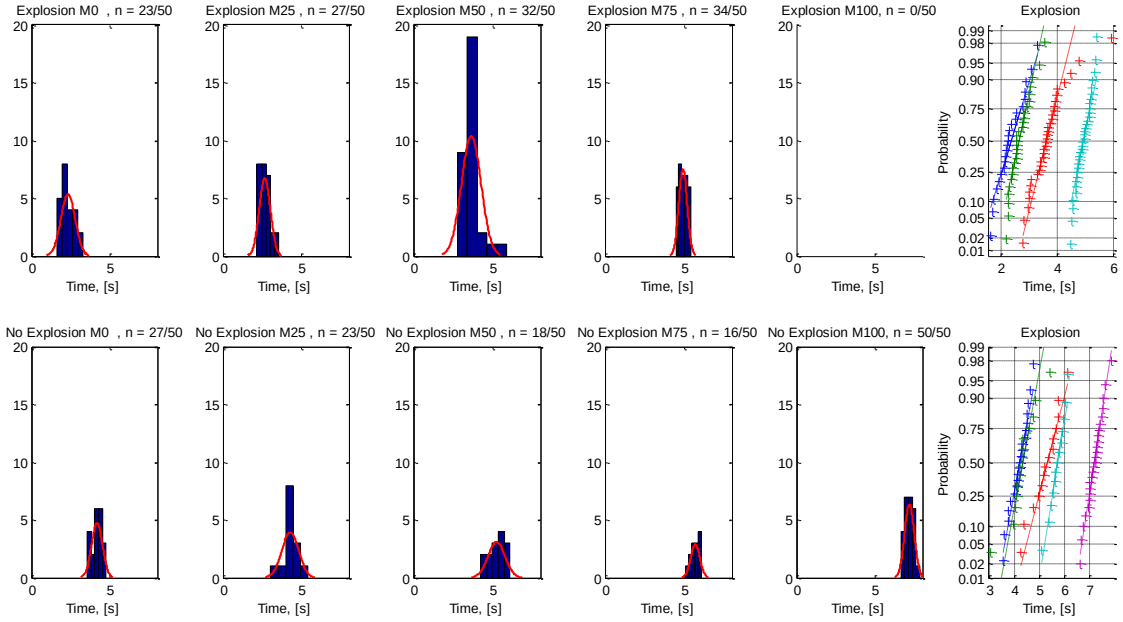

Figure 5-9: Statistical timed trials data for methanol plus bio-oil.

5.7 Additional Frames (Pure Bio-oil)

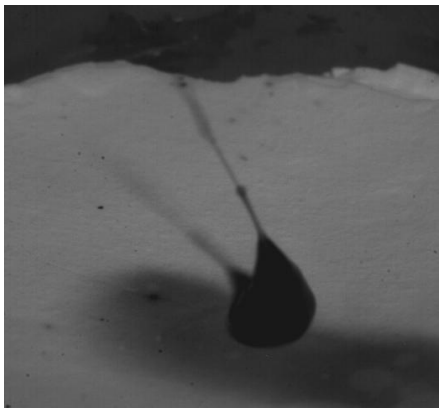

Bio-oil jetting, t = 1174ms

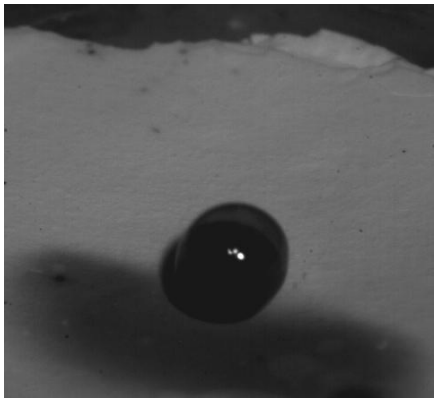

Bio-oil internal bubble formation, t = 1527ms

Figure 5-10: Qualitative frames of pure bio-oil evaporating.

5.7.1 Methanol Evaporation Rates

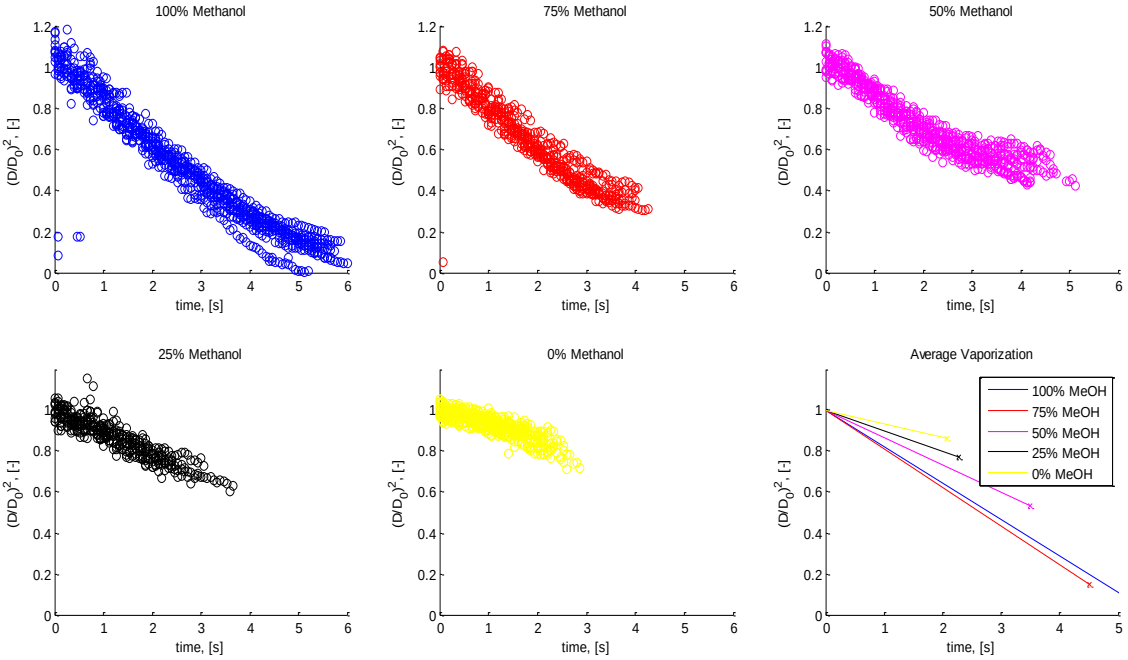

Figure 5-11: Bio-oil/Methanol evaporation curves at various dilutions.

5.7.2 Methanol Evaporation Rates

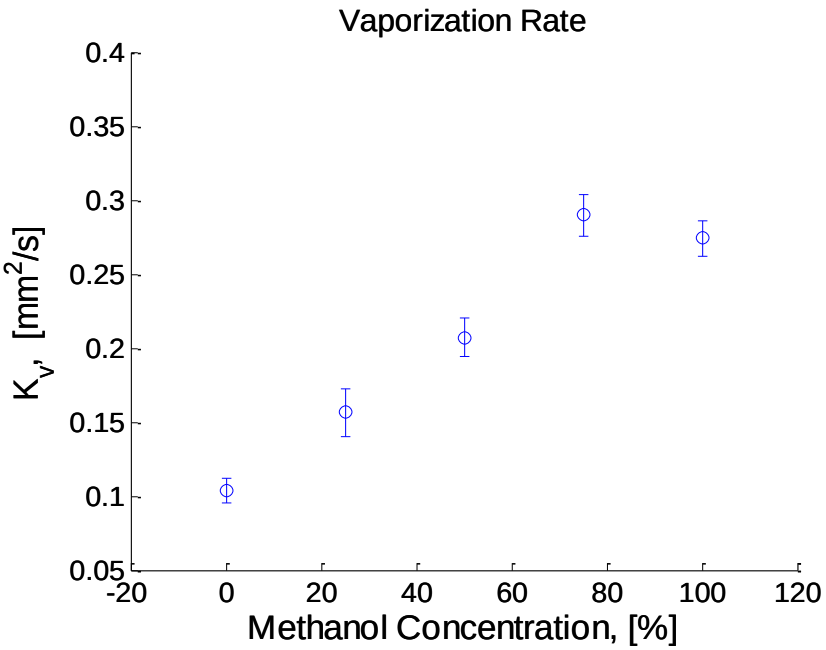

Figure 5-12: Bio-oil evaporation rates at various methanol dilutions

5.8 References

1. S. Czernik, A. V. Bridgwater, Overview of Applications of Biomass Fast Pyrolysis Oil. *Energy & Fuels* **18**, 590-598 (2004)10.1021/ef034067u).
2. M. S. Mettler, D. G. Vlachos, P. J. Dauenhauer, Top ten fundamental challenges of biomass pyrolysis for biofuels. *Energy & Environmental Science* **5**, 7797-7809 (2012).
3. A. Ragauskas, C. Williams, B. Davison, G. Britovsek, J. Cairney, C. Eckert, W. Frederick Jr, J. Hallett, D. Leak, C. Liotta, The path forward for biofuels and biomaterials. *Science* **311**, 484-489 (2006).
4. K. Sanderson, US biofuels: A field in ferment. *Nature* **444**, 673-676 (2006).
5. M. S. Mettler, A. D. Paulsen, D. G. Vlachos, P. J. Dauenhauer, Pyrolytic conversion of cellulose to fuels: levoglucosan deoxygenation via elimination and cyclization within molten biomass. *Energy & Environmental Science* **5**, 7864-7868 (2012).
6. M. S. Mettler, A. D. Paulsen, D. G. Vlachos, P. J. Dauenhauer, The chain length effect in pyrolysis: bridging the gap between glucose and cellulose. *Green Chemistry* **14**, 1284-1288 (2012).
7. A. V. Bridgwater, *Progress in Thermochemical Biomass Conversion* (Blackwell Science Ltd, 2001), vol. 1.
8. D. Mohan, C. U. Pittman, P. H. Steele, Pyrolysis of Wood/Biomass for Bio-oil: A Critical Review. *Energy & Fuels* **20**, 848-889 (2006); published online Epub2006/05/01 (10.1021/ef0502397).
9. J. Piskorz, D. S. Scott, D. Radlein, in *Pyrolysis Oils from Biomass*. (American Chemical Society, 1988), vol. 376, chap. 16, pp. 167-178.
10. J. Yang, P. J. Dauenhauer, A. Ramasubramaniam, The role of water in the adsorption of oxygenated aromatics on Pt and Pd. *Journal of Computational Chemistry* **34**, 60-66 (2013)10.1002/jcc.23107).
11. J. L. Colby, P. J. Dauenhauer, B. C. Michael, A. Bhan, L. D. Schmidt, Improved utilization of biomass-derived carbon by co-processing with hydrogen-rich feedstocks in millisecond reactors. *Green Chemistry* **12**, 378-380 (2010).
12. B. J. Dreyer, P. J. Dauenhauer, R. Horn, L. D. Schmidt, Enhanced Olefin Production from Renewable Aliphatic Feedstocks and Co-Fed Lignin Derivatives Using Experimental Surrogates by Millisecond Catalytic Partial Oxidation. *Industrial & Engineering Chemistry Research* **49**, 1611-1624 (2010); published online Epub2010/02/17 (10.1021/ie9013452).
13. C. Di Blasi, Modeling chemical and physical processes of wood and biomass pyrolysis. *Progress in Energy and Combustion Science* **34**, 47-90 (2008).
14. M. E. Boucher, A. Chaala, C. Roy, Bio-oils obtained by vacuum pyrolysis of softwood bark as a liquid fuel for gas turbines. Part I: Properties of bio-oil and its blends with methanol and a pyrolytic aqueous phase. *Biomass and Bioenergy* **19**, 337-350 (2000)10.1016/s0961-9534(00)00043-x).
15. D. Rennard, P. Dauenhauer, S. Tupy, L. Schmidt, Autothermal catalytic partial oxidation of bio-oil functional groups: esters and acids. *Energy Fuels* **22**, 1318-1327 (2008).
16. C. R. Shaddix, D. R. Hardesty, "Combustion Properties of Biomass Flash Pyrolysis Oils: Final Project Report," (Sandia National Laboratories, 1999).
17. M. J. Wornat, B. G. Porter, N. Y. C. Yang, Single Droplet Combustion of Biomass Pyrolysis Oils. *Energy & Fuels* **8**, 1131-1142 (1994)10.1021/ef00047a018).
18. L. T. Yap, I. M. Kennedy, F. L. Dryer, Disruptive and Micro-Explosive Combustion of Free Droplets in Highly Convective Environments. *Combustion Science and Technology* **41**, 291-313 (1984); published online Epub1984/11/01 (10.1080/00102208408923836).

19. C. K. Law, A Model for the Combustion of Oil/Water Emulsion Droplets. *Combustion Science and Technology* **17**, 29-38 (1977); published online Epub1977/10/01 (10.1080/00102209708946810).
20. C. T. Avedisian, "Fundamental droplet combustion characteristics of mixtures and emulsions: Final report," (1988).
21. T. Kadota, H. Yamasaki, Recent advances in the combustion of water fuel emulsion. *Progress in Energy and Combustion Science* **28**, 385-404 (2002)10.1016/s0360-1285(02)00005-9).
22. J. C. Lasheras, A. C. Fernandez-Pello, F. L. Dryer, On the disruptive burning of free droplets of alcohol/n-paraffin solutions and emulsions. *Symposium (International) on Combustion* **18**, 293-305 (1981)10.1016/s0082-0784(81)80035-5).
23. C. K. Law, Internal boiling and superheating in vaporizing multicomponent droplets. *AIChE Journal* **24**, 626-632 (1978)10.1002/aic.690240410).
24. V. Oja, E. M. Suuberg, Vapor Pressures and Enthalpies of Sublimation of d-Glucose, d-Xylose, Cellobiose, and Levoglucosan. *Journal of Chemical & Engineering Data* **44**, 26-29 (1998)10.1021/je980119b).
25. J. P. Diebold, S. Czernik, Additives To Lower and Stabilize the Viscosity of Pyrolysis Oils during Storage. *Energy & Fuels* **11**, 1081-1091 (1997)10.1021/ef9700339).
26. M. E. Boucher, A. Chaala, H. Pakdel, C. Roy, Bio-oils obtained by vacuum pyrolysis of softwood bark as a liquid fuel for gas turbines. Part II: Stability and ageing of bio-oil and its blends with methanol and a pyrolytic aqueous phase. *Biomass and Bioenergy* **19**, 351-361 (2000)10.1016/s0961-9534(00)00044-1).
27. C. R. Shaddix, P. J. Tennison, Effects of char content and simple additives on biomass pyrolysis oil droplet combustion. *Symposium (International) on Combustion* **27**, 1907-1914 (1998)10.1016/s0082-0784(98)80034-9).
28. E. S. Landry, S. Mikkilineni, M. Paharia, A. J. H. McGaughey, Droplet evaporation: A molecular dynamics investigation. *Journal of Applied Physics* **102**, 124301-124307 (2007).
29. W. L. H. Hallett, N. A. Clark, A model for the evaporation of biomass pyrolysis oil droplets. *Fuel* **85**, 532-544 (2006)10.1016/j.fuel.2005.08.006).
30. V. Stamatov, D. Honnery, J. Soria, Analysis of the Pre-Conditions for Micro-Explosions of Bio-Oil Droplets. *Analysis* **17**, 20 (2005).
31. J. Brett, A. Ooi, J. Soria, The effect of internal diffusion on an evaporating bio-oil droplet – The chemistry free case. *Biomass and Bioenergy* **34**, 1134-1140 (2010)10.1016/j.biombioe.2010.03.006).
32. J. D'Alessio, M. Lazzaro, P. Massoli, V. Moccia, Thermo-optical investigation of burning biomass pyrolysis oil droplets. *Symposium (International) on Combustion* **27**, 1915-1922 (1998)10.1016/s0082-0784(98)80035-0).
33. M. Garcia-Perez, P. Lappas, P. Hughes, L. Dell, A. Chaala, D. Kretschmer, C. Roy, Evaporation and combustion characteristics of biomass vacuum pyrolysis oils. *IFRF Combustion Journal* **200601**, (2006).
34. A. R. Teixeira, K. G. Mooney, J. S. Kruger, C. L. Williams, W. J. Suszynski, L. D. Schmidt, D. P. Schmidt, P. J. Dauenhauer, Aerosol generation by reactive boiling ejection of molten cellulose. *Energy & Environmental Science* **4**, 4306-4321 (2011).
35. D. Rennard, R. French, S. Czernik, T. Josephson, L. Schmidt, Production of synthesis gas by partial oxidation and steam reforming of biomass pyrolysis oils. *International Journal of Hydrogen Energy* **35**, 4048-4059 (2010)10.1016/j.ijhydene.2010.01.143).
36. B. Scholze, C. Hanser, D. Meier, Characterization of the water-insoluble fraction from fast pyrolysis liquids (pyrolytic lignin): Part II. GPC, carbonyl goups, and 13C-NMR. *Journal of analytical and applied pyrolysis* **58-59**, 387-400 (2001)Doi: 10.1016/s0165-2370(00)00173-x).

37. Supplemental material available online.
38. W. S. Rasband. (National Institutes of Health, Bethesda, Maryland, 1997-2011).
39. D. T. Ryddner, M. F. Trujillo, paper presented at the ILASS-Americas 24th Annual Conference on Liquid Atomization and Spray Systems, San Antonio, 2012.
40. C. H. Wang, X. Q. Liu, C. K. Law, Combustion and microexplosion of freely falling multicomponent droplets. *Combustion and Flame* **56**, 175-197 (1984)10.1016/0010-2180(84)90036-1).
41. R. Calabria, F. Chiariello, P. Massoli, Combustion fundamentals of pyrolysis oil based fuels. *Experimental Thermal and Fluid Science* **31**, 413-420 (2007)10.1016/j.expthermflusci.2006.04.010).

SECTION II.

DIFFUSION LIMITATIONS IN ZEOLITES: DOMINANCE OF SURFACE BARRIERS IN MICROPOROUS MASS TRANSPORT

Introduction

Zeolites have been synthesized at laboratory and industrial scales for nearly half a century for their catalytic, absorptive, and separative capabilities owing to their extraordinary molecular sieving capacity.[1-5] They are critical for catalytic upgrading of petrochemicals and fuels and have been adapted for use in the upgrading and separation of bio-fuels. Synthesis of zeolite particles has advanced to the extent that allows for fine control of microporous structure, with well-defined pore networks (dpore < 0.5 nm) and tunable strength of active sites. The combination of design parameters allows zeolite optimization for targeted applications, controlling molecular diffusion, reactivity and absorption capacity.[6-9]

Unique micropore structures with a pore size ranging from 0.5 to 2 nm may, however, also present significant limitations for molecules accessing catalytic active sites located within the micropores due to the slow intracrystalline mass transport in micropore channels. For catalytic reactions in microporous materials, molecules diffuse into the pore network, react at the active site, and diffuse out of the pores.[10] It is well known that diffusion limitations may substantially limit the industrial utilization of these materials in catalysis and adsorption by restricting their effectiveness, activity, selectivity and lifetime.[11] To maximize turnover frequency, synthesis of new microporous materials aims to eliminate the contribution of mass transport to the overall conversion rate. The traditional approach to minimize these mass transport dominated systems is to decrease the particle size thus decreasing the diffusional time. One approach is to synthesize zeolite nanocrystals, which have been achieved by precisely controlling nucleation and crystal growth processes. For example, silicalite-1 particles with MFI zeolite topology have recently been synthesized in uniform sizes as small as 62 nm.[12]

An emerging approach to faster intraparticle mass transport is to introduce secondary mesoporosity in microporous materials resulting in reduced transport length scales. Introducing secondary mesopores into the intrinsic microporous structures can increase the number of accessible micropores and also reduce the characteristic diffusion length, thereby leading to

enhanced catalytic performance.[11, 13-16] These hierarchical structures build on micropores (well-ordered lattice structures, ~2 nm) with mesopores (ordered or disordered pore networks, 2-50 nm) and macropores (interstitial particle voids, > 50 nm). Hard templating methods have allowed for the synthesis of ordered mesoporous zeolites with close-packed zeolite particles as small as 20 nm;[17, 18] close-packing produces a hierarchical structure with well-defined mesopores (6-9 nm), and the whole particle is generated at radii as large as 1 μm.[17, 19] The soft templating method has also led to hierarchical zeolites with auxiliary mesoporosity,[9,10] allowing for micro/mesoporous materials, to be synthesized with length scales approaching that of a single unit cell (pillared,[20, 21] nanosheets,[22] membranes,[23-25] etc). Pentasil structures consist of MFI sheets only one or two unit cells thick, with mesopores of 3-7 nm within particle radii as large as 100 nm.[19, 20] By decreasing transport length scales to a single unit cell, the timescale for diffusion becomes negligibly small in accordance with the square of the particle/sheet size ($\tau = R^2/D$). However, the benefit of hierarchical pore networks on microporous diffusion has yet to be quantified.

Despite decades of study on diffusion in zeolites,[5,12-16] characterization of diffusion in microporous materials remains a significant technical challenge.[26-28] In general, macroscopic methods that measure the apparent/transport diffusivity (e.g. zero length chromatography, gravimetric, frequency response, interference microscopy) predict diffusivities that are orders of magnitude less than those that measure on a microscopic scale (e.g. quasi elastic neutron scattering, pulsed field gradient-nuclear magnetic resonance), which measure the tracer/self diffusivity. Though the relative trend in measured diffusivity values often demonstrate the same activation energies, differences in predicted diffusivities vary as much as three orders of magnitude.[10, 27, 29-32] As a result, this variation has been the topic of significant debate in literature, with specific questions being raised as to whether the differences are due to synthesis methods, adsorbate loading/concentration or surface effects.[26, 27, 32-38]

New mesoporous zeolite structures with microcrystalline domains below 20 nm are dominated by their surfaces, making characterization and/or prediction of their physical and

chemical properties difficult. Recent characterization by zero length chromatography of cyclohexane transport in MFI-structured 3DOm-i has shown that hierarchical, mesoporous materials provide overall faster mass transfer compared to larger single crystals,[3] as expected. However, the benefit of smaller crystalline domains was not as fast as expected; shorter transport length scales did not result in predictably faster transport timescales.[19] Additional characterization by zero length chromatography of cyclohexane transport in MFI has also shown that particle surfaces contribute significantly to the overall rate of transport as particles become smaller.[10] Apparent diffusivity determined by experiment of mesoporous zeolite materials is comprised of two parts (surface and bulk transport) resulting in values of apparent diffusivity that vary by as much as three orders of magnitude as particles vary in size between 20 nm and 3 μm.[39] Moving forward, it is paramount to understand transport limitations of both bulk diffusion and diffusion through the surface for design and utilization of these novel, zeolitic materials.

The following chapters will outline experimental (Zero Length Chromatography, Frequency Response) and computational (Dynamic Monte Carlo) techniques used in this work to describe transport limitations in microporous materials. Mechanistic insight is provided to describe the transport dominating surface barrier limitations in small particles.

References

1. A. Corma, From Microporous to Mesoporous Molecular Sieve Materials and Their Use in Catalysis. *Chem. Rev.* **97**, 2373-2419 (1997); published online EpubSep-Oct (10.1021/cr960406n).
2. J. Čejka, G. Centi, J. Perez-Pariente, W. J. Roth, Zeolite-Based Materials for Novel Catalytic Applications: Opportunities, Perspectives and Open Problems. *Catal. Today* **179**, 2-15 (2012)10.1016/j.cattod.2011.10.006).
3. C. Perego, A. Bosetti, Biomass to Fuels: The Role of Zeolite and Mesoporous Materials. *Microporous Mesoporous Mater.* **144**, 28-39 (2011)10.1016/j.micromeso.2010.11.034).
4. M. A. Snyder, M. Tsapatsis, Hierarchical Nanomanufacturing: From Shaped Zeolite Nanoparticles to High-Performance Separation Membranes. *Angew. Chem. Int. Edit.* **46**, 7560-7573 (2007)10.1002/anie.200604910).
5. M. E. Davis, Ordered porous materials for emerging applications. *Nature* **417**, 813-821 (2002); published online EpubJun (10.1038/nature00785).
6. S. M. Csicsery, Shape-selective catalysis in zeolites. *Zeolites* **4**, 202-213 (1984)http://dx.doi.org/10.1016/0144-2449(84)90024-1).
7. A. Corma, Inorganic solid acids and thei use in acid-catalyzed hydrocarbon reactions. *Chemical Reviews* **95**, 559-614 (1995); published online EpubMay (10.1021/cr00035a006).
8. L. B. Young, S. A. Butter, W. W. Kaeding, Shape selective reactions with zeolite catalysts, III. Selectivity in xylene isomerization, toluene methanol alkylation, and toluene disproportionation over ZSM-5 zeolite catalysts. *Journal of Catalysis* **76**, 418-432 (1982)10.1016/0021-9517(82)90271-8).
9. H. Jobic, W. Schmidt, C. B. Krause, J. Kärger, PFG NMR and QENS diffusion study of n-alkane homologues in MFI-type zeolites. *Microporous and Mesoporous Materials* **90**, 299-306 (2006)http://dx.doi.org/10.1016/j.micromeso.2005.10.020).
10. J. van den Bergh, J. Gascon, F. Kapteijn, in *Zeolites and Catalysis*. (Wiley-VCH Verlag GmbH & Co. KGaA, 2010), pp. 361-387.
11. J. Perez-Ramirez, C. H. Christensen, K. Egeblad, J. C. Groen, Hierarchical Zeolites: Enhanced Utilisation of Microporous Crystals in Catalysis by Advances in Materials Design. *Chem. Soc. Rev.* **37**, 2530-2542 (2008)10.1039/b809030k).
12. R. Watanabe, T. Yokoi, T. Tatsumi, Synthesis and application of colloidal nanocrystals of the MFI-type zeolites. *Journal of Colloid and Interface Science* **356**, 434-441 (2011)http://dx.doi.org/10.1016/j.jcis.2011.01.043).
13. X. Zhang, D. Liu, D. Xu, S. Asahina, K. A. Cychosz, K. V. Agrawal, W. Y. Al, A. Bhan, H. S. Al, O. Terasaki, M. Thommes, M. Tsapatsis, Synthesis of Self-Pillared Zeolite Nanosheets by Repetitive Branching. *Science* **336**, 1684-1687 (2012)10.1126/science.1221111).
14. K. Na, M. Choi, R. Ryoo, Recent Advances in the Synthesis of Hierarchically Nanoporous Zeolites. *Microporous Mesoporous Mater.* **166**, 3-19 (2013)http://dx.doi.org/10.1016/j.micromeso.2012.03.054).
15. M. S. Holm, E. Taarning, K. Egeblad, C. H. Christensen, Catalysis with Hierarchical Zeolites. *Catal. Today* **168**, 3-16 (2011)10.1016/j.cattod.2011.01.007).
16. F. C. Meunier, D. Verboekend, J.-P. Gilson, J. C. Groen, J. Pérez-Ramírez, Influence of Crystal Size and Probe Molecule on Diffusion in Hierarchical ZSM-5 Zeolites Prepared by Desilication. *Microporous Mesoporous Mater.* **148**, 115-121 (2012)10.1016/j.micromeso.2011.08.002).
17. W. Fan, M. A. Snyder, S. Kumar, P.-S. Lee, W. C. Yoo, A. V. McCormick, R. Lee Penn, A. Stein, M. Tsapatsis, Hierarchical nanofabrication of microporous crystals with ordered

mesoporosity. *Nat Mater* **7**, 984-991 (2008)http://www.nature.com/nmat/journal/v7/n12/suppinfo/nmat2302_S1.html).

18. P.-S. Lee, X. Zhang, J. A. Stoeger, A. Malek, W. Fan, S. Kumar, W. C. Yoo, S. Al Hashimi, R. L. Penn, A. Stein, M. Tsapatsis, Sub-40 nm Zeolite Suspensions via Disassembly of Three-Dimensionally Ordered Mesoporous-Imprinted Silicalite-1. *Journal of the American Chemical Society* **133**, 493-502 (2010); published online Epub2011/01/26 (10.1021/ja107942n).
19. C.-C. Chang, A. R. Teixeira, C. Li, P. J. Dauenhauer, W. Fan, Enhanced Molecular Transport in Hierarchical Silicalite-1. *Langmuir* **29**, 13943-13950 (2013); published online Epub2013/11/12 (10.1021/la403706r).
20. X. Zhang, D. Liu, D. Xu, S. Asahina, K. A. Cychosz, K. V. Agrawal, Y. Al Wahedi, A. Bhan, S. Al Hashimi, O. Terasaki, M. Thommes, M. Tsapatsis, Synthesis of Self-Pillared Zeolite Nanosheets by Repetitive Branching. *Science* **336**, 1684-1687 (2012); published online EpubJune 29, 2012 (10.1126/science.1221111).
21. X. Y. Zhang, D. X. Liu, D. D. Xu, S. Asahina, K. A. Cychosz, K. V. Agrawal, Y. Al Wahedi, A. Bhan, S. Al Hashimi, O. Terasaki, M. Thommes, M. Tsapatsis, Direct synthesis of self-pillared zeolite nanosheets by repetitive branching. *Abstracts of Papers of the American Chemical Society* **244**, (2012); published online EpubAug 19
22. M. Choi, K. Na, J. Kim, Y. Sakamoto, O. Terasaki, R. Ryoo, Stable single-unit-cell nanosheets of zeolite MFI as active and long-lived catalysts (vol 461, pg 246, 2009). *Nature* **461**, (2009); published online EpubOct 8 (Doi 10.1038/Nature08493).
23. P. Gao, M. H. Tai, D. D. Sun, Hierarchical TiO2/V2O5 Multifunctional Membrane for Water Purification. *Chempluschem* **78**, 1475-1482 (2013); published online EpubDec (DOI 10.1002/cplu.201300264).
24. K. Du, Y. Y. Liu, I. Wathuthanthri, C. H. Choi, Fabrication of hierarchical nanostructures using free-standing trilayer membrane. *J Vac Sci Technol B* **31**, (2013); published online EpubNov (Unsp 06ff04 Doi 10.1116/1.4821655).
25. C. Yacou, A. Ayral, A. Giroir-Fendler, A. Baylet, A. Julbe, Catalytic membrane materials with a hierarchical porosity and their performance in total oxidation of propene. *Catal Today* **156**, 216-222 (2010); published online EpubOct 31 (DOI 10.1016/j.cattod.2010.04.025).
26. J. Kärger, Measurement of Diffusion in Zeolites—A Never Ending Challenge? *Adsorption* **9**, 29-35 (2003)10.1023/a:1023811229823).
27. D. Ruthven, Diffusion in zeolites—a continuing saga. *Adsorption* **16**, 511-514 (2010)10.1007/s10450-010-9263-9).
28. R. Krishna, Describing the Diffusion of Guest Molecules Inside Porous Structures. *The Journal of Physical Chemistry C* **113**, 19756-19781 (2009); published online Epub2009/11/19 (10.1021/jp906879d).
29. S. Brandani, J. Caro, H. Jobic, J. Kärger, C. Krause, R. Staudt, in *Studies in Surface Science and Catalysis*, Z. G. J. C. Ruren Xu, Y. Wenfu, Eds. (Elsevier, 2007), vol. Volume 170, pp. 981-987.
30. H. Jobic, J. Kärger, C. Krause, S. Brandani, A. Gunadi, A. Methivier, G. Ehlers, B. Farago, W. Haeussler, D. M. Ruthven, Diffusivities of n-Alkanes in 5A Zeolite Measured by Neutron Spin Echo, Pulsed-Field Gradient NMR, and Zero Length Column Techniques. *Adsorption* **11**, 403-407 (2005)10.1007/s10450-005-5958-8).
31. D. M. Ruthven, in *Studies in Surface Science and Catalysis*, B. Laurent, K. Serge, Eds. (Elsevier, 1995), vol. Volume 97, pp. 223-234.
32. S. Brandani, L. J. Dunne, G. Manos, Eds. (Springer Netherlands, 2010), pp. 195-212.
33. L. Gueudré, E. Jolimaître, N. Bats, W. Dong, Diffusion in zeolites: is surface resistance a critical parameter? *Adsorption* **16**, 17-27 (2010)10.1007/s10450-010-9213-6).

34. O. C. Gobin, S. J. Reitmeier, A. Jentys, J. A. Lercher, Comparison of the Transport of Aromatic Compounds in Small and Large MFI Particles. *The Journal of Physical Chemistry C* **113**, 20435-20444 (2009); published online Epub2009/11/26 (10.1021/jp907444c).
35. M. Kocirik, P. Struve, K. Fiedler, M. Bulow, A model for the mass-transfer resistance at the surface of zeolite crystals. *Journal of the Chemical Society, Faraday Transactions 1: Physical Chemistry in Condensed Phases* **84**, 3001-3013 (1988).
36. P. Kortunov, S. Vasenkov, C. Chmelik, J. Kärger, D. M. Ruthven, J. Wloch, Influence of Defects on the External Crystal Surface on Molecular Uptake into MFI-Type Zeolites. *Chemistry of Materials* **16**, 3552-3558 (2004); published online Epub2004/09/01 (10.1021/cm0401645).
37. D. Ruthven, S. Brandani, M. Eic, H. Karge, J. Weitkamp, Eds. (Springer Berlin / Heidelberg, 2008), vol. 7, pp. 45-84.
38. S. J. Reitmeier, A. Jentys, J. A. Lercher, in *Ideas in Chemistry and Molecular Sciences*. (Wiley-VCH Verlag GmbH & Co. KGaA, 2010), pp. 229-253.
39. A. R. Teixeira, C.-C. Chang, T. Coogan, R. Kendall, W. Fan, P. J. Dauenhauer, Dominance of Surface Barriers in Molecular Transport through Silicalite-1. *The Journal of Physical Chemistry C* **117**, 25545-25555 (2013); published online Epub2013/12/05 (10.1021/jp4089595).

CHAPTER 6

ENHANCED MOLECULAR TRANSPORT IN HIERARCHICAL SILICALITE-1

6.1 Introduction

In the past decade, zeolite catalysts with secondary mesoporous structure, known as hierarchical zeolites, have been synthesized by various methods including soft template method using organic surfactants, hard template method using mesoporous carbon and desilication/dealumination method.[1-8] Hierarchical zeolites with both ordered and disordered mesopores or single nanosheet structures have been tested with a large variety of catalytic reactions.[1-4, 9-11] Enhanced catalytic activity, selectivity and catalyst lifetime are often attributed to the reduced diffusion limitation or improved mass transport without providing direct evidence from diffusion measurements. It is worth noting that external surface acid sites and connectivity of mesopores in hierarchical zeolites can also significantly contribute to the catalytic performance of zeolite catalysts. Previous study has also shown that the presence of mesoporosity does not necessarily lead to improved catalytic performance.[12] Therefore, in order to evaluate the benefits derived from mesoporosity, it is necessary to characterize the mass transport behavior by directly measuring molecular diffusivity within hierarchical zeolites and correlate it to the mesopore structures of hierarchical zeolites generated by different synthesis methods.

Enhanced molecular transport in hierarchical zeolites has been demonstrated directly by molecular diffusion measurements with volumetric adsorption, ^{129}Xe NMR, pulsed field gradient NMR and zero length column chromatography (ZLC) methods.[13-19] For example, iso-butane uptake indicated that mesoporous structures in hierarchical ZSM-5 imprinted from carbon black can significantly enhance the uptake rate.[13] Similarly, hierarchical zeolites made from a desilication method demonstrated approximately 100 times faster adsorption than conventional

zeolites, based on neo-pentane uptake measurements.[14] ^{129}Xe NMR and pulsed field gradient (PFG) NMR also demonstrate that mass transport can be significantly altered by both the presence of mesopores and the synthesis methods used to introduce them.[15, 16, 20] A PFG NMR study on water diffusion in zeolite BEA made with organosilane surfactants showed that the presence of the mesopores can enhance the rate of molecular diffusion by a factor of three.[17]

Among the available measurement techniques, the ZLC method can rapidly measure the intracrystalline diffusivity through microporous materials by monitoring the desorption profile from a previously equilibrated sample.[21-23] Developed in 1988 by Eić and Ruthven, it has been widely used to study molecular diffusion in microporous and mesoporous materials.[19, 21, 24-32] However, a systematic study on the relationship between mesoporous structure and mass transport properties of hierarchical zeolites is still lacking due to the difficulty in precisely controlling the size and arrangement of mesopores by synthesis methods.

Advances in the synthesis of hierarchical zeolites with well controlled mesoporosity provide a unique opportunity to study the relationship between mesoporous structure and mass transport in hierarchical zeolites.[1, 4, 6, 8, 10, 33] For example, Zhang et al. recently synthesized self-pillared pentasil (SPP) zeolites with "house of cards" construction (Figure 1a) by repetitive branching crystal growth of MFI topology, with the possible existence of MEL phase at the intersection of orthogonal nanosheets. These nanosheets, with a thickness of ~2 nm, are perpendicularly intergrown, and mesopores are generated from stacking of the nanosheets.[10] Additionally, three dimensionally ordered mesoporous imprinted (3DOm-i) zeolites were synthesized within three dimensionally ordered mesoporous (3DOm) carbon by a hard template method, providing the first hierarchical zeolite with well-controlled ordered mesopores.[6] The 3DOm-i zeolite is composed of spherical primary particles (e.g. 35 nm; Figure 1b) with a close packed structure, having a reduced diffusional length compared to conventional zeolites (Figure 1c).

In the present study, the diffusion behavior of cyclohexane in pure silica SPP and 3DOm-i silicalite-1 crystal with a primary particle size of 35 nm were studied with ZLC and compared to conventional silicalite-1 crystals with varying particle sizes. Diffusional time constants were measured and correlated to characteristic diffusion length providing a simple and direct way to demonstrate the enhanced molecular transport properties of hierarchical zeolites.

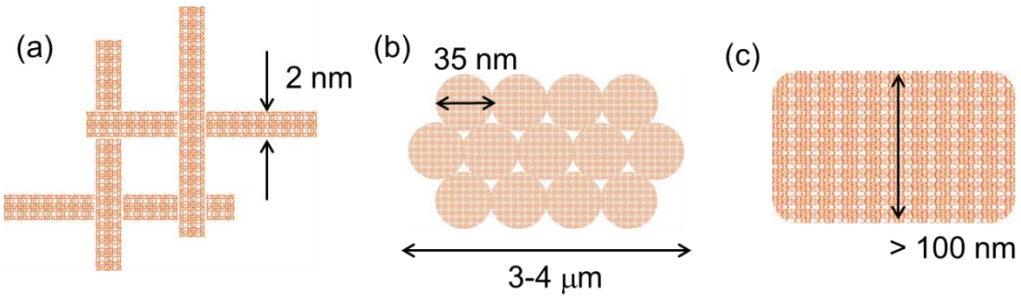

Figure 6-1: Schematic illustration of the dimensions and morphologies of the silicalite-1 crystals used in this study: (a) SPP, (b) 3DOm-i and (c) bulk silicalite-1.

6.2 Materials and Methods

6.2.1 Synthesis of silicalite-1 with variable particle sizes and ordered mesoporous structure

Pure silica self-pillared pentasil (SPP) zeolite was synthesized according to Zhang et al.[10] Tetra(n-butyl)phosphonium hydroxide (40% TBPOH, Aldrich) aqueous solution was added dropwise into tetraethylorthosilicate (TEOS, 98%, Alfa Aesar) with continuous stirring. Deionized water was then added into the mixture to give the composition of SiO_2: 0.3TBPOH: $10H_2O$:4EtOH (note that ethanol was originated from hydrolysis of TEOS). After aged for 12 hr, the clear solution was sealed in a Teflon lined stainless steel autoclave and heated in a 388 K convection oven for four days. The final product was recovered and washed by centrifugation and dried overnight in a 373 K oven.

3DOm-i silicalite-1 was synthesized using the method reported in our previous work.[6] In short, silica colloidal crystals composed of 35 nm silica nanoparticles were used as a hard

template to prepare 3DOm carbon. Silicalite-1 crystals were grown within the 3DOm carbon by steam assisted crystallization method.

Silicalite-1 crystals with the largest dimension of 200 nm and 20 μm were synthesized using methods from literature.[34, 35] For 200 nm silicalite-1 crystal, TEOS, tetrapropylammonium hydroxide (TPAOH, 40%, Alfa Aesar) and deionized water were mixed in a plastic vessel and stirred at 353 K for 24 hours. The obtained gel was transferred to a Teflon lined autoclave and heated at 443 K for 24 hours. The gel composition was SiO_2: 0.25TPAOH: $38H_2O$. The crystals were collected and washed with deionized water by centrifugation until the pH of the supernatant was lower than 9; the resulting slurry was dried in a 373 K oven. For the 20 μm silicalite-1 crystal, tetrapropylammonium bromide (TPABr, 98%, Aldrich) and sodium hydroxide (NaOH, 98%, Aldrich) were dissolved in deionized water. Ludox HS-40 (Aldrich) was then added as silicon source. The resulting solution with a composition of SiO_2: 0.33TPABr: 0.17NaOH: $333H_2O$ was stirred at room temperature for 24 hours then heated at 448 K for two days for crystallization. The solid products were washed with deionized water, collected by filtration, and dried in an oven at 373 K. All as-synthesized silicalite-1 samples were calcined at 823 K with a ramping rate of 1 K/min for 12 hours to remove the organic structure directing agent.

Silicalite-1 crystals were characterized by X-ray diffraction (XRD), scanning electron microscopy (SEM) and nitrogen adsorption-desorption experiments. Powder XRD patterns were collected on X'Pert Pro (PANalytical) diffractometer using Cu K_α radiation with an X'celerator detector. Data was collected in 2θ range from 4° to 40° with a step size of 0.02°. SEM images were collected on Magellan 400 (FEI), equipped with a field-emission gun operated at 3.0 kV with a stage bias of 0.5 V (2.7 V for SPP zeolite) after coating with Pt except for the SPP zeolite. N_2 physisorption isotherms were measured on an Autosorb®-iQ system (Quantachrome) at 77 K after outgassing at 473 K until pressure rise in the test cell was less than 25 mTorr/min. Pore size distribution and cumulative adsorbed volume were calculated by using NLDFT (non-local density functional theory) adsorption model which describes N_2 adsorbed onto silica at 77 K in

cylindrical pores (AsiQwin 1.02, Quantachrome). NLDFT model considers the configuration of adsorbates in pores on a molecular level and is widely used to characterize ordered nanoporous materials with different pore geometries.[36, 37] With adequate fluid-fluid and fluid-solid interaction parameters, it has been used to quantitatively predict the capillary condensation and evaporation transitions of adsorbates in novel hierarchical microporous materials.[10, 38-40]

6.2.2 Diffusion measurement and data analysis

The ZLC setup (shown in Figure 8) used in this work is similar to that developed by Ruthven et al. in their previous work.[21] All gas flow rates were controlled with Brooks 5850E mass flow controllers. Partial pressure of cyclohexane (>99%, Acros Organics) was maintained by equilibrating a low flow helium stream with a liquid cyclohexane reservoir at 283 K. Transfer lines were maintained at 363 K to eliminate condensation in the tubing. Crystalline zeolite samples, typically 5-6 mg, were pressed between two quarter inch stainless steel frits and contained within a ¼" Swagelok union and placed in an isothermal gas chromatograph oven (5890 Series II, Hewlett Packard). Prior to diffusion measurements, the crystals were preheated at 523K for 8 hours under helium flow of 50 mL/min to remove physically adsorbed water. For the 20 μm silicalite-1 sample, a slightly larger amount of sample was needed (20 mg), due to lower number of molecules desorbed from the particles to the gas phase. Cyclohexane was carried by low-flow helium (2.5 mL/min) from the adsorbate tank and further diluted with helium in the main stream (100 mL/min).

Adsorption of cyclohexane (~2 torr) in the silicalite-1 samples begins when a valve is actuated to allow the premixed stream of helium and cyclohexane to flow over the sample chamber, and the uptake is monitored online. Care was taken to ensure the equilibration time was greater than 0.416 R^2/D_{eff} to eliminate partial saturation effects,[22] where D_{eff} is the effective diffusivity of adsorbate in the crystal, and R is the radius of the crystals. After adsorption reached equilibrium, the valve was switched back to pure helium flow. Flow rates of 25-100 mL/min were

used with SPP zeolite at 363 K to examine whether the desorption process was controlled by molecular diffusion in micropores (see Figure 9 in Appendix A), and a purge flow rate of 100 mL/min for helium was selected for SPP zeolite. Similar flow rate experiments were also carried out for the samples with larger characteristic diffusion lengths, suggesting 50 mL/min is sufficient for characteristic lengths of crystals equal to or larger than 3DOm-i silicalite-1 (35 nm in primary particle size). Desorption of adsorbate from the silicalite-1 crystals was monitored by measuring the concentration of adsorbate in helium flow with a flame ionization detector (FID). Each experiment was repeated at least twice, and good reproducibility was observed. A set of typical chromatograms is shown in the Figure 10.

The data was analyzed using linear ZLC analysis of desorption curves developed by Eić and Ruthven.[21]Assuming gas-solid equilibrium and neglecting holdup in the gas phase, the transient mass balance for diffusion from three-dimensional particles is solved with an infinite series for normalized concentration exiting the chamber,

$$\frac{C}{C_0} = 2L\sum_{n=1}^{\infty}\frac{\exp\left(-\frac{\beta_n{}^2 D_{eff}}{R^2}t\right)}{\left[\beta_n{}^2 + L(L-1)\right]} \qquad 6\text{-}1$$

where C is the gas phase adsorbate concentration and C_0 is the initial gas phase adsorbate concentration in the effluent. β_n is the infinite series satisfying

$$\beta_n \cot\beta_n + L - 1 = 0 \qquad 6\text{-}2$$

and L is,

$$L = \frac{1}{3}\frac{FR^2}{KV_s D_{eff}} \qquad 6\text{-}3$$

where F is the purge flow rate, K is the Henry's law constant, V_s is the adsorbent volume. The spherical model chosen here has been verified by the method suggested by Cavalcante et al. (see Figure 11 in Appendix A for details),[31] which shows that the diffusional path of cyclohexane is three-dimensional in silicalite-1 micropores, conforming to the three-dimensional channel

network of MFI topology. Assuming a linear FID response with concentration, the dimensionless concentration was calculated by following equation[41]

$$\frac{C}{C_0} = \frac{I(t) - I_\infty}{I_0 - I_\infty} \qquad 6\text{-}4$$

where I_∞ is the GC-FID signal at long time (the background signal) and I_0 is the initial signal in the desorption curve. In the long time region, the solution of equation (1) can be further reduced to,

$$\frac{C}{C_0} = \frac{2L}{{\beta_1}^2 + L(L-1)} \exp\left(-{\beta_1}^2 \frac{D_{eff}}{R^2} t\right) \qquad 6\text{-}5$$

By plotting $ln(C/C_0)$ vs. time, the long-time slope can be fit to the above relationship. The parameter D_{eff}/R^2 can be extracted from the slope, while L can be determined from the intercept. The long time solution was selected to analyze the experimental ZLC curves in an attempt to mitigate concern of non-linear equilibrium at the initial stage of desorption where gas phase concentrations may be outside the linear region (Henry's law regime) of the adsorption isotherm. The feasibility of using the long-time solution to analyze the ZLC data for both non-linear equilibrium and linear equilibrium system has been demonstrated by Brandani, indicating that the slope of long-time asymptote of a non-linear system, in which the initial gas-solid equilibrium is not in the Henry's law region, is the same as that of a linear system.[42, 43] Also, the concentration of cyclohexane corresponding to the long-time region is in the order of 10^{-2}-10^{-3} Torr, which is in the linear equilibrium region based on adsorption isotherm measurements.[35, 44]

6.3 Results and Discussion

Figure 2 shows XRD patterns of synthesized silicalte-1 crystals, demonstrating characteristic reflection peaks corresponding to MFI topology. The XRD pattern for SPP crystal is broad and consistent with literature results.[10] The peaks are also slightly broadened for 3DOm-i silicalite-1, indicating a relatively small primary particle size. In all synthesized materials, the

XRD data suggests that only MFI phase is present in the crystals and no crystalline impurity is observed.

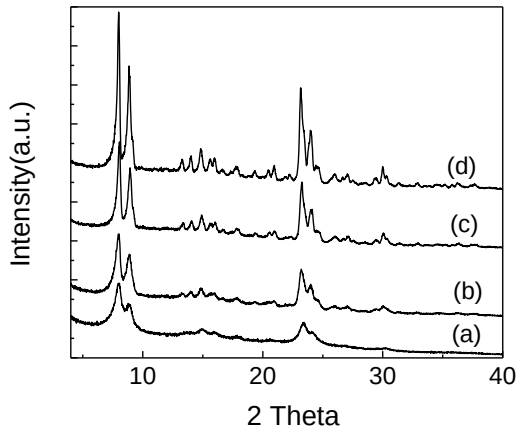

Figure 6-2: X-ray diffraction patterns of (a) SPP, (b) 3DOm-i, (c) 200 nm and (d) 20 μm silicalite-1.

SEM images of the synthesized silicalite-1 crystals are shown in Figure 3. Highly intergrown sheet-like crystals with a house-of-cards arrangement are directly observed in Figure 3a with a particle size of around 150 nm, which is consistent with literature.[10] Mesopores from adjacent perpendicular zeolite nano-sheets can be also observed. The 3DOm-i silicalite-1 shows a crystal size of 3-4 μm (see inset in Figure 3b) composed of orderly packed, well-defined primary particles in spherical shape with a diameter of about 35 nm. Ordered 3DOm mesoporous structure can be ascertained from the interstices between the orderly packed spherical primary particles, which can also be observed in the SEM images (Figure 3b). This highly ordered packing structure is further confirmed by low angle X-ray diffraction (Figure 12). 200 nm and 20 μm silicalite-1 crystals (Figure 3c and d, respectively) synthesized in this study are faceted and monodisperse with typical crystal morphology for large siliceous MFI, again consistent with the XRD data. In these two samples, no mesoporosity is observed within the particles.

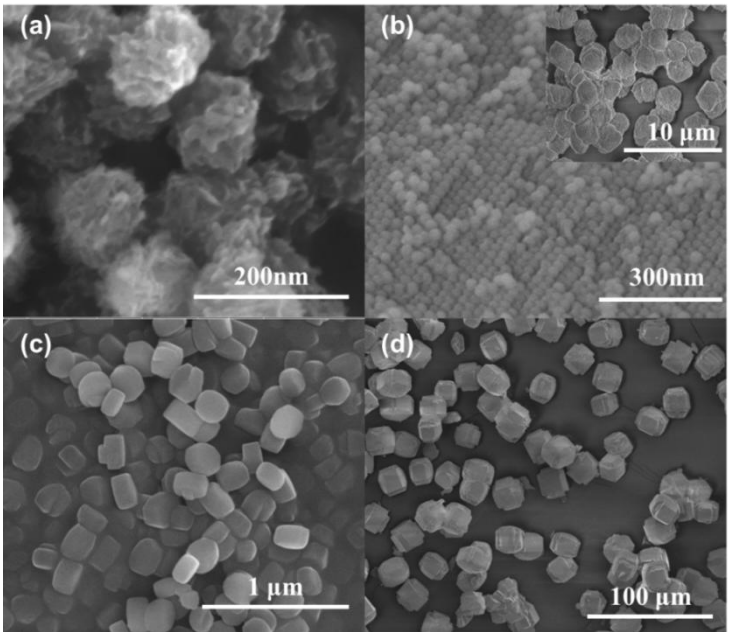

Figure 6-3: SEM images for (a) SPP, (b) 3DOm-i, (c) 200 nm, and (d) 20 μm silicalite-1 crystals.

Nitrogen adsorption/desorption isotherms of considered silicalite-1 crystals are shown in Figure 4a. The isotherm for SPP shows micropore uptake at low relative pressure ($P/P_0 < 0.1$), a gradual increase in gas adsorbed at moderate relative pressure corresponding to mesoporous structures, and a significant increase at high relative pressure ($P/P_0 > 0.9$), similar to the literature data.[10] For 3DOm-i silicalite-1, the microporous and macroporous uptakes are again observed at low and high relative pressures. At moderate relative pressures (0.6 to 0.8), the presence of a hysteresis loop indicates the existence of mesopores corresponding to the imprinted ordered mesoporous structure.[6] For 200 nm and 20 μm crystals, typical type I isotherms for microporous materials are obtained, except for a step at low P/P_0 (0.1~0.2) in 20 μm sample, which relates to disorder-order transition of nitrogen molecules on siliceous MFI (not to pore filling or condensation).[45]

The pore size distribution analysis for the SPP sample (Figure 4b) using the NLDFT adsorption model (see Figure 13 for fitting results) shows a broad distribution of mesopores in the range of 3 to 7 nm, consistent with the literature data.[10] Together with the XRD data and SEM images, it is concluded that self-pillared pentasil zeolite was successfully reproduced. For 3DOm-

i silicalite-1, the NLDFT analysis predicts a narrow mesopore size distribution, centered at ~8 nm, revealing a highly ordered mesoporous structure. The NLDFT model fits the experimental data well (see Figure 14 for fitting results), and the pore size distribution analysis data are consistent with the observations from electron microscopy showing highly ordered interstitial mesopores. Figure 4d shows the cumulative pore volume versus pore width for SPP and 3DOm-i silicalite-1. SPP samples possess more mesopore volume (0.6 cm^3) than 3DOm-i samples (~ 0.45 cm^3), while SPP crystals have some smaller mesopores. Adsorption data of silicalite-1 crystals are summarized in Table 1. Micropore volumes for each sample remain approximately constant, ranging between 0.11-0.13 cm^3/g. This consistency in microporosity further confirms that the MFI type crystal structure is well retained in the hierarchical zeolites. The external surface area (meso- and macropore surface area) calculated from α_s-plot[46] highlights the nanosheet nature of SPP crystal and the presence of mesoporosity in the 3DOm-i silicalite-1 crystals. The SPP illustrated a higher external surface area (305 m^2/g) than the 3DOm-i sample (184 m^2/g). The remaining two silicalite-1 (200 nm and 20 μm) samples presented lower external surface areas due to their larger particle sizes.

Mass transport behavior of cyclohexane within 20 μm silicalite-1 crystals was first studied to validate the ZLC system against literature for the cyclohexane/MFI system. Representative experimental ZLC response curves plotted in a form of $ln(C/C_0)$ versus time at different temperatures are shown in Figure 5a. Effective diffusivities obtained from ZLC measurements (a radius of 11.45 μm was used in the calculation) are shown in an Arrhenius plot together with literature data in Figure 5b. The results from Magalhães were obtained from both gravimetric method and ZLC technique using silicalite-1 crystals with dimensions of 8.9 × 9.4 × 39.0 μm.[28] The data from Cavalcante were also measured by these two methods, however with larger crystals (66 × 66 × 223 μm).[26] Gueudré's results were from gravimetric uptake experiments using similar crystals examined in this study (10.2 μm in radius).[35] In general, the

results obtained from 20 μm silicalite-1 crystals agree well with the literature data obtained from silicalite-1 with similar dimensions. From the Arrhenius plot, the activation energy (50.0 kJ/mol) of intracrytalline diffusion of cyclohexane in the channel of silicalite-1 agrees well with the value reported in literature.[26, 28, 35]

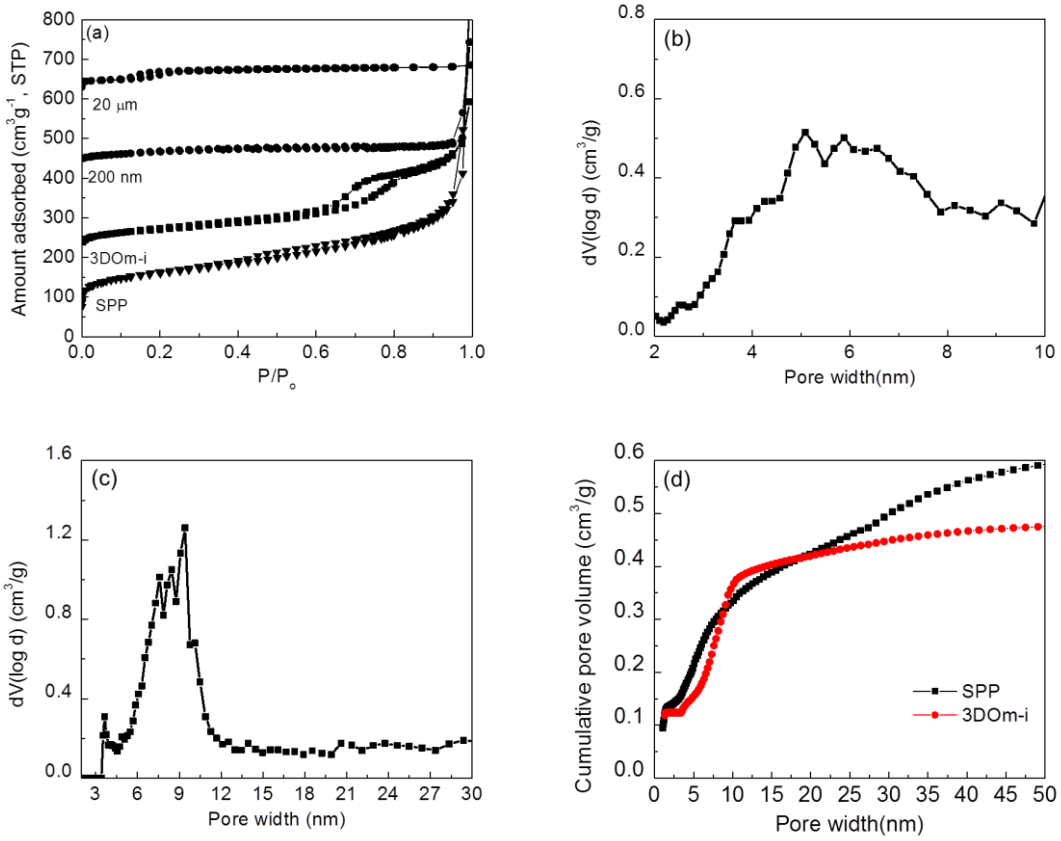

Figure 6-4: Adsorptive characterization of zeolite materials. (a) N_2 physisorption isotherms of studied zeolite crystals. Pore size distributions of (b) SPP and (c) 3DOm-i silcalite-1, and (d) cumulative pore volume were calculated from the NLDFT cylindrical pore adsorption model for SPP and 3DOm-i silicalite-1. Isotherms of 3DOm-i, 200 nm and 20 μm crystals were shifted 150, 350, 550 cm^3/g, respectively, for presentation purpose.

Table 6-1: Physical characteristics of considered zeolite crystals

Sample	Dimensions	SA_{BET}[a] (m^2/g)	SA_{Ext}[b] (m^2/g)	V_{mic}[b] (cm^3/g)
MFI 20 μm	11.45 μm in radius	373	53	0.132
MFI 200 nm	222 nm × 197 nm × 125 nm[c]	380	99	0.133
MFI 3DOm-i	17.5 nm in radius	430	186	0.118
SPP	2 nm in b-direction[d]	537	305	0.110

[a]BET surface area calculated from relative pressure between 0.05-0.25 (0.05-0.1 for 20 μm particle) of adsorption branch by using the Branauer-Emmett-Teller (BET) equation;
[b]External surface area and micropore volume calculated from the α_s-plot;
[c]equivalent radius: $(l*w*h)^{1/3}$= 176 nm
[d]Zhang et al.[10]

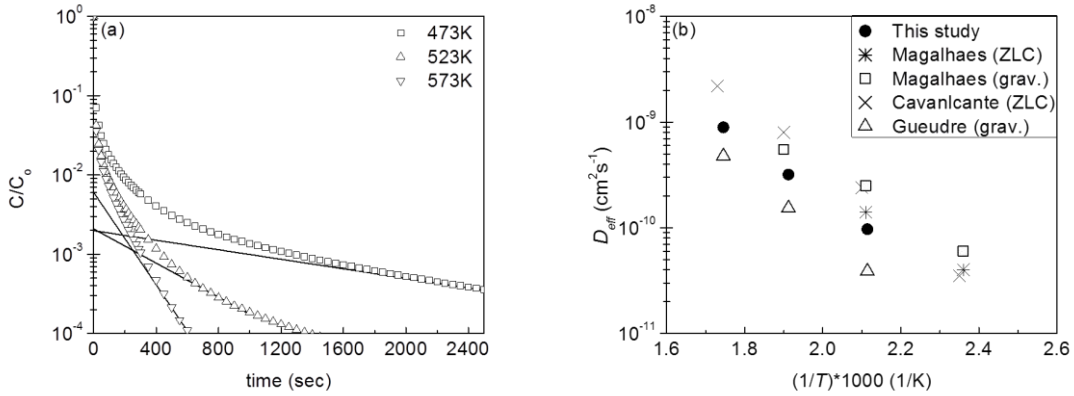

Figure 6-5: (a) ZLC desorption curves of cyclohexane in 20 μm silicalite-1. Symbols represent experimental data, and solid lines are the fitted curves. (b) Arrhenius plot of apparent diffusivity obtained from 20 μm silicalite-1. Literature data are shown for comparison.[26, 28, 35]

Figure 6 shows the experimental ZLC elution curves and fitted long-time analysis slopes (Eq. 5) for SPP, 3DOm-i, and 200 nm silicalite-1. All measurements for these particles were conducted at lower temperatures (323 - 363 K) to allow for adequate temporal resolution of the ZLC elution curves. Figure 6a-c reveal that data points at long time exhibit a clear linear region with slopes that trend with temperature. The parameters (D_{eff}/R^2 and L) extracted from fitting the long-time solution of the diffusion model for different crystals were summarized in the Appendix A (Table 6-2). The linear regions become steeper when temperature increases, indicating that the

diffusion rate of cyclohexane in the samples increases with temperature, as expected from the long-time approximation of the ZLC model. The effective diffusional time constant, R^2/D_{eff}, decreases with temperature as expected (Figure 7). Furthermore, the desorption curves of the three samples at the same testing temperature are plotted in Figure 6d, suggesting the desorption of cyclohexane is faster in SPP (2 nm nanosheets) and 3DOm-i (~ 35 nm primary particles) compared to nanocrystals with an equivalent radius of 176 nm as demonstrated by the steeper slopes at the long-time linear region. This data provides quantitative evidence that introduction of mesoporosity and sheet-like nanostructure indeed enhances mass transfer of cyclohexane in silicalite-1 crystals. At the same temperature (363 K), the effective time constant (R^2/D_{eff}) is two orders of magnitude lower for the mesoporous/nanocrystalline silicalite-1, compared with 20 μm crystals (via extrapolation by Arrhenius equation). The data clearly show that the introduction of mesoporosity and the formation of nanocrystals can effectively shorten the diffusion length, and mass transport of cyclohexane in silicalite-1 can be substantially improved.

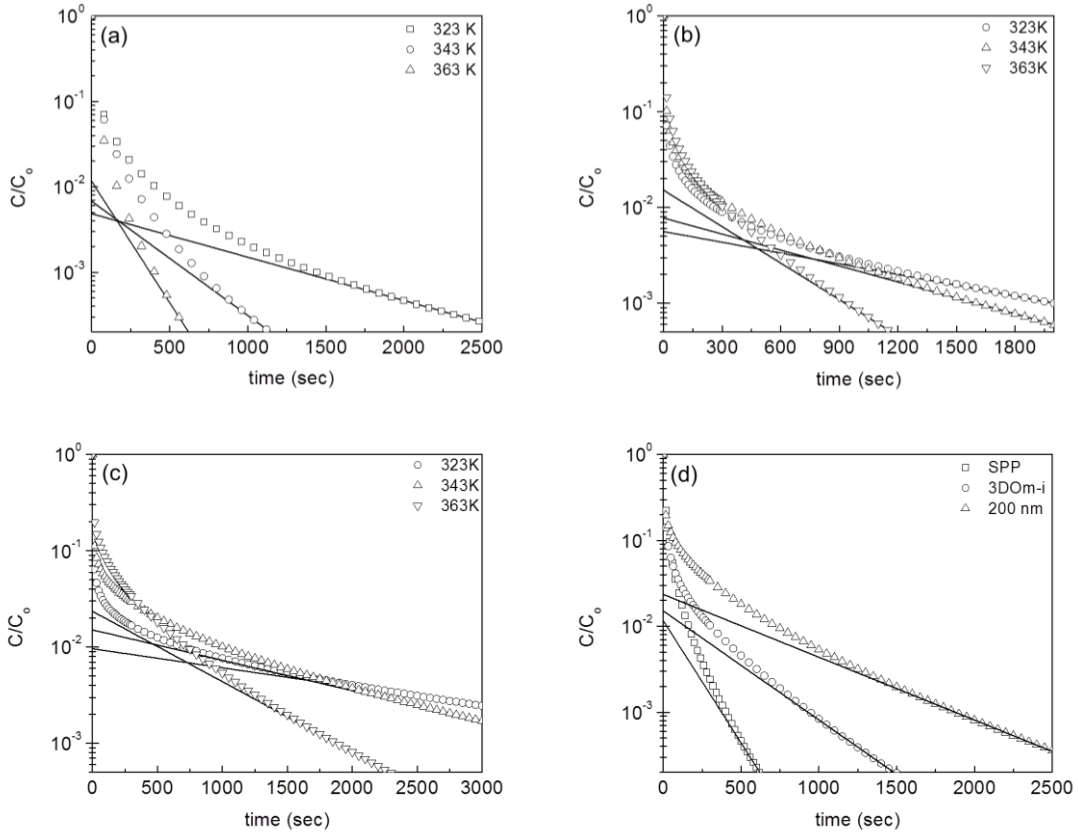

Figure 6-6: Experimental and fitted ZLC desorption curves for (a) SPP, (b) 3DOm-i and (c) 200 nm silicalite-1 at different temperatures. Comparisons of ZLC desorption curves from different silicalite-1 crystals at 363 K (d). Symbols represent experiment points and lines are from long-time analysis fitting.

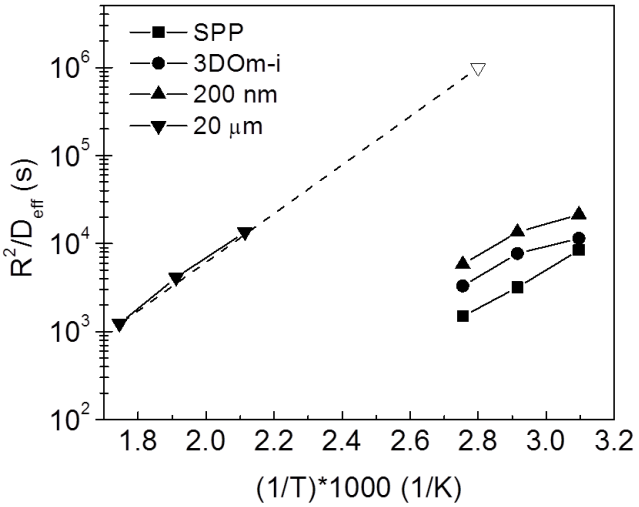

Figure 6-7: Summary of the effective diffusional time constants (R^2/D_{eff}) obtained from ZLC analysis for SPP, 3DOm-i, 200 nm and 20 m silicalite-1 crystals. Data for 20 μm crystal at 363K (1000/T = 2.75; open symbol) is determined from the extrapolation of the existing data collected at higher temperatures using an Arrhenius equation for comparison.

While the mesoporous structures are imposed on the materials studied here, Knudsen diffusion is the dominant transport process in the mesopores since the mean free path of cyclohexane is comparable to the width of the pores.[47] The Knudsen diffusivity (D_K) of a molecule can be estimated by[48]

$$D_K = \frac{d_p}{3} v \qquad 6\text{-}1$$

where d_p represents the pore width and v is the mean molecular velocity. According to kinetic theory, v can be written as,

$$v = \sqrt{\frac{8\mathcal{R}T}{\pi M}} \qquad 6\text{-}2$$

where R is the gas constant, T is the temperature, and M is the molecular weight of the molecule.

At 323 K, assuming the mesopore width is about 5 nm with molar mass of cyclohexane (84.16 g/mol), D_K is 4.8 x 10^{-3} cm^2/s. The time constant for diffusion within the hierarchical zeolite particles (τ) can then be estimated by R^2/D_K, where R is the radius of the entire crystalline particle. The calculated τ is 1.18 x 10^{-8} s and 8.41 x 10^{-6} s for SPP (R = 75 nm) and 3DOm-i silicalite-1 (R = 2000 nm), respectively. Compared with the data in Figure 7 at the same temperature, it appears that the effective diffusional time constants (τ_{eff}) are in the order of 10^3-10^4 s for the mesoporous silialite-1 crystals, which are 10-12 orders of magnitude slower than the transport in the mesopore, as analyzed above. The analysis suggests that the diffusion process in the system is controlled by intracrystalline diffusion rather than transport in the mesopores, and the effective diffusivities obtained here are indicative of the properties of intracrystalline mass transport.

Using the primary particle size of 3DOm-i silicalite-1 and thickness of SPP crystal as the characteristic diffusional length scales (R), D_{eff} of cyclohexane in those samples can be calculated. Since the overall D_{eff} represents the intracrysatlline diffusivity of the material, the diffusivities obtained from hierarchical and bulk crystal with the same micropore structure should be identical.

However, it is demonstrated here that $D_{eff,\ 3DOm}$ is slower than $D_{eff,\ 200nm}$ (2.69 x 10^{-16} and 1.45 x 10^{-14} cm^2/s at 323K, respectively). Even larger discrepancy are observed between SPP crystal composed of intergrown 2 nm zeolitic lamellae (1.19 x 10^{-18} cm^2/s at 323K), being four orders of magnitude lower. This counter-intuitive mass transport behavior is remarkably pronounced in the overall diffusivity for the hierarchical zeolites, indicating additional mass transport limitations should be considered. In addition to the diffusional resistance by the intrinsic micropore network, mass transfer is suspected to be controlled by surface resistances, also called surface barriers.[16, 31, 35, 49-51] The possible origin of the surface barriers have been extensively discussed and probed by experimental and computational methods. Comparative studies with the zeolite/zeotype representatives, ferrierite,[52] silicalite-1/ZSM-5,[53, 54] STA-7[55] and the MOF representative crystals[56] have revealed that the enhanced surface barrier is likely generated by the partial blockage of surface pores and internal defects. Such a surface resistance can be much more prominent when the particle size of the samples is on the order of nanometers due to the high surface area to volume ratio for hierarchical zeolites. In particular, this might be true for SPP and 3DOm-i silicalite-1 due to the rather small primary particle size and nanosheets. The seemingly counter-intuitive result indicates that the molecular transport in the surface layer or close to the surface layer might be crucial for the mass transfer behavior of hierarchical zeolites, and assuming constant diffusivity for zeolite with different crystal sizes and morphologies may lead to significantly overstated mass transport capability. While the overall diffusional time constant is indeed improved by introducing hierarchical porous structures (Figure 7), it is limited by a second uncharacterized and mechanistically undefined mass transfer limitation.

6.4 Conclusions

In order to directly study the influence of mesoporosity in zeolite catalysts on intracrystalline diffusion, self-pillared pentasil (SPP), three dimensionally ordered mesoporous-imprinted (3DOm-i), 200 nm and 20 μm silicalite-1 were synthesized. Mass transfer behavior in those hierarchical zeolites with well-controlled mesoporosity was studied using the ZLC method with cyclohexane. It was shown that extremely thin zeolite lamellae and ordered interconnected mesoporosity in the zeolite crystals can enhance the molecular transport of cyclohexane by orders of magnitude, as observed with the lower diffusional time constants of SPP and 3DOm-i silicalite-1 compared to that in conventional silicalite-1. At the same time, diffusivity of cyclohexane effectively slows as particle size decreases attributed to a secondary surface resistance, which becomes rate limiting for hierarchical zeolites owing to their high external surface to volume ratio. These results suggest that hierarchical microporous zeolites exhibit superior transport capability relative to conventional crystalline particles, but the existence of a secondary surface limitation allows for further improvement by rational design of hierarchical zeolites.

6.5 Appendix A: Supporting Information

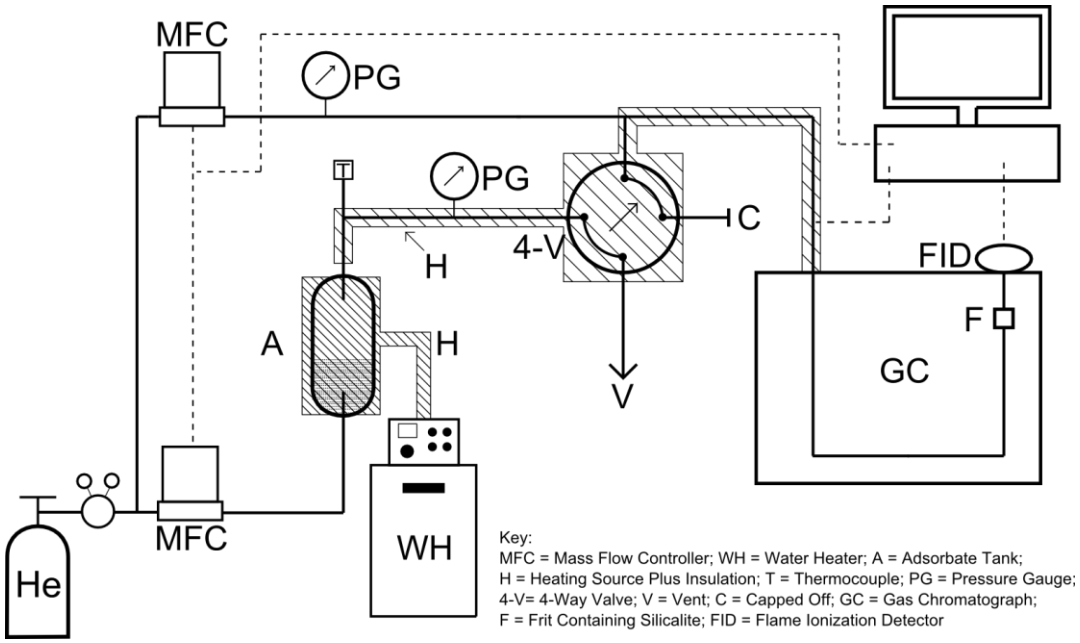

Figure 6-8: Illustrative schematic of the ZLC measurement system used in the study.

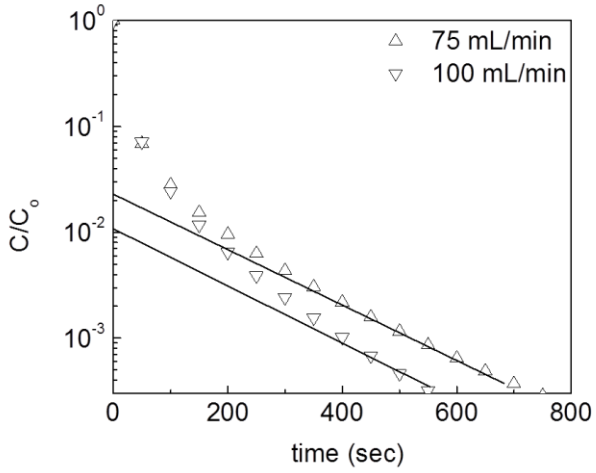

Figure 6-9: The ZLC elution curves from different flow rates at 363 K for SPP zeolite. It shows that, when flow rate is higher than 75 mL/min, the slope of the long time asymptote is almost constant, indicating that the system is kinetically controlled.

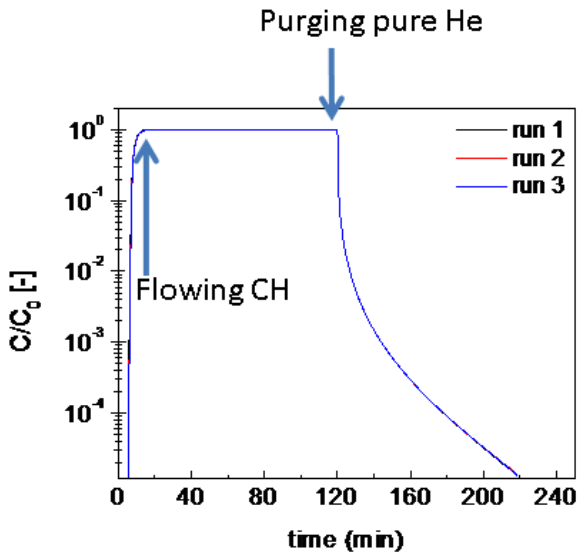

Figure 6-10: ZLC Elution curves of cyclohexane (CH) for SPP sample at 323 K under a helium purge flow rate of 100 mL/min. Three repeats are essentially identical, showing high stability of the system.

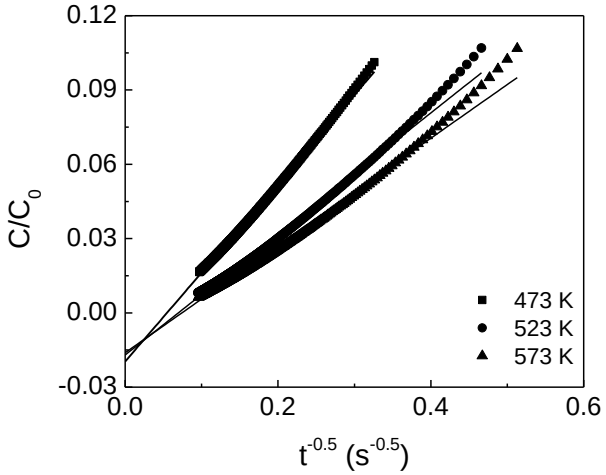

Figure 6-11: The C/C_0 vs. $1/t^{0.5}$ plot for 20 micron crystals at different temperatures. It is obvious that the fitting lines do not go thru origin, which indicates the system can be described by a spherical (three-dimensional) model.

Cavalcante et al. propose that, by using an intermediate time approximation method for ZLC experiment, the diffusion path of the guest molecules can be determined.[31] From a spherical model (three-dimensional),

$$\frac{C}{C_0} = \frac{1}{L}\left[\sqrt{\frac{R^2}{\pi D t}} - 1\right] \qquad 1\text{-}3$$

From a slab model (one-dimensional),

$$\frac{C}{C_0} = \frac{1}{L}\sqrt{\frac{l^2}{\pi Dt}} \qquad 6\text{-}1$$

It is thus apparent that, when plotting reduce concentration with $t^{-0.5}$, the spherical model yields a negative intercept while in the slab model the line should pass origin. In the case of 20 micron crystal (Figure 11), it appears that the diffusion pathway of cyclohexane in silicailte-1 obeys the three-dimensional (spherical) model, as the micropore channel structure of MFI topology is also three-dimensionally connected.

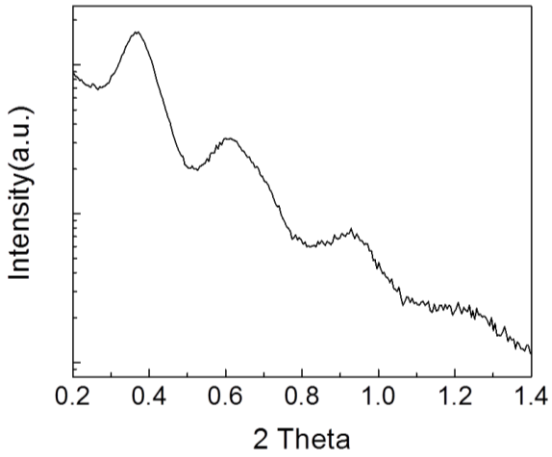

Figure 6-12: Small angle x-ray scattering pattern of 3DOm-i silicalite-1. The reflection peaks indicate the highly ordered mesoporous structure of the hierarchical crystal.

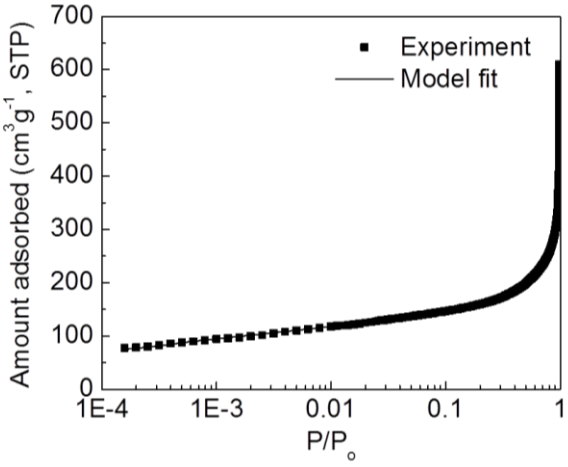

Figure 6-13: Comparison between the experimental N_2 adsorption curve and NLDFT model for SPP silicalite-1.

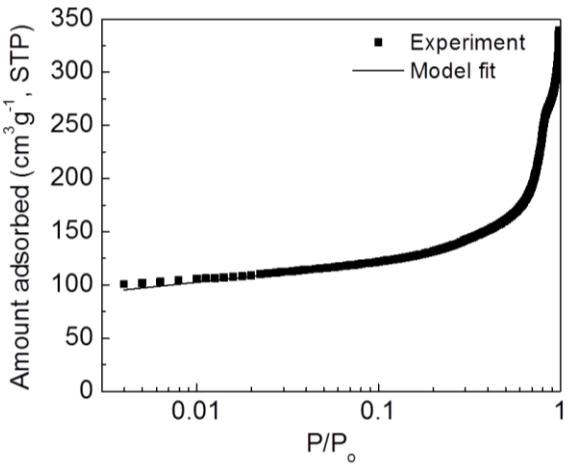

Figure 6-14: Comparison between the experimental N_2 adsorption curve and NLDFT model for 3DOm-i silicalite-1.

Table 6-2: Parameters (Deff/R2 and L) extracted from ZLC elution curves of SPP, 3DOm-i and 200nm silicalite-1

	SPP		3DOm-i		200nm	
Temperature (K)	D_{eff}/R^2	L	D_{eff}/R^2	L	D_{eff}/R^2	L
323	1.19×10^{-4}	408	8.77×10^{-5}	365	4.69×10^{-5}	204
343	3.14×10^{-4}	300	1.30×10^{-4}	220	7.43×10^{-5}	135
363	6.71×10^{-4}	173	3.03×10^{-4}	130	1.72×10^{-4}	89

6.6 References

1. K. Na, M. Choi, R. Ryoo, Recent Advances in the Synthesis of Hierarchically Nanoporous Zeolites. *Microporous Mesoporous Mater.* **166**, 3-19 (2013)http://dx.doi.org/10.1016/j.micromeso.2012.03.054).
2. F. C. Meunier, D. Verboekend, J.-P. Gilson, J. C. Groen, J. Pérez-Ramírez, Influence of Crystal Size and Probe Molecule on Diffusion in Hierarchical ZSM-5 Zeolites Prepared by Desilication. *Microporous Mesoporous Mater.* **148**, 115-121 (2012)10.1016/j.micromeso.2011.08.002).
3. J. Perez-Ramirez, C. H. Christensen, K. Egeblad, J. C. Groen, Hierarchical Zeolites: Enhanced Utilisation of Microporous Crystals in Catalysis by Advances in Materials Design. *Chem. Soc. Rev.* **37**, 2530-2542 (2008)10.1039/b809030k).
4. K. Na, C. Jo, J. Kim, K. Cho, J. Jung, Y. Seo, R. J. Messinger, B. F. Chmelka, R. Ryoo, Directing Zeolite Structures into Hierarchically Nanoporous Architectures. *Science* **333**, 328-332 (2011); published online EpubJul (10.1126/science.1204452).
5. H. Y. Chen, J. Wydra, X. Y. Zhang, P. S. Lee, Z. P. Wang, W. Fan, M. Tsapatsis, Hydrothermal Synthesis of Zeolites with Three-Dimensionally Ordered Mesoporous-Imprinted Structure. *J. Am. Chem. Soc.* **133**, 12390-12393 (2011); published online EpubAug (10.1021/ja2046815).
6. W. Fan, M. A. Snyder, S. Kumar, P. S. Lee, W. C. Yoo, A. V. McCormick, R. L. Penn, A. Stein, M. Tsapatsis, Hierarchical Nanofabrication of Microporous Crystals with Ordered Mesoporosity. *Nat. Mater.* **7**, 984-991 (2008); published online EpubDec (10.1038/nmat2302).
7. S. Lopez-Orozco, A. Inayat, A. Schwab, T. Selvam, W. Schwieger, Zeolitic Materials with Hierarchical Porous Structures. *Adv. Mater.* **23**, 2602-2615 (2011)10.1002/adma.201100462).
8. M. Choi, K. Na, J. Kim, Y. Sakamoto, O. Terasaki, R. Ryoo, Stable single-unit-cell nanosheets of zeolite MFI as active and long-lived catalysts. *Nature* **461**, 246-249 (2009)http://www.nature.com/nature/journal/v461/n7261/suppinfo/nature08288_S1.html) .
9. J. Čejka, G. Centi, J. Perez-Pariente, W. J. Roth, Zeolite-Based Materials for Novel Catalytic Applications: Opportunities, Perspectives and Open Problems. *Catal. Today* **179**, 2-15 (2012)10.1016/j.cattod.2011.10.006).
10. X. Zhang, D. Liu, D. Xu, S. Asahina, K. A. Cychosz, K. V. Agrawal, W. Y. Al, A. Bhan, H. S. Al, O. Terasaki, M. Thommes, M. Tsapatsis, Synthesis of Self-Pillared Zeolite Nanosheets by Repetitive Branching. *Science* **336**, 1684-1687 (2012)10.1126/science.1221111).
11. M. S. Holm, E. Taarning, K. Egeblad, C. H. Christensen, Catalysis with Hierarchical Zeolites. *Catal. Today* **168**, 3-16 (2011)10.1016/j.cattod.2011.01.007).
12. P. Kortunov, S. Vasenkov, J. Kärger, R. Valiullin, P. Gottschalk, M. Fé Elía, M. Perez, M. Stöcker, B. Drescher, G. McElhiney, C. Berger, R. Gläser, J. Weitkamp, The Role of Mesopores in Intracrystalline Transport in USY Zeolite: PFG NMR Diffusion Study on Various Length Scales. *Journal of the American Chemical Society* **127**, 13055-13059 (2005); published online Epub2005/09/01 (10.1021/ja053134r).
13. C. H. Christensen, K. Johannsen, E. Törnqvist, I. Schmidt, H. Topsøe, C. H. Christensen, Mesoporous Zeolite Single Crystal Catalysts: Diffusion and Catalysis in Hierarchical Zeolites. *Catal. Today* **128**, 117-122 (2007)http://dx.doi.org/10.1016/j.cattod.2007.06.082).
14. J. C. Groen, W. Zhu, S. Brouwer, S. J. Huynink, F. Kapteijn, J. A. Moulijn, J. Pérez-Ramírez, Direct Demonstration of Enhanced Diffusion in Mesoporous ZSM-5 Zeolite

Obtained via Controlled Desilication. *J. Am. Chem. Soc.* **129**, 355-360 (2007); published online Epub2007/01/01 (10.1021/ja065737o).

15. K. Cho, H. S. Cho, L.-C. de Ménorval, R. Ryoo, Generation of Mesoporosity in LTA Zeolites by Organosilane Surfactant for Rapid Molecular Transport in Catalytic Application. *Chem. Mater.* **21**, 5664-5673 (2009); published online Epub2009/12/08 (10.1021/cm902861y).
16. Y. Liu, W. Zhang, Z. Liu, S. Xu, Y. Wang, Z. Xie, X. Han, X. Bao, Direct Observation of the Mesopores in ZSM-5 Zeolites with Hierarchical Porous Structures by Laser-Hyperpolarized 129Xe NMR. *J. Phys. Chem. C* **112**, 15375-15381 (2008); published online Epub2008/10/02 (10.1021/jp802813x).
17. R. Valiullin, J. Kaerger, K. Cho, M. Choi, R. Ryoo, Dynamics of Water Diffusion in Mesoporous Zeolites. *Microporous Mesoporous Mater.* **142**, 236-244 (2011); published online EpubJun (10.1016/j.micromeso.2010.12.005).
18. D. Mehlhorn, R. Valiullin, J. Kärger, K. Cho, R. Ryoo, Intracrystalline Diffusion in Mesoporous Zeolites. *ChemPhysChem* **13**, 1495-1499 (2012)10.1002/cphc.201200048).
19. A. Malekian, H. Vinh-Thang, Q. Huang, M. Eić, S. Kaliaguine, Evaluation of the Main Diffusion Path in Novel Micro-Mesoporous Zeolitic Materials with the Zero Length Column Method. *Industrial & Engineering Chemistry Research* **46**, 5067-5073 (2007); published online Epub2007/07/01 (10.1021/ie061497+).
20. D. Mehlhorn, R. Valiullin, J. Kärger, K. Cho, R. Ryoo, Exploring the Hierarchy of Transport Phenomena in Hierarchical Pore Systems by NMR Diffusion Measurement. *Microporous Mesoporous Mater.* **164**, 273-279 (2012)http://dx.doi.org/10.1016/j.micromeso.2012.06.049).
21. M. Eić, D. M. Ruthven, A New Experimental-Technique for Measurement of Intracrystalline Diffusivity. *Zeolites* **8**, 40-45 (1988); published online EpubJan (10.1016/s0144-2449(88)80028-9).
22. S. Brandani, D. M. Ruthven, Analysis of ZLC Desorption Curves for Gaseous Systems. *Adsorption* **2**, 133-143 (1996); published online Epub1996 (10.1007/bf00127043).
23. S. Brandani, D. M. Ruthven, Analysis of ZLC Desorption Curves for Liquid Systems. *Chem. Eng. Sci.* **50**, 2055-2059 (1995); published online EpubJul (10.1016/0009-2509(95)00048-a).
24. J. R. Hufton, D. M. Ruthven, Diffusion of Light Alkanes in Silicalite Studied by The Zero Length Column Method. *Ind. Eng. Chem. Res.* **32**, 2379-2386 (1993); published online Epub1993/10/01 (10.1021/ie00022a022).
25. D. M. Ruthven, P. Stapleton, Measurement of Liquid Phase Counter-Diffusion in Zeolite Crystals by the ZLC Method. *Chem. Eng. Sci.* **48**, 89-98 (1993); published online EpubJan (10.1016/0009-2509(93)80285-x).
26. C. L. Cavalcante, D. M. Ruthven, Adsorption of Branched and Cyclic Paraffins in Silicalite. 2. Kinetics. *Ind. Eng. Chem. Res.* **34**, 185-191 (1995); published online EpubJan (10.1021/ie00040a018).
27. S. Brandani, Z. Xu, D. Ruthven, Transport Diffusion and Self-Diffusion of Benzene in NaX and CaX Zeolite Crystals Studied by ZLC and Tracer ZLC Methods. *Microporous Mater.* **7**, 323-331 (1996); published online EpubDec (10.1016/s0927-6513(96)00010-7).
28. F. D. Magalhães, R. L. Laurence, W. C. Conner, Diffusion of Cyclohexane and Alkylcyclohexanes in Silicalite. *J. Phys. Chem. B* **102**, 2317-2324 (1998); published online EpubMar 26 (10.1021/jp972036s).
29. V.-T. Hoang, Q. Huang, M. Eić, T.-O. Do, S. Kaliaguine, Structure and Diffusion Characterization of SBA-15 Materials. *Langmuir* **21**, 2051-2057 (2005); published online Epub2005/03/01 (10.1021/la048349d).

30. O. C. Gobin, Q. Huang, H. Vinh-Thang, F. Kleitz, M. Eić, S. Kaliaguine, Mesostructured Silica SBA-16 with Tailored Intrawall Porosity Part 2: Diffusion. *J. Phys. Chem. C* **111**, 3059-3065 (2007); published online EpubFeb 22 (10.1021/jp063583t).
31. C. L. Cavalcante, S. Brandani, D. M. Ruthven, Evaluation of The Main Diffusion Path in Zeolites from ZLC Desorption Curves. *Zeolites* **18**, 282-285 (1997); published online EpubApr (10.1016/s0144-2449(97)00014-6).
32. Q. Huang, M. Eić, H. Xiao, S. Kaliaguine, Characterization of the diffusion path in micro- and meso-porous materials from ZLC analysis. *Adsorption* **16**, 531-539 (2010)10.1007/s10450-010-9258-6).
33. H. S. Cho, R. Ryoo, Synthesis of Ordered Mesoporous MFI Zeolite Using CMK Carbon Templates. *Microporous Mesoporous Mater.* **151**, 107-112 (2012)http://dx.doi.org/10.1016/j.micromeso.2011.11.007).
34. R. Watanabe, T. Yokoi, T. Tatsumi, Synthesis and Application of Colloidal Nanocrystals of the MFI-Type Zeolites. *J. Colloid Interface Sci.* **356**, 434-441 (2011); published online EpubApr (10.1016/j.jcis.2011.01.043).
35. L. Gueudré, E. Jolimaite, N. Bats, W. Dong, Diffusion in Zeolites: Is Surface Resistance a Critical Parameter? *Adsorption* **16**, 17-27 (2010); published online EpubJun (10.1007/s10450-010-9213-6).
36. A. V. Neimark, P. I. Ravikovitch, Capillary Condensation in MMS and Pore Structure Characterization. *Microporous Mesoporous Mater.* **44–45**, 697-707 (2001)http://dx.doi.org/10.1016/S1387-1811(01)00251-7).
37. P. I. Ravikovitch, A. V. Neimark, Density Functional Theory of Adsorption in Spherical Cavities and Pore Size Characterization of Templated Nanoporous Silicas with Cubic and Three-Dimensional Hexagonal Structures. *Langmuir* **18**, 1550-1560 (2002); published online Epub2002/03/01 (10.1021/la0107594).
38. M. Thommes, B. Smarsly, M. Groenewolt, P. I. Ravikovitch, A. V. Neimark, Adsorption Hysteresis of Nitrogen and Argon in Pore Networks and Characterization of Novel Micro- and Mesoporous Silicas. *Langmuir* **22**, 756-764 (2006); published online Epub2006/01/01 (10.1021/la051686h).
39. H. S. Cho, K. Miyasaka, H. Kim, Y. Kubota, M. Takata, S. Kitagawa, R. Ryoo, O. Terasaki, Study of Argon Gas Adsorption in Ordered Mesoporous MFI Zeolite Framework. *J. Phys. Chem. C* **116**, 25300-25308 (2012); published online Epub2012/12/06 (10.1021/jp306268d).
40. D. P. Serrano, J. Aguado, G. Morales, J. M. Rodríguez, A. Peral, M. Thommes, J. D. Epping, B. F. Chmelka, Molecular and Meso- and Macroscopic Properties of Hierarchical Nanocrystalline ZSM-5 Zeolite Prepared by Seed Silanization. *Chem. Mater.* **21**, 641-654 (2009); published online Epub2009/02/24 (10.1021/cm801951a).
41. F. Brandani, University of Maine, (2002).
42. S. Brandani, M. A. Jama, D. M. Ruthven, ZLC Measurements under non-linear conditions. *Chemical Engineering Science* **55**, 1205-1212 (2000)http://dx.doi.org/10.1016/S0009-2509(99)00411-X).
43. S. Brandani, Effects of Nonlinear Equilibrium on Zero Length Column Experiments. *Chem. Eng. Sci.* **53**, 2791-2798 (1998)10.1016/s0009-2509(98)00075-x).
44. C. L. Cavalcante, D. M. Ruthven, Adsorption of Branched and Cyclic Paraffins in Silicalite. 1. Equilibrium. *Ind. Eng. Chem. Res.* **34**, 177-184 (1995); published online EpubJan (10.1021/ie00040a017).
45. P. L. Llewellyn, J. P. Coulomb, Y. Grillet, J. Patarin, G. Andre, J. Rouquerol, Adsorption by MFI-Type Zeolites Examined by Isothermal Microcalorimetry and Neutron Diffraction. 2. Nitrogen and Carbon Monoxide. *Langmuir* **9**, 1852-1856 (1993); published online Epub1993/07/01 (10.1021/la00031a037).

46. M. Jaroniec, M. Kruk, J. P. Olivier, Standard Nitrogen Adsorption Data for Characterization of Nanoporous Silicas. *Langmuir* **15**, 5410-5413 (1999); published online EpubAug (10.1021/la990136e).
47. W. M. Deen, *Analysis of Transport Phenomena*. K. E. Gubbins, Ed., Topics in Chemical Engineering (Oxford University Press, Incorporated, New York, 1998).
48. D. M. Ruthven, W. J. DeSisto, S. Higgins, Diffusion in a mesoporous silica membrane: Validity of the Knudsen diffusion model. *Chemical Engineering Science* **64**, 3201-3203 (2009)10.1016/j.ces.2009.03.049).
49. P. Kortunov, S. Vasenkov, C. Chmelik, J. Kärger, D. M. Ruthven, J. Wloch, Influence of Defects on the External Crystal Surface on Molecular Uptake into MFI-Type Zeolites. *Chemistry of Materials* **16**, 3552-3558 (2004); published online Epub2004/09/01 (10.1021/cm0401645).
50. L. Heinke, P. Kortunov, D. Tzoulaki, J. Kärger, The Options of Interference Microscopy to Explore the Significance of Intracrystalline Diffusion and Surface Permeation for Overall Mass Transfer on Nanoporous Materials. *Adsorption* **13**, 215-223 (2007); published online Epub2007/08/01 (10.1007/s10450-007-9048-y).
51. D. M. Ruthven, L. Heinke, J. Kärger, Sorption Kinetics for Surface Resistance Controlled Systems. *Microporous Mesoporous Mater.* **132**, 94-102 (2010)http://dx.doi.org/10.1016/j.micromeso.2010.02.003).
52. J. Kärger, P. Kortunov, S. Vasenkov, L. Heinke, D. B. Shah, R. A. Rakoczy, Y. Traa, J. Weitkamp, Unprecedented Insight into Diffusion by Monitoring the Concentration of Guest Molecules in Nanoporous Host Materials. *Angew. Chem. Int. Edit.* **45**, 7846-7849 (2006)10.1002/anie.200602892).
53. D. Tzoulaki, L. Heinke, W. Schmidt, U. Wilczok, J. Kärger, Exploring Crystal Morphology of Nanoporous Hosts from Time-Dependent Guest Profiles. *Angew. Chem. Int. Edit.* **47**, 3954-3957 (2008)10.1002/anie.200705597).
54. D. Tzoulaki, W. Schmidt, U. Wilczok, J. Kärger, Formation of surface barriers on silicalite-1 crystal fragments by residual water vapour as probed with isobutane by interference microscopy. *Microporous and Mesoporous Materials* **110**, 72-76 (2008)10.1016/j.micromeso.2007.08.041).
55. D. Tzoulaki, L. Heinke, M. Castro, P. Cubillas, M. W. Anderson, W. Zhou, P. A. Wright, J. Kärger, Assessing Molecular Transport Properties of Nanoporous Materials by Interference Microscopy: Remarkable Effects of Composition and Microstructure on Diffusion in the Silicoaluminophosphate Zeotype STA-7. *J. Am. Chem. Soc.* **132**, 11665-11670 (2010); published online Epub2010/08/25 (10.1021/ja104016n).
56. P. V. Kortunov, L. Heinke, M. Arnold, Y. Nedellec, D. J. Jones, J. Caro, J. Kärger, Intracrystalline Diffusivities and Surface Permeabilities Deduced from Transient Concentration Profiles: Methanol in MOF Manganese Formate. *J. Am. Chem. Soc.* **129**, 8041-8047 (2007); published online Epub2007/06/01 (10.1021/ja071265h).

CHAPTER 7

DOMINANCE OF SUFACE BARRIERS IN MOLECULAR TRANSPORT THROUGH SILICALITE-1

7.1 Introduction

It is proposed that discrepancies in apparent diffusivity result from the variation of length scales between the techniques, with the microscopic methods often measuring over just a few lattice cells.[5,18] Evidence for variation across measurement length scales has led to the idea of hindered transport in smaller particles by introducing a second transport limitation resulting from internal crystal grain boundaries, surface pore restrictions, or total pore blockages. The origins of these ideas are examined further in the discussion section of this manuscript.

In this work, we aim to characterize the potential second transport limitation within zeolites by carefully controlling diffusional length scales and measuring the temperature-activated apparent diffusion coefficients. For the first time, a complete set of silicalite-1 particles are synthesized with characteristic length scales varying across three orders of magnitude and apparent diffusivity is characterized for each particle. This comprehensive approach allows for experimental assessment of various theories presented in literature regarding the origin of surface barriers, including surface desorption, pore restriction, and pore blockage.

7.2 Materials and Methods

Seven samples of silicalite-1 were synthesized, as summarized in Table 1. Three-dimensionally ordered mesoporous-imprinted (3DOm-i) silicalite-1 with a primary particle size of 35 nm was synthesized according to Fan *et al.*.[7] In short, 3DOm carbon replica was first synthesized from 35 nm silica nanoparticles, and mesoporous silicalite-1 was synthesized and confined in the voids of the carbon template by using steam-assisted crystallization (SAC).

Structure directing agent (SDA) solution was generated by mixing 3.5 μL of 10 M sodium hydroxide (NaOH, 98%, Aldrich) solution, 1.07 g of tetrapropylammonium hydroxide solution (TPAOH, 40 %, Alfa Aesar), 1.25 mL of ethanol (200 proof, Fisher) and deionized water. In a glass vial, 0.3 mL of the SDA solution was introduced into 0.1 g of carbon to match the pore volume in the carbon material. The mixture was left in a fume hood until full evaporation of ethanol was achieved. To the carbon-SDA mixture, 0.15 mL of tetraethylorthosilicate (TEOS, 98%, Alfa Aesar) was added. The glass vial containing carbon mixture was sealed in a Teflon-lined stainless steel autoclave with three grams of DI water in the vessel without direct contact with the solid mixture. After three hours aging at room temperature, the bomb was put into a preheated 408 K convection oven for two days. The carbon/silicalite-1 composite was washed by filtration and dried in a 373 K oven overnight.

Table 7-1: Silicalite-1 particle size characterization

Nominal Crystal Size	**Length[i] (nm)**	**Width[i] (nm)**	**Height[i] (nm)**	**R[ii] (nm)**	**Error[iii] (nm)**
3 μm	7,680	4,120	1,550	1,800	79
1 μm	1110	730	337	324	16.7
500 nm	659	590	256	231	8.1
300 nm	328	324	188	136	3.07
200 nm	222	197	125	88	3.21
80 nm	118	83.3	61.5	42.3	1.84
3DOm-i	-	-	-	17.5*	-

[i] Measured average from SEM, [ii] $R = (l*w*h)^{1/3}$,
[iii] 95% confidence interval, * Determined from template

Silicalite-1 of different particle sizes ranging from 80 nm to 1 μm were synthesized based on published work.[6] Firstly, TPAOH solution, TEOS and water were mixed in a Teflon vessel and aged at 353 K for one day while stirring. The composition of the gel was SiO_2: 0.25 TPAOH: x H_2O, where x= 11, 38, 60, 100, 400, which corresponds to nominal size of 80 nm, 200 nm, 300 nm, 500 nm, and 1 μm, respectively. The resulting gel was charged into a Teflon-lined stainless

steel autoclave and heated at 443 K for one day. The product was washed by centrifugation until the pH of the supernatant was below nine. The 3 μm silicalite-1 sample was made according to Agger et al.[30] TEOS was added into a solution of tetrapropylammonium bromide (TPABr, 98%, Adrich) and NaOH, and the mixture was allowed to age with stirring at room temperature for eight days. The composition of the gel was SiO_2: 0.1 TPABr: 0.05 Na_2O: 4 EtOH: 98 H_2O. The aged mother gel was then heated in a Teflon-lined stainless steel autoclave at 408 K for 50 hours. The product was washed with copious amount of DI water and dried in 373 K oven overnight. The carbon template for 3DOm-i silicalite-1 and organic structure directing agent occluded in the crystal framework were removed via calcination at 873 K for 24 hours with a ramping rate of 3 K/min.

Crystallinity and phase of the porous materials were characterized by powder x-ray diffraction on a diffractometer (X'Pert Pro, PANalytical) with Cu K_α radiation. The morphology and sizes of the crystals were studied by scanning electron microscopy (Magellan 400 (FEI) or 6320JXV (JOEL)). Samples were spread on carbon tape and coated with Pt prior to being investigated with scanning electron microscopy at an acceleration voltage of 3.0 kV with a stage bias of 500 V if applicable. Larger particles (>200 nm) exhibited 'plate' or 'coffin' geometries, while smaller particles were more spherical, as shown in Figure 1. N_2 adsorption-desorption characterization was carried out on an automated gas sorption analyzer (Autosorb iQ, Quantachrome) at 77 K after outgassing at 473 K under vacuum until the pressure-rise in the cell was less than 25 mTorr/min.

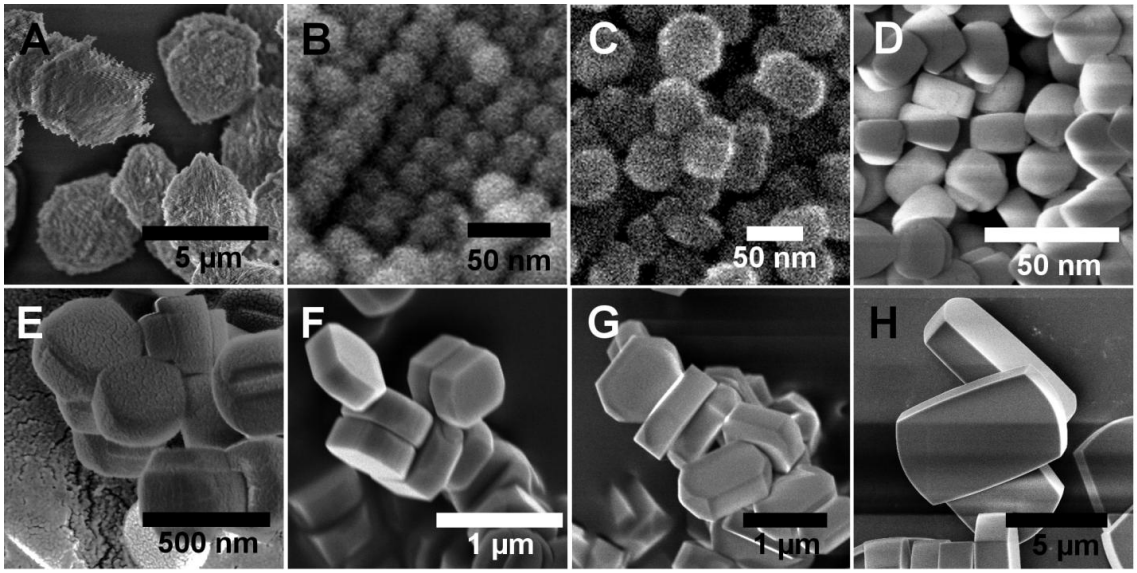

Figure 7-1: SEM images of silicalite-1 particles, as synthesized. Nominal sizes A. & B. 3DOm-i, C. 80 nm, D. 200 nm, E. 300 nm, F. 500 nm, G. 1 µm, H. 3 µm.

Figure 2A shows the XRD patterns for different sizes of silicalite-1 and 3DOm-i silicalite-1. All samples exhibit typical patterns for the MFI topology without indication of crystalline impurities. From the N_2 sorption isotherms (Figure 2B), typical type I isotherms for microporous materials are observed for all samples, with the exception of the 3DOm-i silicalite-1. Steep increase at high relative pressures for small silicalite-1 particles is due to the inter-particle voids and becomes less prominent in larger crystals. Mesoporosity shown for 3DOm-i silicalite-1 originated from the interstices of the ordered packing structure of 35 nm primary MFI spheres. Micropore volume analysis obtained from the *t*-plot method gives micorpore volumes of 0.10-0.13 cm^3/g for all samples, confirming the high quality of the crystals examined in this work.

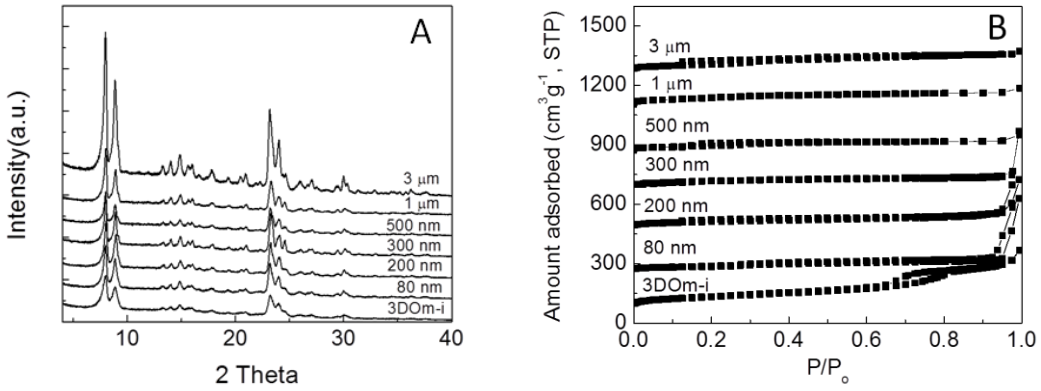

Figure 7-2: **Silicalite-1 Characterization A.** XRD patterns for different sizes of silicalite-1 and 3DOm-i silicalite-1 particles synthesized in this study. **B.** N_2 sorption isotherms for different sizes of silicalite-1 and 3DOm-i silicalite-1. The curves were shifted 200 cm^3/g in step. 3DOm-i silicalite-1 shows existence of mesopores while other isotherms reveal the typical microporous materials nature.

Experimental diffusion data was collected using the zero length chromatography (ZLC) technique developed by Eić and Ruthven[31] and extensively applied to measure diffusion in microporous materials.[32-42] The ZLC method has been developed for both one dimensional (slab) and three dimensional (spherical) pore network geometries.[43] As depicted in Figure 3, a saturated cyclohexane vapor stream (2.3 torr) flows over an isothermal monolayer of porous solid (~5-6 mg) held in place by two porous frits. The effluent is monitored online at 300 hz with a flame ionization detector. Uptake into the pores is provided more than sufficient time (usually about two hours) to reach adsorption equilibrium. A pneumatic valve is then toggled, switching the influent to a highly convective inert helium stream (50 ml/min), and desorption from the chamber is monitored for up to two hours. All flows were controlled with Brooks 5850E mass flow controllers, and temperatures were maintained at 10 °C in the bubbler and 50 °C in the transfer lines. Back pressure before the chamber and in the bubbler was maintained at 5 psi. A modified HP 5890 GC was used to maintain isothermal chamber conditions as well as for valve control and flame ionization detection. Cyclohexane (99.9%, Fisher # C556-4), Middlesex UHP He (99.999%), UHP H_2 (99.999%) and Ultra Zero Air (< 2 ppm H_2O) were used in all experiments. The vapor pressure of cyclohexane was maintained at 2.3 torr during uptake.

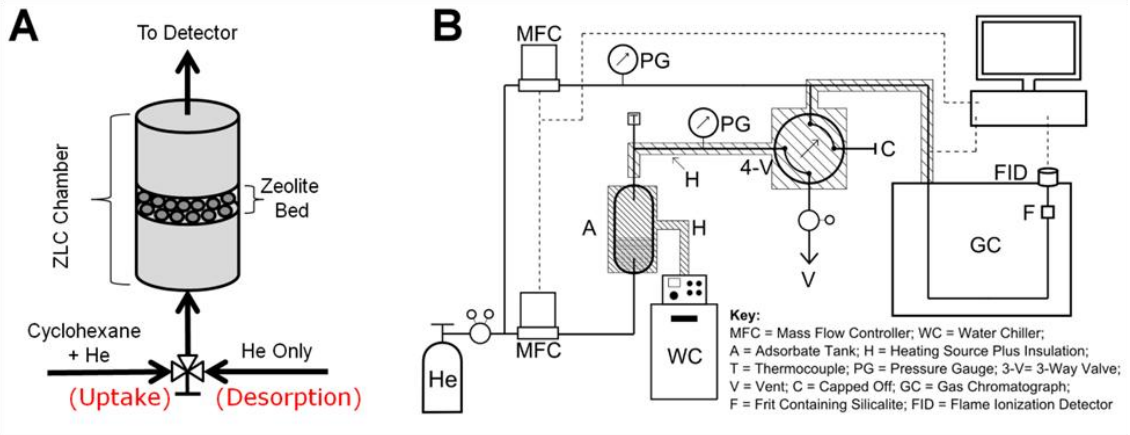

Figure 7-3: **A.** Overview of the ZLC method. A zeolite sample is packed into a ¼ inch isothermal chamber, and cyclohexane vapor is passed over it for two hours. A valve is switched and a pure helium stream flows over the material allowing the transient effluent to be monitored. **B.** Experimental schematic of ZLC set-up.

7.3 Zero Length Chromatography

ZLC was developed by Ruthven and Brandani and extensively used for measuring mass transport in microporous materials.[39] The widely used model, described here as the 'base model,' and several mechanistic models accounting for surface barriers are presented and summarized in Table 2. All models examined here assume 'spherical' geometries due to the three dimensionally interconnected pore network of MFI, as is assumed in literature for the silicalite-1 system[40] and confirmed in Appendix A by using the method of Cavalcante et al.[43]

7.3.1 Base Model

The base ZLC model assumes mass transport is controlled entirely by bulk diffusion. Starting with a one-dimensional, radial mass balance around a zeolite particle for a transient system, the boundary value problem can be summarized by,

Governing Equation:

$$\frac{dq}{dt} = D\nabla_r^2 q \qquad 7\text{-}1$$

Initial Condition:

$$q(r, t = 0) = q_0 = Kc_0 \quad (7\text{-}2)$$

Boundary Conditions:

$$\left.\frac{\partial q}{\partial r}\right|_{r=0} = 0 \quad (7\text{-}3)$$

$$-D\left.\frac{\partial q}{\partial r}\right|_{r=R} = \frac{FR}{3KV_s} q_R = \frac{FR}{3V_s} c \quad (7\text{-}4)$$

where q is the surface concentration, D is the intracrystalline diffusivity, and c is the gas phase concentration. At equilibrium, q is directly related to c by the proportionality constant, K (Henry's Constant). F is the flow rate of gas into the sample chamber with crystals of radius R and total adsorbent volume of V_s. The second boundary condition arises from balancing the fluxes at the surface between the bulk gas phase and the equilibrium surface concentration.

The solution to the transient, three dimensional (spherical) desorption profile in the diffusion controlled regime (L>10) has been solved analytically by Ruthven and Brandani,[39,44]

$$\frac{c}{c_0} = \sum \frac{2L}{\beta_n^2 + (1 - L + \gamma\beta_n^2)^2 + L - 1 + \gamma\beta_n^2} \exp\left(-\beta_n^2 \frac{D_{app}}{R^2} t\right) \quad (7\text{-}5)$$

where,

$$\beta_n \cot \beta_n + L - 1 - \gamma\beta_n^2 = 0 \quad (7\text{-}6)$$

and,

$$L = \frac{\tau_{Diff}}{\tau_{washout}} = \frac{1}{3}\frac{F}{KV_s}\frac{R^2}{D} \quad (7\text{-}7)$$

L represents the ratio of diffusional time through the bulk to the washout time in which the bulk gas accumulated in the cell and weakly physisorbed surface bound molecules deplete from the sample chamber. For gaseous systems, holdup in the sample chamber is often neglected, and gamma is taken as zero.

$$\gamma = \frac{1}{3}\frac{V_f}{KV_s} \cong 0 \quad (7\text{-}8)$$

A two-parameter least squares nonlinear fit is performed on the system of equations 5-7, minimizing the logarithmic error between the experimental desorption profile and equation 5 to determine D and L.

7.3.2 Surface Resistance Model

The base model can be expanded upon by accounting for physical phenomena at the surface. Several researchers have attempted to broadly describe the surface effect by introducing a surface mass transfer limitation that accounts for hindered transport across the surface of a zeolite.[32,36] In the ZLC model, this has been implemented by re-solving the second boundary condition by balancing internal flux $\left(J_{in} = -D\nabla_r q = -D\frac{\partial q}{\partial r}\Big|_R\right)$ with a resistive flux near the surface $\left(J_{surf} = k_s(q_R - q_{surf})\right)$. In this case, a surface barrier is assumed to arise from restricted diffusion through a thin layer just below the surface and is described by the mass transfer coefficient, k_s. Assuming equilibrium between the surface of the particle and the external bulk gases, the second boundary condition becomes,

$$-D\frac{\partial q}{\partial r}\Big|_R = k_s(q_R - q_{surf}) = \frac{FR}{3V_s}c = \frac{FR}{3KV_s}q_{surf} \qquad 1\text{-}9$$

The boundary value problem is then defined by equations (1)-(3), (9).

The solution is identical to equations (5) – (8) with the exception that the parameter L is redefined by,

$$L' = \frac{\tau_{diff}}{\tau_{washout} + \tau_{surf}} = \frac{R^2/3D}{KV_s/F + R/k_s} \qquad 7\text{-}1$$

where L' now represents the ratio of the diffusional time constant to the combined washout and first order mass transfer limitation time constant at the surface.

7.3.3 Kinetic Desorption Model

A more mechanistic model can be applied to the surface boundary by assuming that desorption from a surface site to the bulk becomes rate limiting and the surface is no longer in equilibrium with the bulk gas ('base' and 'surface resistance' models). In the situation where desorption on the outer surface of the particle is potentially rate limiting, the boundary condition can again be modified by performing a flux balance at the surface, equating internal diffusion flux $\left(J_{in} = -D\nabla_r q = -D\frac{\partial q}{\partial r}\Big|_R\right)$ to the first order desorption flux $\left(J_{des} = \frac{k_{des}R}{3}q_R\right)$, giving rise to the boundary condition,

$$-D\frac{\partial q}{\partial r}\Big|_R = \frac{k_{des}R}{3}q_R = \frac{FR}{3V_s}c \qquad 1\text{-}11$$

The boundary value problem is similarly defined by equations (1)-(3), (11).

The solution is identical to equations (5) – (8) with the exception that the parameter L is redefined by,

$$L'' = \frac{\tau_{diff}}{\tau_{des}} = \frac{R^2/3D}{1/k_{des}} \qquad 7\text{-}1$$

where L'' now represents the ratio of intracrystalline diffusion time to the desorption time constant.

7.3.4 Intracrystalline Verification

Intracrystalline transport was verified as rate limiting under experimental conditions by several quantitative and experimental measures. For brevity, the four criteria are outlined here and described in greater detail in Appendix A.

A. **Uptake Condition.** Sufficient time[41] for uptake of the adsorbate (cyclohexane) was provided to allow the crystal to fully equilibrate with the dilute gas stream.

B. **Macroscopic Measurability Condition.** To ensure that the concentration of the gas phase diffusing species was within detection limits, the minimum timescale for diffusion

was calculated to be sufficiently high to attain a measurable desorption profile. This was assessed for the diffusion rates of interest and for the maximum detector sampling frequency.

C. **Internal Transport Condition.** The use of ZLC requires that the rate controlling step is intracrystalline diffusion, not external mass transfer. In the cyclohexane/silicalite-1 system, for the range of temperatures analyzed, the condition is easily satisfied, ranging from $10^7 < \tau_{Diff}/\tau_{ext} < 10^9$, indicating that all considered experiments are limited by internal transport ($\tau_{Diff}/\tau_{ext} \gg 5$).

D. **Kinetic Transport Control.** If the residence time in the sample chamber is too high or the adsorbate is too strongly adsorbed to the surface, the system may be under equilibrium control. The kinetic transport control condition was assessed by calculating L'', which describes the ratio of diffusion time constant to desorption time. The condition was also confirmed experimentally by monitoring the parameter L (the measure of diffusion time to external transport), which ranged from $10 < L < 500$.

The experimental ZLC data obtained in this study were validated against all four criteria, and intracrystalline diffusion was shown to be rate limiting in the cyclohexane/silicalite-1 system at 2.3 torr saturation pressure and T = 50-250 °C for the considered particle sizes.

7.4 Results and Discussion

ZLC desorption curves for all considered particles and temperatures are presented along with model fits in Figure 4. In all cases, there was strong agreement between the two parameter model fit (D_{app} and L) and experimental desorption curves. L values for all conditions were always above 10, indicating internal particle transport limitations, and average diffusivity values of three runs per data point are reported in Figure 5.

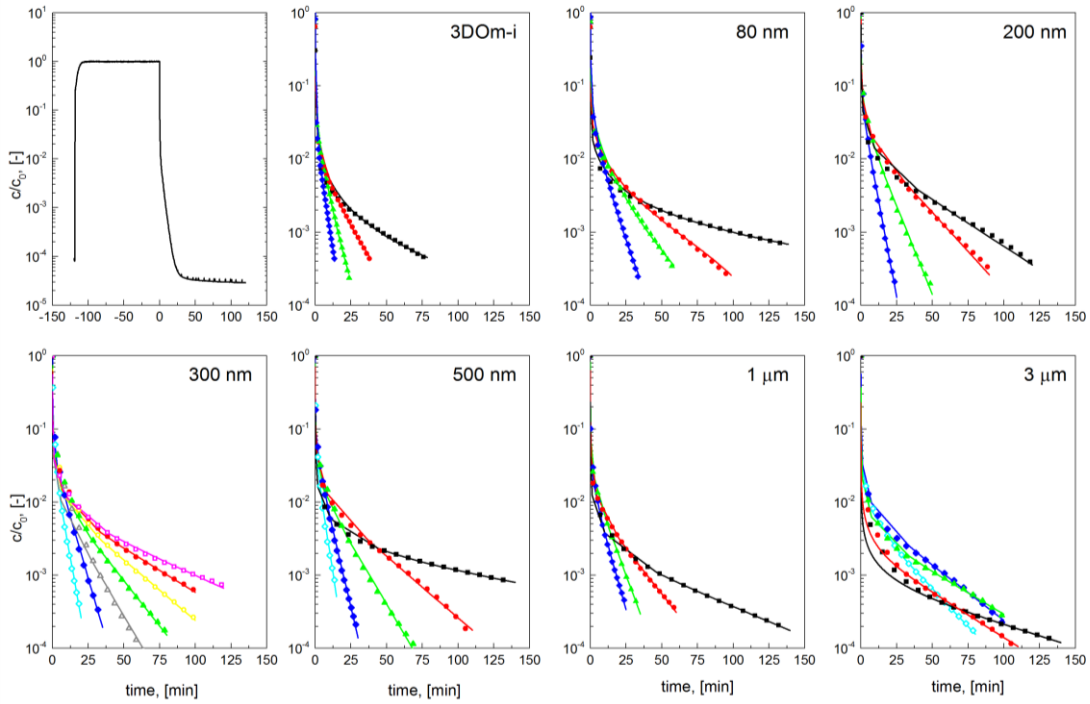

Figure 7-4: Cyclohexane/Silicalite-1 Desorption Profiles. Isothermal diffusion desorption curves (data points) and model fits (solid curves). T = 50 °C (■), 60°C (□), 70°C (●), 80°C (○), 90°C (▲), 100°C (△), 110°C (♦), 130°C (◊).

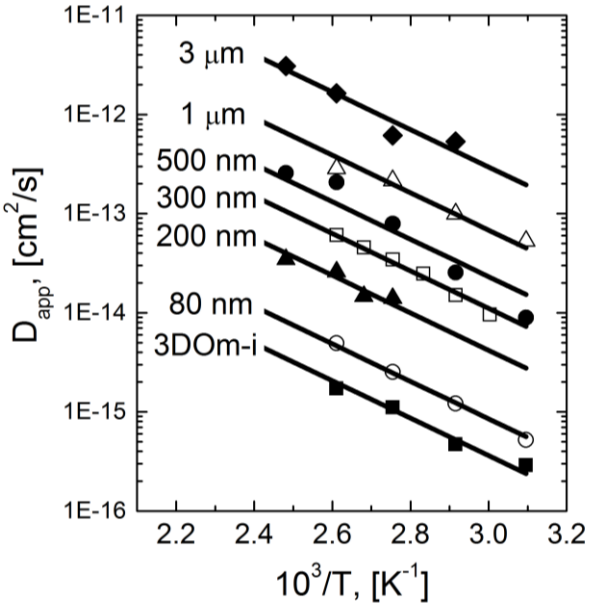

Figure 7-5: Cyclohexane/Silicalite-1 Arrhenius Plot. Experimentally observed diffusion coefficients conform to the Arrhenius relationship, exhibiting constant activation energy and significantly different pre-exponential factors. Nominal sizes: 3DOm-i (■), 80 nm (○), 200 nm (▲), 300 nm (□), 500 nm (●), 1 µm (Δ), 3 µm (♦).

The apparent diffusivity, D_{app}, represents the macroscopically observed diffusivity through the particle. It is calculated by dividing the square of the diffusional length scale, R, by the diffusional time constant from equation 5 ($\tau = R^2/D_{app}$). The diffusion coefficient is known to be temperature activated in accordance with the Arrhenius relationship,[16]

$$D = D_0 \exp\left(-\frac{E_a}{\mathcal{R}T}\right) \qquad 1\text{-}13$$

where the activation energy, E_a, is the energy required by a diffusing molecule to jump between lattice cages to perform the rate limiting transport step. Because all silicalite-1 particles exhibit identical porous structure, E_a should be constant for all silicalite-1 particle sizes.[16] This behavior is consistent with the systems studied here where the Arrhenius slopes are statistically equal for all the particles as presented in Figure 5. Solid lines represent constant activation energy fits, where the constant activation energy was taken to be the arithmetic mean of the seven samples (E_a= 38 ± 4 kJ/mol). This is in the range of literature values of the intracrystalline activation energy which utilizes several experimental techniques to obtain values of 56.6[24], 33.8[45], 26.4[46], 64.8[47], 50.6[48] and 53.5[49] kJ/mol.[24] In this work, no significant trend was observed between the apparent activation energy and particle size, indicating a common transport mechanism through all particle sizes that is not enthalpically different from transport within the bulk of the particle.

Values of the pre-exponential appear to asymptotically approach a constant value as particle size increases (Figure 6), corresponding to bulk diffusion coefficients for large particles in the range of those previously reported in literature.[40] As represented in Figure 10, diffusivity values for large particles (R= 1, 3 μm) in this study correspond well with those measured previously in literature (R=3, 7, 50 μm), which is believed to represent bulk intracrystalline diffusion.

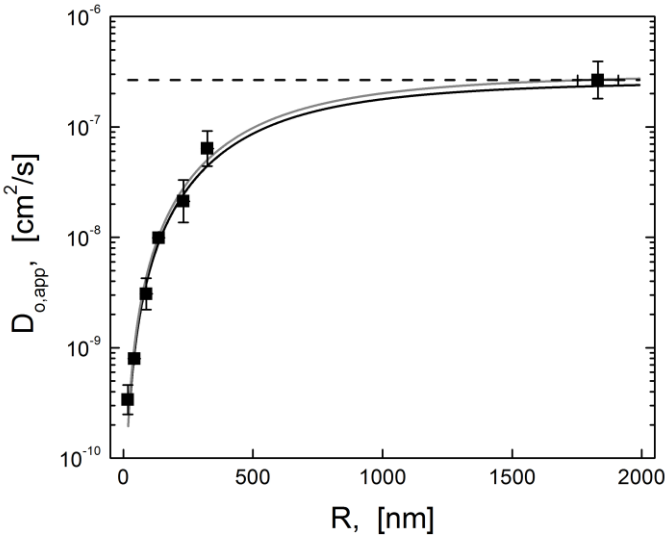

Figure 7-6: Apparent Diffusivity Pre-exponential and Model Fits. The pre-exponential to the apparent diffusivity, (■), is observed to decrease over orders of magnitude as particle size becomes smaller. Models for pore narrowing (——) and pore blockage (——) appear to fit the experimental data, while the kinetic surface desorption mechanism (- - -) does not.

Interestingly, the apparent pre-exponential factor, D_0, is not constant; it decreases over three orders of magnitude as particle size decreases (Figure 6. The contribution of the apparent pre-exponential to the overall apparent diffusivity appears to be responsible for the drastic decreases in diffusion coefficients observed in small particles in Figure 6. The pre-exponential factor of the Arrhenius form of the diffusion coefficient has been interpreted to be the entropic contribution in transition state theory, [16,29,50]

$$D_0 = \frac{a^2 \omega(T)}{2\pi} \exp\left(-\frac{\Delta S(T)}{k_B}\right) \qquad 1\text{-}14$$

with the lattice dimensions (a), site vibrational frequency (ω), and entropy of a lattice step. Because these parameters all depend on the adsorbate/host interaction and do not vary with respect to particle size, the pre-exponential factor should remain constant. As there is a strong dependence on particle sizes here (Figure 4, Figure 5), a different mechanistic explanation is necessary to justify the divergence in diffusivity values for small particles.

The precipitous reduction in apparent diffusion coefficients with smaller particle sizes indicates the presence of a second transport phenomenon dependent on particle size. The two broad classes of mechanistic justification discussed here are internal grain boundaries and surface barriers. Several mechanisms focus on the surface, suggesting that either an entropic effect associated with the reorientation or tortuosity of the diffusing molecule at the surface[51,52] or an extension of the diffusional length scale near the surface.[36,53] Each proposed secondary rate limitation is discussed and evaluated in the subsequent sections for their ability to describe the particle size dependence of the experimentally-determined diffusion coefficients.

7.4.1 Internal Grain Boundaries

Boundaries that exist at the crystalline interface within zeolites (internal grain boundaries) are considered to be a possible cause for mass transfer limitations to intracrystalline diffusion. In the MFI coffin-shaped crystal, ordered grain boundaries exist that are believed to hinder internal diffusion by causing discontinuous pore channels.[54,55] It is proposed that the presence of these barriers, which can be either impermeable or semi-permeable, significantly reduces adsorbate flux through the particle on a macroscopic scale.[22,54] Vasenkov et al. performed kinetic Monte Carlo simulations and PFG-NMR diffusion studies through MFI and suggested that the outer surface does not play a significant role on apparent diffusion.[56,57] Instead, the authors suggest the presence of permeable grain boundaries and intergrowths as diffusion limitations. These internal blockages were observed experimentally using a combination of spectroscopic, scattering and microscopy techniques, where accumulation of diffusing molecules at grain boundaries was observed with pore misalignments at angles as small as 0.5-2°.[54]

In addition to grain boundaries, intergrowths or crystal defects within the MFI structure have also been suggested as responsible for macroscopically observed diffusion barriers.[58,59] These internal barriers result from the synthesis process and are believed to cause regular defects. While the presence of internal crystal defects not ordered on a crystal grain boundary

(intergrowths) may be responsible for a decrease in transport time through the particle, the dependence of the diffusivity on particle size suggests it is not responsible for the strong size dependence observed in the transport rate.

7.4.2 Surface Barriers

A 'surface barrier' is a general term for any resistance to mass transfer at or near the surface of a zeolite pore. While the mechanism contributing to a surface mass transport limitation has not been conclusively identified, surface barriers in small particles have been claimed to account for up to 60% of overall mass transfer.[24] The surface barrier phenomenon has been explained by numerous mechanisms including surface coking, strongly adsorbed diffusing molecules, accumulation near pores, strongly bound water molecules, a slow kinetic desorption step, pore narrowing, and total pore blockages.[18,24,25,32,36,50,51,60-64]

The simplest analysis of surface barriers assumes a mass transfer coefficient at the particle surface to describe an undefined mechanism.[24,32,65] In these models, bulk diffusion is assumed to describe transport in the internal crystal domain while desorption from the surface to the bulk gas is assumed to be in equilibrium. Unlike the traditional solution, however, an intermediary transport step is introduced in which a mass transfer resistance ($\tau_m = 1/k_m$) exists between the bulk crystal and the surface.

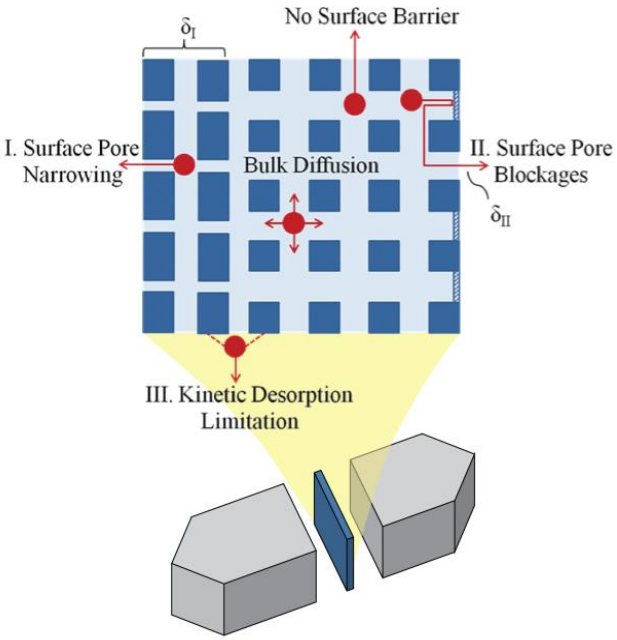

Figure 7-7: Qualitative Visualization of Surface Barriers. Mechanistic transport across the zeolite surface is described as either having no transport barrier, surface pore narrowing (I), surface pore blockages (II), or kinetic desorption limitations (III).

Three specific mechanisms for surface barriers are presented, discussed and evaluated here in an attempt to determine the origin of the secondary transport limitation. The mechanisms considered are qualitatively described in Figure 7 and summarized mathematically in Table 2. narrowing of the pores at the surface (Mechanism I); extension of the diffusional length scale near the surface due to total pore blockages (Mechanism II); and desorption of molecules from the surface to the bulk gas phase (Mechanism III). Full derivations for each mechanism are provided in Appendix A.

Table 7-2: Zeolite Diffusion Models. Boundary conditions, dimensionless fitting parameter L, and apparent Arrhenius pre-exponential, Dapp,0 are presented for the four mass transfer models describing pure intracrystalline diffusion (Base), and three mechanistic derivations of surface barriers.

	Model	BC at Surface	L	$D_{app,0}$
-	Base	$-D\left.\frac{\partial q}{\partial r}\right\|_R = \frac{FR}{3KV_s}q_R = \frac{FR}{3V_s}c$	$L = \frac{\tau_{Diff}}{\tau_{washout}} = \frac{1}{3}\frac{F}{KV_s}\frac{R^2}{D}$	D_0
I	Surface Resistance (Pore Narrowing)	$-D\left.\frac{\partial q}{\partial r}\right\|_R = k(q_R - q_{surf}) = \frac{FR}{3V_s}c = \frac{FR}{3KV_s}q_{surf}$	$L' = \frac{\tau_{diff}}{\tau_{washout} + \tau_{surf}} = \frac{R^2/3D}{KV_s/F + R/k_s}$	$R^2\left[\frac{(R-\delta_I)^2}{D_0} + \frac{\delta_I^2}{D_{s,0}}\right]^{-1}$
II	Pore Blockage	Same as base	Same as base	$D_0\left[1 + \left(\frac{\delta_{II}}{R}\right)^2\right]^{-1}$
III	Kinetic Desorption	$-D\left.\frac{\partial q}{\partial r}\right\|_R = \frac{k_{des}R}{3}q_R = \frac{FR}{3V_s}c$	$L'' = \frac{\tau_{diff}}{\tau_{des}} = \frac{R^2/3D}{1/k_{des}}$	$\frac{k_{des,0}D_0}{k_{des,0}\exp\left(\frac{E_{Diff} - E_{app}}{\mathcal{R}T}\right) + \frac{D_0}{R^2}\exp\left(\frac{-\Delta H_{ads} - E_{app}}{\mathcal{R}T}\right)}$

7.4.2.2 Surface Pore Narrowing (I)

It is possible to explain surface barrier limitations as a step through the surface that is slower than the bulk due to surface pore narrowing. A comprehensive study on the morphology of MFI crystals has identified a "crust" on the outer surface of particles, 10-200 nm in thickness ,resulting from the synthesis process.[54] This crust is believed to be responsible for mass transport rate limitations due to inherent structural difference through the layer.

Lercher and co-workers have proposed that a transport step at the surface that is enthalpically different from the bulk can be rate limiting in small crystals.[66] The authors describe overall diffusion through the particle as a series of three kinetic steps: adsorption to the surface, diffusion into a surface defect layer, and bulk diffusion into the crystal. In large particles (>3 μm), model predictions fit to frequency response data identify bulk crystal diffusion control, while small particles (< 100 nm) are proposed to be limited by either transport across the surface or desorption from the surface to the bulk gas phase. Gueudré et al. studied diffusion of cyclohexane in two different sizes of MFI crystals and qualitatively reports a temperature activated surface barrier effect different from bulk diffusion.[24]

In our study, an additive mechanistic model is proposed and quantitatively compared to experimentally observed diffusion coefficients for several temperatures. In this model, a finite crust of length δ_I is assumed to penetrate into the surface of the particle. The apparent time scale is then assumed to be a linear combination of the two transport timescales, namely bulk diffusion and diffusion through the surface,

$$\tau_{app} = \frac{R^2}{D_{app}} = \tau_{bulk} + \tau_s \qquad 1\text{-}15$$

where $\tau_{bulk} = {R_{bulk}}^2/D$, is the timescale for diffusion through the bulk, $\tau_s = \delta_I^2/D_s$ is the timescale through the crust, and $R = R_{bulk} + \delta_I$. In this case, pore narrowing is represented

mechanistically by a diffusion constant different than that of the bulk ($D_s \neq D$). Applying the Arrhenius relationship to relate the apparent pre-exponential to the surface length scales, the apparent pre-exponential can be algebraically solved to obtain,

$$D_{0,app} = R^2 \left[\frac{(R - \delta_I)^2}{D_0} \exp\left(\frac{E_{Diff} - E_{app}}{\mathcal{R}T} \right) + \frac{\delta_I^2}{D_{0,s}} \exp\left(\frac{E_s - E_{app}}{\mathcal{R}T} \right) \right]^{-1} \qquad 7\text{-}1$$

This description implies that the slope of the Arrhenius curves should change with particle size. However, as observed in this work and literature, no dependence of E_{app} on particle size is observed, and the activation energy associated with transport through the surface, E_s, and bulk appear to be equal.

In the case of pore narrowing, diffusion through a crust (or across a single layer) is hindered by an entropic surface effect such as a reorientation of a molecule at the pore surface.[51,67] Based on the constant activation energy observed experimentally (in Figure 6), with the assumption that $E_{Diff} = E_s = E_{app}$, equation 16 reduces to the entropic contribution to the apparent pre-exponential to diffusion,

$$D_{app,0} = R^2 \left[\frac{(R - \delta_I)^2}{D_0} + \frac{\delta_I^2}{D_{s,0}} \right]^{-1} \qquad 7\text{-}2$$

where the bulk pre-exponential factor, D_0, is taken to be the asymptotic value for large particles, $D_0 = 2.7 \times 10^{-7}$ cm^2/s. The model fit then reduces to the two parameters: penetration depth of the surface barrier, δ_I, and the pre-exponential factor for diffusion across the barrier, $D_{s,0}$. The model can be fit with the experimental data set $D_{app,0}(R)$, and the resulting fit is represented in Figure 6. The predicted crust penetration depth is estimated as δ_I = 25 nm.

A surface crust thickness of 25 nm is reasonable when compared to known structural differences observed penetrating into the surface of MFI (10-200 nm).[54] The pore narrowing model predicts a hindered diffusion coefficient at the surface with $D_0 = 3.4 \times 10^{-10}$ cm^2/s. In this model, this extremely slow diffusivity results entirely from the pre-exponential to the diffusion coefficient in the Arrhenius relationship.

7.4.2.3 Pore Blockage (II)

An alternative theory for surface barriers examines the possibility of physical blockages of surface pores. Pore blockages cause an extension of the diffusional length scale due to the additional path a molecule must travel to locate an open surface pore. Support for the surface pore blockage theory has arisen from experiments measuring diffusivity across modified zeolite surfaces by surface etching with hydrofluoric acid[24,68] and deposition of an amorphous surface layer via silylation[36,69]. Pore blockage at the surface was also proposed by Reitmeir et al., who claimed that the absence of variation in activation energy associated with the Arrhenius form of diffusivity, D, supports only closed pores; in their view, pore restriction should alter the activation energy in the surface region. [29] Brandani studied the correlation between diffusivity and displacement of n-alkanes in silicalite-1 across several length scales and concluded that smaller diffusivities were likely caused by a longer diffusional path, not a slower diffusion rate.[20] This is important, because it means that the self diffusivity, which represents a single molecule jumping through the lattice, remains constant while the apparent (transport) diffusivity across the entire particle is observed to be slower.

Blockage of pores at the zeolite particle surface will lead to longer diffusion paths and apparent transport length scales. It also suggests that a surface pore blockage effect should be more pronounced in smaller particles where the additional path length needed for a diffusing molecule to find an open pore becomes comparable to the bulk transport length scale (particle diameter). Kärger and co-workers developed an interference microscopy technique that allowed for spatially and temporally resolved concentration profiles of single zeolite particles. [22, 71, 78] In this work, the authors are able to decouple bulk diffusion and surface permeability in metal organic frameworks (MOFs) [61,70,71]. An accumulation of diffusing molecules is observed at the surface, however the permeability across the surface was shown to exhibit the same activation energy as the bulk, indicating that the same fundamental transport step.[61] Because the activation

energy remains constant, the mechanisms for the bulk and surface are likely the same, again indicative of diffusion control across the surface, likely due to surface pore blockages.

In this work, mechanistic evaluation is provided to assess the possibility of pore blockages in silicalite-1. As with the pore narrowing mechanism, the observed transport time is assumed to be an additive combination of the bulk transport ($\tau_{bulk} = R^2/D$) and diffusion across the surface barrier $\left(\tau_s = \delta_{II}^2/D\right)$. In this case, the diffusion constants through the bulk and the surface are both assumed to be identical, and equation 15 can be solved for the apparent pre-exponential,

$$D_{app,0} = D_0 \left[1 + \left(\frac{\delta_{II}}{R}\right)^2\right]^{-1} \qquad 7\text{-}1$$

Relaxing the constraint that D_0 must be the asymptotic value, the model fit shown in Figure 6 predicts parameters $D_0 = 3.1 \times 10^{-7}$ cm^2/s, and $\delta_{II} = 740$ nm. The first parameter, D_0, predicts an intracrystalline diffusivity pre-exponential similar to that predicted earlier for the bulk $\left(D_{0,bulk} = 2.7 \times 10^{-7}\right)$, which is consistent with the theory that the diffusivity remains constant, while the diffusional length scale increases in smaller particles. The additional diffusion length of 740 nm represents the additional distance a molecule must travel to locate an open surface pore. In situations where the fraction of surface pore blockages is significant, the additional length can be larger than the particle itself. In conclusion, pore blockage agrees well with the experimental results and offers an explanation for the observed secondary transport limitation.

7.4.2.4 Surface Desorption (III)

The final surface barrier mechanism evaluates slow surface desorption relative to bulk diffusion. By this mechanism, adsorbates can rapidly diffuse to the particle surface, but they are blocked from exiting the pore by high surface coverage on the external particle surface. In zeolite membranes and small crystals where little or no bulk lattice exists, it may be possible to be transport limited by desorption from the surface to the bulk gas phase.[16,72] This theory was first

presented by Barrer et al. who described a surface evaporation step;[73,74] however, it has yet to be supported experimentally.[75,76] The possibility of a desorption limitation was considered at steady state by Kärger and co-workers who determined that, under desorption control ($k_{des} << D/\ell$), the timescale becomes dominated by the desorption time, $\tau_s = 1/k_{des}$, and the timescale associated with transport to the bulk phase from the surface (permeability) is expected to be independent of particle size. While the desorption step presumes a difference in activation energy as the elution process transitions from bulk diffusion (E_{Diff}) to desorption (ΔH_{des}), mechanisms such as this cannot be discounted; the activation energy for cyclohexane diffusion in silicalite-1 ($E_a = 26 - 56$ kJ/ mol[40]) has been reported to be similar to the heat of desorption ($-\Delta H_{ads} = 57.3$ kJ/ mol[40]).

The desorption limitation mechanism is evaluated assuming additive timescales (equation 15), where the timescale for a molecule to desorb from the surface to the bulk gas phase is $\tau_s = 1/k_{des}$. In this case, both the bulk diffusion coefficient and the kinetic desorption constant are assumed to be temperature activated according to the Arrhenius and Polanyi-Wigner[77] relationships $\left(k_d = k_{des,0} \exp\left(-\frac{E_{des}}{RT}\right)\right)$, respectively. Assuming that the desorption energy is equal to the enthalpy of desorption, $E_{des} \approx -\Delta H_{ads} \neq E_{Diff}$, and the desorption rate is first order, the pre-exponential factor of the Arrhenius form of the apparent diffusion coefficient, D_{app}, becomes,

$$D_{app,0} = \frac{k_{des,0} D_0}{k_{des,0} \exp\left(\frac{E_{Diff} - E_{app}}{\mathcal{R}T}\right) + \frac{D_0}{R^2} \exp\left(\frac{-\Delta H_{ads} - E_{app}}{\mathcal{R}T}\right)} \qquad 7\text{-}1$$

where $k_{des,0}$ is the frequency factor for the first order desorption rate constant, ΔH_{ads} is taken as 57.3 kJ/mol,[40] E_{app} is the experimentally averaged activation energy (38 ± 4 kJ/mol), and the bulk diffusion parameters are again assumed to be the asymptotic value observed in large particles ($D_0 = 2.7 \times 10^{-7}$ cm^2/s, $E_{Diff} = 38$ kJ/mol). The pre-exponential in the Polanyi-Wigner relationship is taken as, $k_{des,0} = 10^{13}$ s^{-1}, as a common assumption for the jump frequency.[77]

In the range of temperatures examined in this study, the predicted desorption-controlled model is shown in Figure 6, where negligible dependence on particle size is observed. This is due to the extremely fast desorption step compared to bulk diffusion $\left(L'' = \frac{\tau_{Diff}}{\tau_{des}} \sim 10^8 - 10^9\right)$, even in small particles. This result suggests that the system is not desorption controlled. Furthermore, for desorption to be relevant to the overall rate, either the pre-exponential, $k_{d,0}$, would have to be many orders of magnitude smaller, or the difference between the enthalpy of desorption ($-\Delta H_{ads}$) and the activation energy for diffusion ($E_{a,diff}$) would need to be substantially larger, which literature has suggested is not the case.[40]

7.5 Implications

New hierarchical microporous materials with ordered or disordered mesoporosity are currently being synthesized with microporous frameworks and particle length scales as thin as single unit cells.[7,11] However, surface barriers have been shown here to be prevalent and even dominant in small zeolite particles and are likely due to structural differences/defects of pores at or near the surface. In preparation and characterization of such materials, special consideration should be made to ensure structurally pure zeolite surfaces with unhindered transport due to substantial surface defects. As the surface appears exceptionally important and susceptible to blockages/restrictions in small particles, protection of the surface from unnecessary exposure to chemical or mechanical blockages by development of ordered, mesoporous or templated materials is necessary to maximize the turnover potential of hierarchical materials. Conclusions

Direct evidence is presented to support secondary, size-dependent transport limitations in small microporous particles. A set of well-defined silicalite-1 particles was synthesized of known size spanning three orders of magnitude, and apparent diffusion coefficients of cyclohexane/silicalite-1 were measured by zero length chromatography. Arrhenius temperature dependence of measured apparent diffusivities confirmed that all particles were temperature-

activated with the same activation energy. However, the pre-exponential factor for the apparent diffusion constant was observed to decrease over three orders of magnitude as particle size decreased. Variation in apparent diffusivity was examined by three mechanisms including surface pore constriction, surface pore blockage, and surface desorption of cyclohexane. While desorption of cyclohexane was insufficient to explain the drastic reduction of apparent cyclohexane diffusivity in small particles, surface pore constriction/blockage was viable.

Nomenclature

a	Length of a single lattice step
c	Gas phase effluent concentration
q	Adsorbate surface concentration
D, D_{app}	Intracrystalline diffusion coefficient and apparent diffusion coefficient
D_0, $D_{app,0}$, $D_{s,0}$	Arrhenius pre-exponential factor for intracrystalline, apparent, and surface diffusion respectively.
E_{Diff}, E_{app}, E_s	Activation energies for diffusion, apparent diffusion, and surface barriers
F	Convective volumetric flow rate through the diffusion chamber
ΔH_{ads}	The heat of adsorption of a molecule adsorbing to the surface of a zeolite
K	Dimensionless equilibrium constant (Henry's constant)
k_B	Boltzmann's constant, 1.3806×10^{-23} J/K
k_{des}	First order kinetic desorption rate constant
k_s	First order mass transfer coefficient
L, L', L''	Ratio of diffusional time to secondary transport time constant (eq. 7, 10, 12)
r	Spacial coordinate in spherical particle
R	Diffusional length scales in spherical coordinates, $R = (l*w*h)^{1/3}$
$\mathcal{R}$	Ideal gas constant, 8.314 J mol^{-1} K^{-1}
ΔS	Entropy change associated with a molecule diffusing into a micropore
t	Desorption time
V_f	Fluid volume
V_s	Adsorbent volume
β_n	Infinite series defined by equation 6
γ	Ratio of accumulation in the fluid to the solid, defined by equation 8
δ_I, δ_{II}	Surface barrier length scales for (I) crust, and (II) additional diffusion length
τ	Transport time constant
ω	Vibrational frequency of an adsorbed molecule on a zeolite

7.6 Appendix A: Supporting Information

7.6.1 ZLC Model Assumptions: Sphere vs. Slab

The ZLC model has been solved for both one dimensional, and three dimensional, pore geometries. In some systems, the selection is straightforward based on the known microcrystalline framework. In the case of MFI, which is known to have a three dimensional interconnected pores, the spherical model is often assumed.[78] However, with large rigid molecules such as p-xylene, some researchers argue that transport is dominated by straight pores, not the sinusoidal pores; and the three dimensional nature of the network is not observed.[79] An analytical method has been developed by Cavalcante et al.[80] for determining which model is appropriate for a specific absorbent/absorbate system and is employed here.

The theory derives an intermediate time approximation of the ZLC model (equations 1-4 of the manuscript) for both the 'spherical' and 'slab' models,

Spherical Solution:

$$\frac{c}{c_0} = \frac{1}{L}\left[\sqrt{\frac{R^2}{\pi D t}} - 1\right]$$

Slab Solution:

$$\frac{c}{c_0} = \frac{1}{L}\sqrt{\frac{l^2}{\pi D t}}$$

By plotting the dimensionless concentration versus $\sqrt{t}$, the intercept will either pass through zero (one-dimensional slab model) or have a finite value (three-dimensional sphere model). Our results for temperatures of 50-110 °C in the 400 nm particle are shown here in Figure 9. The nonzero values of the slope confirm the validity of our three dimensional approximation and the selection of the spherical model for analysis.

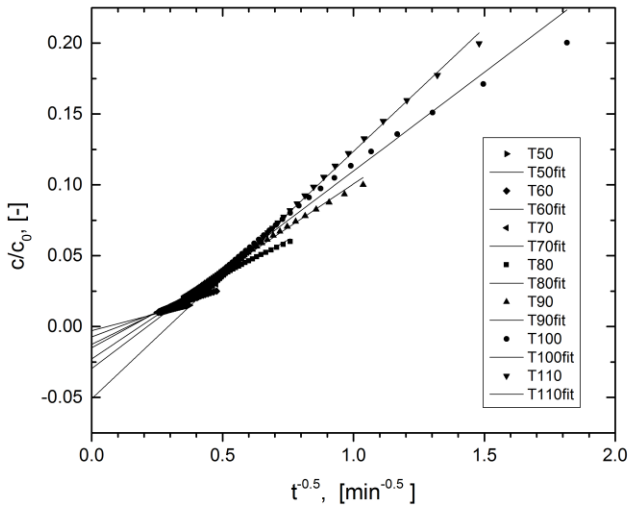

Figure 7-8: Desorption curves of cyclohexane in silicalite at several temperatures, indicating the three-dimensional diffusion path.

7.6.2 Intracrystalline Verification

Intracrystalline transport was verified as rate limiting under experimental conditions by the following methods quantitatively assessing four conditions as described below.

Uptake Condition

Sufficient time should be allowed for crystals in the chamber to completely equilibrate before desorption begins. The minimum adsorption uptake time can be calculated by the following relationship,[81]

$$t_{uptake} > 0.416\frac{R^2}{D} \qquad 1\text{-}20$$

For all submicron particle sizes considered here, two hours was determined to be sufficient. Larger particle sizes were verified as fully saturated by obtaining identical desorption curves for four or six hours of adsorption uptake time.

Macroscopic Measurability

The experimental measurement is limited by the ability to measure desorption at a rate sufficiently slow to determine the diffusion constant. In the case where a flame ionization

detector is used to quantify adsorbate concentration, a minimum of several seconds of desorption is required. The condition for the time constant must fall within the constraint,

$$\frac{D}{R^2} < 0.01\ s^{-1} \qquad 7\text{-}1$$

Using literature values where D is presumed constant irrespective of particle size, this criterion is not met in all cases. Generally, it is not met for particle sizes below 100 nm or temperatures above 110 °C. In this study and in literature, however, apparent diffusivity is observed strongly decreasing with particle size. Using experimentally fit diffusional time constants, the criterion is satisfied for all particle sizes below 130 °C, with a largest time constant of 6.2e-4 s^{-1}.

Internal Transport Condition

A third consideration compares internal (diffusion) or external (film convection) transport timescales. As with the equilibrium condition, a dimensionless quantity can be calculated to determine the transport regime. In this case, L can be modified to account for external mass transfer. Substituting $N_{Sh} = \frac{2k_s R}{D_m}$,[78, 82] equation 10 from the manuscript reduces to,

$$L' = \frac{\tau_{diff}}{\tau_{washout} + \tau_{surf}} = \frac{R^2/3D}{KV_s/F + R/k_s} = \frac{R^2/3D}{KV_s/F + 2/N_{Sh}D_m} \qquad 7\text{-}2$$

When the second term in the denominator is sufficiently small compared to the first, the external film can be neglected. Assuming $N_{Sh} = 2$,[78] the condition reduces to,

$$\frac{\tau_{Diff}}{\tau_w} = \frac{D_m}{KD} \gg 5 \qquad 7\text{-}3$$

Bulk diffusion of cyclohexane in the gas phase was estimated as 0.5 cm^2/s using the Fuller-Schettler-Giddings correlation.[83] In the cyclohexane/silicalite-1 case for the range of temperatures analyzed, the condition is easily satisfied, ranging from $10^7 < \tau_{Diff}/\tau_w < 10^9$, indicating that all considered experiments are limited by internal transport.

Kinetic Transport Control

This condition compares the timescale for intracrystalline diffusion to the time needed to effectively washout the sample chamber. If the washout time is too slow, it is assumed that the bulk gas is in equilibrium with the surface, and thus no kinetic information can be obtained. Equilibrium control occurs when the adsorbate is strongly adsorbed or the intracrystalline diffusivity is relatively high. This criterion is assessed by monitoring the dimensionless quantity, L, which is the ratio of diffusion to washout times, and can be calculated as,

$$L = \frac{\tau_{diff}}{\tau_{equil}} = \frac{R^2/D}{3KV_s/F} > 1 \qquad 7\text{-}4$$

Eic and Ruthven[84] establish the condition that L > 1, allowing for the condition,

$$\frac{\nu R}{KD} > 6 \qquad 7\text{-}5$$

Under the most unfavorable conditions, (T=300 °C, R=17.5 nm, K = 3.1e4, D = 8.9e-13 cm^2/s, ν = 2.6 cm/s), the left hand side of the inequality of Eq. S8 is calculated as 12.5. Most operating conditions studied in our work yield significantly higher values (10^2 to 10^4). Additionally, L is an experimental fitting parameter and has been determined to be between 10-500 for the sizes and temperatures analyzed. This indicates that all considered experiments are not under equilibrium control.

7.6.3 ZLC Literature Comparisons

To confirm the validity of our zero length chromatography technique, a comparison of diffusion coefficients measured in the literature for cyclohexane/MFI systems is presented at several temperatures in Figure 10. Particle sizes in literature ranged from 0.25 to 50 micron. Smaller particles (0.25 μm, 1 μm) overlap well with our experimentally measured values. Larger particles collapse onto a single curve as the effect of surface resistance becomes negligible, while the mass transport limitation is clearly noticeable by the drastically lower measurements made in small particles in this study. The similarity of the slopes across all particle sizes and techniques qualitatively indicates the consistency in activation energies measured. Diffusion measurements

are made at higher temperatures in larger particles due to the longer time required to perform the measurement.

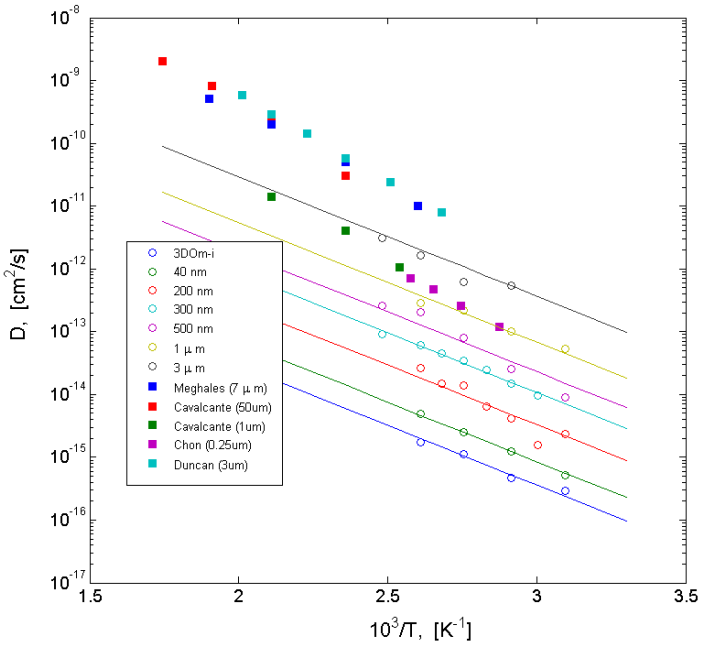

Figure 7-9: **Supplementary Figure S2**: Diffusion coefficients for particles measured in this study (open circles) and literature (closed squares).

7.6.4 Full Derivation of Surface Barrier Models

7.6.4.1 Pore Narrowing

Assume transport timescales for bulk diffusion and diffusion across the crust (narrow pores) are additive and sum to the apparent transport time constant,

$$\tau_{app} = \frac{R^2}{D_{app}} = \tau_{bulk} + \tau_s \qquad 1\text{-}26$$

Substituting in the diffusional time constant for the bulk and the surface,

$$\frac{R^2}{D_{app}} = \frac{R_{bulk}^2}{D} + \frac{\delta_l^2}{D_s} \qquad 7\text{-}1$$

By assuming that the total particle size is the sum of the composite length scales,

$$R = R_{bulk} + \delta_I \tag{7-2}$$

$$\frac{R^2}{D_{app}} = \frac{(R-\delta_I)^2}{D} + \frac{\delta_I^2}{D_s} \tag{7-3}$$

Applying the Arrhenius relationship to all diffusion constants, the relationship becomes,

$$\frac{R^2}{D_{0,app}\exp\left(-\frac{E_{app}}{\mathcal{R}T}\right)} = \frac{(R-\delta_I)^2}{D_0\exp\left(-\frac{E_{Diff}}{\mathcal{R}T}\right)} + \frac{\delta_I^2}{D_{0,s}\exp\left(-\frac{E_s}{\mathcal{R}T}\right)} \tag{7-4}$$

The relationship can be algebraically manipulated to solve for $D_{0,app}$

$$\frac{R^2}{D_{0,app}} = \frac{(R-\delta_I)^2\exp\left(\frac{E_{Diff}-E_{app}}{\mathcal{R}T}\right)}{D_0} + \frac{\delta_I^2\exp\left(\frac{E_s-E_{app}}{\mathcal{R}T}\right)}{D_{0,s}} \tag{7-5}$$

$$D_{0,app} = R^2\left[\frac{(R-\delta_I)^2}{D_0}\exp\left(\frac{E_{Diff}-E_{app}}{\mathcal{R}T}\right) + \frac{\delta_I^2}{D_{0,s}}\exp\left(\frac{E_s-E_{app}}{\mathcal{R}T}\right)\right]^{-1} \tag{7-6}$$

Since no change in activation energy was observed experimentally as a function of particle size, it is assumed that the activation energy of the surface effect is equal to that of the bulk, hence the simplification,

$$E_{Diff} = E_s = E_{app} \tag{7-7}$$

$$D_{0,app} = R^2\left[\frac{(R-\delta_I)^2}{D_0} + \frac{\delta_I^2}{D_{0,s}}\right]^{-1} \tag{7-8}$$

7.6.4.2 Pore Blockage

In the same way as with the pore narrowing, the transport steps through the bulk and the surface are again assumed to be additive,

$$\tau_{app} = \frac{R^2}{D_{app}} = \tau_{bulk} + \tau_s \tag{1-35}$$

In this case, the surface step is also a diffusion step, and the diffusion constants through the bulk and across the surface are assumed to be identical. Additionally, the length scales are no

longer additive, but rather the bulk length scale is equal to that of the particle, and the surface barrier length scale, δ_{II}, is independent of the particle size.

$$\frac{R^2}{D_{app}} = \frac{R^2}{D} + \frac{\delta_{II}^2}{D} = \frac{R^2 + \delta_{II}^2}{D} \quad 7\text{-}1$$

Again, the Arrhenius relationship is introduced,

$$\frac{R^2}{D_{0,app} \exp\left(-\frac{E_{app}}{\mathcal{R}T}\right)} = \frac{R^2 + \delta_{II}^2}{D_0 \exp\left(-\frac{E_{Diff}}{\mathcal{R}T}\right)} \quad 7\text{-}2$$

Which can then be algebraically solved for $D_{0,app}$,

$$\frac{R^2}{D_{0,app}} = \frac{R^2 + \delta_{II}^2}{D_0 \exp\left(\frac{E_{app} - E_{Diff}}{\mathcal{R}T}\right)} \quad 7\text{-}3$$

$$D_{0,app} = R^2 \left[\frac{R^2 + \delta_{II}^2}{D_0}\right]^{-1} \exp\left(\frac{E_{app} - E_{Diff}}{\mathcal{R}T}\right) \quad 7\text{-}4$$

$$D_{0,app} = D_0 \left[1 + \left(\frac{\delta_{II}}{R}\right)^2\right]^{-1} \exp\left(\frac{E_{app} - E_{Diff}}{\mathcal{R}T}\right) \quad 7\text{-}5$$

In this case, the apparent activation energy is equal to the activation energy for diffusion as there is only one mechanistic transport step.

$$D_{0,app} = D_0 \left[1 + \left(\frac{\delta_{II}}{R}\right)^2\right]^{-1} \quad 7\text{-}6$$

7.6.4.3 Kinetic Desorption

Again, additive time constants are assumed for the bulk diffusion and kinetic surface desorption steps.

$$\tau_{app} = \frac{R^2}{D_{app}} = \tau_{bulk} + \tau_s \quad 1\text{-}42$$

In this case, the second transport step is assumed to be approximated by first order kinetics, with a rate constant, k_{des}. No secondary length scale is required.

$$\frac{R^2}{D_{app}} = \frac{R^2}{D} + \frac{1}{k_{des}} \quad 7\text{-}1$$

Similar to the Arrhenius relationship, the Polanyi-Wigner relationship[85] can be used to represent the temperature dependence of the desorption rate constant.

$$k_{des} = k_{des,0} \exp\left(\frac{-E_{des}}{\mathcal{R}T}\right) \quad 7\text{-}2$$

$$\frac{R^2}{D_{app,0} \exp\left(\frac{-E_{app}}{\mathcal{R}T}\right)} = \frac{R^2}{D_0 \exp\left(\frac{-E_{Diff}}{\mathcal{R}T}\right)} + \frac{1}{k_{des,0} \exp\left(\frac{\Delta H_{ads}}{\mathcal{R}T}\right)} \quad 7\text{-}3$$

$$\frac{R^2}{D_{app,0}} = \frac{R^2 \exp\left(\frac{E_{Diff} - E_{app}}{\mathcal{R}T}\right)}{D_0} + \frac{\exp\left(\frac{-\Delta H_{ads} - E_{app}}{\mathcal{R}T}\right)}{k_{des,0}} \quad 7\text{-}4$$

$$D_{app,0} = \frac{k_{des,0} D_0}{k_{des,0} \exp\left(\frac{E_{Diff} - E_{app}}{\mathcal{R}T}\right) + \frac{D_0}{R^2} \exp\left(\frac{-\Delta H_{ads} - E_{app}}{\mathcal{R}T}\right)} \quad 7\text{-}5$$

7.7 References

1 Csicsery, S. M. Shape-Selective Catalysis in Zeolites. *Zeolites* **1984**, *4*, 202-213.

2 Corma, A. Inorganic Solid Acids and Their Use in Acid-Catalyzed Hydrocarbon Reactions. *Chem. Rev.* **1995**, *95*, 559-614.

3 Young, L. B.; Butter, S. A.; Kaeding, W. W. Shape Selective Reactions with Zeolite Catalysts, iii. Selectivity in Xylene Isomerization, Toluene Methanol Alkylation, and Toluene Disproportionation over ZSM-5 Zeolite Catalysts. *J. Catal.***1982**, *76*, 418-432.

4 Jobic, H.; Schmidt, W.; Krause, C. B.; Kärger, J. PFG NMR and QENS Diffusion Study of n-Alkane Homologues in MFI-Type Zeolites. *Micropor.Mesopor. Mat.* **2006**, *90*, 299-306.

5 van den Bergh, J.; Gascon, J.; Kapteijn, F. Diffusion in Zeolites – Impact on Catalysis. In *Zeolites and Catalysis*; Wiley-VCH Verlag GmbH & Co. KGaA, 2010; pp 361-387.

6 Watanabe, R.; Yokoi, T.; Tatsumi, T. Synthesis and Application of Colloidal Nanocrystals of the MFI-Type Zeolites. *J. Colloid Interf. Sci.* **2011**, *356*, 434-441.

7 Fan, W.; Snyder, M. A.; Kumar, S.; Lee, P.-S.; Yoo, W. C.; McCormick, A. V.; Lee Penn, R.; Stein, A.; Tsapatsis, M. Hierarchical Nanofabrication of Microporous Crystals with Ordered Mesoporosity. *Nat. Mater.* **2008**, *7*, 984-991.

8 Lee, P.-S.; Zhang, X.; Stoeger, J. A.; Malek, A.; Fan, W.; Kumar, S.; Yoo, W. C.; Al Hashimi, S.; Penn, R. L.; Stein, A.; Tsapatsis, M. Sub-40 nm Zeolite Suspensions via Disassembly of Three-Dimensionally Ordered Mesoporous-Imprinted Silicalite-1. *J. Amer. Chem. Soc.* **2010**, *133*, 493-502.

9 Na, K.; Jo, C.; Kim, J.; Cho, K.; Jung, J.; Seo, Y.; Messinger, R. J.; Chmelka, B. F.; Ryoo, R. Directing Zeolite Structures Into Hierarchically Nanoporous Architectures. *Science* **2011**, *333*, 328-332.

10 Choi, M.; Na, K.; Kim, J.; Sakamoto, Y.; Terasaki, O.; Ryoo, R. Stable Single-Unit-Cell Nanosheets of Zeolite MFI as Active and Long-Lived Catalysts. *Nature* **2009**, *461*, 246-249.

11 Zhang, X.; Liu, D.; Xu, D.; Asahina, S.; Cychosz, K. A.; Agrawal, K. V.; Al Wahedi, Y.; Bhan, A.; Al Hashimi, S.; Terasaki, O.; Thommes, M.; Tsapatsis, M. Synthesis of Self-Pillared Zeolite Nanosheets by Repetitive Branching. *Science* **2012**, *336*, 1684-1687.

12 Tiselius, A. Adsorption and Diffusion in Zeolite Crystals. *J. Phys. Chem.* **1936**, *40*, 223-232.

13 Auerbach, S. M.; Carrado, K. A.; Dutta, P. K. *Handbook of Zeolite Science and Technology*; M. Dekker, 2003.

14 Brandani, S.; Caro, J.; Yang, X.; Jobic, H.; Kärger, J.; Lercher, J.; Jentys, A.; Staudt, R.; Möller, A.; Ruthven, D.; Shah, D. B.; Schmidt, W. Recent Developments in the Measurement of Diffusion in Zeolites, 2007.

15 Kärger, J.; Ruthven, D. M. *Diffusion in Zeolites and Other Microporous Solids*; Wiley, 1992.

16 Auerbach, S. M.; Kärger, J.; Vasenkov, S. *Diffusion in zeolites*; Marcel Dekker Inc.: New York, 2003.

17 Kärger, J. Measurement of Diffusion in Zeolites—A Never Ending Challenge? *Adsorption* **2003**, *9*, 29-35.

18 Ruthven, D. Diffusion in Zeolites—A Continuing Saga. *Adsorption* **2010**, *16*, 511-514.

19 Krishna, R. Describing the Diffusion of Guest Molecules Inside Porous Structures. *J. Phys. Chem. C* **2009**, *113*, 19756-19781.

20 Brandani, S.; Caro, J.; Jobic, H.; Kärger, J.; Krause, C.; Staudt, R. Diffusion of n-Alkanes in Zeolites: The benefit of Observation Over Different Length Scales. In *Studies in Surface Science and Catalysis*; Ruren Xu, Z. G. J. C., Wenfu, Y., Eds.; Elsevier, 2007; Vol. 170; pp 981-987.

21 Jobic, H.; Kärger, J.; Krause, C.; Brandani, S.; Gunadi, A.; Methivier, A.; Ehlers, G.; Farago, B.; Haeussler, W.; Ruthven, D. M. Diffusivities of n-Alkanes in 5A Zeolite Measured by Neutron Spin Echo, Pulsed-Field Gradient NMR, and Zero Length Column Techniques. *Adsorption* **2005**, *11*, 403-407.

22 Ruthven, D. M. Diffusion in Zeolites. In *Studies in Surface Science and Catalysis*; Laurent, B., Serge, K., Eds.; Elsevier, 1995; Vol. 97; pp 223-234.

23 Brandani, S. Macroscopic Measurement of Adsorption and Diffusion in Zeolites Adsorption and Phase Behaviour in Nanochannels and Nanotubes; Dunne, L. J., Manos, G., Eds.; Springer Netherlands, 2010; pp 195-212.

24 Gueudré, L.; Jolimaître, E.; Bats, N.; Dong, W. Diffusion in Zeolites: Is Surface Resistance a Critical Parameter? *Adsorption* **2010**, *16*, 17-27.

25 Gobin, O. C.; Reitmeier, S. J.; Jentys, A.; Lercher, J. A. Comparison of the Transport of Aromatic Compounds in Small and Large MFI Particles. *J. Phys. Chem. C* **2009**, *113*, 20435-20444.

26 Kocirik, M.; Struve, P.; Fiedler, K.; Bulow, M. A Model for the Mass-Transfer Resistance at the Surface of Zeolite Crystals. *J. Chem. Soc. Far. T. 1* **1988**, *84*, 3001-3013.

27 Kortunov, P.; Vasenkov, S.; Chmelik, C.; Kärger, J.; Ruthven, D. M.; Wloch, J. Influence of Defects on the External Crystal Surface on Molecular Uptake into MFI-Type Zeolites. *Chem. Mater.* **2004**, *16*, 3552-3558.

28 Ruthven, D.; Brandani, S.; Eic, M. Measurement of Diffusion in Microporous Solids by Macroscopic Methods Adsorption and Diffusion; Karge, H., Weitkamp, J., Eds.; Springer Berlin / Heidelberg, 2008; Vol. 7; pp 45-84.

29 Reitmeier, S. J.; Jentys, A.; Lercher, J. A. Understanding Transport in MFI-Type Zeolites on a Molecular Basis. In *Ideas in Chemistry and Molecular Sciences*; Wiley-VCH Verlag GmbH & Co. KGaA, 2010; pp 229-253.

30 Agger, J. R.; Hanif, N.; Cundy, C. S.; Wade, A. P.; Dennison, S.; Rawlinson, P. A.; Anderson, M. W. Silicalite Crystal Growth Investigated by Atomic Force Microscopy. *J. Amer. Chem. Soc.* **2003**, *125*, 830-839.

31 Eić, M.; Ruthven, D. M. A New Experimental Technique for Measurement of Intracrystalline Diffusivity. *Zeolites* **1988**, *8*, 40-45.

32 Ruthven, D. M.; Vidoni, A. ZLC Diffusion Measurements: Combined Effect of Surface Resistance and Internal Diffusion. *Chem. Eng. Sci.* **2012**, *71*, 1-4.

33 Huang, Q.; Eić, M.; Xiao, H.; Kaliaguine, S. Characterization of the Diffusion Path in Micro- and Meso-Porous Materials from ZLC Analysis. *Adsorption* **2010**, *16*, 531-539.

34 Malekian, A.; Vinh-Thang, H.; Huang, Q.; Eić, M.; Kaliaguine, S. Evaluation of the Main Diffusion Path in Novel Micro-Mesoporous Zeolitic Materials with the Zero Length Column Method. *Ind. Eng. Chem. Res.* **2007**, *46*, 5067-5073.

35 Gunadi, A.; Brandani, S. Diffusion of Linear Paraffins in NaCaA Studied by the ZLC Method. *Micropor. Mesopor. Mat.* **2006**, *90*, 278-283.

36 Duncan, W.; Möller, K. Diffusion in Surface Modified ZSM-5 Studied Using the ZLC Method. *Adsorption* **2005**, *11*, 259-273.

37 Brandani, F. Development and Application of the Zero Length Column (ZLC) Technique for Measuring Adsorption Equilibria, University of Maine, 2002.

38 Eić, M.; Micke, A.; Kočiríik, M.; Jama, M.; Zikánová, A. Diffusion and Immobilization Mechanisms in Zeolites studied by ZLC Chromatography. *Adsorption* **2002**, *8*, 15-22.

39 Ruthven, D. M.; Brandani, S. Measurement of Diffusion in Porous Solids by Zero Length Column (ZLC) Methods. In *Membrane Science and Technology*; Kanellopoulos, N. K., Ed.; Elsevier, 2000; Vol. 6; pp 187-212.

40 Duncan, W. L.; Möller, K. P. On the Diffusion of Cyclohexane in ZSM-5 Measured by Zero-Length-Column Chromatography. *Ind. Eng. Chem. Res.* **2000**, *39*, 2105-2113.

41 Brandani, S.; Ruthven, D. M. Analysis of ZLC Desorption Curves for Gaseous Systems. *Adsorption* **1996**, *2*, 133-143.
42 Eić, M.; Ruthven, D. M. Intracrystalline Diffusion of Linear Paraffins and Benzene in Silicalite Studied by the ZLC Method. In *Studies in Surface Science and Catalysis*; Jacobs, P. A., Santen, R. A. v., Eds.; Elsevier, 1989; Vol. 49; pp 897-905.
43 Cavalcante, C. L.; Brandani, S.; Ruthven, D. M. Evaluation of the Main Diffusion Path in Zeolites from ZLC Desorption curves. *Zeolites* **1997**, *18*, 282-285.
44 Brandani, S.; Ruthven, D. M. Analysis of ZLC Desorption Curves for Liquid Systems. *Chem. Eng. Sci.* **1995**, *50*, 2055-2059.
45 Wu, P.; Debebe, A.; Ma, Y. H. Adsorption and Diffusion of C6 and C8 Hydrocarbons in Silicalite. *Zeolites* **1983**, *3*, 118-122.
46 Ban, H.; Gui, J.; Duan, L.; Zhang, X.; Song, L.; Sun, Z. Sorption of Hydrocarbons in Silicalite-1 Studied by Intelligent Gravimetry. *Fluid Phase Equilibr.* **2005**, *232*, 149-158.
47 Xiao, J.; Wei, J. Diffusion Mechanism of Hydrocarbons in Zeolites—ii. Analysis of Experimental Observations. *Chem. Eng. Sci.* **1992**, *47*, 1143-1159.
48 Chon, H.; Park, D. H. Diffusion of Cyclohexanes in ZSM-5 Zeolites. *J. Catal.* **1988**, *114*, 1-7.
49 Cavalcante, C. L., Jr.; Ruthven, D. M. Adsorption of Branched and Cyclic Paraffins in Silicalite. 2. Kinetics. *Ind. Eng. Chem. Res.* **1995**, *34*, 185-191.
50 Gobin, O. C.; Reitmeier, S. J.; Jentys, A.; Lercher, J. A. Role of the Surface Modification on the Transport of Hexane Isomers in ZSM-5. *J. Phys. Chem. C* **2011**, *115*, 1171-1179.
51 Ford, D. M.; Glandt, E. A Molecular Simulation Approach to Studying Mass Transfer Across Surface Barriers; Pinnavaia, T., Thorpe, M., Eds.; Springer US, 2002; pp 319-334.
52 Ford, D. M.; Glandt, E. D. Steric Hindrance at the Entrances to Small Pores. *J. Membrane Sci.* **1995**, *107*, 47-57.
53 Gupta, A.; Snurr, R. Q. A Study of Pore Blockage in Silicalite Zeolite Using Free Energy Perturbation Calculations. *J. Phys. Chem. B* **2005**, *109*, 1822-1833.
54 Karwacki, L.; Kox, M. H. F.; Matthijs de Winter, D. A.; Drury, M. R.; Meeldijk, J. D.; Stavitski, E.; Schmidt, W.; Mertens, M.; Cubillas, P.; John, N.; Chan, A.; Kahn, N.; Bare, S. R.; Anderson, M.; Kornatowski, J.; Weckhuysen, B. M. Morphology-Dependent Zeolite Intergrowth Structures Leading to Distinct Internal and Outer-Surface Molecular Diffusion Barriers. *Nat. Mater.* **2009**, *8*, 959-965.
55 Newsome, D. A.; Sholl, D. S. Molecular Dynamics Simulations of Mass Transfer Resistance in Grain Boundaries of Twinned Zeolite Membranes. *J. Phys. Chem. B* **2006**, *110*, 22681-22689.
56 Vasenkov, S.; Böhlmann, W.; Galvosas, P.; Geier, O.; Liu, H.; Kärger, J. PFG NMR Study of Diffusion in MFI-Type Zeolites: Evidence of the Existence of Intracrystalline Transport Barriers. *J. Phys. Chem. B* **2001**, *105*, 5922-5927.
57 Vasenkov, S.; Kärger, J. Evidence for the Existence of Intracrystalline Transport Barriers in MFI-Type Zeolites: A Model Consistency Check Using MC Simulations. *Micropor. Mesopor. Mat.* **2002**, *55*, 139-145.
58 Muller, G.; Narbeshuber, T.; Mirth, G.; Lercher, J. A. Infrared Microscopic Study of Sorption and Diffusion of Toluene in ZSM-5. *J. Phys. Chem.* **1994**, *98*, 7436-7439.
59 Ruthven, D. M. Transport in Microporous Solids. In *Fluid Transport in Nanoporous Materials*; Conner, W. C., Fraissard, J. P., Division, N. P. D., Eds.; Springer in cooperation with NATO Public Diplomacy Division, 2006.
60 Krutyeva, M.; Vasenkov, S.; Yang, X.; Caro, J.; Kärger, J. Surface Barriers on Nanoporous Particles: A New Method of Their Quantitation by PFG NMR. *Micropor. Mesopor. Mat.* **2007**, *104*, 89-96.

61 Hibbe, F.; Chmelik, C.; Heinke, L.; Pramanik, S.; Li, J.; Ruthven, D. M.; Tzoulaki, D.; Kärger, J. The Nature of Surface Barriers on Nanoporous Solids Explored by Microimaging of Transient Guest Distributions. *J. Amer. Chem. Soc.* **2011**, *133*, 2804-2807.

62 Chmelik, C.; Varma, A.; Heinke, L.; Shah, D. B.; Kärger, J.; Kremer, F.; Wilczok, U.; Schmidt, W. Effect of Surface Modification on Uptake Rates of Isobutane in MFI Crystals: An Infrared Microscopy Study. *Chem. Mater.* **2007**, *19*, 6012-6019.

63 Ruthven, D. M. Adsorption and Desorption Kinetics for Diffusion Controlled Systems with a Strongly Concentration Dependent Diffusivity. *Diffusion Fundamentals* **2007**, *6*, 51.1-51.11.

64 Tzoulaki, D.; Schmidt, W.; Wilczok, U.; Kärger, J. Formation of Surface Barriers on Silicalite-1 Crystal Fragments by Residual Water Vapour as Probed with Isobutane by Interference Microscopy. *Micropor. Mesopor. Mat.* **2008**, *110*, 72-76.

65 Ruthven, D.; Brandani, F. ZLC Response for Systems with Surface Resistance Control. *Adsorption* **2005**, *11*, 31-34.

66 Gobin, O. C.; Reitmeier, S. J.; Jentys, A.; Lercher, J. A. Diffusion Pathways of Benzene, Toluene and p-Xylene in MFI. *Micropor. Mesopor. Mat.* **2009**, *125*, 3-10.

67 Reitmeier, S. J.; Gobin, O. C.; Jentys, A.; Lercher, J. A. Enhancement of Sorption Processes in the Zeolite H-ZSM5 by Postsynthetic Surface Modification. *Angew. Chemie. Int. Edit.* **2009**, *48*, 533-538.

68 Gueudré, L.; Bats, N.; Jolimaître, E. Effect of Surface Resistance on Cyclohexane Uptake Curves in Silicalite-1 Crystals. *Micropor. Mesopor. Mat.* **2012**, *147*, 310-317.

69 Zheng, S.; Tanaka, H.; Jentys, A.; Lercher, J. A. Novel Model Explaining Toluene Diffusion in HZSM-5 After Surface Modification. *J. Phys. Chem. B* **2003**, *108*, 1337-1343.

70 Heinke, L.; Tzoulaki, D.; Chmelik, C.; Hibbe, F.; van Baten, J. M.; Lim, H.; Li, J.; Krishna, R.; Kärger, J. Assessing Guest Diffusivities in Porous Hosts from Transient Concentration Profiles. *Phys. Rev. Lett.* **2009**, *102*, 065901.

71 Gueudré, L.; Binder, T.; Chmelik, C.; Hibbe, F.; Ruthven, D. M.; Kärger, J. Micro-Imaging by Interference Microscopy: A Case Study of Orientation-Dependent Guest Diffusion in MFI-Type Zeolite Host Crystals. *Materials* **2012**, *5*, 721-740.

72 Ramanan, H.; Auerbach, S. M. Modeling Jump Diffusion in Zeolites: I. Principles and Methods. In *Fluid Transport in Nanoporous Materials*; Conner, W. C., Fraissard, J., Eds.; Springer Netherlands, 2006; Vol. 219; pp 93-125.

73 Barrer, R. M. Flow Into and Through Zeolite Beds and Compacts. *Langmuir* **1987**, *3*, 309-315.

74 Barrer, R. M.; Rosemblat, M. A. Observations on Sorption and Desorption Kinetics of n-Hexane in Zeolite H-RHO. *Zeolites* **1982**, *2*, 231-233.

75 Magalhães, F. D.; Laurence, R. L.; Conner, W. C. Transport of n-Paraffins in Zeolite T. *AIChE J.* **1996**, *42*, 68-86.

76 Kärger, J.; Ruthven, D. M. On the Comparison Between Macroscopic and N.M.R. Measurements of Intracrystalline Diffusion in Zeolites. *Zeolites* **1989**, *9*, 267-281.

77 Thomas, J. M.; Thomas, W. J. *Principles and Practice of Heterogeneous Catalysis*; Wiley, 1997.

78. W. L. Duncan, K. P. Möller, On the Diffusion of Cyclohexane in ZSM-5 Measured by Zero-Length-Column Chromatography. *Industrial & Engineering Chemistry Research* **39**, 2105-2113 (2000); published online Epub2000/06/01 (10.1021/ie9907573).

79. F. D. d. M. Magalhaes, Ph.D., University of Massachusetts Amherst, United States -- Massachusetts (1997).

80. C. L. Cavalcante, S. Brandani, D. M. Ruthven, Evaluation of the main diffusion path in zeolites from ZLC desorption curves. *Zeolites* **18**, 282-285 (1997)10.1016/s0144-2449(97)00014-6).
81. S. Brandani, D. M. Ruthven, Analysis of ZLC desorption curves for gaseous systems. *Adsorption* **2**, 133-143 (1996)10.1007/bf00127043).
82. M. Eić, D. M. Ruthven, in *Studies in Surface Science and Catalysis*, P. A. Jacobs, R. A. v. Santen, Eds. (Elsevier, 1989), vol. 49, pp. 897-905.
83. D. Green, R. Perry, *Perry's Chemical Engineers' Handbook, Eighth Edition*. (McGraw-Hill Education, 2007).
84. M. Eić, D. M. Ruthven, A new experimental technique for measurement of intracrystalline diffusivity. *Zeolites* **8**, 40-45 (1988)10.1016/s0144-2449(88)80028-9).
85. J. M. Thomas, W. J. Thomas, *Principles and Practice of Heterogeneous Catalysis*. (Wiley, 1997).

CHAPTER 8

ON ASYMMETRIC SURFACE BARRIERS IN MFI ZEOLITES REVEALED BY FREQUENCY RESPONSE

8.1 Introduction

Characterization of diffusion in porous zeolite materials requires knowledge of the characteristic length scales of particles and the type of mass transport. While bulk gas-phase diffusion (adsorbate-adsorbate interactions) in large pores is fast, mass transfer slows within mesopores as guest-host interacts occur more frequently and Knudsen diffusion dominates as diffusivity becomes a function of pore diameter at low pressures.[10,11] As the pore diameter is further decreased comparable to the kinetic diameter of the adsorbate (guest molecule), diffusion is characterized by the configurational diffusion regime and the rate of diffusion is governed by a series of adsorption steps and molecule re-orientation.[10,11] In some cases, existence of systems with both small mesopores and small microcrystalline domains has led to rate-controlling transport in both the micropores and mesopores.[1] This complication is avoided in this experimental study (this paper) by: (a) selection of purely microporous MFI-structured zeolites (silicalite-1, pore size = 5.5-6 $Å^2$), and (b) selection of a slow-diffusing adsorbate, cyclohexane (critical molecular diameter, 6.8 $Å^2$), such that diffusion through the bulk of zeolites are shown to be solely configurational diffusion.[3] For these conditions, temperature activated diffusion coefficients obtained from experimental methods, D_{app}, represent the rate coefficients associated with the rate limiting elementary step of moving from one stable site to an adjacent stable site within the microporous zeolite framework. In the case of the bulk crystal, this coefficient is characteristic of the intracrystalline diffusivity (D), and is temperature-activated in accordance with the Arrhenius relationship, (E_a).

While bulk mass transport in zeolites is widely studied, little is known with regard to fundamental understanding of transport at or near the surface of zeolites.[4, 5] It is understood that additional transport limitations beyond bulk particle diffusion must be considered due to internal grain boundaries and defects,[6-8] surface adsorption/desorption,[9, 10] and most recently the possibility of structural defects at the surface causing partial or total pore blockages.[11-13] The contributions of these potential secondary mass transfer limitations have been probed by several experimental techniques that have been developed to study diffusion in microporous materials.[14, 15] The techniques are classified as either equilibrium measurements (PFG-NMR,[16] Tracer-ZLC[17]) or transport measurements (Frequency Response,[18] ZLC,[11] gravimetric[19, 20]), where the two sets of measured diffusivities are not identical. Equilibrium techniques measure the self-diffusivity (or tracer diffusivity) under equilibrium conditions, while transport techniques measure the transport diffusivity (or apparent diffusivity) in the presence of concentration gradients. The two values can be related by the Darken relationship, which accounts for different loadings by describing the transport diffusivity (D_{app}) as being proportional to the self-diffusivity (D_s) with the proportionality factor being the local slope of the adsorption isotherm.[21, 22] Despite the wide array of experimental techniques and thermodynamic correction factors, differences in observed diffusion coefficients have been reported to vary as many as three orders of magnitude for different techniques.[4, 5] Recently, the same trend was also observed by the use of a single technique and attributed to the strong size-dependence of the apparent diffusion coefficient, leading to the conclusion that transport limitations at or near the surface (surface barriers) dominate the observed mass transport in small zeolite particles.[3, 11]

In this work, we evaluate the relative contributions to mass transfer of cyclohexane in a range of silicalite-1 particle sizes using frequency response. Experimental data collected over a range of particle sizes and temperatures are compared with the existing base model for adsorbate diffusion as well as the Yasuda surface resistance model,[23] which accounts for desorption rate limitations at the surface. A new model is developed to account for the surface limitation which

allows for different kinetics between uptake and release (i.e. bidirectional) of adsorbates through the surface. Deconvoluting the kinetics of bulk diffusion from the surface barrier for both uptake into the pores and release of the pores provides the first mechanistic insight (e.g. kinetic energy barriers) into the nature of MFI surface barriers.

8.2 Methods.

Silicalite-1 particles were synthesized and characterized as described previously.[11, 24] In short, TPAOH solutions, SEOS and water were combined and aged at 353 K for one day while continuously stirring. The gel composition was set with SiO_2 = 0.25, and stoichiometric ratios of TPAOH to water of 11, 28, 100 and 400 for the 80 nm, 200 nm, 500 nm, and 1µm samples, respectively. The gel was then heated at 443 K for one day, then washed and centrifuged until the supernatant pH fell below nine. The largest sample (3 µm) was synthesized by a slightly different method,[11, 25] aging TPABr and NaOH, at 323 K for eight days first. The gel was formed with the composition SiO_2:0.1 TPABr:0.05 Na_2O:4 EtOH:98H_2O, which was then heated in an autoclave at 408 K for 50 h before being washed thoroughly with DI water and dried at 373 K overnight.

Particles size distributions and morphologies were determined using a Magellan 400 (FEI) or 6320JXV (JEOL) to perform scanning electron microscopy (SEM, Figure 1 A-E, Table 1). Samples were prepared on a carbon tape then coated with Pt before being scanned. Acceleration voltages of 3.0 kV with a stage bias of 500 V were used. In all cases, particle size distributions were narrow, validating the monodisperse synthesis.

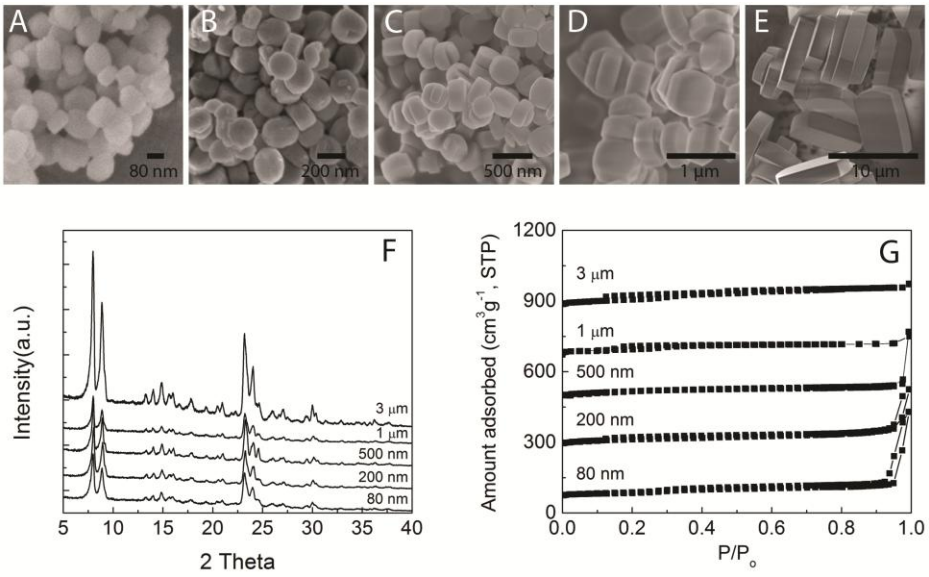

Figure 8-1: **Characterization of Zeolite Particles.** (A) SEM micrographs show monodisperse particles of "coffin" geometry for the five particles examined in this study. (B) XRD data show the scattering patterns and high level of crystallinity typical of purely MFI structured zeolites. (C) N_2 adsorption isotherms exhibit a purely microporous regime for all particles.

Table 8-1: Physical Dimensions of Silicalite-1 Particles.

Nominal Crystal Size	Length (nm)	Width (nm)	Height (nm)	R* (nm)
3 µm	7,680	4,120	1,550	1,800
1 µm	1110	730	420	430
500 nm	460	460	256	231
200 nm	190	170	90	88
80 nm	80	60	60	42.3

$$* \mathbf{R} = \sqrt[3]{\frac{(\mathbf{L}\times\mathbf{W}\times\mathbf{H})\times\mathbf{3}}{\mathbf{4}\times\boldsymbol{\pi}}}$$

X-ray diffraction (XRD) was performed on a 'Pert Pro by PANalytical with Cu K_α radiation. For all crystal sizes, characteristic reflections form MFI were observed (Figure 1F) without indication of crystalline impurities, confirming the crystallinity and structure of silicalite-1. Nitrogen adsorption isotherms were obtained on an Autosorb iQ by Quantachrome. Samples were outgassed at 473 K until pressure changes were observed below 25 mTorr/min. Isotherms

were collected at 77 K (Figure 1G), and shown to exhibit the large microporous regime typical of MFI for all particles. Micropore volumes calculated by the t-plot method were all in the range of 0.10-0.13 cm^3/g, indicating the high expected range for purely MFI structured material.

8.2.1 Frequency Response Apparatus.

The frequency response (FR) method was first established by Yasuda to investigate adsorption[26] then later and diffusion of guest sorbates into porous materials.[27] In this method, the pressure response of a closed sorption chamber under periodic volume perturbations with different frequencies is recorded and fit to a theoretical adsorption/diffusion model. Due to the wide range of the perturbation frequencies available, the frequency response method is able to measure diffusion coefficients that span several orders of magnitude.

A schematic diagram of the frequency response apparatus is presented in Figure 2 and described in detail by Turner et al.[18] The analytical apparatus is composed of a servomotor (R), bellows pump, sample chamber (A), rapid differential pressure transducer (P), dosing manifold, vacuum system (V), and data acquisition system. The servomotor (R) is equipped with an integrated PID controller which allows control of the position and speed of the motor shaft in the range of 0.001-40 Hz. A bellows pump is placed between the motor (R) and the sorption chamber (A) and is used to drive the sinusoidal volume change. The sample chamber (A) is a 316 stainless 4-way cross with a supported stage and imbedded thermocouple. Copper sealed flanges are used to maintain high vacuum (10^{-6} – 10^{-8} torr) inside the chamber. The total volume (neutral bellow displacement) of the camber is 584 cm^3, while the bellows can displace ± 2% of the total volume. The chamber is maintained at isothermal temperatures (set to $50 < T < 275$ °C) by performing PID control on three band heaters located around the entire chamber and allowing sufficient time for thermal equilibration. The sample size (bed thickness) is maintained sufficiently small such that no temperature or pressure gradients exist across the bed. The pressure transducer (P2) on the sorption chamber (A) is a MKS Baratron 10 torr differential capacitance manometer. The

transducer is fixed to the sorption chamber (A) and the referenced to a 150 cm^3 ballast (B). The ballast is housed in an isothermal water bath (T) to maintain constant reference pressure. The dosing manifold is comprised of a stainless steel four-way cross and a three-way tee with a total volume of 270 cm^3. Two inlets (L1, L2) are fixed to the dosing manifold and allow for dosing of either a constant pressure gaseous adsorbate from upper inlet (L1), or a known partial vapor pressure liquid adsorbate from lower port (L2). The entire system is equipped with an ultra-high vacuum pumping system (V) to allow for complete pump-down prior to dosing. The vacuum system (V) consists of a rotary rough pump and turbo-molecular pump which allows for evacuation to 10^{-8} torr.

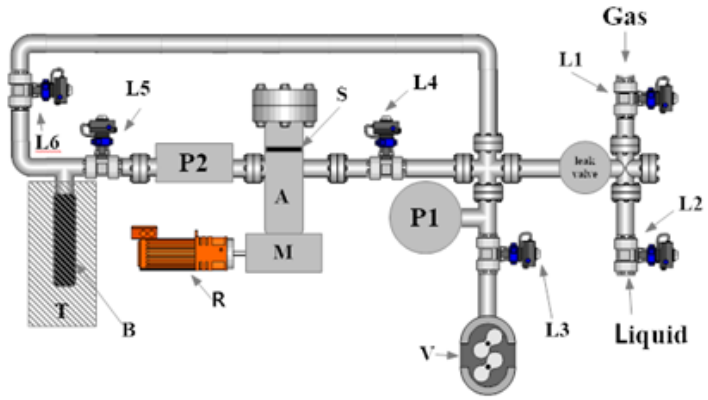

Figure 8-2: **Schematic Depicting the Experimental Frequency Response Apparatus for Measuring Diffusion in Zeolites.** A sinusoidal volume change is induced in the sample chamber, and the corresponding pressure response is fit to coupled particle/chamber mass balances.

8.2.2 Frequency Response Experiment.

Five monodisperse silicalite-1 samples of particles varying over three orders of magnitude in size were synthesized and characterized,[11] as summarized in Table 1. Figure 1 shows the scanning electron micrographs, x-ray diffraction and nitrogen adsorption isotherms for all silicalite-1 samples used in this study. Although all zeolite samples exhibited the "coffin" geometry, the three dimensional nature of MFI pore network makes a spherical geometry more representative for diffusion analysis in small particles, as has previously been shown.[11, 28]

Prior to each run, zeolite samples (150 mg) were degassed inside the sorption chamber overnight at 373 K, 10^{-8} torr. The sorbate (cyclohexane, previously degassed by the "freeze-pump-thaw" method) was then introduced to the sorption chamber at a constant partial pressure through a leak valve, and the sorbate/sorbent system was allowed to reach equilibrium at the desired pressure. A sine-wave volume perturbation of 2% was then applied to the chamber, and an online data acquisition system recorded the transient pressure response from the pressure transducer. For larger zeolite samples (3 μm, 1 μm), a frequency range of 0.0025 to 10 Hz was scanned over 28 steps. For smaller zeolite samples (500 nm, 200 nm, 80 nm), a frequency range of 0.01 to 10 Hz was scanned over 23 steps.

The range of measurable particle sizes analyzed in the frequency response apparatus was considered to ensure measureable mass transport. The diffusional time constant must fall within the measurable transport time range such that the corner frequency (the peak of the out-of-phase function, described in section 3) is within the experimental frequency bounds (0.0025 Hz to 10 Hz for the present system). For this reason, larger particles require the frequency range to be extended. Similarly, the range of diffusivities being examined are at relatively high temperatures compared to previous study by ZLC to ensure operation in the proper regime.[11] For the diffusion-controlled case, the lower and upper limits of the particle size can be validated by substituting the frequency range and diffusion coefficient into, $f = \frac{D}{R^2}$. While this criteria is met for the large particle base case $\left(\frac{D}{R^2} \sim 10^{-3}\ s^{-1}\right)$, the apparent transport timescale no longer scales with the particle size in small particles. Specifically, the transport limitations examined in this study shift the apparent diffusivity to lower values, causing the corner frequency to fall within experimental limits, and thus this criterion is achieved (Figure 4).

8.3 Frequency Response – Theory.

Several models have been proposed in literature to describe mass transport between gases and solids. Each model describes the rate limited transport phenomena that results in macroscopically observed mass transfer rates. In this study, experimental data were fit to three models: (i) a base model describing intracrystalline diffusion, (ii) Yasuda's surface resistance model which adds a surface adsorption/desorption limitation, and (iii) a new model which allows for an asymmetric surface barrier (Model IV in Figure 3).

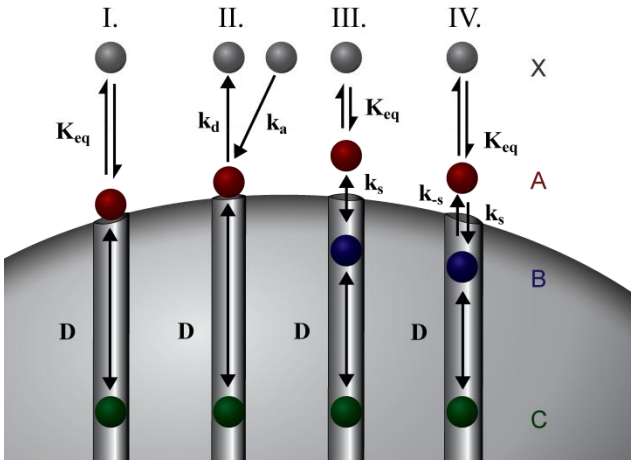

Figure 8-3: **Schematic Representation of Four Zeolite Mass Transport Models.** (I.) Base case, (II.) Yasuda surface resistance, (III.) Ruthven surface barrier, (IV.) Teixeira-Qi asymmetric surface barrier.

The first frequency response model was derived by Yasuda to study the adsorption-desorption of gas molecules onto non-porous metal oxide surfaces.[26] The derivation was based on the Taylor series expansion of the general adsorption-desorption rate equation $\left(R_j = R_{j,e} + \frac{\partial R_j}{\partial P}(P - P_e) + \frac{\partial R_j}{\partial A}(A - A_e)\right)$ and the mass balance within the entire chamber. The kinetics of the adsorption/desorption steps are described by Langmuir kinetics as,[23, 29]

$$\frac{d}{dt}N = k_j P(N_s - N) - k_{-j}N = (k_j P + k_{-j})N + k_j P N_s \qquad 8\text{-}1$$

Since the volume and pressure of the system are changing with time, the theoretical model was expressed in terms of real (in-phase) and imaginary (out-of-phase) parts as shown below.

$$\frac{v}{p}\sin\varphi = \sum_j \frac{k_j \omega}{{k_{-j}}^2 + \omega^2} \qquad 8\text{-}2$$

$$\frac{v}{p}\cos\varphi - 1 = \sum_j \frac{k_j k_{-j}}{{k_{-j}}^2 + \omega^2} \qquad 8\text{-}3$$

where the Langmuir adsorption and desorption rate constants are respectively defined as,

$$k_j = \frac{RT}{V_e}\left(\frac{\partial R_j}{\partial P}\right)_e \qquad 8\text{-}4$$

$$k_{-j} = -\left(\frac{\partial R_j}{\partial A_j}\right)_e \qquad 8\text{-}5$$

R_j is the adsorption rate of species j. A_j is the amount of surface species j. The phase lag of the pressure response is represented by $\varphi = \varphi_z - \varphi_b$, where φ_z and φ_b are the phase lags measured with and without sorbent, respectively. The amplitude ratio of the volume displacement, v, is assessed in the absence of sorbent, and the pressure amplitude ratio, p, is observed with the sorbent in response to the volume change.

8.3.1 Model I: Base Case.

The adsorption-desorption model was modified by Yasuda to investigate the diffusion process within zeolites (Figure 3, Model I).[30, 31] In this case, the rates of surface adsorption and desorption are assumed to be infinite, implying the overall process is controlled by intracrystalline diffusion. Analytical solutions of in-phase and out-of-phase are derived in Appendix A. The functions were derived by combining Fick's first and second laws (diffusion in the pores), Henry's law (equilibrium at the surface), and the overall mass balance in the chamber. For a diffusion process occurring within a spherical zeolite, the two characteristic functions for the in-phase (Eq. 6) and out-of-phase (Eq. 7) are as follows:

$$\frac{v}{p}\sin\varphi = K\delta_s = \frac{6K}{\eta}\left[\frac{1}{2}\left(\frac{\sinh\eta + \sin\eta}{\cosh\eta - \cos\eta}\right) - \frac{1}{\eta}\right] \quad 8\text{-}1$$

$$\frac{v}{p}\cos\varphi - 1 = K\delta_C = \frac{K}{\eta}\left\{\frac{\sinh\eta + \sin\eta}{\cosh\eta + \cos\eta}\right\} \quad 8\text{-}2$$

where,

$$\eta = \sqrt{\frac{2\omega R^2}{D}}, \qquad K = \frac{RTV_S}{V_e}K_H \quad 8\text{-}3$$

V_S is the volume of the zeolite, V_e is the equilibrium volume of the chamber, and K_H is Henry's law constant. R is the particle radius, and D is the intracrystalline diffusion coefficient.

8.3.2 Model II: Yasuda Surface Resistance.

Yasuda extended the base model to describe the case where rates of adsorption and desorption on the surface are not infinite (Figure 3, Model II). In this surface resistance model, the kinetic contribution to the rate exists in accordance with traditional Langmuir adsorption/desorption kinetics (Eq. 1) such that the timescale for adsorption/desorption may contribute significantly to the overall transport time.[30, 31] In this case, in-phase and out-of-phase functions are,

$$\delta_S^{SR} = \left(\frac{a\kappa_a}{\omega}\right)\left[1 - \left(\frac{ak_a}{\omega}\right)\left\{\frac{\frac{a\kappa_a}{\omega} + c\delta_s}{\bar{\theta}}\right\}\right] \quad 8\text{-}1$$

$$\delta_c^{SR} = \left(\frac{a\kappa_a}{\omega}\right)^2\left\{\frac{a + c\delta_c}{\bar{\theta}}\right\} \quad 8\text{-}2$$

Where δ_c and δ_s and the in-phase and out-of-phase functions described for the base case, and

$$\bar{\theta} = \left[\left(\frac{a\kappa_a}{\omega}\right) + c\delta_s\right]^2 + (a + c\delta_c)^2 \quad 8\text{-}3$$

$$a = \left(\frac{dA}{dP}\right)_e\left(\frac{d(A+C)}{dP}\right)_e^{-1} = 1 - c \quad 8\text{-}4$$

In Eq. 12, "A" represents the amount of species on the surface, and "C" is that within the pores. From the definition of the Langmuir isotherm at the surface (Eq. 1), $\kappa_a$is the sum of adsorption and desorption rate constants ($\kappa_a = k_aP + k_d$). The parameter $a\kappa_a$ physically represents the inverse time scale of surface resistance. The magnitude of the surface barrier effect can be inferred from the area to the right of the intersection between in-phase and out-phase

function curves. Mathematically, the magnitude of the cross area depends on the value of dimensionless number, λ, which characterizes the ratio of diffusion time scale to surface resistance time scale,

$$\lambda = \frac{\tau_D}{\tau_s} = a\kappa_a \frac{R^2}{D} \qquad 8\text{-}5$$

8.3.3 Model IV: Teixeira-Qi (T-Q).

The surface-barrier model derived by Yasuda assumes that the rates of mass transfer into and out of the surface are related to equilibrium by the Langmuir relationship (Eq. 1). While this model accurately describes the situation where surface barriers arise from adsorption/desorption limitations, it does not describe the other mechanisms for surface barriers (pore narrowing, pore blockage). Ruthven previously removed the Langmuir constraint in lieu of a lumped symmetrical barrier at the surface for the desorption case (Figure 3, Model III).[32] However, the Ruthven model does not extend to the combined uptake/release system where separate rates into and out of the surface may be observed. Owing to these limitations, a new surface-barrier model with two surface rate constants (forward and reverse) is derived to improve upon the previous surface restriction. In this model, the following assumptions are made:

1. Diffusion inside the zeolite is assumed to be Fickian
2. The diffusion coefficient and surface rate parameters are solely functions of temperature and are independent of concentration (valid for dilute systems) and particle size
3. Periodic volume perturbation is small (< 2%)
4. The total surface concentration (C_R) is the sum of the outer surface concentration "A" and inner surface concentration "B"

The governing mass balance within a spherical zeolite particle can be expressed as,

$$\frac{\partial C}{\partial t} = \frac{D}{r^2}\frac{\partial}{\partial r}\left\{r^2\frac{\partial C}{\partial r}\right\} \quad 8\text{-}1$$

At the center of the zeolite, the symmetry boundary condition is,

$$\left.\frac{\partial C}{\partial r}\right|_{r=0} = 0 \quad 8\text{-}2$$

The boundary condition at the surface arises by balancing the internal flux (Fickian) with the flux through the surface. In this case, the flux at the surface is described as the sum of the rates into and out of the surface,

$$J_s = \frac{R}{3}[k_s A - k_{-s} B] \quad 8\text{-}3$$

Where J_s is the surface flux, k_{-s} is the rate constant associated with release from the surface, and k_s is the uptake rate constant, and "A" is in equilibrium with the gas in accordance with Henry's Law. Applying assumptions 3 and 4, Eq. 16 becomes

$$J_s = k_s\frac{R}{3}C_R - (k_{-s} + k_s)\frac{R}{3}\frac{k_s}{k_{-s}}A \quad 8\text{-}4$$

This surface flux has to be balanced with the diffusion flux giving rise to the second boundary condition,

$$\left.\frac{dC}{dr}\right|_R = \frac{-R}{3D}\left[k_s\left(C_R - C_{R,e}\right) - (k_{-s} + k_s)\frac{k_s}{k_{-s}}\left(\frac{K_H}{V_s}(P - P_e)\right)\right] \quad 8\text{-}5$$

where $K_H = \frac{d(V_s A)}{dP}$, is the local Henry's constant. The above boundary value problem can be further non-dimensionalised as follows,

$$\frac{\lambda}{1+\lambda}\frac{\partial \bar{C}}{\partial \tau} = \frac{1}{\eta^2}\frac{\partial}{\partial \eta}\left(\eta^2\frac{\partial \bar{C}}{\partial \eta}\right) \quad 8\text{-}6$$

with boundary conditions,

$$\left.\frac{d\bar{C}}{d\eta}\right|_{\eta=0} = 0 \quad 8\text{-}7$$

$$\left.\frac{d\bar{C}}{d\eta}\right|_{\eta=1} = -\frac{R^2}{3D}k_s(\bar{C} - \bar{P}) \quad 8\text{-}8$$

where,

$$\eta \equiv \frac{r}{R}, \qquad \tau \equiv \frac{t}{t_D + t_S} = \frac{t}{\frac{R^2}{D} + \frac{1}{k_s + k_{-s}}} = \frac{Dt}{R^2}\left(1 + \frac{1}{\lambda}\right)^{-1}$$
$$\lambda \equiv \frac{t_D}{t_s} = \left(\frac{D}{R^2}\frac{1}{k_s + k_{-s}}\right)^{-1}, \bar{C} \equiv \frac{C - C_e}{C_e} \qquad 8\text{-}9$$

The above boundary value problem can be solved by using Laplace transform and the resulting concentration profile is,

$$\tilde{C} = \frac{1}{\eta}\left[\frac{R^2}{3D}k_s\tilde{P}\ \sinh\frac{\left(\sqrt{\frac{\lambda}{1+\lambda}}s\,\eta\right)}{\left[-\sinh\left(\sqrt{\frac{\lambda}{1+\lambda}}s\right) + \sqrt{\frac{\lambda}{1+\lambda}}s\cosh\left(\sqrt{\frac{\lambda}{1+\lambda}}s\right) + \frac{R^2}{3D}(k_s\sinh\left(\sqrt{\frac{\lambda}{1+\lambda}}s\right)\right]}\right] \qquad 8\text{-}10$$

where "s" is Laplace variable and tilde denotes a Laplace transformed variable. Next, consider the total mass balance within the entire chamber (gas phase + zeolite),

$$sn_e(\tilde{p} - \tilde{v}) + s\left\{NC_e\int_0^V \tilde{C}dV\right\} = 0 \qquad 8\text{-}11$$

After substitution of Eq. 23 into Eq. 24, a numerical solution of frequency response can be obtained as,

$$Q = \frac{K(k_s)\frac{R^2}{D}\left\{\sqrt{\frac{1+\lambda}{\lambda\, s}}\cosh\left(\sqrt{\frac{\lambda}{1+\lambda}}s\right) - \frac{1+\lambda}{\lambda\, s}\sinh\left(\sqrt{\frac{\lambda}{1+\lambda}}s\right)\right\}}{\left[-\sinh\left(\sqrt{\frac{\lambda}{1+\lambda}}s\right) + \sqrt{\frac{\lambda}{1+\lambda}}s\cosh\left(\sqrt{\frac{\lambda}{1+\lambda}}s\right) + \frac{R^2}{3D}(k_s\sinh\left(\sqrt{\frac{\lambda}{1+\lambda}}s\right)\right]} \qquad 8\text{-}12$$
$$= \frac{\tilde{v}}{\tilde{p}} - 1$$

Similar to Yasuda's model, Eq. 13 can be expressed in terms of a real part (in-phase) and imaginary part (out-of-phase). The solution was solved numerically in Matlab and expressed as,

$$\frac{v}{p}\sin\varphi = \mathrm{Re}(Q) \qquad 8\text{-}13$$
$$\frac{v}{p}\cos\varphi - 1 = -\mathrm{Im}(Q) \qquad 8\text{-}14$$

Data fitting was performed using Matlab by performing a four parameter least squares optimization for parameters: D, K, k_s, k_{-s}. The optimization was performed simultaneously for all particle sizes at each temperature to minimize the square of the summed errors of the in-phase and out-of-phase frequency response data and model fits. Results

Pressure-volume response curves were obtained for the five particles described in Table 2 at four temperatures in the range of 423-513 K. Periodic, steady state data were obtained for each particle size at frequencies ranging between 0.0025-10 Hz and were transformed to the in-phase and out-phase functions described by the left side of Eq. 6 and Eq. 7, respectively (Figure 4, data points).

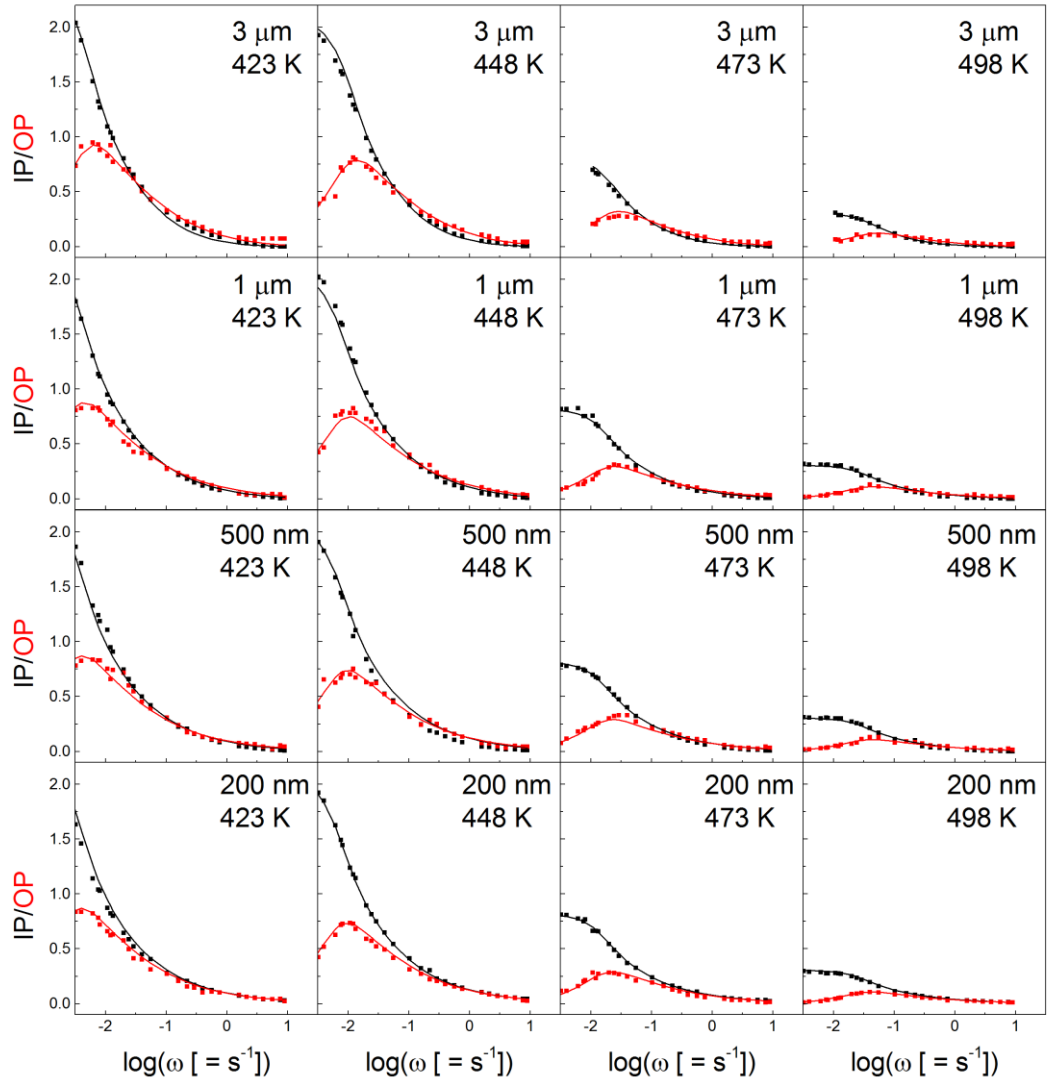

Figure 8-4: **In-Phase (IP) and Out-of-Phase (OP) Frequency Response of Cyclohexane in Silicalite-1 with T-Q Model Fit.** Transformed pressure response data represented as in-phase (■) and out-of-phase (■) data collected at each frequency. Solid lines represent the Teixeira-Qi model fit for each temperature.

The base case (Figure 3, Model I), was first used to fit the experimental data. However, the base model poorly fit the data in small particles due the cross of the in-phase and out-of-phase data. As is noted by literature, poor fitting is indicative of a "surface barrier" or "surface resistance" near the zeolite surface, and a model accounting for surface limitations is required to accurately describe the mass transfer process.[18]

Model parameter optimizations for Yasuda's surface resistance model (Eq. 9-12, Model II) and the T-Q surface resistance model (Eq. 25-27, Model IV) were performed using a log-normal least squares optimization for the respective in-phase and out-of-phase functions, as shown in Figure 9 and Figure 4, respectively. The Yasuda surface resistance model requires a three parameter fit (**D**, $\boldsymbol{\kappa_a}$, **K**) to determine the intracrystalline diffusion constant, Langmuir rate constant, and the equilibrium constant between surface adsorbed species and bulk gas phase species. In the case of the T-Q model, the surface limitation is captured by the two parameters, "$\mathbf{k_s}$" and "$\mathbf{k_{-s}}$", which represent the forward and reverse mass transfer rates at the zeolite surface. In both cases, characteristic mass transfer timescales are observed as the corner frequencies of the out-of-phase function, represented by the peaks in the data of Figure 4. As temperature increases, peaks are observed to shift to higher frequencies (right), indicating faster overall transport rates. Similarly, as particle sizes decreased, a corresponding shift is observed to higher frequencies, again indicating a transition to faster transport rates as is typical for diffusion-controlled processes. Data for the large particles are characteristic of intracrystalline diffusion-controlled systems, where the in-phase and out-of-phase data do not cross; the single corner frequency occurs at a frequency characteristic of the diffusional time constant. Also, for large particles, the base model fit (Model I) exhibits similar fitting parameters to those obtained by the Yasuda surface resistance model (Model II). For small particles, however, the overlap between the two characteristic functions becomes significant, indicating an increasing transition to surface-controlled mass transfer limitations.

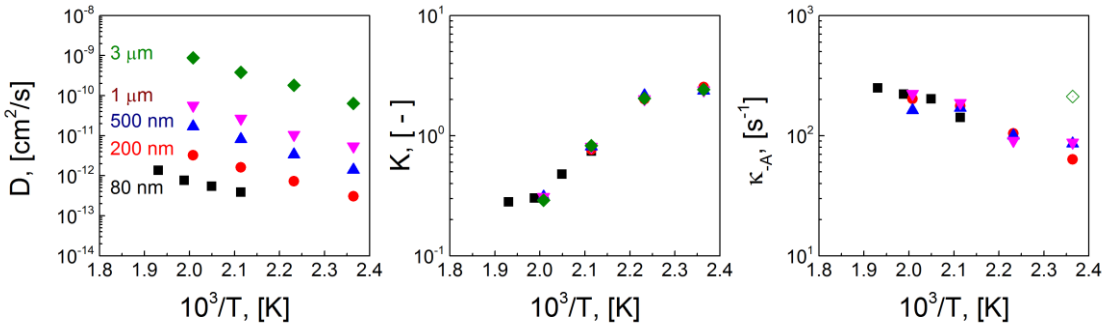

Figure 8-5: **Yasuda Surface Resistance Model.** The Yasuda surface resistance model fit was performed independently at each particle size and temperature. While the equilibrium constant and surface barrier parameter collapse for all particles, significant size-dependence is observed in the diffusion coefficient, indicating that the Langmuir resistance does not accurately capture the observed surface barriers here.

By introducing a rate limitation at the surface, both the Yasuda surface resistance and T-Q models fit the raw experimental data well, as observed in Figure 4 and Figure 9. Fitting parameters for the Yasuda surface resistance and T-Q model are summarized in Table 3. For both model fits, the equilibrium constant obtained from fitting, K, is associated with Henry's constant by Eq. 8 . The equilibrium constant was activated in accordance with the van't Hoff relationship,[33]

$$K = K_0 \exp\left(\frac{-\Delta U_0}{\mathcal{R}T}\right) = K_0 \exp\left(\frac{-\Delta H_s^{ads}}{\mathcal{R}T} - 1\right) \qquad 8\text{-}1$$

where ΔH_s^{ads} is the heat of adsorption associated with cyclohexane reversibly adsorbing or desorbing from the *outer zeolite surface*. The heat of adsorption to the *outer surface* of the zeolite is shown here to be ΔH_s^{ads} = 45.8 ± 11.4 kJ/mol. As expected, this parameter is independent of particle size and is only a function of temperature and the equilibrium pressure.

For Model II (Yasuda surface resistance), the apparent diffusivity, D_{app}, is a strong function of particle size, as shown in Figure 5. The data exhibit an Arrhenius relationship for diffusion for each particle with constant activation energy. However, the pre-exponential is observed to decrease drastically with decreasing particle size, indicating that a second, size-dependent phenomenon becomes rate relevant in small particles. Dependence of the apparent

diffusion coefficient with particle size is explored in greater detail in the discussion section of this text.

The T-Q model accounts for both gas/surface equilibrium and surface resistance, and the transport timescales for intracrystalline diffusion are extracted and plotted versus inverse temperature in Figure 6. Measured values of diffusivity collapse for all zeolite particles, indicating intracrystalline diffusion is independent of particle size, as is physically expected. Both constants describing the rate through the surface (k_s and k_{-s}) and apparent diffusivity are temperature activated in accordance with an Arrhenius relationship, as shown below.

$$D = D_0 \exp\left(-\frac{E_a}{\mathcal{R}T}\right)$$
$$k_s = k_{s,0} \exp\left(-\frac{E_{a,s}}{\mathcal{R}T}\right) \qquad 8\text{-}2$$
$$k_{-s} = k_{-s,0} \exp\left(-\frac{E_{a,-s}}{\mathcal{R}T}\right)$$

where E_a, $E_{a,s}$and $E_{a,-s}$ are the activation energies for diffusion, uptake and release from the exterior/interior surface, respectively. If all silicalite-1 particles are assumed to share the same surface and bulk structures, all respective activation energies should be constant irrespective of particle size, which is consistent with the model fits presented here and in good agreement with literature values for diffusion of cyclohexane in silicalite-1.[3]

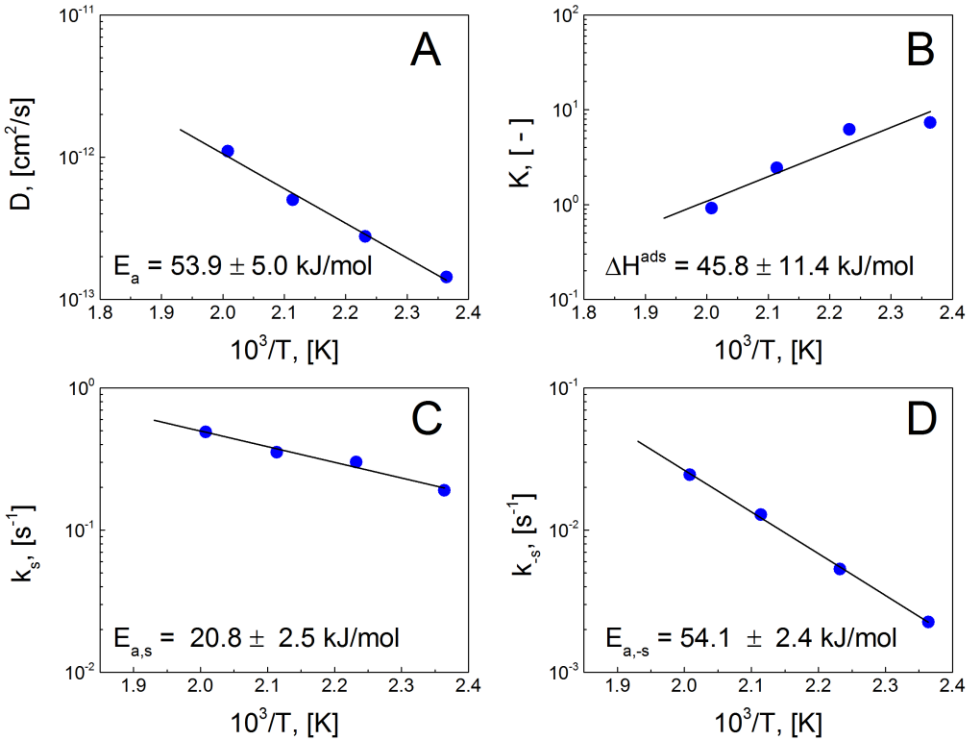

Figure 8-6: The four parameter Teixeira-Qi model was fit at each temperature, with respective constants plotted with inverse temperature. All parameters are temperature activated, with the activation energies of the intracrystalline diffusivity and surface release matching.

8.4 Discussion

Three models were independently evaluated to describe the volume-pressure frequency response data for cyclohexane in silicalite-1. The base case (Model I), has been widely used to describe diffusion-controlled mass transport in microporous materials. This model arises from solving the one-dimensional spherical transient diffusion system with a sinusoidal boundary condition describing the equilibrated surface concentration (Henry's Law). As equilibrium is always assumed at the surface in this model, the externally observed pressure response is dependent on the equilibrium constant, diffusivity and particle size only. The base model works well to describe systems where diffusion within the bulk of the crystal is rate dominating, and all other rate limitations (adsorption/desorption, external boundary layers, surface defects, internal

grain boundaries, etc.) are negligible. This criteria often holds true for slow-diffusing molecules and for large particles ($D/R^2 < 10^{-3}$ s^{-1}). Experimentally, deviation from the base case is directly observed by a cross in the in-phase and out-of-phase function/data. In the work presented in this study, as with other cases in the literature,[18, 34] the base case was not able to describe the cyclohexane/silicalite-1 system for small particles. For this reason, other models were considered that describe series transport processes.

In the case of a surface limitation, macroscopic transport observed experimentally is described by two series processes: Fickian diffusion in the micropores and transport at or through the surface. In the case where the timescale for the surface transport is sufficiently small ($\tau_s \ll \tau_D$), surface transport is not rate limiting, and experimentally characterized mass transfer collapses to the base case. However, if there exists a transport limitation at the surface with a timescale on the order of or higher than the diffusional timescale, then the limitation must be mathematically described to fit the experimental data. The frequency response model for the base case can then be modified replacing the assumption of equilibrium at the particle surface in lieu of a kinetic boundary condition.

The mostly widely used model to describe frequency response mass transfer data containing surface limitations, or "surface barriers," is described by Yasuda.[34] In this model, the kinetic rate limitation through the surface is assumed to arise from the rate of adsorption/desorption. Langmuirian kinetics (Eq. 1) are assumed to describe the competitive rates of adsorption and desorption, resulting in a modified boundary condition and solution to the in-phase and out-of-phase curves. Unlike the base model, the Yasuda model was able to fit the experimental response curves (Figure 9) by introducing the additional fitting parameter, κ_{-A}. The in-phase and out-of-phase data can then be fit by $f(D, K, \kappa_{-A})$, where the three parameters represent the bulk diffusivity, the equilibrium constant (ratio of adsorption/desorption rate constants), and lumped Langmuir parameter (function of the adsorption/desorption constants). Alternatively, this can be evaluated in terms of more familiar parameters such that the data can be

fit as $f(D, k_a, k_d)$, where the response is now a function of the Langmuir rate parameters for adsorption and desorption described by Eq. 1. The fitting parameters extracted from Figure 9 are described in Figure 3. While the introduction of a rate limitation at the surface was able to fit the raw data obtained from frequency response, the extracted parameters do not accurately describe the physical system; the diffusion coefficients demonstrate strong particle size dependence, which is inconsistent with Fick's Law for configurational diffusion through microporous channels. Identical molecule/pore combinations should exhibit identical bulk diffusion coefficients regardless of particle size.

The Teixeira-Qi (T-Q) model was developed to introduce an asymmetric surface barrier that removes the constraint relating the adsorption and desorption rate constants to a Langmuir relationship ($K_{eq} = k_a/k_d$)). Similar to the previous case, this model utilizes a boundary condition arising from the balance of the diffusive flux and the flux through the surface. While equilibrium is still assumed between the gas phase and the external surface (similar to the base and Yasuda surface resistance cases), the kinetic steps of permeating into and out of the surface independently contribute to the overall transport timescales. As shown in Figure 4, the T-Q model fit to the raw frequency response data is similar to that of the Yasuda surface resistance model described earlier. The crossing of the in-phase and out-of-phase curves is well captured, and the fitting parameters are summarized in Figure 6 and Table 2. However, a single set of temperature-activated fitting parameters is able to accurately describe cyclohexane transport in all particles across multiple orders of magnitude in size. The diffusivity parameter collapses onto a single curve which obeys the Arrhenius relationship for diffusion (Eq. 29). The additional two parameters represent the rate constants for penetrating into and out of the surface (k_s, k_{-s}), each of which is temperature activated in a similar manner (Eq. 29). The rate entering into the pores was observed to be up to an order of magnitude higher than that observed describing the release from the pores, which is consistent with interference microscopy studies performed during both

uptake and desorption of large particles, where the transport through the surface was observed to be an order of magnitude faster during uptake.[35]

Table 8-2: Frequency Response Parameters Obtained from Fitting Models I (Base), II (Yasuda) and IV (Teixeira-Qi).

		I. Base Case[a]		II. Yasuda Surface Resistance			IV. T-Q Bi-directional Surface Resistance[b]			
	T (K)	$D\times10^{12}$ (cm^2/s)	K (-)	$D\times10^{12}$ (cm^2/s)	K (-)	κ_{-A} (s^{-1})	$D\times10^{12}$ (cm^2/s)	K (-)	k_s (s^{-1})	k_{-s} (s^{-1})
3 μm	423	62.6	2.40	63.8	2.42	212.0	0.14	7.35	0.19	0.0026
	448	168	2.03	181.7	2.05	-	0.28	6.22	0.30	0.0053
	473	376	0.83	381.8	0.83	-	0.50	2.45	0.35	0.0128
	498	741	0.30	886.1	0.29	-	1.10	0.91	0.49	0.0244
1 μm	423	-	-	5.43	2.39	87.7	0.14	7.35	0.19	0.0026
	448	-	-	10.61	2.02	90.8	0.28	6.22	0.30	0.0053
	473	-	-	26.92	0.81	188.1	0.50	2.45	0.35	0.0128
	498	-	-	56.78	0.31	223.1	1.10	0.91	0.49	0.0244
500 nm	423	-	-	1.39	2.37	85.8	0.14	7.35	0.19	0.0026
	448	-	-	3.39	2.17	100.3	0.28	6.22	0.30	0.0053
	473	-	-	8.16	0.81	170.5	0.50	2.45	0.35	0.0128
	498	-	-	17.02	0.31	163.2	1.10	0.91	0.49	0.0244
200 nm	423	-	-	0.31	2.54	63.5	0.14	7.35	0.19	0.0026
	448	-	-	0.72	2.02	104.5	0.28	6.22	0.30	0.0053
	473	-	-	1.61	0.77	177.0	0.50	2.45	0.35	0.0128
	498	-	-	3.23	0.30	203.0	1.10	0.91	0.49	0.0244
80 nm	473	-	-	0.39	0.74	141.7	-	-	-	-
	488	-	-	0.55	0.48	202.1	-	-	-	-
	503	-	-	0.77	0.30	221.7	-	-	-	-
	518	-	-	1.36	0.28	249.4	-	-	-	-

[a] Fit only obtainable for largest particle
[b] Model optimization was performed over entire particle size domain such that only one set of parameters exist at each temperature.

8.4.1 Temperature Activation

Literature-reported values for diffusion of cyclohexane in silicalite-1 often report similar activation energies (30-60 kJ/mol),[2, 3, 11, 36-39] despite orders of magnitude differences in diffusivity. The activated step in all these cases is claimed to be intracrystalline diffusion of cyclohexane within microporous MFI channels. Figure 7 depicts the energies associated with the series processes of intracrystalline diffusion, transport through the surface and

adsorption/desorption to the gas phase. The two surface parameters exhibited different activation energies, indicating the asymmetric nature of the surface barrier. The parameter for uptake into the surface exhibited an activation energy of $E_{a,s}$ = 20.8 ± 2.5 kJ/mol, while exiting the surface was activated similar to that of diffusion, $E_{a,-s}$ = 54.1 ± 2.4 kJ/mol. In this work, an intracrystalline activation energy of 53.9 ± 5.0 kJ/mol was observed, which is consistent with previously reported values. The equilibrium constant was also activated in accordance with the van't Hoff relationship (Eq. 28). In this study, the heat of adsorption *to the surface* (ΔH_s^{ads}) was observed as 45.8 ± 11.4 kJ/mol.

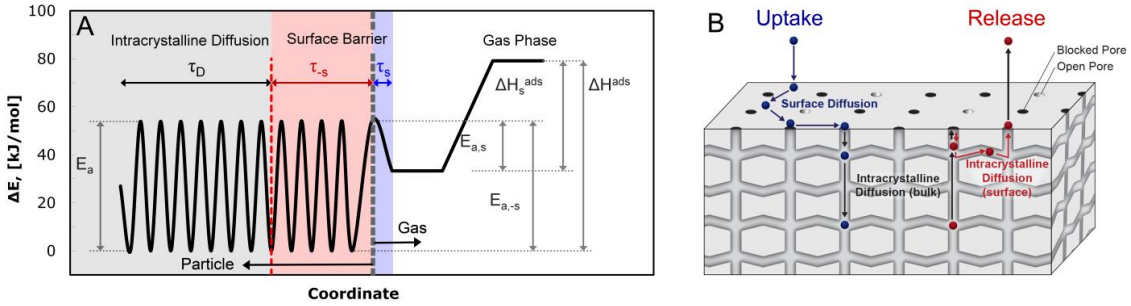

Figure 8-7: **Zeolite Mass Transport with Surface Pore Blockages. A.** Energy diagram for intracrystalline bulk diffusion (E_a, τ_D), surface heat of adsorption (ΔH_s^{ads}), uptake surface barrier ($E_{a,s}$, τ_s), release surface barrier ($E_{a,-s}$, τ_{-S}), and heat of adsorption (ΔH^{ads}). **B.** During uptake (blue), surface pore blockages cause a molecule to adsorb, undergo surface diffusion until finally locating and entering into an open pore. During the release from the zeolite (red), a molecule diffuses to the surface after which it must continue to diffuse within the lattice until locating and exiting an open pore.

Kinetics of cyclohexane transport from inside the particle to the gas phase are thermodynamically consistent with the heat of adsorption of cyclohexane. As shown in Figure 7, the heat of adsorption of cyclohexane in silicalite-1 should be related to the surface release activation energy ($E_{a,-s}$), surface uptake activation energy ($E_{a,s}$), and the heat of adsorption to the surface (ΔH_s^{ads}) by the following relationship,

$$\Delta H^{ads} = E_{a,-s} - E_{a,s} + \Delta H_s^{ads}$$

$$\Delta H^{ads}\ (kJ/mol) = [54.1 \pm 2.4] - [20.8 \pm 2.5] + (45.8 \pm 11.4) = (79.1 \pm 16.3\ kJ/mol) \quad 8\text{-}1$$

The sum of the three energy barriers when added by Eq. 30 equals 79.1±16.3 kJ/mol, which is inclusive of values of the heat of adsorption of cyclohexane in silicalite-1 when

accounting for experimental error. Previous studies have measured the heat of adsorption into large silicalite-1 particles to be 63.2 kJ/mol[33] and 70 kJ/mol.[40] Close agreement by Eq. 30 between measured kinetics and independently measured heat of adsorption provides strong support for the validity of the T-Q model.

8.4.2 Transport Barriers

Barriers to intracrystalline diffusion have been proposed in numerous forms ranging from the intergrowths, internal grain boundaries and pore saturation to kinetically-limited adsorption/desorption, surface pore narrowing and surface pore blockages. Surface barriers and their potential applications to the microporous materials examined in this study are explored here and summarized in Table 3.

Table 8-3: Proposed Mechanisms of Surface Barriers and Associated Kinetic Criteria.

Mechanism/ Limitation	Ref.	Criteria Met	Criteria Not Met	Conclusion
Internal Barriers Subcrystal grain boundaries, intergrowths and internal defects slow intracrystalline transport.	[12] [19] [51] [52]	$D_{app} < D$ $E_{app} = \text{constant}$	$D \neq f(R)$	Does not account for size dependence.
Adsorption/ Desorption (Yasuda Surface Resistance) Timescale associated with adsorption/desorption to the outer surface from the gas phase is slow relative to internal diffusion.	[21] [28] [44]	$\tau_{app} = f(R) = \frac{R^2}{D} + \frac{1}{k_a P} + \frac{1}{k_d}$ $k_a \neq f(R)$ $k_d \neq f(R)$	$D \neq f(R)$ $k_a P \ll 10^{13}\, s^{-1}$	Does account for size dependence. Surface parameters do not scale properly.
Pore Narrowing[1-3] Surface pores are narrowed/partially obstructed causing an energetic barrier to penetrate the surface.	[12] [56] [57]	$\tau_{app} = f(R) = \frac{R^2}{D} + \frac{1}{k_a P} + \frac{1}{k_d}$	$k_s \neq k_{-s}$ $E_{a,-s} > E_a$	Does account for size dependence. Surface kinetics are not symmetrical. Increase to energetic barrier is not observed.
Pore Blockage[2, 4-6] A substantial fraction of pores are blocked at the surface, causing an increase in the diffusional length scale associated with release	[12] [45] [62] [63]	$\tau_{app} = f(R) = \frac{R^2}{D} + \frac{1}{k_a P} + \frac{1}{k_d}$ $k_s \neq k_{-s}$ $E_a = E_{-s} > E_s$	-	Does account for size dependence and asymmetric surface barriers with energetics described by intracrystalline diffusion barriers and adsorption enthalpies.

8.4.2.2 Internal Barriers

Intrinsic internal barriers are proposed to exist resulting from particle synthesis during crystal growth of MFI-structured zeolites.[45, 46] Silicalite-1 is not a single crystal but rather is composed of several subcrystals whose interface presents an internal grain boundary with pore misalignments as small as 0.5-2°.[8] Additionally, both intergrowths and internal defects are possible within single particles. While such internal barriers are present and likely contribute to the macroscopically observed rate, they are not thought to lead to the drastic size-dependent inhibition observed in these experiments and others.[11]

8.4.2.3 Surface Barriers: Energetic

Anactivation barrier exists for a molecule being transported from a bulk gas to the inner surface of a zeolite prior to entering the purely intracrystalline transport domain. During uptake, a molecule travels in the gas phase to the particle, adsorbs to the outer surface, re-orients and enters into a pore. Though usually considered fast (surface permeability ~ 10^{-5} - 10^{-7} cm/s) [35] when compared to configurational diffusion (< 10^{-6} cm^2/s) ,[47] it can present a possible rate limitation for small particles. As concentrations are dilute, no substantial boundary layer is expected, making the first possible rate limitation associated with the adsorption and desorption of a molecule from the gas phase in close proximity to the outer solid surface. For zeolite systems, this rate is captured by the Langmuir relationship, where $\tau_s = \left(\frac{1}{k_a P} + \frac{1}{k_d}\right)$. In the case of this study, typical values of this time constant range from 10^0 – 10^2 s, which is shorter than the smallest diffusional time ($\tau_D > 10^2$ s), again validating the assumption of equilibrium between the surface and the gas phase.

The final step is associated with the both enthalpic and entropic molecular confinement at or near the pore surface. The enthalpic contribution to the rate of pore entering is associated with the guest molecule (cyclohexane, critical diameter = 6.0-6.9 Å, kinetic diameter = 5.7 Å)[33] undergoing a high energy transition to enter within the micropores of silicalite-1 (~5.5 Å).[48]

The entropic contribution of molecules entering pores, which is thought to apply during uptake, can potentially lead to a decrease in the pre-exponential for diffusion as described by Ford et al.[49] and the relationship,[10]

$$D_0 = \frac{a^2\, w(T)}{2\pi} \exp\left(-\frac{\Delta S(T)}{k_B}\right) \qquad 8\text{-}1$$

Molecular rearrangement is expected to reduce the pre-exponential for diffusion during the uptake process, as no such rearrangement is needed upon release. Additionally, the temperature contribution to the diffusion coefficient from the pre-exponential is not dominant when compared to the enthalpic effect $\left(\exp\left(-\frac{E_a}{RT}\right)\right)$, and therefore the observed temperature

dependence should remain attributed to intracrystalline diffusion. In this work, it is shown that the activation energy to enter the pores ($E_{a,s}$ = 20.8 kJ/mol) is substantially less than that of intracrystalline diffusivity (E_a = 53.9 kJ/mol), indicating that the mechanism for pore blockage during uptake is likely not due to molecular rearrangement.

Enthalpic barriers during uptake are possible in the case of surface pore narrowing (i.e. structural changes to pores at the surface).[41, 42] In this case, deviation from the MFI structure at the surface could result in a higher energy barrier through a surface defect ($E_{a,s} > E_a$). However, previous experimental work studying the desorption process (ZLC) has demonstrated that no significant difference in activation energies was observed between particles exhibiting surface barrier transport control (small particles) and those exhibiting purely intracrystalline diffusion control (large particles).[11] This result is again affirmed here, where the activation energy for the intracrystalline diffusivity is comparable to the rate constant describing release from the surface (E_{-s} = 54.1 kJ/mol ~ E_a = 53.9 kJ/mol), and less than that into the surface (E_s = 20.8 kJ/mol < E_a = 53.9 kJ/mol). For these reason, it is concluded that the elementary step governing release of molecules from the intracrystalline domain to the bulk gas *at the surface* is likely similar to the mechanism of mass transfer by intracrystalline diffusion (and different from the mechanism describing entering *into the surface).*

8.4.2.4 Surface Barriers: Structural.

Simply put, surface pore blockages can be present when surface defects block the entrance to micropores such that diffusing guest molecules cannot enter/exit. In this case, the flux into a surface is controlled by adsorption, surface diffusion to an open pore and entering into the pore. Flux out of a particle through a surface is controlled by intracrystalline diffusion until a molecule reaches an open pore at the surface. The former is observed to be rate controlling in guest uptake, while the latter is observed during release. By using the frequency response technique with the T-Q model, the two processes are decoupled at the surface, and the kinetic

constants and activation energies are determined. As depicted in Figure 7B, molecules diffusing out of the pores encounter an additional diffusional path length, δ, which presents as a slower macroscopically observed transport rate $\left(\tau = \frac{R^2}{D} + \frac{\delta^2}{D}\right)$. The additional length does not, however, affect the activation energy, because the mechanism of transport remains the same. In the uptake case, the observed transport time scale is associated with a molecule adsorbing to the external surface, diffusing to an open pore, and entering the pore.

The exact nature or structural contribution of surface pore blockages is difficult to elucidate experimentally. This challenge arises from an inability to fully characterize surface termination of the crystalline structure which results from crystal growth. The manifestation of surface blockages could arise from several types of structural defects. Firstly, large areas of uncoordinated lattice or amorphous silica may exist in patches on the surface such that entire regions are blocked, causing patches of surface barriers. Alternatively, pore blockages could be distributed across the particle surface by surface terminated configurations that block pores or obstruct molecules from exiting a pore at the surface.

The presence of surface defects resulting from amorphous or unaligned islands on the surface has been discussed in literature in varying contexts (defects, terraces, islands, nanoparticle aggregation, growth mechanism).[25, 43, 50-53] Such defects are shown to arise in some cases from interpenetrating dangling silanol bonds causing terraces at the surface.[25] However, these features constitute a relatively small fraction of total surface pores, and pore blockages across a wider area must be considered.[44]

The work of Kärger and co-workers has described the presence of physical surface pore blockages as a possible mechanism for describing this surface resistance to diffusion in microporous materials.[13, 35, 44, 54, 55] In MFI, it was proposed that most of the surface pores exhibit blockages, with only a very small fraction allowing transport through the surface.[35] Such blockages are proposed to be surface structure dependent, and thus the fraction of blocked pores

is expected to remain constant, irrespective of particle size. Furthermore, a comparison of transport rates across "cracks" in the bulk portion of a zeolite (fully open pores) versus the outer surface pores reveals slower transport across the as-synthesized surface.[50] Surface etching has been shown to have no effect on these more prominent barriers.[50]

The observed hindered surface permeability is consistent with the theory that pore blockages arise from random surface terminations/amorphous blockages, where the outermost pores differ structurally from the bulk.[56]. With current imaging techniques, however, surface terminations are difficult to visualize experimentally, and the presence of sub-nanometer defects at the surface is not commonly characterized. Experimental techniques including atomic force microscopy (AFM),[25, 51, 57] scanning electron microscopy (SEM),[52], and high resolution transmission electron microscopy (HRTEM)[51, 57, 58] have been used to resolve the post-synthesis surface structure of zeolites, with the best resolution being on the order of several angstroms. While large facets including crystal faces, steps, islands, and grain boundaries are observed on the order of nanometers, surface termination, pore openings, and small defects leading to blockage are considerably more difficult to capture. Existing experimental techniques are unable to definitively describe surface termination and pore blockages on the surface of zeolites.[59] This level of description requires resolution of one angstrom or less due to observe the small pore size of the ten-member MFI rings (5.6 Å). Additionally, it has also been proposed that the use of TEM and STEM to examine the surface of crystals for pore blockage or restrictions will provide an artificially clean appearing surface due to the ability of the technique to penetrate the surface.[52]

Theoretical studies have attempted to describe the growth and surface termination of zeolites. The structure of the pores at the surface is believed to be a direct result of the final growth termination steps during particle synthesis. Recent work by Lupelescu and Rimer has utilized *in situ* atomic force microscopy (AFM) to examine the layered growth mechanism and confirm the initial deposition of a silica nanoparticles followed directed rearrangement of the amorphous silica to the MFI structure.[53] The resulting surface represents a thermodynamically

stable termination of the dangling Si-O bonds. The pores at the surface are modeled computationally using free energy surface minimization techniques, allowing for the prediction of surface termination structures.[60, 61] In MFI, the use of FTIR microscopy on the surface of silicalite-1 has explored the defect density, and determined that locally spaced silanol groups are likely hydrogen bonded.[25] This bridging across so-called 'defects,' may lead to pore blockages. At this point, a significant gap exists in the literature with respect to both direct experimental visualization and indirect theoretical calculations of surface pore blockages in zeolites.

8.4.3 Implications to Hierarchical Materials

Moving forward, surface barriers will have profound impact on the use of zeolites in hierarchical materials where the diffusional length scales are drastically decreased with the introduction of mesopores. In such materials, groups are able to synthesize microporous materials with length scales on the order of a single lattice cell (~2 nm, MFI).[3, 62, 63] While from a practical standpoint, these materials are observed to exhibit substantially improved mass transport properties when compared to traditional large particle zeolites, significant limitations have been shown to still exist.[3] By extracting the measured time constants for the series transport steps described in this work, a relationship is constructed relating the timescale associated with penetrating the surface barrier to that of the bulk particle. Figure 8 shows the experimental values for the cyclohexane/silicalite-1 system at several temperatures and particle sizes. As particle size decreases, a linear relationship is observed versus particle size, as expected by an intracrystalline diffusion controlled system where the time constant scales with the square of particle size. Plotted at smaller particle sizes, however, are calculated time constants for the hierarchical particles (3DOm-i and SPP). These materials tend toward a purely surface-controlled case which has been shown to be rate dominating in these small particles. While the establishment of the asymmetric structural surface barrier described in this work moves toward understanding the transport limitations at the surface of zeolites, further understanding is needed to elucidate the cause and

means of removal of such barriers, thus allowing mesoporous materials to achieve their full potential.

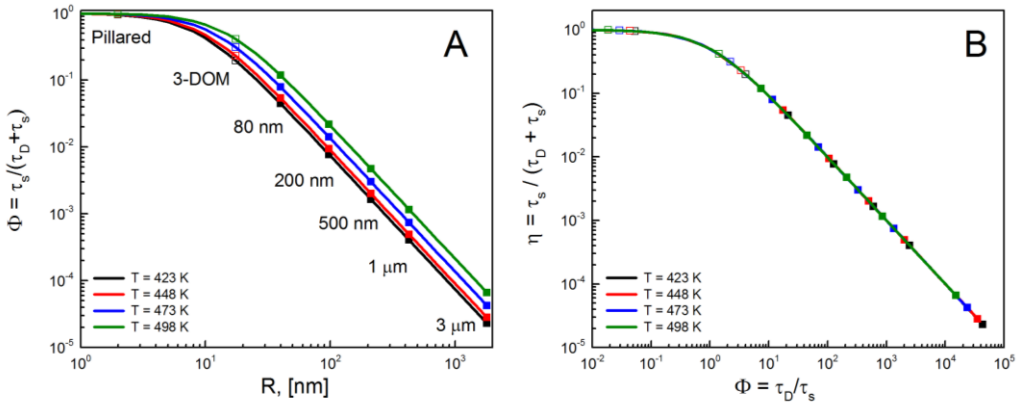

Figure 8-8: **Surface and Bulk Mass Transfer** Time Constants for Mesoporous Materials. Experimentally measured time constants allow for determination of relative surface barriers (closed symbols) in silicalite-1. Surface limitations in microporous materials is shown to be rate relevant in small particles, and calculations for hierarchical materials (open symbols) including the 3DOm-i and Pillared materials are predicted to experience transport rates dominated by surface barriers.

8.5 Conclusions

For the first time, surface barriers in silicalite-1 are characterized experimentally to exhibit asymmetric kinetic and energy dependences, whereby separate mechanisms are rate controlling for entering and exiting surface pores. Using the frequency response technique, surface barriers are shown to become rate relevant and eventually dominate mass transport into and out of small silicalite-1 particles (< 100 nm). Mechanistic insight is provided showing the uptake step to exhibit a low activation barrier, while both intracrystalline diffusion and surface release steps exhibit the same activation energies. Structural blockages at the surface of most pores are proposed to describe the observed surface limitation. Despite kinetic characterization of surface limitations, conclusive evidence of surface pore blockages has yet to resolve the surface of MFI to determine the distribution of surface termination structures to quantify the extent of structural pore blockages.

8.6 Appendix A: Supporting Information

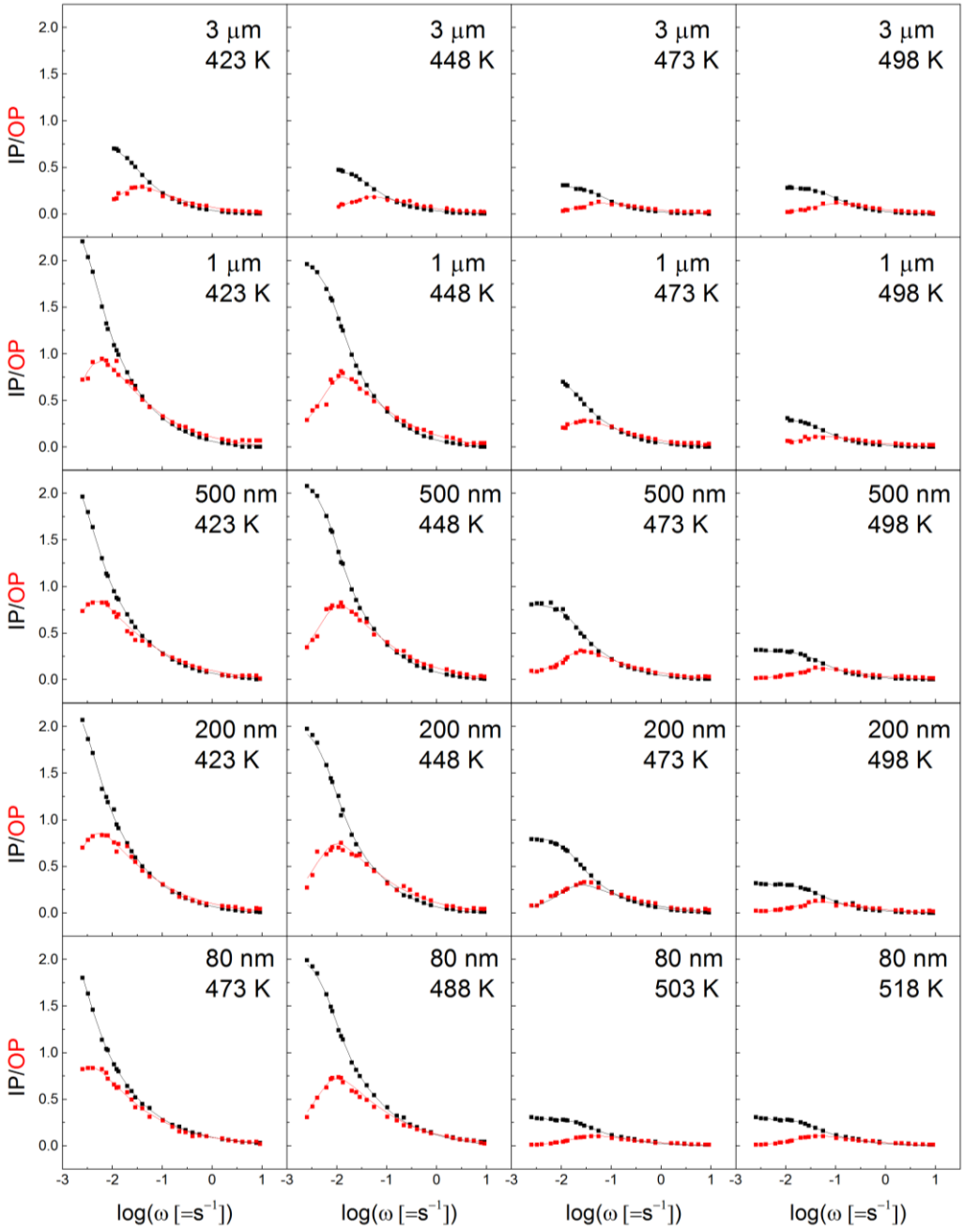

Figure 8-9: **Figure S1. Yasuda Surface Resistance Model Fit to Frequency Response Data.** Transport characteristics of five particles of silicalite-1 (80 nm, 200 nm, 500 nm, 1 µm, 3 m) were studied by frequency response (points) with cyclohexane at 473-518 K. Data were fit to the Yasuda surface resistance model (solid lines).

Table 8-4: Raw Frequency Response Data of 80 nm Silicalite-1 Particles. Rows in the table correspond to applied frequency, ω. 'In' and 'Out" columns correspond to the transformed pressure-volume frequency of the in-phase and out-of-phase function at each temperature.

	200 °C	**200 °C**	**215 °C**	**215 °C**	**230 °C**	**230 °C**	**245 °C**	**245 °C**
log(ω [s^{-1}])	**In**	**Out**	**In**	**Out**	**In**	**Out**	**In**	**Out**
0.95	0.0028	0.0154	0.0039	0.0214	0.0012	0.0232	0.0021	0.0074
0.88	0.0041	0.0245	0.0041	0.0264	0.0143	0.0123	0.0031	0.0175
0.75	0.0063	0.0255	0.0051	0.0255	0.0189	0.0235	0.0041	0.0217
0.60	0.0083	0.0276	0.0082	0.0347	0.0057	0.0256	0.0062	0.0201
0.46	0.0120	0.0324	0.0112	0.0343	0.0072	0.0195	0.0088	0.0237
0.32	0.0156	0.0343	0.0143	0.0437	0.0103	0.0305	0.0129	0.0304
0.20	0.0231	0.0406	0.0214	0.0606	0.0135	0.0237	0.0163	0.0341
-0.12	0.0483	0.0885	0.0400	0.0817	0.0275	0.0531	0.0336	0.0547
-0.25	0.0591	0.0907	0.0509	0.0813	0.0358	0.0560	0.0448	0.0648
-0.40	0.0820	0.1125	0.0670	0.1022	0.0482	0.0658	0.0577	0.0784
-0.54	0.1051	0.1024	0.0811	0.1415	0.0599	0.0782	0.0759	0.0943
-0.66	0.1271	0.1465	0.1003	0.1317	0.0772	0.0880	0.0939	0.0972
-0.80	0.1620	0.1690	0.1285	0.1439	0.0983	0.0992	0.1257	0.1100
-0.99	0.2207	0.1903	0.1685	0.1465	0.1317	0.1022	0.1660	0.1220
-1.25	0.3372	0.2596	0.2630	0.1817	0.2004	0.1299	0.2261	0.1098
-1.40	0.4159	0.2932	0.3193	0.1741	0.2360	0.1092	0.2464	0.0638
-1.54	0.5035	0.2831	0.3690	0.1468	0.2547	0.0721	0.2681	0.0589
-1.61	0.5493	0.2796	0.4053	0.1319	0.2674	0.0658	0.2672	0.0392
-1.70	0.6002	0.2187	0.4240	0.1240	0.2694	0.0656	0.2728	0.0430
-1.88	0.6764	0.2197	0.4571	0.1027	0.3069	0.0397	0.2785	0.0303
-1.92	0.6952	0.1677	0.4675	0.1058	0.3079	0.0436	0.2873	0.0212
-1.97	0.7015	0.1564	0.4738	0.0783	0.3081	0.0321	0.2788	0.0192

Table 8-5: Raw Frequency Response Data of 200 nm Silicalite-1 Particles. Rows in the table correspond to applied frequency, ω. 'In' and 'Out" columns correspond to the transformed pressure-volume frequency of the in-phase and out-of-phase function at each temperature.

	150 °C	**150 °C**	**175 °C**	**175 °C**	**200 °C**	**200 °C**	**225 °C**	**225 °C**
log(ω [s^{-1}])	**In**	**Out**	**In**	**Out**	**In**	**Out**	**In**	**Out**
0.95	0.0020	0.0711	0.0028	0.0429	0.0010	0.0341	0.0021	0.0243
0.88	0.0017	0.0714	0.0041	0.0440	0.0031	0.0243	0.0031	0.0230
0.75	0.0019	0.0714	0.0160	0.0409	0.0061	0.0441	0.0041	0.0234
0.60	0.0031	0.0725	0.0219	0.0321	0.0012	0.0440	0.0051	0.0203
0.46	0.0212	0.0532	0.0313	0.0724	0.0203	0.0436	0.0068	0.0254
0.32	0.0373	0.0679	0.0422	0.0953	0.0268	0.0453	0.0091	0.0317
0.20	0.0480	0.0852	0.0526	0.1073	0.0335	0.0546	0.0146	0.0363
-0.12	0.0857	0.1243	0.0995	0.1525	0.0507	0.0867	0.0218	0.0521
-0.25	0.1053	0.1432	0.1176	0.1855	0.0635	0.0990	0.0315	0.0483
-0.40	0.1372	0.1765	0.1576	0.1968	0.0825	0.1171	0.0364	0.0645
-0.54	0.1670	0.2164	0.2009	0.2279	0.1127	0.1323	0.0461	0.0787
-0.66	0.2012	0.2275	0.2318	0.2793	0.1352	0.1542	0.0667	0.0782
-0.80	0.2449	0.2674	0.2911	0.3149	0.1606	0.1857	0.0790	0.0902
-0.99	0.3108	0.3284	0.3815	0.4152	0.2127	0.2179	0.1213	0.0993
-1.25	0.4311	0.4291	0.5470	0.4915	0.3148	0.2582	0.1800	0.1029
-1.40	0.5420	0.5052	0.6627	0.5782	0.3917	0.2733	0.2152	0.1086
-1.54	0.6541	0.6245	0.7941	0.6249	0.4598	0.2802	0.2466	0.0856
-1.61	0.7059	0.6887	0.8738	0.6980	0.5149	0.2730	0.2591	0.1088
-1.70	0.8025	0.7029	0.9901	0.7282	0.5605	0.2625	0.2723	0.0614
-1.88	0.9883	0.7722	1.2507	0.7932	0.6576	0.2426	0.2876	0.0482
-1.92	1.0381	0.9222	1.2939	0.8123	0.6716	0.2032	0.2877	0.0617
-1.97	1.0932	0.8262	1.3754	0.7632	0.7002	0.2072	0.3078	0.0648
-2.09	1.2659	0.8798	1.5725	0.6923	-	-	-	-
-2.12	1.3228	0.9290	1.5965	0.7220	-	-	-	-
-2.21	1.5050	0.9477	1.6940	0.4562	-	-	-	-
-2.40	1.8786	0.9129	1.8754	0.4343	-	-	-	-
-2.49	2.0381	0.7349	1.9255	0.3913	-	-	-	-
-2.60	2.2070	0.7211	1.9601	0.2902	-	-	-	-

Table 8-6: Raw Frequency Response Data of 500 nm Silicalite-1 Particles. Rows in the table correspond to applied frequency, ω. 'In' and 'Out" columns correspond to the transformed pressure-volume frequency of the in-phase and out-of-phase function at each temperature.

	150 °C	**150 °C**	**175 °C**	**175 °C**	**200 °C**	**200 °C**	**225 °C**	**225 °C**
log(ω [s^{-1}])	**In**	**Out**	**In**	**Out**	**In**	**Out**	**In**	**Out**
0.95	0.0083	0.0097	0.0067	0.0318	0.0078	0.0313	0.0018	0.0153
0.88	0.0025	0.0420	0.0108	0.0401	0.0085	0.0357	0.0021	0.0150
0.75	0.0137	0.0426	0.0130	0.0231	0.0083	0.0319	0.0031	0.0205
0.60	0.0203	0.0418	0.0214	0.0539	0.0101	0.0228	0.0050	0.0216
0.46	0.0303	0.0321	0.0316	0.0642	0.0214	0.0342	0.0067	0.0246
0.32	0.0363	0.0417	0.0420	0.0804	0.0251	0.0432	0.0103	0.0390
0.20	0.0461	0.0482	0.0522	0.1070	0.0337	0.0505	0.0089	0.0292
-0.12	0.0804	0.0930	0.0987	0.1451	0.0647	0.0736	0.0215	0.0411
-0.25	0.0951	0.1232	0.1237	0.1660	0.0719	0.1007	0.0213	0.0505
-0.40	0.1217	0.1438	0.1495	0.1969	0.1012	0.1128	0.0417	0.0386
-0.54	0.1485	0.1805	0.2012	0.2411	0.1130	0.1242	0.0514	0.0757
-0.66	0.1805	0.2038	0.2482	0.3084	0.1319	0.1472	0.0616	0.0772
-0.80	0.2161	0.2359	0.2910	0.3083	0.1513	0.1688	0.0719	0.0979
-0.99	0.2798	0.2719	0.3751	0.4026	0.2201	0.2103	0.1079	0.1089
-1.25	0.4031	0.3710	0.5421	0.4837	0.3030	0.2631	0.1701	0.1120
-1.40	0.4703	0.4164	0.6523	0.6166	0.3828	0.2902	0.2092	0.1292
-1.54	0.5615	0.4263	0.7691	0.6371	0.4598	0.3029	0.2142	0.0988
-1.61	0.6215	0.4928	0.8532	0.7025	0.4961	0.3131	0.2572	0.0768
-1.70	0.7023	0.5217	0.9685	0.7272	0.5590	0.2873	0.2748	0.0723
-1.88	0.8607	0.7023	1.2441	0.7832	0.6619	0.2372	0.3039	0.0522
-1.92	0.8781	0.6723	1.2610	0.8269	0.6824	0.2170	0.2958	0.0519
-1.97	0.9503	0.7236	1.3691	0.7826	0.7565	0.1780	0.2998	0.0514
-2.09	1.1158	0.8048	1.5842	0.7965	0.7549	0.1577	0.3128	0.0411
-2.12	1.1360	0.8281	1.6052	0.7678	0.7519	0.1342	0.3077	0.0310
-2.21	1.3041	0.8260	1.7552	0.7567	0.8274	0.1299	0.3109	0.0283
-2.40	1.6388	0.8259	1.9729	0.4658	0.8191	0.1030	0.3121	0.0182
-2.49	1.7991	0.8074	2.0218	0.4255	0.8190	0.0855	0.3181	0.0173
-2.60	1.9655	0.7374	2.0778	0.3483	0.8072	0.0948	0.3189	0.0140

Table 8-7: Raw Frequency Response Data of 1.0 μm Silicalite-1 Particles. Rows in the table correspond to applied frequency, ω. 'In' and 'Out" columns correspond to the transformed pressure-volume frequency of the in-phase and out-of-phase function at each temperature.

	150 °C	**150 °C**	**175 °C**	**175 °C**	**200 °C**	**200 °C**	**225 °C**	**225 °C**
log(ω [s^{-1}])	**In**	**Out**	**In**	**Out**	**In**	**Out**	**In**	**Out**
0.95	0.0093	0.0432	0.0110	0.0424	0.0063	0.0323	0.0017	0.0163
0.88	0.0115	0.0532	0.0116	0.0424	0.0084	0.0424	0.0021	0.0254
0.75	0.0148	0.0231	0.0173	0.0513	0.0143	0.0240	0.0032	0.0163
0.60	0.0218	0.0434	0.0191	0.0321	0.0153	0.0345	0.0052	0.0126
0.46	0.0300	0.0645	0.0216	0.0474	0.0216	0.0344	0.0072	0.0134
0.32	0.0415	0.0674	0.0407	0.0727	0.0283	0.0452	0.0103	0.0315
0.20	0.0480	0.0752	0.0454	0.0763	0.0338	0.0566	0.0134	0.0266
-0.12	0.0843	0.0981	0.0842	0.1342	0.0627	0.1026	0.0248	0.0483
-0.25	0.1054	0.1139	0.1071	0.1614	0.0790	0.1131	0.0341	0.0463
-0.40	0.1317	0.1348	0.1393	0.1963	0.0981	0.1216	0.0373	0.0563
-0.54	0.1599	0.1645	0.1721	0.2487	0.1238	0.1536	0.0487	0.0722
-0.66	0.2056	0.1727	0.1902	0.2881	0.1437	0.1669	0.1020	0.0824
-0.80	0.2261	0.2386	0.2470	0.2430	0.1792	0.1920	0.0921	0.0927
-0.99	0.3020	0.3068	0.3290	0.3143	0.2256	0.2131	0.1133	0.0809
-1.25	0.4213	0.3913	0.4622	0.4502	0.3227	0.2708	0.1699	0.1312
-1.40	0.4993	0.4542	0.5258	0.5215	0.4005	0.3293	0.2136	0.1290
-1.54	0.5952	0.5472	0.6323	0.6242	0.4753	0.3293	0.2467	0.1130
-1.61	0.6602	0.6013	0.7350	0.6132	0.5178	0.3208	0.2582	0.0783
-1.70	0.7478	0.7159	0.8390	0.6290	0.5716	0.2997	0.2736	0.0692
-1.88	0.9084	0.7406	1.1048	0.6730	0.6671	0.2592	0.3008	0.0609
-1.92	0.9488	0.6574	1.0484	0.7531	0.6772	0.2471	0.3008	0.0485
-1.97	1.1094	0.7548	1.2540	0.7027	0.7007	0.2283	0.2998	0.0525
-2.09	1.1893	0.8290	1.4045	0.7049	0.7359	0.2141	0.3058	0.0382
-2.12	1.2430	0.8290	1.4452	0.6717	0.7459	0.1914	0.3081	0.0318
-2.21	1.3305	0.8359	1.5851	0.6283	0.7598	0.1806	0.3021	0.0309
-2.40	1.7160	0.8249	1.8275	0.6562	0.7783	0.1176	0.3083	0.0202
-2.49	1.8648	0.7826	1.9076	0.4053	0.7895	0.0780	0.3121	0.0185
-2.60	2.0691	0.7022	1.9756	0.2724	0.7918	0.0803	0.3180	0.0233

Table 8-8: Raw Frequency Response Data of 3.0 μm Silicalite-1 Particles. Rows in the table correspond to applied frequency, ω. 'In' and 'Out" columns correspond to the transformed pressure-volume frequency of the in-phase and out-of-phase function at each temperature.

	150 °C	**150 °C**	**175 °C**	**175 °C**	**200 °C**	**200 °C**	**225 °C**	**225 °C**
log(ω [s^{-1}])	**In**	**Out**	**In**	**Out**	**In**	**Out**	**In**	**Out**
0.95	0.0308	0.0213	0.0422	0.0263	0.0225	0.0142	0.0123	0.0115
0.88	0.0329	0.0423	0.0422	0.0312	0.0324	0.0123	0.0133	0.0126
0.75	0.0400	0.0414	0.0542	0.0512	0.0324	0.0163	0.0153	0.0154
0.60	0.0412	0.0422	0.0620	0.0612	0.0315	0.0321	0.0184	0.0154
0.46	0.0534	0.0529	0.0729	0.0683	0.0399	0.0338	0.0225	0.0195
0.32	0.0618	0.0612	0.0903	0.0823	0.0469	0.0345	0.0266	0.0264
0.20	0.0719	0.0812	0.1044	0.1028	0.0537	0.0451	0.0277	0.0271
-0.12	0.1029	0.1023	0.1456	0.1352	0.0718	0.0567	0.0431	0.0309
-0.25	0.1236	0.1103	0.1661	0.1563	0.1090	0.0684	0.0503	0.0512
-0.40	0.1406	0.1024	0.2018	0.1773	0.1099	0.0791	0.0534	0.0513
-0.54	0.1690	0.1444	0.2292	0.2082	0.1412	0.1130	0.0701	0.0564
-0.66	0.2054	0.1551	0.3056	0.2208	0.1633	0.1275	0.0812	0.0685
-0.80	0.2264	0.2068	0.3238	0.2711	0.1756	0.1604	0.0943	0.0719
-0.99	0.2781	0.2719	0.4146	0.3127	0.2402	0.1910	0.1130	0.0822
-1.25	0.4066	0.3108	0.5421	0.4173	0.3268	0.2121	0.1614	0.1019
-1.40	0.4482	0.4012	0.6488	0.4917	0.3714	0.2453	0.1943	0.1050
-1.54	0.5209	0.4126	0.7491	0.5221	0.4364	0.2675	0.2175	0.0965
-1.61	0.5862	0.4947	0.8163	0.5734	0.4905	0.2773	0.2361	0.0898
-1.70	0.6438	0.5741	0.8951	0.5921	0.5439	0.2837	0.2509	0.0879
-1.88	0.8002	0.6292	1.1434	0.6809	0.6594	0.2717	0.2721	0.0546
-1.92	0.8236	0.6232	1.1755	0.7280	0.6615	0.2303	0.2748	0.0515
-1.97	0.8724	0.6596	1.2384	0.7360	0.6640	0.2834	0.2807	0.0454
-2.09	1.0282	0.7218	1.4460	0.7271	0.7674	0.2136	0.2741	0.0342
-2.12	1.0384	0.7821	1.4907	0.7177	0.7507	0.2043	0.2743	0.0348
-2.21	1.1389	0.8233	1.6248	0.6251	0.7735	0.1591	0.2879	0.0228
-2.40	1.4584	0.8353	1.8507	0.5178	0.8077	0.1146	0.2918	0.0183
-2.49	1.6341	0.8353	1.9237	0.4228	0.8108	0.1166	0.2976	0.0109
-2.60	1.8020	0.8241	1.9912	0.3096	0.8092	0.1250	0.3059	0.0118

8.6.1 Yasuda's Base Model - Mathematical Derivation.

$$X \rightleftharpoons A \rightleftharpoons C$$

The first step (adsorption) is very fast, and the rate is therefore controlled by intracrystalline diffusion.

1. Solving For the Concentration Profile within the Crystal Domain

Fick's law

$$\frac{\partial C}{\partial t} = \frac{D}{r^2}\frac{\partial}{\partial r}\left(r^2 \frac{\partial C}{\partial r}\right) \qquad 8\text{-}1$$

Boundary Conditions (Symmetry condition +Henry's law):

$$\left.\frac{\partial C}{\partial r}\right|_{r=0} = 0, \qquad C_{r=R} - C_e = K_H(P - P_e) \qquad 8\text{-}2$$

Dimensionless Form:

$$\eta = \frac{r}{R}, \qquad \tau = \frac{Dt}{R^2}, \qquad \bar{c} \equiv \frac{C - C_e}{C_e} \qquad 8\text{-}3$$

$$\frac{\partial \bar{c}}{\partial \tau} = \frac{1}{\eta^2}\frac{\partial}{\partial \eta}\left(\eta^2 \frac{\partial \bar{c}}{\partial \eta}\right) \qquad 8\text{-}4$$

Boundary Conditions

$$\left.\frac{\partial \bar{c}}{\partial \eta}\right|_{\eta=0} = 0, \qquad c_{\eta=1} = \left(\frac{K_H P_e}{C_e}\right)\bar{p} = \bar{p} \qquad 8\text{-}5$$

To simplify, assume,

$$\bar{c} = \frac{f(\eta, \tau)}{\eta} \qquad 8\text{-}6$$

$$\frac{\partial f}{\partial \tau} = \frac{\partial^2 f}{\partial \eta^2} \qquad 8\text{-}7$$

Apply Laplace Transform to Solve PDE

$$L_\tau\left[\frac{\partial f}{\partial \tau}\right] = L_\tau\left[\frac{\partial^2 f}{\partial \eta^2}\right], \qquad \tilde{f} \equiv \int_0^\infty f \exp[-s\tau]\, d\tau \qquad 8\text{-}8$$

$$\int_0^\infty \frac{\partial f}{\partial \tau}\exp(-s\tau)\, d\tau = \int_0^\infty \frac{\partial^2 f}{\partial \eta^2}\exp(-s\tau)\, d\tau \qquad 8\text{-}9$$

For left hand side, integration by parts:

$$\int_0^\infty \frac{\partial f}{\partial \tau}\exp(-s\tau)\,d\tau = \int_0^\infty \{\partial f \exp(-s\tau)\} \tag{8-10}$$

$$\text{LHS} = f\exp(-s\tau)|_0^\infty - \int_0^\infty \{fd(\exp(-s\tau))\} = s\int_0^\infty \{f\exp[-st]\,dt\} = s\tilde{f} \tag{8-11}$$

For right hand side:

$$\frac{\partial^2}{\partial \eta^2}\int_0^\infty f\exp(-s\tau)\,d\tau = \frac{\partial^2 \tilde{f}}{\partial \eta^2} \tag{8-12}$$

Laplace Transformed PDE

$$s\tilde{f} = \frac{\partial^2 \tilde{f}}{\partial \eta^2} \tag{8-13}$$

General Solution:

$$\tilde{f}(\eta) = K_1\cosh\left(\sqrt{s}\,\eta\right) + K_2\sinh\left(\sqrt{s}\ \eta\right) \tag{8-14}$$

$$\tilde{c} = \frac{\tilde{f}}{\eta} = \tilde{c} = \frac{1}{\eta}\left[K_1\cosh\left(\sqrt{s}\,\eta\right) + K_2\sinh\left(\sqrt{s}\,\eta\right)\right] \tag{8-15}$$

Apply BC's

At the center of the sphere, concentration has to be finite, so

$$K_1 = 0 \tag{8-16}$$

Equilibrium BC

$$\tilde{c}(\eta = 1) = K_2\sinh\left(\sqrt{s}\,\right) = \tilde{p} \tag{8-17}$$

Solution

$$\tilde{c}(\eta) = \frac{\tilde{p}}{\eta}\frac{\sinh\left(\sqrt{s}\,\eta\right)}{\sinh\left(\sqrt{s}\,\right)} \tag{8-18}$$

2. Mass Balance

$$\frac{dX}{dt} + \frac{dB}{dt} = 0, \qquad B = N\int_0^R C(r,t)dV \tag{8-19}$$

Where X is the amount of species in the gas phase, B is that within the zeolite.
Assume ideal gas,

$$\frac{d}{dt}\left(\frac{PV}{\mathcal{R}T}\right)+\frac{dB}{dt}=0 \tag{8-20}$$

$$\frac{1}{\mathcal{R}T}\{PV'+P'V\}+\frac{dB}{dt}=0 \tag{8-21}$$

For frequency response:

$$V=V_e(1-v(t)),\qquad \frac{dV}{dt}=-V_e\,\frac{dv}{dt} \tag{8-22}$$

$$P=P_e\big(1+p(t)\big),\qquad \frac{dP}{dt}=P_e\frac{dp}{dt} \tag{8-23}$$

$$\frac{P_eV_e}{RT}\left\{(1+p)\left(-\frac{dv}{dt}\right)+\left(\frac{dp}{dt}\right)(1-v)\right\}+\frac{dB}{dt}=0 \tag{8-24}$$

Because a small volume change,

$$1+p\cong 1,\qquad 1-v\cong 1 \tag{8-25}$$

$$\frac{P_eV_e}{\mathcal{R}T}\left\{\left(\frac{d(-v)}{dt}\right)+\left(\frac{dp}{dt}\right)\right\}+\frac{d(B-B_e)}{dt}=0,\qquad n_e=\frac{P_eV_e}{\mathcal{R}T} \tag{8-26}$$

$$n_e\frac{d(-v)}{d\tau}+n_e\frac{dp}{d\tau}+\frac{d(B-B_e)}{d\tau}=0 \tag{8-27}$$

Applying a Laplace Transform,

$$n_e\int_0^\infty\frac{d(-v)}{d\tau}\exp[-s\tau]\,d\tau+n_e\int_0^\infty\frac{d(p)}{d\tau}\exp[-s\tau]\,d\tau+\int_0^\infty\frac{d(B-B_e)}{d\tau}\exp[-s\tau]\,d\tau=0 \tag{8-28}$$

$$n_e[-s\tilde{v}]+n_e[s\tilde{p}]+s\big(\widetilde{B}-\widetilde{B_e}\big)=0,\qquad \widetilde{B}-\widetilde{B_e}=C_e\tilde{C} \tag{8-29}$$

Substitute internal concentration profile for$\widetilde{B}-\widetilde{B_e}$,

$$n_e[-s\tilde{v}+1]+n_e[s\tilde{p}-1]+s\left\{NC_e\int_0^V\tilde{C}dV\right\}=0 \tag{8-30}$$

$$n_e[-s\tilde{v}+s\tilde{p}]+s\left\{NC_e\int_0^R\frac{\tilde{p}}{\eta}\frac{\sinh\big(\sqrt{s}\,\eta\big)}{\sinh\big(\sqrt{s}\,\big)}d\left(\frac{4}{3}\pi r^3\right)\right\}=0 \tag{8-31}$$

Where N is the number of zeolite particles.

$$n_e[-s\tilde{v} + s\tilde{p}] + s\left\{NC_e 4\pi R^3 \int_0^R \frac{\tilde{p}}{\eta} \frac{\sinh(\sqrt{s}\,\eta)}{\sinh(\sqrt{s}\,)} \eta^2 d\eta\right\} = 0 \quad 8\text{-}32$$

$$n_e[-s\tilde{v} + s\tilde{p}] + s\left\{\frac{NC_e 4\pi R^3 \tilde{p}}{\sinh(\sqrt{s}\,)} \int_0^1 \eta \sinh(\sqrt{s}\,\eta)\, d\eta\right\} = 0 \quad 8\text{-}33$$

Integration by parts:

$$n_e[-s\tilde{v} + s\tilde{p}] + s\left\{\frac{NC_e 4\pi R^3 \tilde{p}}{\sinh(\sqrt{s}\,)} \left[\frac{\eta}{\sqrt{s}} \cosh(\sqrt{s}\eta)\Big|_0^1 - \int_0^1 \cosh(\sqrt{s}\eta)\, d\left(\frac{\eta}{\sqrt{s}}\right)\right]\right\} = 0 \quad 8\text{-}34$$

$$n_e[-s\tilde{v} + s\tilde{p}] + s\left\{\frac{NC_e 4\pi R^3 \tilde{p}}{\sinh(\sqrt{s}\,)} \left[\frac{\eta}{\sqrt{s}} \cosh(\sqrt{s}\eta)\Big|_0^1 - \int_0^1 \frac{\cosh(\sqrt{s}\eta)}{\sqrt{s}} d\eta\right]\right\} = 0 \quad 8\text{-}35$$

$$n_e[-s\tilde{v} + s\tilde{p}] + s\left\{\frac{NC_e 4\pi R^3 \tilde{p}}{\sinh(\sqrt{s}\,)} \left[\frac{1}{\sqrt{s}} \cosh(\sqrt{s}) - \frac{0}{\sqrt{s}} \cosh(0) - \frac{1}{s} \sinh(\sqrt{s}\eta)_0^1\right]\right\} = 0 \quad 8\text{-}36$$

$$n_e[-s\tilde{v} + s\tilde{p}] + s\left\{\frac{NC_e 4\pi R^3 \tilde{p}}{\sinh(\sqrt{s}\,)} \left[\frac{1}{\sqrt{s}} \cosh(\sqrt{s}) - \frac{0}{\sqrt{s}} \cosh(0) - \frac{1}{s} \sinh(\sqrt{s})\right]\right\} = 0 \quad 8\text{-}37$$

$$n_e[-s\tilde{v} + s\tilde{p}] + s\left\{\frac{NC_e 4\pi R^3 \tilde{p}}{\sinh(\sqrt{s}\,)} \left[\frac{1}{\sqrt{s}} \cosh(\sqrt{s}) - \frac{0}{\sqrt{s}} \cosh(0) - \frac{1}{s} \sinh(\sqrt{s})\right]\right\} = 0 \quad 8\text{-}38$$

$$n_e[-s\tilde{v} + s\tilde{p}] + s\left\{NC_e 4\pi R^3 \tilde{p} \left[\frac{1}{\sqrt{s}} \coth(\sqrt{s}) - \frac{1}{s}\right]\right\} = 0 \quad 8\text{-}39$$

$$\tilde{v} = \tilde{p} + \frac{NC_e 4\pi R^3 \tilde{p}}{n_e} \left[\frac{1}{\sqrt{s}} \coth(\sqrt{s}) - \frac{1}{s}\right] \quad 8\text{-}40$$

Define G(s) as transfer function:

$$G(s) = \frac{\tilde{p}}{\tilde{v}} = \left\{1 + \frac{NC_e 4\pi R^3}{n_e} \left[\frac{1}{\sqrt{s}} \coth(\sqrt{s}) - \frac{1}{s}\right]\right\}^{-1} \quad 8\text{-}41$$

$$G(s) = \frac{\tilde{p}}{\tilde{v}} = \left\{1 + \frac{\frac{K_H P_e}{C_e} NC_e 4\pi R^3}{P_e V_e / \mathcal{R}T} \left[\frac{1}{\sqrt{s}} \coth(\sqrt{s}) - \frac{1}{s}\right]\right\}^{-1} \quad 8\text{-}42$$

$$G(s) = \frac{\tilde{p}}{\tilde{v}} = \left\{1 + \frac{N4\pi R^3 K_H \mathcal{R}T}{V_e} \left[\frac{1}{\sqrt{s}} \coth(\sqrt{s}) - \frac{1}{s}\right]\right\}^{-1} \quad 8\text{-}43$$

Define

$$K = \frac{N4\pi R^3 K_H \mathcal{R}T}{3V_e} = \frac{\mathcal{R}TV_s}{V_e} K_H \quad 8\text{-}44$$

$$G(s) = \frac{\tilde{p}}{\tilde{v}} = \left\{1 + 3K\left[\frac{1}{\sqrt{s}}\coth\left(\sqrt{s}\right) - \frac{1}{s}\right]\right\}^{-1} \quad 8\text{-}45$$

Converting to the regular domain by applying inverse Laplace transform.
For Frequency response, concentration inside the particle can be expressed as:

$$C = C_e\{1 + C_e\exp(i(\omega^*\tau + \varphi - \varphi_1)\} \quad 8\text{-}46$$
$$\bar{c} = \{\exp(i(\omega^*\tau + \varphi - \varphi_1))\}$$

Where φ donates phase lag of pressure response, φ_1 is the phase lag of concentration. $\omega^*$is the dimensionless form of angular frequency.

From general definition of laplace transform, we have,

$$\frac{\partial\bar{c}}{\partial t} = i\omega\exp(i\left(\omega^*\tau + \varphi - \varphi_1\right) \quad 8\text{-}47$$

$$L_\tau\left[\frac{\partial\bar{c}}{\partial t}\right] = \int_0^\infty \exp(-s\tau)\, i\omega^*\exp\left(i\left(\omega^*\tau + \varphi - \varphi_1\right)\right) d\tau = i\omega^*\tilde{c} \quad 8\text{-}48$$

$$L_\tau\left[\frac{\partial\bar{c}}{\partial t}\right] = s\tilde{c} \quad 8\text{-}49$$

$$s = i\omega^*, \qquad \omega^* = \frac{\omega R^2}{D} \quad 8\text{-}50$$

To do the inverse Laplace transform, we replace Laplace variable s with reduced angular frequency $i\omega^*$. Thus, the inverse Laplace transform can be expressed as,

$$Q = \frac{\bar{v}}{\bar{p}} - 1 = 3K\left[\frac{1}{(1+i)\eta^*}\coth\left((1+i)\eta^*\right) - \frac{1}{(1+i)^2\eta^{*2}}\right] \quad 8\text{-}51$$

where,

$$\eta^* = \sqrt{\frac{\omega^*}{2}} \quad 8\text{-}52$$

Separate the real and imaginary parts of transfer function G,

$$Re(G) = \frac{Q + Q^*}{2} \quad 8\text{-}53$$

$$\mathrm{Re(G)} = \frac{3}{2}\mathrm{K}\left\{\left[\frac{1}{(1+\mathrm{i})\eta^*}\coth\left((1+\mathrm{i})\eta^*\right) + \frac{\mathrm{i}}{2\eta^{*2}}\right] + \left[\frac{1}{(1-\mathrm{i})\eta^*}\coth\left((1-\mathrm{i})\eta^*\right) + \frac{-\mathrm{i}}{2\eta^{*2}}\right]\right\} \quad 8\text{-}54$$

$$\mathrm{Re(G)} = \frac{3}{2}\mathrm{K}\left\{\left[\frac{\coth\left((1+\mathrm{i})\eta^*\right)}{(1+\mathrm{i})\eta^*}\right] + \left[\frac{\coth\left((1-\mathrm{i})\eta^*\right)}{(1-\mathrm{i})\eta^*}\right]\right\} \quad 8\text{-}55$$

$$\mathrm{Re(G)} = \frac{3}{2}\mathrm{K}\left\{\frac{\coth\left((1+\mathrm{i})\eta^*\right)(1-\mathrm{i}) + \coth\left((1-\mathrm{i})\eta^*\right)(1+\mathrm{i})}{(1+\mathrm{i})(1-\mathrm{i})\eta^*}\right\} \quad 8\text{-}56$$

$$\mathrm{Re(G)} = \frac{3}{2}\mathrm{K}\left\{\frac{(1-\mathrm{i})\coth\left((1+\mathrm{i})\eta^*\right) + (1+\mathrm{i})\coth\left((1-\mathrm{i})\eta^*\right)}{2\eta^*}\right\} \quad 8\text{-}57$$

$$\mathrm{Re(G)} = \frac{3}{4\eta^*}\mathrm{K}\left\{\frac{(1-\mathrm{i})\cosh\left((1+\mathrm{i})\eta^*\right)}{\sinh\left((1+\mathrm{i})\eta^*\right)} + \frac{(1+\mathrm{i})\cosh\left((1-\mathrm{i})\eta^*\right)}{\sinh\left((1-\mathrm{i})\eta^*\right)}\right\} \quad 8\text{-}58$$

$$\mathrm{Re(G)} = \frac{3}{4\eta}\mathrm{K}\left\{\frac{(1-\mathrm{i})\cosh\left((1+\mathrm{i})\eta^*\right)\sinh\left((1-\mathrm{i})\eta^*\right) + (1+\mathrm{i})\cosh\left((1-\mathrm{i})\eta^*\right)\sinh\left((1+\mathrm{i})\eta^*\right)}{\sinh\left((1+\mathrm{i})\eta^*\right)\sinh\left((1-\mathrm{i})\eta^*\right)}\right\} \quad 8\text{-}59$$

$$\mathrm{Re(G)} = \frac{3\mathrm{K}}{4\eta}\left\{\frac{\mathrm{NUM}}{\mathrm{DEN}}\right\} \quad 8\text{-}60$$

$$\mathrm{DEN} = \sinh\left((1+\mathrm{i})\eta^*\right)\sinh\left((1-\mathrm{i})\eta^*\right) \quad 8\text{-}61$$

$$\mathrm{DEN} = \left[\frac{\exp[(1+\mathrm{i})\eta^*] - \exp[-(1+\mathrm{i})\eta^*]}{2}\right]\cdot\left[\frac{\exp[(1-\mathrm{i})\eta^*] - \exp[-(1-\mathrm{i})\eta^*]}{2}\right] \quad 8\text{-}62$$

$$\mathrm{DEN} = \left[\frac{\exp[2\eta^*] - \exp[-(2\mathrm{i})\eta^*] - \exp[(2\mathrm{i})\eta^*] + \exp[-2\eta^*]}{4}\right] \quad 8\text{-}63$$

$$\mathrm{DEN} = \frac{1}{2}[\cosh(2\eta^*) - \cosh(\mathrm{i}2\eta^*)] = \frac{1}{2}[\cosh(2\eta^*) - \cos(2\eta^*)] \quad 8\text{-}64$$

Similar procedure for numerator,

$$\mathrm{NUM} = \sinh(2\eta) - \sin(2\eta) \quad 8\text{-}65$$

$$\mathrm{Re}(Q) = \frac{3K}{2\eta}\left\{\frac{\sinh(2\eta) - \sin(2\eta)}{\cosh(2\eta) - \cos(2\eta)}\right\} \quad \text{8-66}$$

Note: same procedure for the imaginary

$$\mathrm{Im}(Q) = -\frac{3K}{\eta}\left\{\frac{1}{2}\left[\frac{\sinh(2\eta) + \sin(2\eta)}{\cosh(2\eta) - \cos(2\eta)}\right] - \frac{1}{2\eta}\right\} \quad \text{8-67}$$

In phase and out-of phase function of base case:

$$Q = \begin{cases} \mathrm{Re}(Q) = \dfrac{v}{p}\cos(\phi) - 1 \\ -\mathrm{Im}(Q) = \dfrac{v}{p}\sin(\phi) \end{cases} \quad \text{8-68}$$

8.6.2 T-Q Model – Mathematical Derivation

Assumptions:

- $A + B = C_R$
- Because small fluctuations in J_s, $J_s \cong 0$

1. Mass Balance around a zeolite particle:

$$\frac{\partial C}{\partial t} = \frac{D}{r^2}\frac{\partial}{\partial r}\left(r^2 \frac{\partial C}{\partial r}\right) \tag{8-1}$$

Where C(r,t) is the adsorbed concentration

1.1. Boundary Conditions

1.1.1. Symmetry at center

$$\left.\frac{\partial C}{\partial r}\right|_{r=0} = 0 \tag{8-2}$$

1.1.2.Equilibrium at surface

1.1.2.1. Flux From Diffusion

$$J_D = -D \left.\frac{dC}{dr}\right|_R [=] \frac{mol}{s \cdot m^2} \tag{8-3}$$

1.1.2.2. Surface Barrier Flux

Assume mass transfer coefficient, not Langmuir.

$$J_s = k_s\left(\frac{\frac{4}{3}\pi R^3}{4\pi R^2}\right)A - k_{-s}\left(\frac{\frac{4}{3}\pi R^3}{4\pi R^2}\right)B \tag{8-4}$$

$$J_s = k_s\frac{R}{3}A - k_{-s}\frac{R}{3}B \tag{8-5}$$

Assumption 4 in the main text

$$C_R = B + A \tag{8-6}$$

$$J_s = k_s\frac{R}{3}C_R - (k_{-s} + k_s)\frac{R}{3}B \tag{8-7}$$

When $J_s = 0$, $A_e = \frac{k_{-s}}{k_s}B_e$

Since small change from equilibrium (assumption 3 in the main text).

$$A = \frac{k_{-s}}{k_s} B \tag{8-8}$$

$$J_s = k_s \frac{R}{3} C_R - (k_{-s} + k_s) \frac{R}{3} \frac{k_s}{k_{-s}} A \tag{8-9}$$

Applying Henry's Law:

$$\frac{d(V_s A)}{dP} = K_H, \qquad V_s(A - A_e) = K_H(P - P_e), \qquad A = \frac{K_H}{V_s}(P - P_e) + A_e \tag{8-10}$$

$$J_s = k_s \frac{R}{3} C_R - (k_{-s} + k_s) \frac{k_s}{k_{-s}} \frac{R}{3} \left(A_e + \frac{K_H}{V_s}(P - P_e) \right) \tag{8-11}$$

$$C_{R,e} = B_e + A_e \tag{8-12}$$

$$A_e = \frac{k_{-s}}{k_s} B_e \tag{8-13}$$

$$A_e = \frac{k_{-s}}{(k_{-s} + k_s)} C_{R,e} \tag{8-14}$$

$$J_s = k_s \frac{R}{3} (C_R - C_e) - (k_{-s} + k_s) \frac{k_s}{k_{-s}} \frac{R}{3} \left(\frac{K_H}{V_s}(P - P_e) \right) \tag{8-15}$$

1.1.2.3. Balance Fluxes

$$J_D = J_s \tag{8-16}$$

$$-D \left. \frac{dC}{dr} \right|_R = k_s \frac{R}{3} \left(C_R - C_{R,e} \right) - (k_{-s} + k_s) \frac{k_s}{k_{-s}} \frac{R}{3} \left(\frac{K_H}{V_s}(P - P_e) \right) \tag{8-17}$$

$$\left. \frac{dC}{dr} \right|_R = \frac{-R}{3D} \left[k_s \left(C_R - C_{R,e} \right) - (k_{-s} + k_s) \frac{k_s}{k_{-s}} \left(\frac{K_H}{V_s}(P - P_e) \right) \right] \tag{8-18}$$

Define following non-dimensional parameters,

$$\eta = \frac{r}{R}, \qquad \tau = \frac{t}{t_D + t_S} = \frac{t}{\frac{R^2}{D} + \frac{1}{k_s + k_{-s}}} = \frac{Dt}{R^2} \left(1 + \frac{1}{\lambda} \right)^{-1}, \lambda = \frac{t_D}{t_s} = \left(\frac{D}{R^2} \frac{1}{k_s + k_{-s}} \right)^{-1}, \overline{c} \equiv \frac{C - C_e}{C_e}$$

$$\frac{\lambda}{1+\lambda}\frac{\partial \bar{c}}{\partial \tau} = \frac{1}{\eta^2}\frac{\partial}{\partial \eta}\left(\eta^2 \frac{\partial \bar{c}}{\partial \eta}\right) \tag{8-19}$$

Define

$$\bar{c} = \frac{f(\eta, \tau)}{\eta} \tag{8-20}$$

$$\frac{\lambda}{1+\lambda}\frac{\partial f}{\partial \tau} = \frac{\partial^2 f}{\partial \eta^2} \tag{8-21}$$

1.1. Apply Laplace Transform to Solve PDE

$$L_\tau\left[\frac{\lambda}{1+\lambda}\frac{\partial f}{\partial \tau}\right] = L_\tau\left[\frac{\partial^2 f}{\partial \eta^2}\right], \qquad \tilde{f} \equiv \int_0^\infty f\, exp[-s\tau]\, d\tau \tag{8-22}$$

Similar to Yasuda's base model,

$$\tilde{C} = \frac{1}{\eta}\left[K_1\, cosh\left(\sqrt{\frac{\lambda}{1+\lambda}}\, s\, \eta\right) + K_2\, sinh\left(\sqrt{\frac{\lambda}{1+\lambda}}\, s\, \eta\right)\right] \tag{8-23}$$

$$\frac{d\tilde{C}}{d\eta} = \frac{1}{\eta^2}\left[\left(K_1\eta\sqrt{\frac{\lambda}{1+\lambda}}\, s - K_2\right) sinh\left(\eta\sqrt{\frac{\lambda}{1+\lambda}}\, s\right) + \left(K_2\eta\sqrt{\frac{\lambda}{1+\lambda}}\, s - K_1\right) cosh\left(\eta\sqrt{\frac{\lambda}{1+\lambda}}\, s\right)\right] \tag{8-24}$$

1.1.2.4. Apply BC's

At $\eta = 0$, $\tilde{c}$ must be finite, therefore

$$K_1 = 0 \tag{8-25}$$

Surface BC

$$\left.\frac{dC}{dr}\right|_R = \frac{-R}{3D}\left[k_s\left(C_R - C_{R,e}\right) - \left(k_{-s} + k_s\right)\frac{k_s}{k_{-s}}\left(\frac{K_H}{V_s}\left(P - P_e\right)\right)\right] \tag{8-26}$$

Dimensionless form:

$$\left.\frac{d\,\bar{C}}{d\eta}\right|_{\eta=1} = \frac{R^2}{-3D}\left[k_s\bar{C} - \left(k_{-s} + k_s\right)\frac{k_s}{k_{-s}}\frac{K_H}{V_s}\frac{P_e\bar{P}}{C_e}\right], \tag{8-27}$$

$$K_H P_e = A_e = \frac{k_{-s}}{(k_{-s} + k_s)} C_e \tag{8-28}$$

$$\left.\frac{d\tilde{C}}{d\eta}\right|_{\eta=1} = -\frac{R^2}{3D} k_s \left(\tilde{C} - \tilde{P}\right) \tag{8-29}$$

$$\left.\frac{\partial\tilde{C}}{\partial\eta}\right|_{\eta=1} = \frac{1}{\eta^2}\left[\left(K_1\eta\sqrt{\frac{\lambda}{1+\lambda}s} - K_2\right) sinh\left(\eta\sqrt{\frac{\lambda}{1+\lambda}s}\right) + \left(K_2\eta\sqrt{\frac{\lambda}{1+\lambda}s} - K_1\right) cosh\left(\eta\sqrt{\frac{\lambda}{1+\lambda}s}\right)\right] = -\frac{R^2}{3D} k_s \left(\tilde{C} - \tilde{P}\right) \tag{8-30}$$

$$\left[(-K_2)\, sinh\left(\sqrt{\frac{\lambda}{1+\lambda}s}\right) + \left(K_2\sqrt{\frac{\lambda}{1+\lambda}s}\right) cosh\left(\sqrt{\frac{\lambda}{1+\lambda}s}\right)\right] = -\frac{R^2}{3D} k_s \left(\frac{1}{\eta} K_2\, sinh\left(\sqrt{\frac{\lambda}{1+\lambda}s}\,\eta\right) - \tilde{P}\right) \tag{8-31}$$

$$K_2 = \frac{R^2}{3D} k_s \left[-sinh\left(\sqrt{\frac{\lambda}{1+\lambda}s}\right) + \sqrt{\frac{\lambda}{1+\lambda}s}\, cosh\left(\sqrt{\frac{\lambda}{1+\lambda}s}\right) + \frac{R^2}{3D} k_s\, sinh\left(\sqrt{\frac{\lambda}{1+\lambda}s}\right)\right]^{-1} \tag{8-32}$$

Substituting back into the solution,

$$\tilde{C} = \frac{1}{\eta}\left[\frac{R^2}{3D} k_s \tilde{P}\; sinh\left(\sqrt{\frac{\lambda}{1+\lambda}s}\,\eta\right)\right]\left[-sinh\left(\sqrt{\frac{\lambda}{1+\lambda}s}\right) + \sqrt{\frac{\lambda}{1+\lambda}s}\, cosh\left(\sqrt{\frac{\lambda}{1+\lambda}s}\right)\frac{R^2}{3D}\left(k_s\, sinh\left(\sqrt{\frac{\lambda}{1+\lambda}s}\right)\right]^{-1} \tag{8-33}$$

2. Mass balance within the Chamber:

$$\frac{dX}{dt} + \frac{Nd(X')}{dt} = 0 \tag{8-34}$$

Where X is the amount of species in the gas phase, X' is the amount of species within the zeolite, and N is the total number of zeolite particles.

$$\frac{dX}{dt} + \frac{d}{dt}\left[\int_0^R NC\ d\left(\frac{4}{3}\pi r^3\right)\right] = 0 \tag{8-35}$$

From previous solution,

$$n_e[-s\tilde{v}] + n_e[s\tilde{p}] + s\left\{NC_e \int_0^V \tilde{C}dV\right\} = 0 \tag{8-36}$$

$$-\tilde{v} + \tilde{p} + \left\{\frac{NC_e}{n_e} \int_0^V \tilde{C}dV\right\} = 0 \tag{8-37}$$

Define

$$Q = \frac{NC_e}{n_e\tilde{p}} \int_0^V \tilde{C}dV = \frac{\tilde{v}}{\tilde{p}} - 1 \tag{8-38}$$

$$Q = \frac{NV_sC_e}{n_e}\frac{R^2}{D}k_s \frac{\left\{\int_0^1 \eta\ sinh\left(\sqrt{\frac{\lambda}{1+\lambda}s}\,\eta\right)d\eta\right\}}{\left[-sinh\left(\sqrt{\frac{\lambda}{1+\lambda}s}\right) + \sqrt{\frac{\lambda}{1+\lambda}s}\,cosh\left(\sqrt{\frac{\lambda}{1+\lambda}s}\right) + \frac{R^2}{3D}k_s\,sinh\left(\sqrt{\frac{\lambda}{1+\lambda}s}\right)\right]} \tag{8-39}$$

$$\frac{\frac{3NV_sC_e}{n_e}\frac{R^2}{3D}(k_s)\left\{\frac{1}{\sqrt{\frac{\lambda}{1+\lambda}s}}cosh\left(\sqrt{\frac{\lambda}{1+\lambda}s}\right) - \frac{1}{\frac{\lambda}{1+\lambda}s}sinh\left(\sqrt{\frac{\lambda}{1+\lambda}s}\right)\right\}}{\left[-sinh\left(\sqrt{\frac{\lambda}{1+\lambda}s}\right) + \sqrt{\frac{\lambda}{1+\lambda}s}\,cosh\left(\sqrt{\frac{\lambda}{1+\lambda}s}\right) + \frac{R^2}{3D}k_s\,sinh\left(\sqrt{\frac{\lambda}{1+\lambda}s}\right)\right]} = \frac{\tilde{v}}{\tilde{p}} - 1 \tag{8-40}$$

Define, $K \equiv \frac{NV_sC_e}{n_e}$

Numerical solution:

8-41

$$\frac{3Kk_s\frac{R^2}{3D}\left\{\frac{1}{\sqrt{\frac{\lambda}{1+\lambda}s}}cosh\left(\sqrt{\frac{\lambda}{1+\lambda}s}\right)-\frac{1}{\frac{\lambda}{1+\lambda}s}sinh\left(\sqrt{\frac{\lambda}{1+\lambda}s}\right)\right\}}{-sinh\left(\sqrt{\frac{\lambda}{1+\lambda}s}\right)+\sqrt{\frac{\lambda}{1+\lambda}s}\,cosh\left(\sqrt{\frac{\lambda}{1+\lambda}s}\right)+k_s\frac{R^2}{3D}sinh\left(\sqrt{\frac{\lambda}{1+\lambda}s}\right)}=\frac{\tilde{v}}{\tilde{p}}-1$$

8.7 References

1. M. R. Bonilla, R. Valiullin, J. Kärger, S. K. Bhatia, Understanding Adsorption and Transport of Light Gases in Hierarchical Materials Using Molecular Simulation and Effective Medium Theory. *The Journal of Physical Chemistry C*, (2014)10.1021/jp5028228).
2. C. L. Cavalcante, Jr., D. M. Ruthven, Adsorption of Branched and Cyclic Paraffins in Silicalite. 2. Kinetics. *Industrial & Engineering Chemistry Research* **34**, 185-191 (1995); published online Epub1995/01/01 (10.1021/ie00040a018).
3. C.-C. Chang, A. R. Teixeira, C. Li, P. J. Dauenhauer, W. Fan, Enhanced Molecular Transport in Hierarchical Silicalite-1. *Langmuir* **29**, 13943-13950 (2013); published online Epub2013/11/12 (10.1021/la403706r).
4. D. Ruthven, Diffusion in zeolites—a continuing saga. *Adsorption* **16**, 511-514 (2010)10.1007/s10450-010-9263-9).
5. J. Kärger, Measurement of Diffusion in Zeolites—A Never Ending Challenge? *Adsorption* **9**, 29-35 (2003)10.1023/a:1023811229823).
6. P. Kortunov, S. Vasenkov, C. Chmelik, J. Karger, D. M. Ruthven, J. Wloch, Influence of defects on the external crystal surface on molecular uptake into MFI-type zeolites. *Chem Mater* **16**, 3552-3558 (2004); published online EpubSep 7 (Doi 10.1021/Cm0401645).
7. D. A. Newsome, D. S. Sholl, Molecular Dynamics Simulations of Mass Transfer Resistance in Grain Boundaries of Twinned Zeolite Membranes. *The Journal of Physical Chemistry B* **110**, 22681-22689 (2006); published online Epub2006/11/01 (10.1021/jp063287g).
8. L. Karwacki, M. H. F. Kox, D. A. Matthijs de Winter, M. R. Drury, J. D. Meeldijk, E. Stavitski, W. Schmidt, M. Mertens, P. Cubillas, N. John, A. Chan, N. Kahn, S. R. Bare, M. Anderson, J. Kornatowski, B. M. Weckhuysen, Morphology-dependent zeolite intergrowth structures leading to distinct internal and outer-surface molecular diffusion barriers. *Naure Materials* **8**, 959-965 (2009)http://www.nature.com/nmat/journal/v8/n12/suppinfo/nmat2530_S1.html).
9. D. M. Ruthven, in *Fluid Transport in Nanoporous Materials*, W. C. Conner, J. Fraissard, Eds. (Springer Netherlands, 2006), vol. 219, pp. 9-40.
10. J. Kärger, S. Vasenkov, S. M. Auerbach, S. M. Auerbach, Ed. (Marcel Dekker Inc.: New York, 2003).
11. A. R. Teixeira, C.-C. Chang, T. Coogan, R. Kendall, W. Fan, P. J. Dauenhauer, Dominance of Surface Barriers in Molecular Transport through Silicalite-1. *The Journal of Physical Chemistry C* **117**, 25545-25555 (2013); published online Epub2013/12/05 (10.1021/jp4089595).
12. A. Gupta, R. Q. Snurr, A Study of Pore Blockage in Silicalite Zeolite Using Free Energy Perturbation Calculations. *The Journal of Physical Chemistry B* **109**, 1822-1833 (2005); published online Epub2005/02/01 (10.1021/jp047391e).
13. F. Hibbe, C. Chmelik, L. Heinke, S. Pramanik, J. Li, D. M. Ruthven, D. Tzoulaki, J. Kärger, The Nature of Surface Barriers on Nanoporous Solids Explored by Microimaging of Transient Guest Distributions. *Journal of the American Chemical Society* **133**, 2804-2807 (2011)10.1021/ja108625z).
14. D. Ruthven, S. Brandani, M. Eic, H. Karge, J. Weitkamp, Eds. (Springer Berlin / Heidelberg, 2008), vol. 7, pp. 45-84.
15. D. M. Ruthven, in *Fluid Transport in Nanoporous Materials*, W. C. Conner, J. Fraissard, Eds. (Springer Netherlands, 2006), vol. 219, pp. 151-186.
16. P. Y. Ghi, D. J. T. Hill, A. K. Whittaker, PFG-NMR measurements of the self-diffusion coefficients of water in equilibrium poly(HEMA-co-THFMA) hydrogels.

Biomacromolecules **3**, 554-559 (2002); published online EpubMay-Jun (Doi 10.1021/Bm010169k).
17. A. Iliyas, M. Eic, M. H. Zahedi-Niaki, S. Vasenkov, Toward observation of single-file diffusion using the tracer zero-length column method. *J Phys Chem B* **112**, 3821-3825 (2008); published online EpubMar 27 (Doi 10.1021/Jp710314c).
18. M. D. Turner, L. Capron, R. L. Laurence, W. C. Conner, The design and construction of a frequency response apparatus to investigate diffusion in zeolites. *Rev Sci Instrum* **72**, 4424-4433 (2001); published online EpubDec (Doi 10.1063/1.1408931).
19. L. Gueudré, N. Bats, E. Jolimaître, Effect of surface resistance on cyclohexane uptake curves in Silicalite-1 crystals. *Microporous and Mesoporous Materials* **147**, 310-317 (2012)http://dx.doi.org/10.1016/j.micromeso.2011.06.032).
20. D. M. Ruthven, Diffusion in type A zeolites: New insights from old data. *Microporous and Mesoporous Materials* **162**, 69-79 (2012)10.1016/j.micromeso.2011.12.025).
21. H. G. Karge, J. Weitkamp, *Adsorption and diffusion*. Molecular sieves (Springer, Berlin, 2008), pp. xiii, 400 p.
22. D. M. Ruthven, Transport in microporous solids - Part II: Measurement of micropore diffusivities. *Nato Sci Ser Ii Math* **219**, 151-186 (2006).
23. Y. Yasuda, Frequency response method for study of the kinetic behavior of a gas-surface system. 1. Theoretical treatment. *The Journal of Physical Chemistry* **80**, 1867-1869 (1976); published online Epub1976/08/01 (10.1021/j100558a010).
24. R. Watanabe, T. Yokoi, T. Tatsumi, Synthesis and application of colloidal nanocrystals of the MFI-type zeolites. *Journal of Colloid and Interface Science* **356**, 434-441 (2011)http://dx.doi.org/10.1016/j.jcis.2011.01.043).
25. J. R. Agger, N. Hanif, C. S. Cundy, A. P. Wade, S. Dennison, P. A. Rawlinson, M. W. Anderson, Silicalite Crystal Growth Investigated by Atomic Force Microscopy. *Journal of the American Chemical Society* **125**, 830-839 (2003); published online Epub2003/01/01 (10.1021/ja020899f).
26. Y. Yasuda, Frequency-Response Method for Study of Kinetic-Behavior of a Gas-Surface System .1. Theoretical Treatment. *J Phys Chem-Us* **80**, 1867-1869 (1976)Doi 10.1021/J100558a010).
27. Y. Yasuda, Determination of vapor diffusion coefficients in zeolite by the frequency response method. *The Journal of Physical Chemistry* **86**, 1913-1917 (1982); published online Epub1982/05/01 (10.1021/j100207a036).
28. W. L. Duncan, K. P. Möller, On the Diffusion of Cyclohexane in ZSM-5 Measured by Zero-Length-Column Chromatography. *Industrial & Engineering Chemistry Research* **39**, 2105-2113 (2000); published online Epub2000/06/01 (10.1021/ie9907573).
29. I. Langmuir, The Adsorptio of Gases on Plane Surfaces of Glass, Mica and Platinum. *Journal of the American Chemical Society* **40**, 1361-1403 (1918); published online Epub1918/09/01 (10.1021/ja02242a004).
30. Y. Yasuda, Frequency-Response Method for Investigation of Gas-Surface Dynamic Phenomena. *Heterogen Chem Rev* **1**, 103-124 (1994); published online EpubJun (
31. Y. Yasuda, Frequency-Response Method for Investigation of Various Dynamic Phenomena Occurring Simultaneously in a Gas Zeolite System. *Stud Surf Sci Catal* **84**, 1331-1338 (1994).
32. D. Ruthven, F. Brandani, ZLC Response for Systems with Surface Resistance Control. *Adsorption* **11**, 31-34 (2005)10.1007/s10450-005-1090-z).
33. C. L. Cavalcante, Jr., D. M. Ruthven, Adsorption of Branched and Cyclic Paraffins in Silicalite. 1. Equilibrium. *Industrial & Engineering Chemistry Research* **34**, 177-184 (1995); published online Epub1995/01/01 (10.1021/ie00040a017).

34. Y. Yasuda, Detection of Surface Resistance in a Gas/Porous-Adsorbent System by Frequency Response Method. *Bulletin of the Chemical Society of Japan* **64**, 954-961 (1991)10.1246/bcsj.64.954).
35. L. Gueudré, T. Binder, C. Chmelik, F. Hibbe, D. M. Ruthven, J. Kärger, Micro-Imaging by Interference Microscopy: A Case Study of Orientation-Dependent Guest Diffusion in MFI-Type Zeolite Host Crystals. *Materials* **5**, 721-740 (2012).
36. L. Gueudré, E. Jolimaître, N. Bats, W. Dong, Diffusion in zeolites: is surface resistance a critical parameter? *Adsorption* **16**, 17-27 (2010)10.1007/s10450-010-9213-6).
37. P. Wu, A. Debebe, Y. H. Ma, Adsorption and diffusion of C6 and C8 hydrocarbons in silicalite. *Zeolites* **3**, 118-122 (1983)10.1016/0144-2449(83)90199-9).
38. J. Xiao, J. Wei, Diffusion mechanism of hydrocarbons in zeolites—II. Analysis of experimental observations. *Chemical Engineering Science* **47**, 1143-1159 (1992)http://dx.doi.org/10.1016/0009-2509(92)80237-7).
39. H. Chon, D. H. Park, Diffusion of cyclohexanes in ZSM-5 zeolites. *Journal of Catalysis* **114**, 1-7 (1988)10.1016/0021-9517(88)90002-4).
40. F. D. Magalhães, R. L. Laurence, W. C. Conner, Diffusion of Cyclohexane and Alkylcyclohexanes in Silicalite. *The Journal of Physical Chemistry B* **102**, 2317-2324 (1998); published online Epub1998/03/01 (10.1021/jp972036s).
41. S. J. Reitmeier, A. Jentys, J. A. Lercher, in *Ideas in Chemistry and Molecular Sciences*. (Wiley-VCH Verlag GmbH & Co. KGaA, 2010), pp. 229-253.
42. O. C. Gobin, S. J. Reitmeier, A. Jentys, J. A. Lercher, Comparison of the Transport of Aromatic Compounds in Small and Large MFI Particles. *The Journal of Physical Chemistry C* **113**, 20435-20444 (2009); published online Epub2009/11/26 (10.1021/jp907444c).
43. O. C. Gobin, S. J. Reitmeier, A. Jentys, J. A. Lercher, Role of the Surface Modification on the Transport of Hexane Isomers in ZSM-5†. *The Journal of Physical Chemistry C* **115**, 1171-1179 (2011); published online Epub2011/02/03 (10.1021/jp106474x).
44. C. Chmelik, A. Varma, L. Heinke, D. B. Shah, J. Kärger, F. Kremer, U. Wilczok, W. Schmidt, Effect of Surface Modification on Uptake Rates of Isobutane in MFI Crystals: An Infrared Microscopy Study. *Chemistry of Materials* **19**, 6012-6019 (2007); published online Epub2007/11/01 (10.1021/cm071632o).
45. S. Vasenkov, W. Böhlmann, P. Galvosas, O. Geier, H. Liu, J. Kärger, PFG NMR Study of Diffusion in MFI-Type Zeolites: Evidence of the Existence of Intracrystalline Transport Barriers. *The Journal of Physical Chemistry B* **105**, 5922-5927 (2001); published online Epub2001/06/01 (10.1021/jp003899f).
46. C. Chmelik, P. Kortunov, S. Vasenkov, J. Kärger, Internal Transport Resistances and their Influence on Diffusion in Zeolites as Traced by Microscopic Measuring Techniques. *Adsorption* **11**, 455-460 (2005); published online Epub2005/07/01 (10.1007/s10450-005-5967-7).
47. D. M. Ruthven, in *Fluid transport in nanoporous materials*, W. C. Conner, J. P. Fraissard, N. P. D. Division, Eds. (Springer in cooperation with NATO Public Diplomacy Division, 2006).
48. D. Theodorou, J. Wei, Diffusion and reaction in blocked and high occupancy zeolite catalysts. *Journal of Catalysis* **83**, 205-224 (1983)http://dx.doi.org/10.1016/0021-9517(83)90043-X).
49. D. M. Ford, E. Glandt, T. Pinnavaia, M. Thorpe, Eds. (Springer US, 2002), pp. 319-334.
50. P. Kortunov, S. Vasenkov, C. Chmelik, J. Kärger, D. M. Ruthven, J. Wloch, Influence of Defects on the External Crystal Surface on Molecular Uptake into MFI-Type Zeolites. *Chemistry of Materials* **16**, 3552-3558 (2004); published online Epub2004/09/01 (10.1021/cm0401645).

51. G. González, W. Stracke, Z. Lopez, U. Keller, A. Ricker, R. Reichelt, Characterization of Defects and Surface Structures in Microporous Materials by HRTEM, HRSEM, and AFM. *Microscopy and Microanalysis* **10**, 224-235 (2004)doi:10.1017/S1431927604040097).
52. Z. Liu, N. Fujita, K. Miyasaka, L. Han, S. M. Stevens, M. Suga, S. Asahina, B. Slater, C. Xiao, Y. Sakamoto, M. W. Anderson, R. Ryoo, O. Terasaki, A review of fine structures of nanoporous materials as evidenced by microscopic methods. *Microscopy* **62**, 109-146 (2013); published online EpubFebruary 1, 2013 (10.1093/jmicro/dfs098).
53. A. I. Lupulescu, J. D. Rimer, In Situ Imaging of Silicalite-1 Surface Growth Reveals the Mechanism of Crystallization. *Science* **344**, 729-732 (2014); published online EpubMay 16, 2014 (10.1126/science.1250984).
54. D. Tzoulaki, L. Heinke, H. Lim, J. Li, D. Olson, J. Caro, R. Krishna, C. Chmelik, J. Kärger, Assessing Surface Permeabilities from Transient Guest Profiles in Nanoporous Host Materials. *Angewandte Chemie International Edition* **48**, 3525-3528 (2009)10.1002/anie.200804785).
55. L. Heinke, J. Kärger, Correlating Surface Permeability with Intracrystalline Diffusivity in Nanoporous Solids. *Physical Review Letters* **106**, 074501 (2011).
56. M. Thommes, S. Mitchell, J. Pérez-Ramírez, Surface and Pore Structure Assessment of Hierarchical MFI Zeolites by Advanced Water and Argon Sorption Studies. *The Journal of Physical Chemistry C* **116**, 18816-18823 (2012); published online Epub2012/09/06 (10.1021/jp3051214).
57. I. Díaz, E. Kokkoli, O. Terasaki, M. Tsapatsis, Surface Structure of Zeolite (MFI) Crystals. *Chemistry of Materials* **16**, 5226-5232 (2004); published online Epub2004/12/01 (10.1021/cm0488534).
58. K. Yoshida, Y. Sasaki, H. Kurata, High-resolution imaging of zeolite with aberration-corrected transmission electron microscopy. *AIP Advances* **3**, - (2013)doi:http://dx.doi.org/10.1063/1.4802244).
59. D. S. C. C. Richard A. Catlow, Ben Slater, Dewi W. Lewis, J. Carlos G. Pereira, in *Handbook of Zeolite Science and Technology*, S. M. Auerbach, Ed. (Marcel Dekker Inc.: New York, 2003), chap. 4.
60. B. Slater, J. D. Gale, C. R. A. Catlow, T. Ohsuna, O. Terasaki, in *Studies in Surface Science and Catalysis*, M. C. E. van Steen, L. H. Callanan, Eds. (Elsevier, 2004), vol. Volume 154, Part B, pp. 1197-1203.
61. B. Slater, C. R. A. Catlow, Z. Liu, T. Ohsuna, O. Terasaki, M. A. Camblor, Surface Structure and Crystal Growth of Zeolite Beta C. *Angewandte Chemie International Edition* **41**, 1235-1237 (2002)10.1002/1521-3773(20020402)41:7<1235::AID-ANIE1235>3.0.CO;2-R).
62. X. Zhang, D. Liu, D. Xu, S. Asahina, K. A. Cychosz, K. V. Agrawal, Y. Al Wahedi, A. Bhan, S. Al Hashimi, O. Terasaki, M. Thommes, M. Tsapatsis, Synthesis of Self-Pillared Zeolite Nanosheets by Repetitive Branching. *Science* **336**, 1684-1687 (2012); published online EpubJune 29, 2012 (10.1126/science.1221111).
63. M. Choi, K. Na, J. Kim, Y. Sakamoto, O. Terasaki, R. Ryoo, Stable single-unit-cell nanosheets of zeolite MFI as active and long-lived catalysts. *Nature* **461**, 246-249 (2009)http://www.nature.com/nature/journal/v461/n7261/suppinfo/nature08288_S1.html.

CHAPTER 9

2D SURFACE STRUCTURES IN SMALL ZEOLITE (MFI) CRYSTALS

9.1 Introduction

Zeolites are an important class of microporous materials with applications in catalysis[1,2,3] and separations (membranes)[4,5] for energy and materials industries. With well-defined pore networks (d_{pore} < 2 nm) and tunable active sites, zeolites provide unique capability for dense catalytic materials with tunable activity. Moreover, tunable pore networks dependent on the framework allow for molecular sieving with high selectivity based on adsorbate/pore size exclusion. Optimal processing of chemical species with zeolites for catalysis and separations relies on maximizing molecule movement within micropores of crystalline particles.

An emerging approach to faster molecular transfer through zeolite membranes or catalysts introduces secondary mesoporosity in microporous materials. A new class of micro- and mesoporous materials are now being produced with length scales approach that of a single unit cell (pillared,[6,7] nanosheets,[8] membranes,[9,10,11] etc.) as shown in Figure 1. These structures employ a hierarchy of pores with micropores determined by the crystalline lattice (well ordered, <2 nm), mesopores (ordered or disordered networks, 2-50 nm), and macropores comprised of interstitial void spaces. For example, single crystalline zeolite as large as several microns utilize 3DOm-i design consisting of MFI crystals 35 nm in size which are close-packed generating intracrystalline mesopores of six to nine nanometers.[12,13] Even smaller structures include self-pillared pentasil (SPP) consisting of only a single unit cell.[5] Decrease in the apparent distances across particles translates to short distances molecules must travel to traverse membranes or access catalytic active sites.

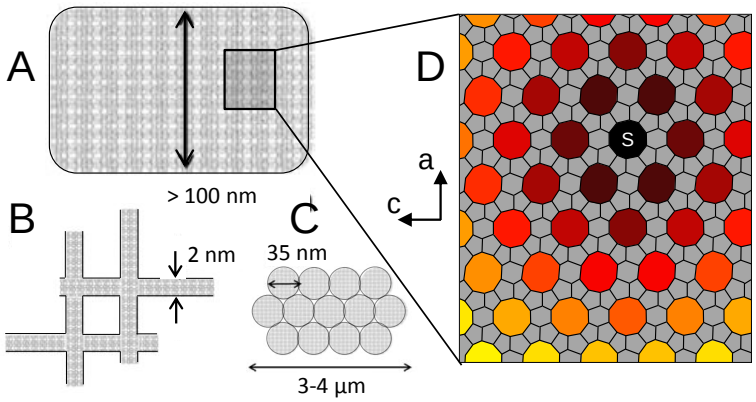

Figure 9-1: Performance of Mesoporous/Microporous Materials is Dominated by Molecular Permeation through Surface Pore Distributions. A. Crystalline MFI particles (>100 nm). B. SPP Pentasil Structures (2 nm). C. 3DOm-i MFI particles (20-40 nm). D. MFI surfaces (b-axis projection) exhibit a distribution of distances between pore openings.

Despite shorter crystalline domains, new hierarchical crystalline domains are dominated by their surfaces. Ordered and disordered mesopores within hierarchical zeolites and single nanosheets have been tested for a large number of catalytic reactions.[14, 15, 16, 17] However, catalytic enhancement is not necessarily achieved from the presence of mesoporosity.[18]. Moreover, introduction of mesopores has improved but not led to the *predicted* rate of enhancement in molecular transport; mesopores can facilitate reduction in diffusional time constants but are ultimately limited by the structure of their surfaces.[19]

The importance of zeolite surface structures at the nanometer scale is not unexpected. As stated by Tsapatsis and co-workers in 2004, "Information on the external surface structure…may also be useful in understanding catalytic and adsorption properties, especially when crystal sizes approach nanoscale dimensions and the role of external surface becomes of increased significance."[20]The kinetic influence of surfaces has been observed via classical uptake/release experiments[21, 22, 23] and interference microscopy.[24] Recently, the kinetics of surface permeation in silicalite-1 (MFI) have shown experimentally to dominate in small particles (<100 nm).[25]. Permeation through the pore surface was found to exhibit identical transition state energy as molecular transfer through the pore, supporting the hypothesis that a fraction of surface pores, $\phi_{SP,}$ in MFI zeolites are completely blocked ($0 < \phi_{SP} < 1$).[26]

The existence of kinetic limitations arising from surface pore structures (i.e. blockages or bridges) is at odds with high resolution surface imaging, which appears to show open surface terminations. Aberration-corrected high resolution transmission electron microscopy (AC-HRTEM) of commercial HZSM-5 resolves the individual atomic columns of zeolite, providing the appearance of a clean crystal MFI structure.[27] HR-TEM of small silicalite-1 particles indicates that particles terminate with defined crystalline edges,[20,28,29] consistent with other zeolites FAU, L, and BEA;[30, 31, 32] no significant amorphous silica surface layer was observed. Additionally, in situ AFM of growing silicalite-1 steps appears consistent with crystalline growth, exhibiting steps of unit cell length.[33] The surface-terminating crystalline nature of silicalite-1 therefore indicates that surface pore blockages potentially result from subtle structural changes at the surface that are difficult to characterize by microscopy.

In this work, we aim to characterize the 2D structure (fraction of surface pore openings) of surface blockages via the kinetic impact of adsorbates permeating the surface of silicalite-1. As depicted in Figure 1D, hydrocarbons attempting to pass between the external surface and the bulk crystal must locate a surface pore opening. For molecules entering/leaving the particle, the difference between a pristine surface and a defective surface will result in a distribution of times associated with the random paths molecules traverse from the initial pore opening (labeled "S" in Figure 1D) and the eventual open surface pore. As shown, the b-axis projection of silicalite-1 has two axes of symmetry, resulting in a complex behavior of randomly moving molecules to find and pass through pore openings. Moreover, as particles are synthesized smaller (<100 nm), adsorbates blocked at one pore can move not only to other pore openings but to entirely new surfaces, depending on: (i) the distances involved, (ii) the fraction of pore openings, and (iii) the size/shape of the crystalline particle. Here, we conduct experimental measurements of surface/bulk permeation of a common adsorbate, benzene; parallel computational effort evaluates a large distribution of rates derived from a kinetic Monte Carlo simulation of silicalite-1, with

variable properties. Comparison of experimental surface permeation rates and predicted surface permeation models allow for estimation of the 2D structure of silicalite-1 particles.

9.2 Computational Methods:

Dynamic Monte Carlo (DyMC) simulations were performed on single crystal MFI particles for single benzene molecules diffusing out of a discrete-space lattice domain. The simulations were conducted within a domain constructed of a predefined periodic internal domain with static external boundary conditions. The multiscale model is described by three domains: 1.) the particle domain which describes the geometric bounds of the crystal, 2.) the unit cell domain describing the c.a. 2 nm periodic repeating MFI unit, and 3.) the particle surface, describing the discrete pore openings at the surface.

Diffusion in microporous materials has been previously shown to be described as a Poisson process with Markovian dynamics describing the random nature of elemental lattice jumps. Jump rates from thermodynamically stable internal adsorption sites to adjacent sites have been previously calculated using transition state theory, and are described in the algorithm method description.

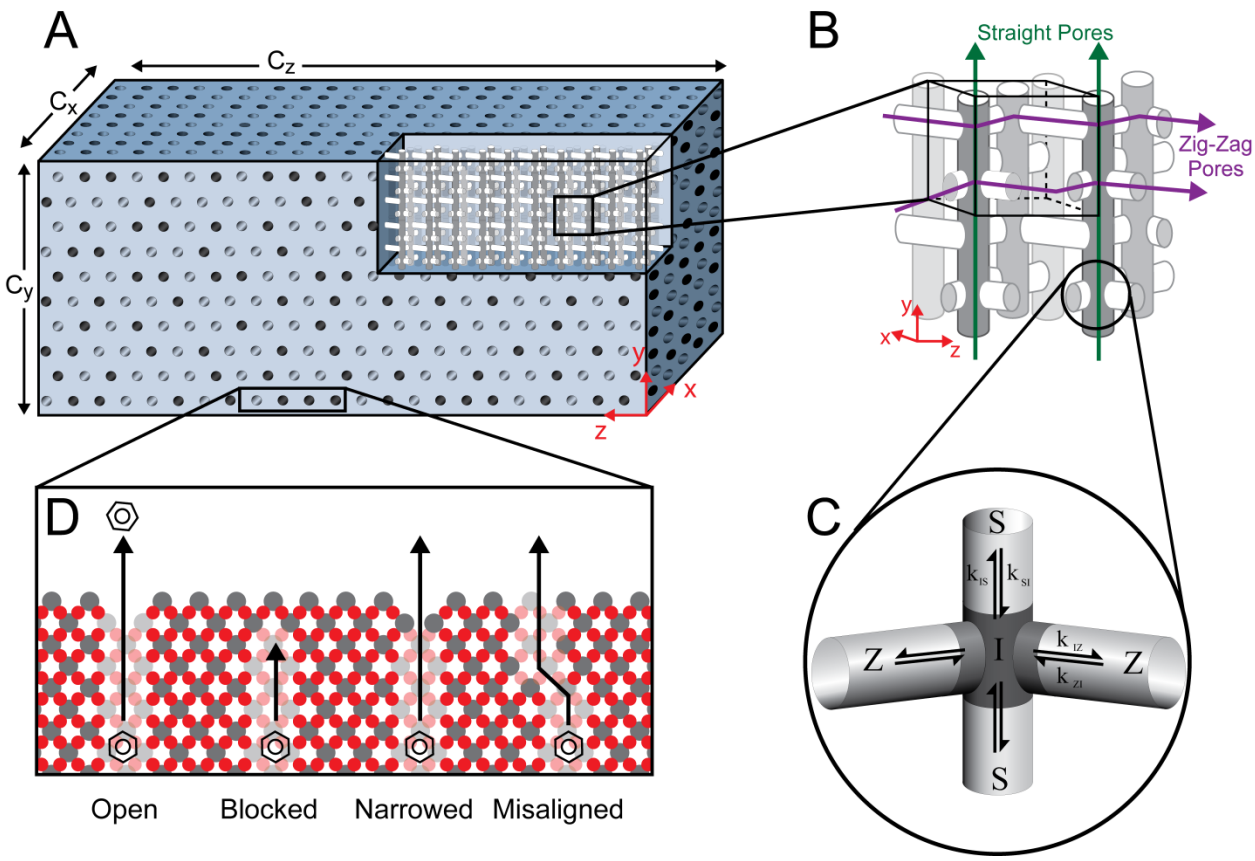

Figure 9-2: **A.** Single crystal particle domain in Cartesian coordinates with rectangular geometry. **B.** Internal domain is composed of straight an zig-zag pores oriented in the y and x directions. **C.** Three descrete sites are identified, (Z, I, S), and jump rates are defined for transitions between sites. **D.** Surface pore blockages may arise from a number of structural effects including bridging, narrowing, and pore misalignment.

9.2.2 Particle Domain:

As depicted if Figure 2A, the particle domain is constructed in Cartesian coordinates with particle cubic particle geometries of size $\langle C_x, C_y, C_z \rangle$. Though three planes of symmetry exist, simulations were performed on whole crystals to allow for extremely high surface pore blockage fractions on small particles. To optimize computing power, a repeating unit cell was used to simulate the internal domain. For the scope of this study, particles are assumed to be composed of a single crystal with straight pores oriented in the y-direction

9.2.3 Unit Cell Domain:

The internal domain within MFI crystals is comprised of a repeating unit cell of size c.a. 2 nm. Each unit, shown in Figure 2B, is made up of straight channels, oriented in the y-direction, and zig-zag or sinusoidal pores with net directionality in the z-direction. Travel along the x-dimension is achieved by combined steps in the y- and z-directions.

Within the unit cell, substantial symmetry exists such that the system can be described as a combination of straight and sinusoidal channels and their intersections (Figure 2C). Molecular dynamics and density functional theory have been used to identify stable adsorption sites within silicalite-1 domain.[1, 2] For the benzene/silicalite-1 system, Forester et al. have identified the existence of three distinct, stable adsorption sites.[2] The sites are identified as local minima in the free energy due to the adsorption of benzene to the lattice structure. As described by Figure 2C, sites are located in the straight pores (S), zig-zag pores (Z), and the intersection of the two (I).

Macroscopically observed transport rates for diffusing molecules within MFI crystals are governed by the stochastic jumps between the thee stable sites, with energetic determined by the transition between adjacent sites.

9.2.4 Surface Domain:

In the simulations performed in this work, each external surface is discretized into C_i/δ distinct cells, where k denotes the particle dimension, ($k = x, y, z$). For large particles ($R > 80$ nm), the surface is discritized with a mesh size of $\delta = 2$ nm, while for small particle simulations ($R <= 80$ nm), the mesh size is reduced to $\delta = 0.2$ nm such that the possibility of blocking as few as one single pore per face is allowed. For each external surface, a two dimensional binary matrix is constructed (β_k), defining each discrete site randomly as either open (1) or blocked (0) for the surface normal to the indexed direction. The probability of open pores at the external surface is an input parameter for the simulations, and is defined as the ratio of area of discrete blockages to total external surface area,

$$p_{open} = \frac{n_{open\ pores}}{n_{total\ pores}} = \sum_{k=1}^{3} \left[\delta^2 \frac{\sum\sum \beta_k}{\prod_{\ell \neq i} C_\ell} \right]$$

In this work, blocked pores are assumed to be completely impenetrable, and thus a molecule can only escape the internal domain by passing through an open pore. Pore blockage fractions were assessed between the ideal crystal ($p_{open} = 1$), and a crystal with the vast majority of surface pores being blocked, ($p_{open} = 10^{-4}$). Extreme blockage fractions were only simulated for crystals of substantial size such that the target probability could be achieved with at least one open pore per external surface.

9.2.5 Jump Kinetics:

To perform the simulations, elementary jump rates are required for transition from each stable internal site to an adjacent site. Three sites have been identified as local free energy minima using transition state theory for the adsorption of benzene in silicalite-1.[2] The resulting sites were centered in the straight pores (S), zig-zag pores (Z), and their intersections (I). The kinetic transitions for the four distinct jump probabilities were calculated according to Forester et al..

In this study, the guest molecules are assumed to be dilute within the particle domain, and thus guest-guest interactions are neglected. This assumption is applied to allow for measurement of the self diffusion, valid for dilute systems.

9.2.6 DyMC Algorithm

Dynamic Monte Carlo simulations were conducted by performing a fixed lattice variable time kinetic Monte Carlo algorithm which was projected onto a fixed time scale post-simulation. The algorithm follows the method suggested by Karger, Vasenov and Auerbach.[3] A guest molecule performs a jump at each simulation iteration and system time and spatial coordinates are incremented accordingly.

The simulation is initiated with a guest molecule randomly placed within the internal particle domain at position x_0,

$$0 < x_0 < C$$

The site is assigned as S, Z or I by random selection, weighted by the equilibrium adsorption distribution determined by Forester et al..[2] The iterative jump sequence is then initiated. For each step, a weighted probability distribution is calculated accounting for each possible step such that the probability of a successful step from stable size i to adjacent site j is defined as,

$$p_j = \frac{k_{ij}}{\sum_i k_{ij}}, \qquad k_{ij} = \frac{1}{\tau_{ij}}$$

The rate constant for each possible step, k_{ij}, is determined by either the intrinsic kinetics of the site-to-site jump rate (internal jump) or the external boundary condition for jumps that result in traversing the external surface of the particle (i.e. $k_{ij} = 0$ for blocked pores).

$$k_{ij} = \begin{cases} 0, & x_k > C_k, \beta_k(i,j) = 0 \\ k_{SI}, & S \rightarrow I \\ k_{IS}, & I \rightarrow S \\ k_{ZI}, & Z \rightarrow I \\ k_{IZ}, & I \rightarrow Z \end{cases}$$

Where $\beta_k(i,j)$ denotes the discrete surface mesh site through which a successful jump from i to j would pass, and x is the resulting spatial location.

A random number generator is utilized to decide which event will take place based on the weighted probability vector, p. Once an event is chosen, both time and space are iterated,

$$t = t + \Delta t$$

$$x = x + \Delta x$$

The probability matrix is then recalculated, and the simulation iterates until the exit condition is met. In these simulations, a successful escape is achieved when a molecule jumps beyond the exterior surface in x, y or z,

$$x_k > C_k$$

Dynamic Monte Carlo simulations were performed on particles with cubic lattice geometries and sizes of $C_x = C_y = C_z$ = 2, 5, 10, 20, 40, 80, 160, 320 nm. Pore blockages were applied in increasing intensity with fractional pore blockages of $p_{open} = 10^{0}, 10^{-0.5}, 10^{-1}, 10^{-1.5}, 10^{-2}, 10^{-3}, 10^{-4}$. Single particle simulations were performed with $M_{guests} = 10^{4}$-10^{6} guest molecules and constrained to a maximum number of jumps, $N_{max} = 10^{8}$.

9.2.7 Validation:

Two forms of validation were performed on the DyMC system. First, bulk particle simulations were performed to validate the unit cell code. Root mean squared displacements in x, y and z were tracked with time and averaged. The Einstein relationship was fit to the linear displacement versus time data sets, and the diffusion coefficients were extracted.

$$D_i = \frac{(x - x_0)^2}{t}$$

Diffusion coefficients were determined (Figure 3) to be D_x = 2.6e-9 cm^2/s, D_y = 1.3e-9 cm^2/s, D_z = 0.4e-9 cm^2/s , D = 1.4e-9 cm^2/s, in good agreement with Forester et al..

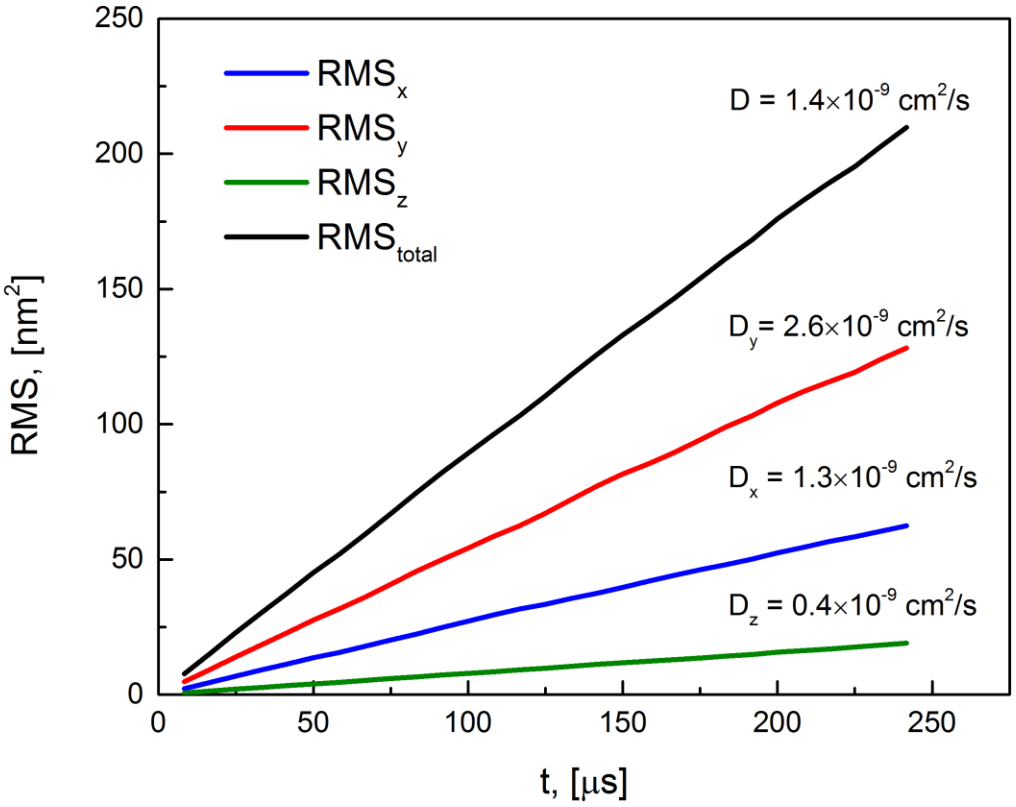

Figure 9-3: Validation of DyMC simulations performed on a large particle with no surface interactions. Guest molecule displacement is shown to be proportional to the diffusion time in accordance with the Einstein relationship.

Similarly, diffusion coefficients were extracted from full particle simulations in the absence of surface barriers and determined to scale with particle size in accordance with diffusional timeconstant,

$$\tau_D = \frac{R^2}{D}$$

Diffusivities were shown to be constant, irrespective of particle size and in good agreement with determination by the Einstein method.

9.3 Experimental

Zero Length Chromatography (ZLC) was used to experimentally measure the apparent diffusivity values of benzene in silicalite-1 particles of various sizes. Particle synthesis and characterization has been described in previous work,[4] as well as the design and validation of the ZLC apparatus.[5] In brevity, standard crystallite growth methods were utilized to synthesize highly crystalline monodisperse particles of silicalite-1 which were characterized by scanning electron microscopy and x-ray diffraction. The ZLC technique saturates a thin layer of microporous silicalite-1 particles (4 mg) with a low partial pressure of benzene vapor in flow before switching to a highly convective inert helium stream and measures the transient effluent concentration by flame ionization. The release profile is fit to a transient transport model to extract the apparent diffusivities.

9.4 Results

Escape times were recorded for each simulation and values are plotted as cumulative distribution for each particle size and blockage fraction in Figure 4. As pore blockages are introduced, escape times increase with particle size. The phenomenon is more drastically observed in small particles where large shifts are observed even with small increases to pore blockages. In large particles, substantially larger fractions of blockages are required to induce such a shift.

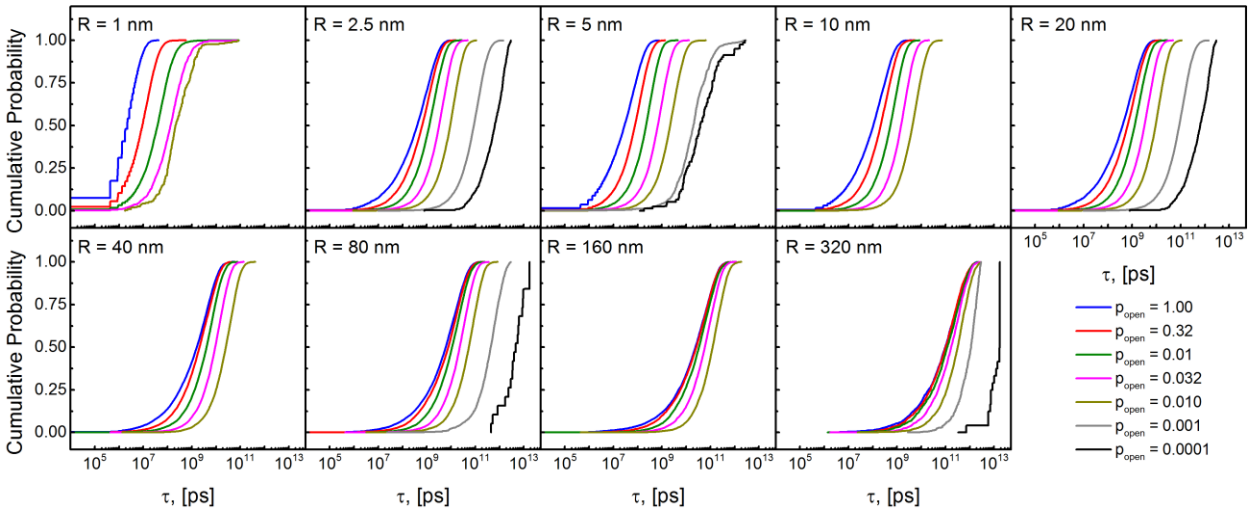

Figure 9-4: Cumulative escape time distributions for single molecules diffusing within a single cubic MFI crystal of dimensions ranging from single lattice (R = 1 nm) to bulk crystal (R = 320 nm). For each size, the probability of open pores was systematically decreased from 100% to 0.01 %.

From the probability distributions, a log-normal fit is performed to extract the average escape times for diffusing molecules under each simulation condition. From these timeconstants, the apparent diffusivity is extracted and plotted versus particle size in Figure 5. For the ideal particle (no surface barrier), little to no dependence on particle size is observed, indicating that the timeconstant scales with particle size as expected for intracrystalline diffusion control, $\tau_D = \frac{R^2}{D}$. The smallest particle examined represents a single crystal of a single lattice cell, and as such shows some deviation from ideality due to its cubic geometry. As the fraction of open pores is decreased, the curves for large particles converge to the bulk diffusivity. However, the apparent diffusivity exhibits increasing divergence from the pure intracrystalline diffusivity values in small particles due to the increasing surface to volume ratios causing the barriers to be more exaggerated in small particles.

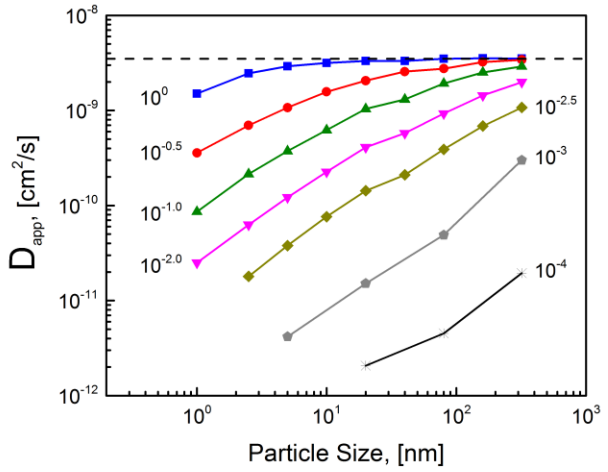

Figure 9-5: Apparent diffusivities for increasing fractions of blocked pores were extracted from the cumulative probability distributions for each simulation and plotted versus particle size. The ideal crystal (blue) represents the bulk diffusion coefficient and exhibited no dependence on particle size. Increasing fractions of blocked pores introduces over two orders of magnitude in apparent diffusion coefficients for small particles.

Characteristic traces of the diffusion path in a large and small particle are visualized in Figure 6. Simulations are initiated with a molecule at the center of the domain and allowed to progress until a successful jump through the surface to the external domain occurs. For the ideal crystal (p_{open} = 1), the molecule path is visualized as the transition from the black sphere, along the black-red gradient to the final escape location (red sphere). As pore blockages are introduced with p_{open} = 0.10 and 0.01, the additional diffusional paths are shown as green and blue paths respectively. In the large particle (Figure 6A), the diffusional path and thus the apparent diffusional time is dominated by the black-to-red transition for all shown surface conditions. This is in direct contrast to the small particle (Figure 6B) which depicts the pathlength transition to being dominated by the additional diffusional length resulting from pore blockages.

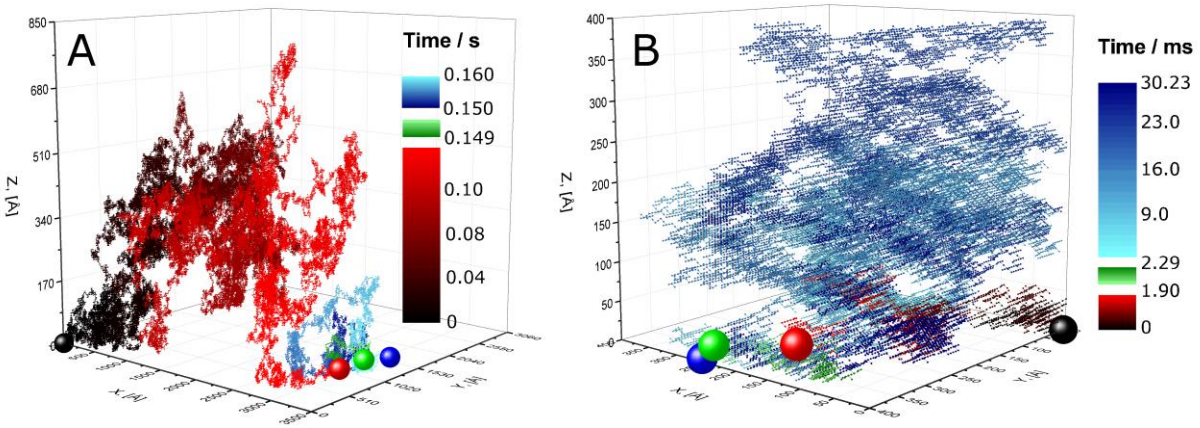

Figure 9-6: Trace of characteristic diffusing molecules in a MFI particle with various pore blockages. A molecule starting at the particle center (black sphere), undergoes random jumps (black to red path) until reaching an outer surface and escaping (red sphere). If 90% of pores are blocked, the additional path is added (green) before exiting (green sphere). The final extension to the diffusional path length is observed with 99% of surface pores being blocked (blue trace) before finally exiting the surface (blue sphere). The relative contribution of the surface pore blockages shifts from unsubstantial increases to the diffusional length scale in large particles (**A.** R = 320 nm) to dominating the transport in small particles (**B.** R = 40 nm).

Simulations were also performed to capture the pathlength and time associated with the surface barrier. To do this, molecules were randomly placed at a site located on the inner external surface such that a single successful jump in one direction would result in an escape from the particle domain. As with the full particle simulations, position and time were tracked, and time distributions were plotted for each fraction of pore blockages and particle size (Figure 7). As with the previous simulations, increasing blockages shifted the timescales associated with escaping to higher times. However, unlike the full particle simulations, the shift was observed to be more substantial in larger particles where the ratio of internal to surface sites is increased.

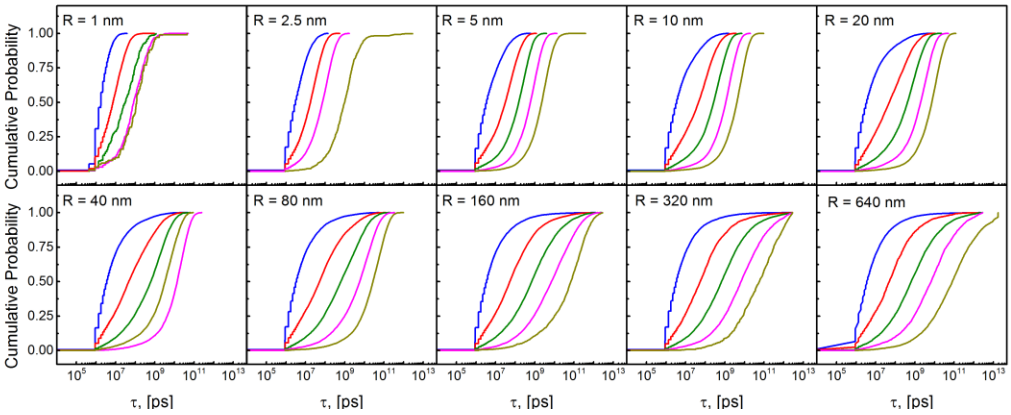

Figure 9-7: Escape times for a particle starting on the inner surface of a particle and diffusing through internal jumps until successfully exiting the particle. Cumulative distributions are plotted for escape times at several particle sizes and probabilities of open surface pores.

The average time associated with escape is nearly constant for the ideal particles (Figure 8A). As particle sizes the timescale associated with escaping the surface asymptotes as the sample dimension becomes sufficiently large that the particle approximates a semi-infinite medium. Similarly, examining the guest molecule displacement reveals little mobility for the ideal crystal, and substantially more mobility as blockages are introduced. The average displacements plotted here are limited by the maximum possible displacement defined by the particle geometry. Again, the values approach asymptotic values and become independent of particle size as the particle becomes sufficiently large that the simulations approach a semi-infinite medium. This effect is further observed in Figure 8C where a molecule initially placed on the xy plane (Z = R), transitions from escaping from the original surface on which it was positioned (low fraction of blockages, large particle sizes) to an equilibrium distribution of surfaces (high fraction of pore blockages, small particles).

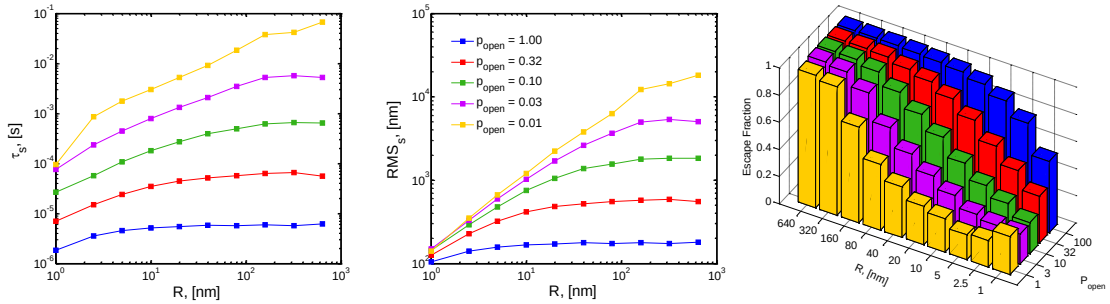

Figure 9-8: **A.** Time required to escape an ideal crystal displayed no dependence on particle size . Introducing pore blockages increased the escape time at each particle size. A near linear dependence on particle size was observed at low particle sizes before the particle size became a semiinfinite medium with no particle size dependence. The smallest crystal representing a single lattice cell showed lower escape times due to the cubic geometry. **B.** The root mean square displacement showed a similar effect with the ideal crystal showing little displacement from the initial location, while larger fractions of pore blockages exhibit greater displacements. **C.** Particles initially centered on the internal surface of x-y plane at at Z = R escape the particle through the X, Y or Z surface. In large particles and those with few surface pore blockages, nearly all molecules exit the Z surface. Smaller particles with substantial pore blockages exit through a distribution of X, Y and Z surfaces.

ZLC curves were collected at T = 50, 70, 90, 110 °C for benzene in silicalite-1 particles of sizes, R = 3 μm, 1 μm, 700 nm, 200 nm, 62 nm. The release profiles and model fits are shown in Figure 9 in the "short time" analyses described by Ruthven et al. The resulting values for apparent diffusivity are plotted in the typical Arrhenius format in Figure 10. As with other molecules in silicalite-1,5 benzene displays a substantial particle size dependence for the apparent diffusivity while the energetics remain constant. The apparent diffusivity is observed to decrease over three orders of magnitude as the particle size decreases from 3 μm to 62 nm.

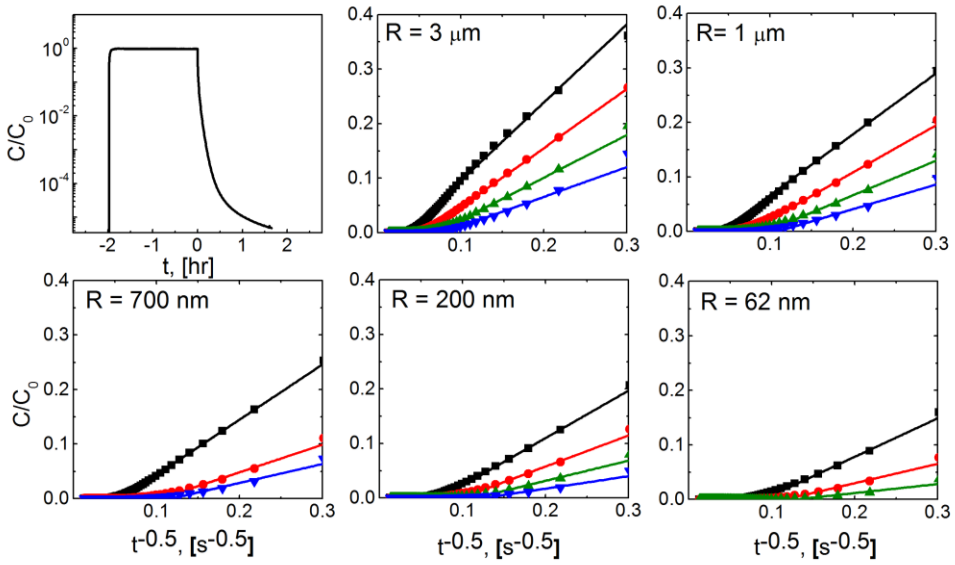

Figure 9-9: Zero Length Chromatography release profiles for benzene in silicalite-1 particles ranging from 62 nm – 3 μm at temperatures from 50-110 C. Short time analysis fits (solid lines) were performed on the linear region of the release profiles.Black:50C, Red:70, Green:90, Blue:110

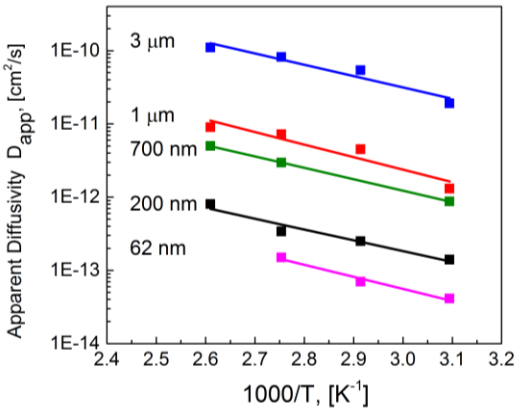

Figure 9-10: Arrhenius relationships plotting apparent diffusivity for temperatures from 50 – 110 C for five distinct particle sizes ranging three orders of magnitude. Constant activation energies are observed, with a pre-exponential decreasing over orders of magnitude, indicating a diffusion controlled surface barrier. Activation energy = 30 kJ/mol-K.

By performing both simulations and experiments on particles ranging in size over several orders of magnitude, comparison of the two can be performed. Figure 11 displays the dimensionless ratio of the surface timeconstant to the intracrystalline diffusional timeconstant, $\lambda = \tau_s/\tau_D$ versus particle size. The experimental values for the contribution to the apparent diffusivities by the surface are most closely captured by surface pore blockages that result in popen ~ 10^{-3}.

9.5 Discussion:

The emergence of hierarchical zeolites has introduced an avenue for the fastest reaction and transport turnover in zeolitic systems. Lengthscales equal to that of a single lattice cell, c.a. 2 nm, have allowed for rapid access to internal sites and rapid transport through the crystals. However, the predicted potential for ultrafast diffusion through such materials ($\tau \sim 10^{-8}$–10^{-6} s)[6] has not yet been realized due to the existence of a second, rate controlling phenomena in small particles.

Combined transport/energetic studies have recently demonstrated that silicalite-1 exhibits a surface-dominated rate whereby the macroscopically observed transport rate is controlled by the transport through the surface, not the bulk of the microporous particles. Furthermore, it was shown that the energetic of both the uptake and release states are consistent with an asymmetric barrier whose energies match that of the adsorption (uptake) and diffusion (release) processes.

Surface pore blockages occur as a result of either a partial restriction or total bridging of surface pores. While high resolution TEM, SEM and AFM techniques have all attempted to visualize the small pore opening within MFI crystals (~5.6 A), no technique available has yet been able to characterize the surface to the level of resolution required to directly visualize blockages.

Recent work has attempted to characterize the true crystal morphology and pore orientation of MFI particles. However, due to the complex growth mechanism and various synthesis techniques, the existence of intergrowths, subcrystals and defects makes specificity of crystal morphology on such a level limiting, especially in small (< 1 μm) particles.

Elucidating the exact surface structure of zeolites remains a significant challenge and is the target of both experimental and theoretical studies.[4, 5, 7-9] Highly dependent on the synthesis methods, the surface is expected to result from a thermodynamic relaxation of dangling bonds at the outer surface of the particle during the final stages of crystallite growth.10 Additionally, the removal of structural directing agents, calcination, silylation and post synthesis acid treatment

steps may result in achieving several types of surface terminations, as described in Figure 2D. Such openings, partial or total blockages can present macroscopically as diffusional rate limitation.

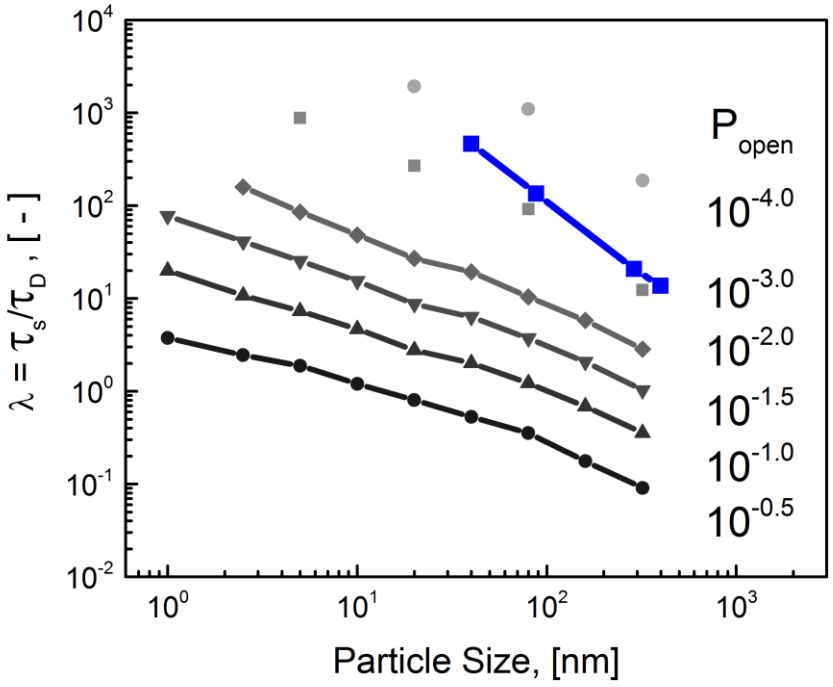

Figure 9-11: Dimensionless surface parameter transitions from bulk intraparticle diffusion controlled (lambda < 0) to surface controlled (lambda > 0) in small particles. Experimental diffusion parameters extracted from ZLC fall within the surface limited regime comparable to the 99.9% blocked simulations.

Surface barriers have been broadly discussed in literature as a possible class of transport limitations that contribute to the hindered transport in zeolite particles. Specifically, they have been traditionally discussed as a means of resolving macroscopic experimental techniques (ZLC, Frequency Response, Gravimetric) with those which examine small displacements within particle domains (PFG-NMR, QENS). Recently, the theory has been examined from a mechanistic standpoint, with post synthesis techniques such as hydrofluoric acid etching, surface silylation and various calcination techniques. While etching does visually produce a cleaner surface and at first glance appear to remove surface barriers, further research has revealed the later to be a result of introducing mesoporosity by harsh acid treatments.

9.5.1 Conclusions

Dynamic Monte Carlo simulations have been utilized to demonstrate the significance of surface pore blockages in MFI zeolites. To achieve experimentally observed diffusion limitations, pore blockages are predicted to exist blocking the vast majority of surface pores (>99.9%).

9.6 Supplementary Figures

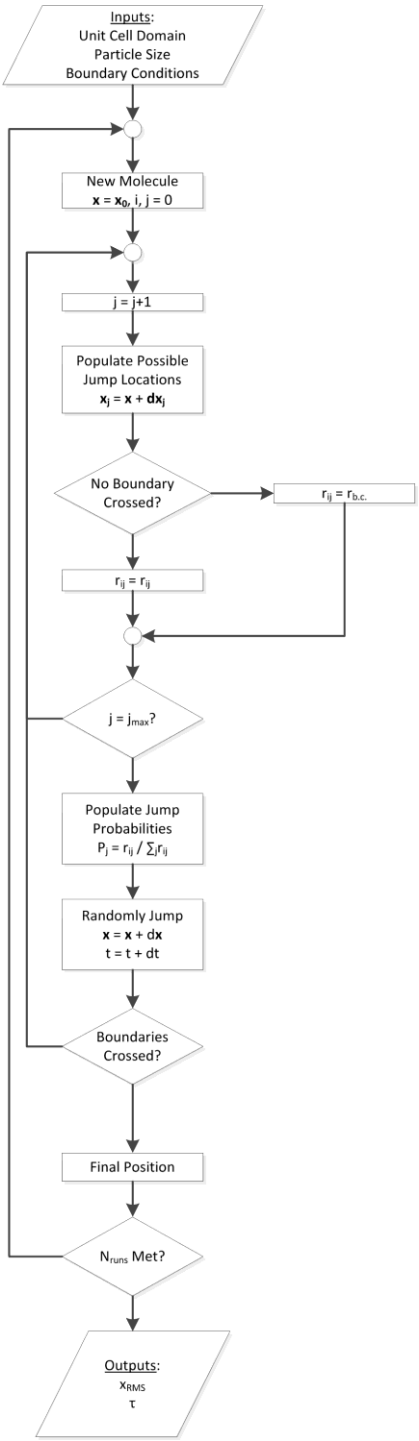

Figure 9-12: Agorithm for DyMC Simulations.

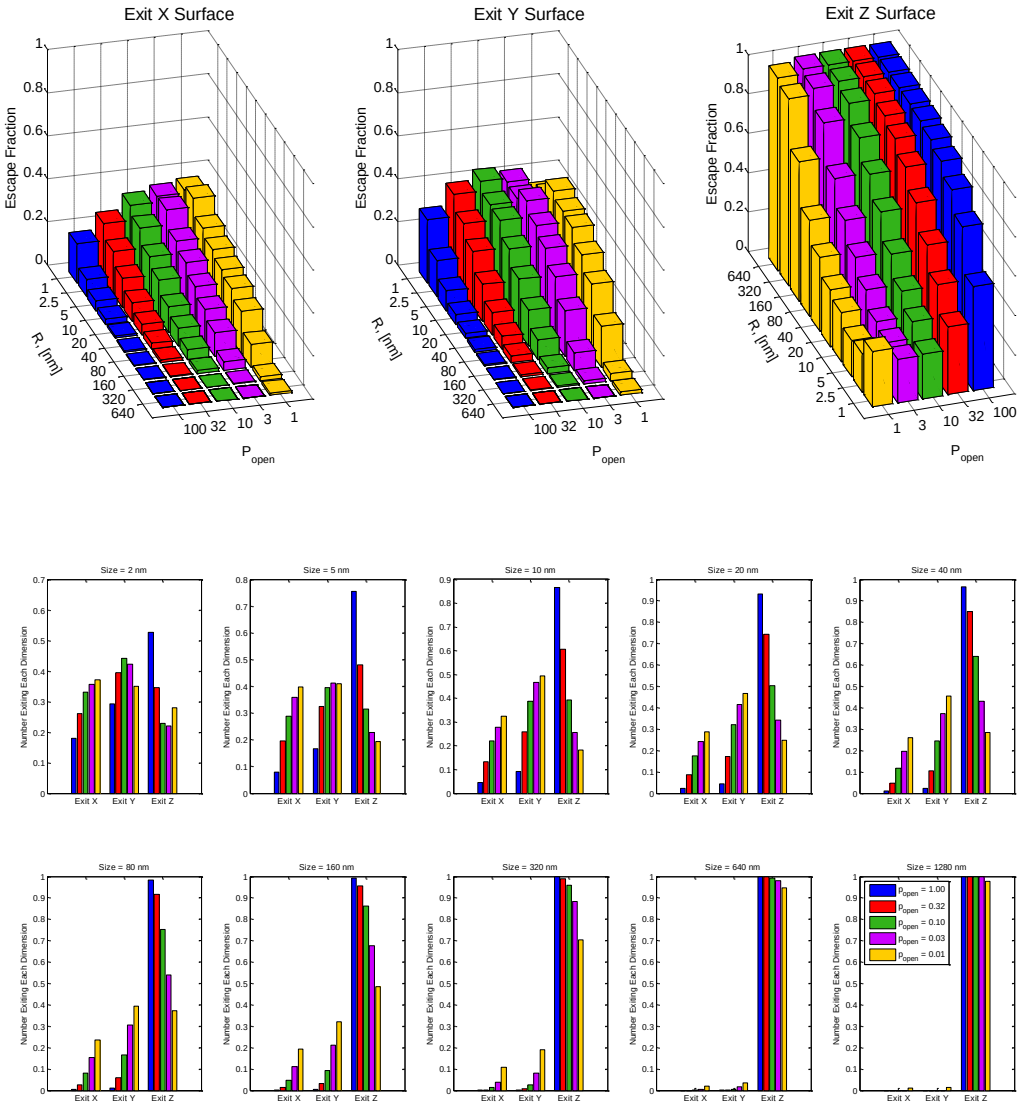

Figure 9-13: The apparent transport time varies in accordance with the typical scaling for a diffusion controlled system in particles without pore blockages (black). Large particles all converge to the intracrystalline controlled case, however small particles diverge with over an order of magnitude increase in transport time in the 0.97 blocked case

9.7 References

1. Chun-Chih Chang, S.K. Green, C.L. Williams, P.J. Dauenhauer, W. Fan "Ultra-Selective Cycloaddition of Dimethylfuran for Renewable p-Xylene with H-BEA," Green Chemistry 2014, 16, 585.
2. Moliner, M.; Roman-Leshkov, Y.; and Davis, M.E., "Tin-containing Zeolites Are Highly Active Catalysts for the Isomerization of Glucose in Water," *Proc. Nat. Acad. Sci.*, **107**, 6164-6168 (2010).
3. J.D. Rimer, M. Kumar, R. Li, A.I. Lupulescu, M.D. Oleksiak, "Tailoring the physicochemical properties of zeolite catalysts," Catalysis Science and Technology 2014, 4, 3762-3771.
4. Yuan, W. H.; Lin, Y. S.; Yang, W. S. J. Am. Chem. Soc. 2004, 126 (15), 4776-4777.
5. Lai, Z. P.; Bonilla, G.; Diaz, I.; Nery, J. G.; Sujaoti, K.; Amat, M. A.; Kokkoli, E.; Terasaki, O.; Thompson, R. W.; Tsapatsis, M.; Vlachos, D. G. Science 2003, 300 (5618), 456-460.
6. Zhang, X. Y.; Liu, D. X.; Xu, D. D.; Asahina, S.; Cychosz, K. A.; Agrawal, K. V.; Al Wahedi, Y.; Bhan, A.; Al Hashimi, S.; et al. Synthesis of Self-Pillared Zeolite Nanosheets by Repetitive Branching. Science 2012, 336, 1684−1687.
7. Zhang, X. Y.; Liu, D. X.; Xu, D. D.; Asahina, S.; Cychosz, K. A.; Agrawal, K. V.; Al Wahedi, Y.; Bhan, A.; Al Hashimi, S.Direct Synthesis of Self-Pillared Zeolite Nanosheets by Repetitive Branching. Abstracts of Papers, 244th National Meeting of the American Chemical Society, Philadelphia, PA, Aug 19−23, 2012244
8. M. Choi, K. Na, J. Kim. Y. Sakamoto, O. Terasaki, R. Ryoo, "Stable single-unit-cell nanosheets of zeolite MFI as active and long-lived catalysts," Nature 2009, 461, 246-249.
9. Gao, P.; Tai, M. H.; Sun, D. D. Hierarchical TiO2/ V2O5Multifunctional Membrane for Water Purification. ChemPlusChem 2013, 78, 1475−1482.
10. Du, K.; Liu, Y. Y.; Wathuthanthri, I.; Choi, C. H. Fabrication of Hierarchical Nanostructures Using Free-Standing Trilayer Membrane. J. Vac. Sci. Technol., B: Microelectron. Nanometer Struct.□Process., Meas., Phenom. 2013, 31, 06FF04−06FF041-11.
11. Yacou, C.; Ayral, A.; Giroir-Fendler, A.; Baylet, A.; Julbe, A. Catalytic Membrane Materials with a Hierarchical Porosity and Their Performance in Total Oxidation of Propene. Catal. Today 2010, 156, 216−222.
12. Fan, W.; Snyder, M. A.; Kumar, S.; Lee, P.-S.; Yoo, W. C.; McCormick, A. V.; Lee Penn, R.; Stein, A.; Tsapatsis, M. Hierarchical Nanofabrication of Microporous Crystals with Ordered Mesoporosity. Nat. Mater. 2008, 7, 984−991.
13. Chang, C.-C.; Teixeira, A. R.; Li, C.; Dauenhauer, P. J.; Fan, W. Enhanced Molecular Transport in Hierarchical Silicalite-1. Langmuir 2013, 29, 13943−13950.
14. Čejka, J.; Centi, G.; Perez-Pariente, J.; Roth, W. J. Zeolite-Based Materials for Novel Catalytic Applications: Opportunities, Perspectives and Open Problems. Catal. Today 2012, 179, 2−15.
15. Perez-Ramirez, J.; Christensen, C. H.; Egeblad, K.; Groen, J. C. Hierarchical Zeolites: Enhanced Utilisation of Microporous Crystals in Catalysis by Advances in Materials Design. Chem. Soc. Rev. 2008, 37, 2530−2542.
16. Na, K.; Choi, M.; Ryoo, R. Recent Advances in the Synthesis of Hierarchically Nanoporous Zeolites. Microporous Mesoporous Mater. 2013, 166, 3−19.
17. Holm, M. S.; Taarning, E.; Egeblad, K.; Christensen, C. H. Catalysis with Hierarchical Zeolites. Catal. Today 2011, 168, 3−16.
18. Kortunov, P.; Vasenkov, S.; Karger, J.; Valiullin, R.; Gottschalk,¨P.; FéElía, M.; Perez, M.; Stöcker, M.; Drescher, B.; McElhiney, G.; Berger, C.; Glaser, R.; Weitkamp, J. The

Role of Mesopores in¨Intracrystalline Transport in USY Zeolite: PFG NMR Diffusion Study on Various Length Scales. J. Am. Chem. Soc. 2005, 127, 13055−13059
19. Chun-Chih Chang, A.R. Teixeira, C. Li, P.J. Dauenhauer, Wei Fan, "Enhanced molecular transport in hierarchical silicalite-1," Langmuir 2013, 29, 13943.
20. I. Diaz, E. Kokkoli, O. Terasaki, M. Tsapatsis, "Surface structure of zeolite (MFI) crystals" Chem. Mater. 2004, 16, 5226.
21. Karger, J.; Pfeifer, H. *J. Chem. Soc., Faraday Trans.* **1991**, *87*, 1989.
22. Micke, A.; Bulow, M.; Kocirik, M. *J. Phys. Chem.* **1994**, *98*, 924.
23. Grenier, P.; Meunier, F.; Gray, P. G.; Ka¨ rger, J.; Xu, Z.; Ruthven, D. M. *Zeolites* **1994**, *14*, 242.
24. P. Kortunov, S. Vasenkov, C. Chmelik, J. Karger, D.M. Ruthven, J. Wloch, "Influence of defects on the external crystal surface on molecular uptake into MFI-type zeolites," Chem. Mater. 2004, 16, 3552.
25. A.R. Teixeira, C.C. Chang, T. Coogan, R. Kendall, W. Fan, P.J. Dauenhauer, "Dominance of Surface Barriers in Molecular Transport through Silicalite-1," Journal of Physical Chemistry C 2013, 117, 25545.
26. A.R. Teixeira, X. Qi, C.C. Chang, W. Fan, W.C. Conner, P.J. Dauenhauer, "On asymmetric surface barriers in MFI zeolites revealed by frequency response," Journal of Physical Chemistry C 2014, 118(38), 22166.
27. K. Yoshida, Y. Sasaki, H. Kurata, "High-resolution imaging of zeolite with aberration-corrected transmission electron microscopy," AIP Advances 2013, 3, 042113.
28. S. Kumar, T.M. Davis, H. Ramanan, R.L. Penn, M. Tsapatsis, "Aggregative growth of silicalite-1," J. Phys. Chem. B 2007, 111, 3398-3403.
29. O.C. Gobin, S.J. Reitmeier, A. Jentys, J.A. Lercher, "Role of surface modification on the transport of hexane isomers in ZSM-5," J. Phys. Chem. C 2011, 115, 1171-1179.
30. Ohsuna, T.; Horikawa, Y.; Hiraga, K.; Terasaki, O. *Chem. Mater.* **1998**, *10* (3), 688-691.
31. Alfredsson, V.; Ohsuna, T.; Terasaki, O.; Bovin, J.-O. *Angew. Chem. Int. Ed.* **1993**, *32* (8), 1210-1213.
32. Slater, B.; Catlow, C. R. A.; Liu, Z.; Ohsuna, T.; Terasaki, O.; Camblor, M. A. *Angew. Chem. Int. Ed.* **2002**, *41* (7), 1235-1237.
33. A.I. Lupulescu, J.D. Rimer, "In situ imaging of silicalite-1 surface growth reveals the mechanism of crystallization," Science 2014, 344, 729.

CONCLUSIONS

The purpose of this thesis was to 1) develop an understanding of the fundamental transport phenomena controlling reactive liquid intermediate cellulose during fast pyrolysis, and 2) reveal the mechanism for the rate controlling mass transfer limitations dominating turnover in small and hierarchical zeolite particles.

Chapters 1, 2 and 3 describe the existence of the reactive liquid intermediate that exists during biomass pyrolysis under high heat flux at temperatures greater than 500 °C. The mechanism for nonvolatile transport during biomass fast pyrolysis has been elucidated in Chapters1 and 2; aerosol ejections were experimentally visualized and the reactive boiling ejection mechanism was confirmed computationally. At higher heat fluxes, intermediate liquid cellulose is observed to dewet ablative pyrolysis surfaces, undergoing film boiling causing the Leidenfrost effect described in Chapter 3. Surface chemistry and structural effects were explored and described to increase heat flux and shift the Leidenfrost transition temperature. Two new techniques were developed (Quantitative Carbon Detector, Diffuse Reflectance *in situ* Spectroscopy of Particles, Chapter 4) to advance the capability of quantitatively describing the complex reaction system controlling biomass fast pyrolysis. Finally, bio-oil fluid dynamics were explored (Chapter 5) during heating, and microexplosions were visualized and mechanistically explored. Collectively, this work on biomass pyrolysis provided a new level of insight into the heat and mass transport mechanisms controlling the conversion processes, with specific insight being presented on the intermediate liquid phase.

Chapters 6 through 8 focused on revealing the existence of substantial mass transport limitations dominating the transport into small and hierarchical zeolites (Chapters 6 and 7). Such limitations were observed to decrease the transport rates by as much as three orders of magnitude, and a size-dependant relationship was established to explore several possible mechanisms for the limitations including internal defects, surface pore narrowing, and surface pore blockages

(Chapters 7 and 8). By examinging the transport rates at several temperatures for many particles under uptake and release conditions, the energetics of the surface effect were established experimentally and the barriers were determined to likely occur from the blockage of the majority of surface pores. Additionally, dynamic Monte Carlo simulations were performed to elucidate the role of surface pore blockages on the model MFI system (Chapter 9). The work in this second section provided fundamental insight into the existence and mechanism of diffusion limitations in zeolites. Moving forward, this rate limitation and mechanism will dominate the new class of hierarchical materials with lengthscales being synthesize on the order of nanometers.

FUTURE DIRECTIONS AND RECOMMENDATIONS

The insight provided here with regard to cellulose and biomass fast pyrolysis enhanced the fundamental understanding of the existence of the reactive liquid intermediate and several key mechanisms dominating its dynamics. Howerver, substantial work remains in advancing both the fundementals and implications of these understandings. From the fundamental perspective, the transient composition and reactivity of the liquid melt are not yet understood. Specifically, at what is the pathway from solid biopolymer to liquid oligermer, and how do those oligomers progress to volatile components. The existence of heat and mass transfer limitations within the reacting particle (0.01-1 mm) should also be explored with particular emphasis on the phase transitions from solid to liquid and liquid to vapor. Exploration of the residence time distributions and correlations to product distributions could provide insight into pathways for tuning the complex reaction chemistry occurring during biomass pyrolysis.

From the applied perspective, using existing basic understanding of the liquid melt, new approaches for controlling the reaction environment can be proposed such that the product yields and distribution can be tuned. Specifically, elucidating the impact of heat and mass transport limitations (heating rates, particle size), surface structure (polished, rough, templated, macropores, micropores), and surface chemistry (acidity, functionalization). Such tenability may cause superior wetting (and thus heating), promote dewetting (reduce surface chemistry/nucleation), and increase residence time in the melt (thus allowing for secondary reactions). Also, while the mechanism for aerosol generation is shown in this work, steps need to be made toward understanding the role of the solid surfaces (cellulose and substrate) on nucleating bubble formation, and determining whether aerosols can be promoted or surprised in reaction systems.

The work on describing the role of surface barriers on microporous diffusion in small and hierarchical zeolites has proved to be a substantial challenge due to the lack of experimental

resolution of the surface structure of zeolites and theoretical understanding of the growth and relaxation mechanism for zeolite surfaces. Moving forward, the most impactful insight into the existence and cause of these surface barriers should come from an experimental investigation of the surface structure of zeolites. While some work has been performed to characterize surface structures using AFM, HRTEM and scanning HRTEM, insufficient resolution has been provided to observe the sub angstrom level resolution needed to observe even small deviations in pore geometries that can result in transport barriers. From a macroscopic scale, diffusion experiments (ZLC, FR, gravimetric, IFM) can be designed to examine the role of guest molecule size, shape, and adsorption energy on these barriers. The discrepancies observed between uptake and release profiles may also provide an interesting perspective for examining the mechanism at the surface. Additionally, post synthesis surface modifications (HF etching, amorphous silica layers, etc.) have been performed in an attempt to reduce the barriers, however increased rates have only been observed due to the introduction of disordered mesopores. If applied in a systematic manner, however, these techniques may help elucidate the mechanisms for surface barriers. Additionally, the use of a simpler lattice structure with either fewer intergrowths or one dimensional pores may allow for further simplification of the complex system.